MTL TR 90-46 AD-A228 958

A COMPUTATIONAL AND EXPERIMENTAL INVESTIGATION OF MODE I FRACTURE IN AN ELASTOMER

CLAUDIA J. QUIGLEY
MECHANICS AND STRUCTURES BRANCH

September 1990

DTIC
ELECTE
NOV 14 1990
S
E D

US ARMY
LABORATORY COMMAND
MATERIALS TECHNOLOGY LABORATORY

U.S. ARMY MATERIALS TECHNOLOGY LABORATORY
Watertown, Massachusetts 02172-0001

90 11 13 198

DISPOSITION INSTRUCTIONS

REPORT DOCUMENTATION PAGE		READ INSTRUCTIONS BEFORE COMPLETING FORM
1. REPORT NUMBER MTL TR 90-46	2. GOVT ACCESSION NO.	3. RECIPIENT'S CATALOG NUMBER
4. TITLE *(and Subtitle)* A COMPUTATIONAL AND EXPERIMENTAL INVESTIGATION OF MODE I FRACTURE IN AN ELASTOMER		5. TYPE OF REPORT & PERIOD COVERED Final Report
		6 PERFORMING ORG. REPORT NUMBER
7. AUTHOR(s) Claudia J. Quigley		8. CONTRACT OR GRANT NUMBER(s)
9. PERFORMING ORGANIZATION NAME AND ADDRESS U.S. Army Materials Technology Laboratory Watertown, Massachusetts 02172-0001 ATTN: SLCMT-MRS		10. PROGRAM ELEMENT, PROJECT, TASK AREA & WORK UNIT NUMBERS
11. CONTROLLING OFFICE NAME AND ADDRESS U.S. Army Laboratory Command 2800 Powder Mill Road Adelphi, Maryland 20783-1145		12. REPORT DATE September 1990
		13. NUMBER OF PAGES 223
14. MONITORING AGENCY NAME & ADDRESS *(if different from Controlling Office)*		15. SECURITY CLASS. *(of this report)* Unclassified
		15a. DECLASSIFICATION/DOWNGRADING SCHEDULE

16. DISTRIBUTION STATEMENT *(of this Report)*

Approved for public release; distribution unlimited.

17. DISTRIBUTION STATEMENT *(of the abstract entered in Block 20, if different from Report)*

19. KEY WORDS *(Continue on reverse side if necessary and identify by block number)*

Fractures (materials) .	Crack propagation
Elastomers	Fracture properties
Cavitation	Tearing

20. ABSTRACT *(Continue on reverse side if necessary and identify by block number)*

(SEE REVERSE SIDE)

Block No. 20

ABSTRACT

A thickness effect was identified in the Mode I fracture of incompressible hyper-elastic materials. The plane strain mechanical crack tip field was examined under the assumptions of small scale nonlinearity using the finite element method. The effect of the constitutive law on the numerical results was determined by using two different invariants of the Rivlin constitutive model: the Mooney-Rivlin law and the third order invariant. Crack tip field quantities from both constitutive laws agreed with the nonlinear asymptotic solution for this problem, although the region of dominance was small. The nature of the nonlinear crack tip zone was characterized both geometrically and kinematically. Application of a local cavitation criterion to the mechanical crack tip field showed a relationship between the physical properties of a carbon black filled natural rubber and a critical cavitation event ahead of the crack tip to the amount of subcritical crack growth prior to crack propagation.

Experiments were also performed to study the thickness effect under near plane strain conditions. Deeply notched cylindrical dumbbell test specimens made from a carbon black filled elastomer were loaded in tension until fracture at finite strains. A failure process consisting of extensive blunting of the crack tip, delamination, and stable crack extension normal to the load direction (i.e., orthogonal to the pre-existing crack plane) was observed. This process was initialized under small loads and continued until ultimate rupture of the test specimen into two pieces. As the specimen elongated, the thickness of successive layers of delaminated material and the incremental amount of stable crack extension increased. Load and CMOD histories were smooth and could not be related to the localized material failure occurring under deformation. The value of the J-integral at catastrophic rupture was $400 kJ/m^2$. A model was presented to explain this failure process.

Preface

The research presented in this report was performed at the U.S. Army Materials Technology Laboratory in Watertown, Massachusetts and at the Massachusetts Institute of Technology in Cambridge, Massachusetts. This report is an excerpt of the Master's thesis of the author. The thesis was completed in January, 1990, under the supervision of Professor David M. Parks, in the Department of Mechanical Engineering at the Massachusetts Institute of Technology.

I would like to acknowledge the support of my husband, Joe, and my son, Joey, whose support and encouragement made this thesis possible.

I also thank the following employees at the Army Materials Technology Laboratory for their assistance in the experimental investigation: Robert Dooley, Christopher Cavallaro, Robert Anatasi, Kristin Weight, and Thomas Harkins. Their expertise contributed to the success and timely completion of the experimental work.

Finally, I would like to thank my supervisor at the Army Materials Technology Laboratory, Dr. Arthur Johnson, and my thesis supervisor, Professor David Parks, for their guidance and support throughout the completion of this research.

Accession For		
NTIS GRA&I		☒
DTIC TAB		☐
Unannounced		☐
Justification		
By		
Distribution/		
Availability Codes		
Dist	Avail and/or Special	
A-1		

Contents

List of Figures

List of Tables

Chapter 1

Introduction

1.1 Scope of Investigation

Elastomers are polymers, consisting of long flexible chainlike molecules, interconnected by crossbonds, a phenomenon referred to as crosslinking. Their mechanical behavior can be classified as nonlinear elastic. Material properties, such as the Young's modulus are small compared to metals and ceramics. Typical values of the Young's modulus are of the order 10 MPa for rubber while for metals, the Young's modulus is much higher, approximately 10^4 MPa. Elastomers are nearly incompressible materials with a Poisson's ratio close to 1/2 and high bulk moduli in comparison to their shear or Young's moduli.

This investigation identifies a thickness effect in the Mode I fracture of elastomer materials. Interest in this subject arose from premature internal failure of Army tank track pads, which are thick elastomer blocks bonded to steel plates. While much fracture research has been performed on thin elastomer sheets, few experimental or numerical studies in the literature have addressed failure of *thick* elastomer materials.

A thickness effect in the failure of metals [1] and certain ductile polymers [2] has been documented, suggesting that thickness may also influence fracture in elastomers. This effect, though, may not be the same as that found in other materials. Void formation in elastomers has been shown to be a thickness dependent process, where the conditions for void formation, e.g., high triaxiality of stress, can be enhanced by increasing the thickness of the test specimen [3,4].

Both numerical and experimental studies were performed to characterize this thickness effect. First, a computational analysis of a Mode I crack under plane

strain conditions determined the nonlinear elastic crack tip field and its region of dominance when the nonlinear elastic field is confined to a small region around the crack tip. The results were compared to the nonlinear elastic asymptotic solution [5,6] for this problem. A local cavitation criterion was also applied to determine the location of void formation in front of the crack tip. Previous numerical studies [7] of a Mode I plane strain crack have been limited to only determining the value of the J-integral and did not examine the stress field close to the crack tip.

In addition, experiments were conducted to investigate the failure process, under near plane strain conditions, in a carbon black filled elastomer. A conventional test specimen for examining failure in thick elastomers under near plane strain conditions has not been reported in the literature so that an appropriate test specimen had to be designed. The fracture process was observed both qualitatively and quantitatively, confirming that a thickness effect is present in the failure mode of these materials.

As a prelude to the research reported here, the failure process in thin elastomer sheets will be described and literature supporting the premise that thickness influences the mode of failure in hyperelastic materials will be presented.

1.2 Approach

A fracture mechanics approach was taken in this investigation. Material behavior is described by continuum mechanics, and here it is assumed that elastomers are homogeneous and isotropic. The underlying basis of fracture mechanics is that a unique singular stress strain field exists at the crack tip and that the amplitude of this singular field can sometimes be determined from energy balance considerations. A critical energy release rate, G_c, is defined where crack extension and material failure will occur when the energy release rate exceeds G_c. This approach is limiting in the sense that elastomers can exhibit molecular anisotropy and because stresses and strains in elastomers are temperature and rate dependent functions, a consequence of viscoelasticity. In addition, viscoelastic mechanisms play an important role in failure processes [8,9].

Another approach taken to describe fracture in these material is the molecular theory of fracture [10,11,9] which assumes that failure occurs through the breakage of primary bonds or through the breakage of chains at or between crosslinks. The time and temperature dependence of the stress fields can be explained by the deformation behavior of the molecules and the finite extensibility of the molecular strands. This approach employs a stress based failure criterion.

1.3 Hysteresis

Elastomers are self-reinforcing in that they possess built-in mechanisms which delay and retard crack growth. The high extensibility and chain alignment of rubbers allow large strains to exist at the crack tip, promoting crack tip blunting. During tensile deformations at slow deformation rates, elastomer molecules may slide apart and fresh surface area is created by surface enlargement [9]. (This phenomenon is also found in knotty tearing, to be discussed below.) Energy dissipating mechanisms, or hysteresis, also assist crack tip blunting and in subcritical crack growth, hysteresis may decrease the intensity of the crack tip stress field by weakening the material at the crack tip [11]. At rupture, the energy density is directly related to the amount of hysteresis measured in the material [12]. Because elastomers are able to dissipate energy through hysteresis, less energy is available for crack growth and rupture [8].

Hysteresis is attributed to many factors, such as stress softening or the Mullins effect, internal friction, strain-induced crystallization, structural breakdown, and the presence of two-phase material systems, such as copolymers [8,2]. Each of these factors contributes to fracture resistance. A final source of energy dissipation is heat generated under fatigue loading.

Internal friction or viscosity refers to the rearrangement of molecular chains as they deform. This phenomenon is strongly temperature dependent. The viscosity characterizes the immobility of molecular segments and decreases with increasing temperature. Viscous stresses at constant temperature also depend on the rate of deformation and are more dominant at high rates. At the glass transition temperature, T_g, the viscosity becomes sufficiently small, while at temperatures below T_g, elastomers are more stiff and will fracture under smaller deformations.

When an elastomer is stretched to a high strain and then unloaded, the unloading stress strain path is below the loading path, as in Figure 1.1, dissipating energy during the deformation cycle. This phenomenon is called stress softening or the Mullins effect. For filled rubbers, permanent set is also present where, upon completion of a load deformation cycle, a small but measurable amount of residual deformation remains. In crack growth, the material close to the crack undergoes a full load deformation cycle. Referring to Figure 1.2, material at the crack tip is highly deformed, and when the crack extends, load is removed from this highly deformed material as the new traction-free crack surface is created. Consequently, a volume element of material at the crack tip undergoes a load deformation cycle as it becomes new surface area during crack extension.

Strain-induced crystallization refers to the formation of nonpermanent microcrystalline regions in natural rubbers undergoing large deformations. When load is removed. the crystalline regions melt. Regions of strain-induced crystallization have been found at the highly deformed crack tip [3.9]. However. as the crack extends. microcrystals melt and reform. dissipating energy in the process. Rubbers exhibiting this type of behavior, such as natural rubbers, have greater tearing energies than those such as SBR, which do not strain-crystallize.

Structural breakdown of a filled elastomer occurs when long chains of carbon black or other filler particles and/or bonds between th ller particles and the rubber molecules are broken under deformation. The energy expended in structural breakdown is irreversible.

1.4 Tearing Energy

1.4.1 Definition

Rivlin and Thomas [13] developed the tearing energy theory by extending the Griffith fracture criterion to include irreversible energy losses. Given a crack of length L. the tearing energy, T, is defined as

$$-\left(\frac{\partial U}{\partial L}\right)_P \left(\frac{1}{t}\right) \geq T ,$$

(1.1)

where $(\partial U/\partial L)$ denotes the change in potential energy per unit crack extension at constant load. P, and t is the specimen thickness. Equation (1.1) simply states that crack propagation in rubber occurs when the energy required for crack growth exceeds the tearing energy. which includes the surface energy required for the creation of new fracture surfaces, as well as localized irreversible energy losses at the crack tip. The tearing energy is equivalent to G_c when crack extension occurs.

The tearing energy has been experimentally proven independent of the load conditions and in-plane aspects of specimen geometry [13] for quasi-static crack growth. The test specimens, to be discussed below, are designed such that small amounts of irreversible elasticity are present only at the crack tip, even though large deformations may be found throughout the test specimen.

The magnitude of the tearing energy at the onset of tearing is T_c. As the test specimen is slowly extended, small amounts of crack extension, approximately 0.01 mm. are found under small loads. As the load is increased, the crack extends
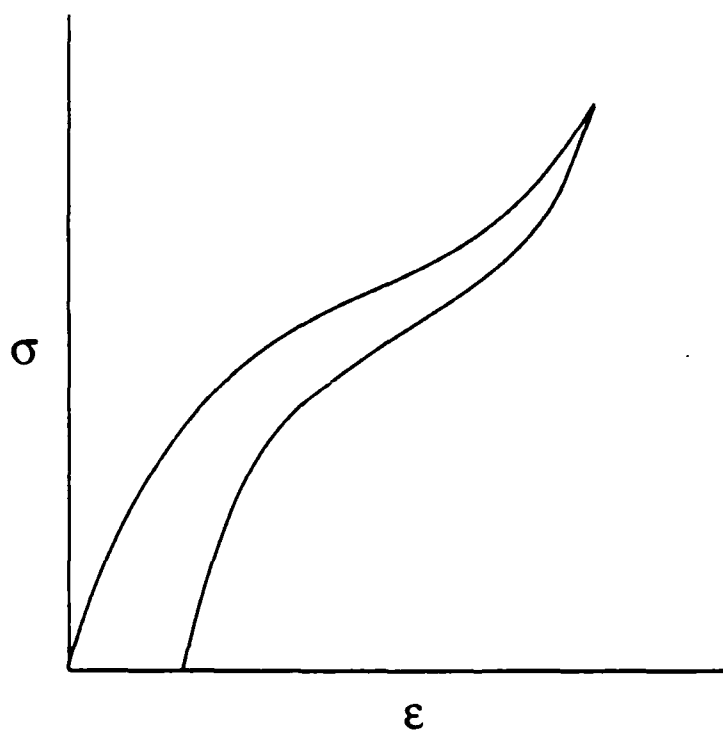
Figure 1.1: A loading and unloading path in an elastomer.

L

Highly deformed material at the crack tip (A).

L + δL

A

Highly deformed material (A) is now part of the traction free crack surface through crack extension.
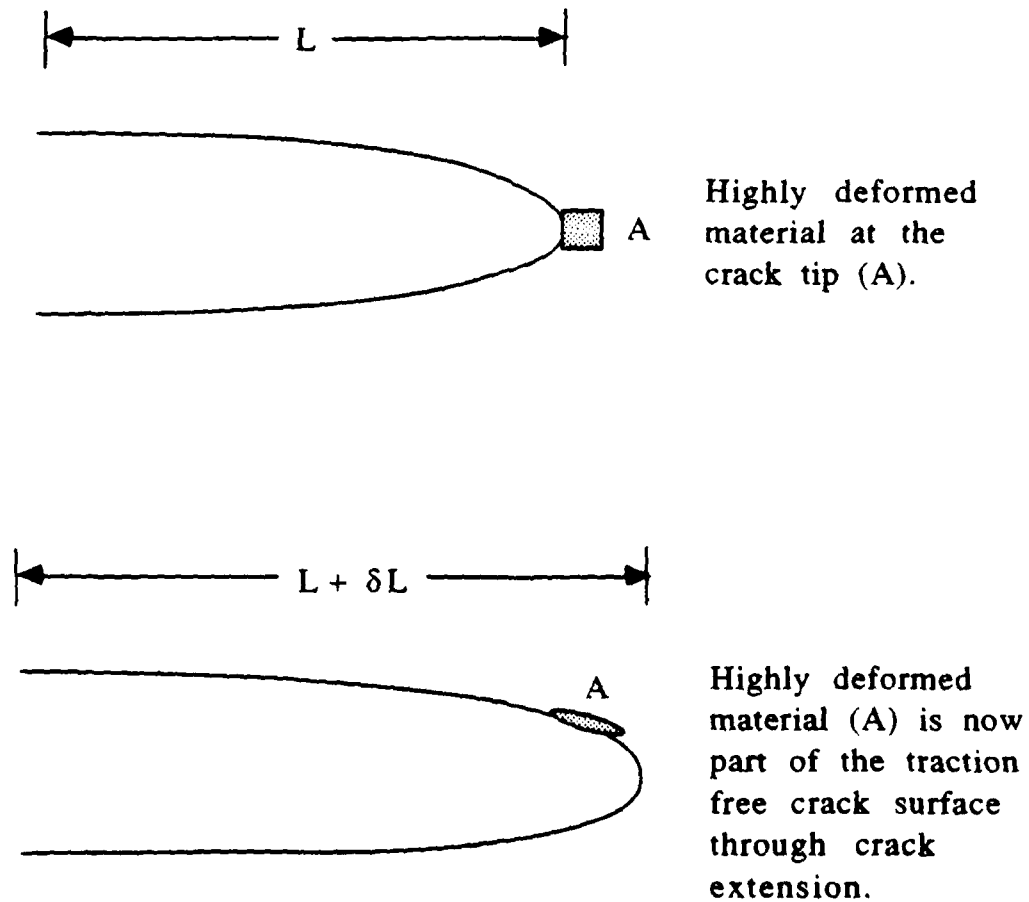
Figure 1.2: Material at the crack tip undergoing a load deformation cycle.

further. Catastrophic rupture occurs when the crack suddenly grows by several millimeters. When additional load is applied, the crack continues to grow by this amount. The tearing energy, T_c, is measured when catastrophic rupture begins and is considered a material property.

The dependence of the the tearing energy on the rate of crack propagation, i.e., the rate at which the specimen is deformed, and the temperature [14,15] demonstrate that a single value of the tearing energy required for crack propagation does not exist for a given elastomer. Typical master curves for the tearing energy, Figure 1.3, illustrates this dependence. At high strain rates and low temperatures, experimentally measured values of the tearing energy are higher compared to those at low strain rates and high temperatures, although the slopes of these curves may not be steadily increasing with temperature or rate of tearing.

1.4.2   Test Specimens for Measuring Tearing Energy

The test specimens most commonly used to measure tearing energy in thin elastomer sheets are the single-edge crack, the pure shear, and the trouser tear specimens. Specimen geometries are shown in Figure 1.4 as well as equations for determining T_c. These expressions for T_c are based on the assumptions that the region of irreversible energy losses are confined to a small region at the crack tip and that L is large compared to the specimen thickness. In addition, these specimens were designed so that large regions exist where simple deformations are present, i.e., simple extension in the single-edge crack specimen and pure shear in the pure shear specimen. The single-edge crack and the pure shear specimen measure the tearing energy under Mode I failure while the trouser tear specimen measures the tearing energy in anti-plane shear, Mode III. In Mode III, T_c is approximately 50% greater than in Mode I [16].

1.4.3   Equivalence to J-Integral

For a stationary crack extending in the x_1-direction and oriented as in Figure 1.5, the path independent J-integral [17] can be represented as

$$J = \int_\Gamma [W n_1 - s_i u_{i,1}] \, dS \ , \tag{1.2}$$

where W denotes the strain energy, n_1 is the unit normal in the x_1 direction, s_i is the nominal traction vector, and u_i is the displacement field. The J-integral is evaluated along any suitable contour, Γ, which encloses the crack tip and dS
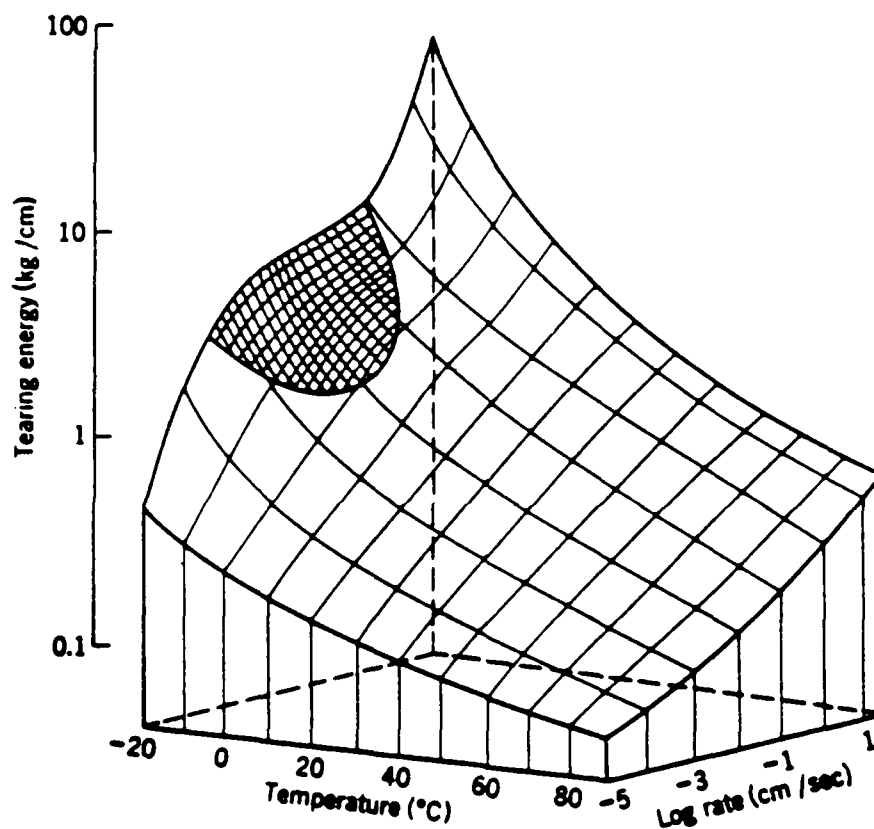
(a) SBR gum vulcanizate (shaded portion denotes region where stick-slip tearing is found.)

Figure 1.3: Tearing energy surface for an SBR gum vulcanizate and its dependence on the temperature and the rate of tearing. From Greensmith, H.W., Rupture of rubber. VII. "Comparison of Tear and Tensile Rupture Measurement", *J. App. Poly. Sci.*, 3(8), (1960), p.189.

1.4 TEARING ENERGY
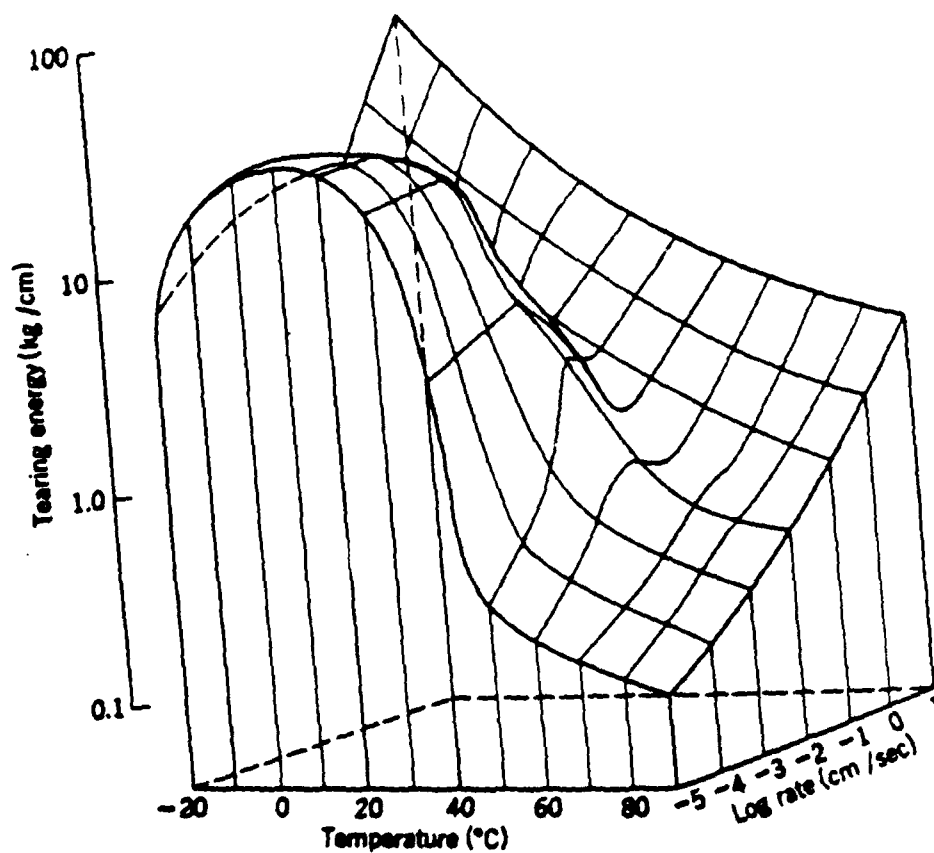
(b) Carbon black filled SBR.

Figure 1.3: Tearing energy surface for an SBR gum vulcanizate and its dependence on the temperature and the rate of tearing.
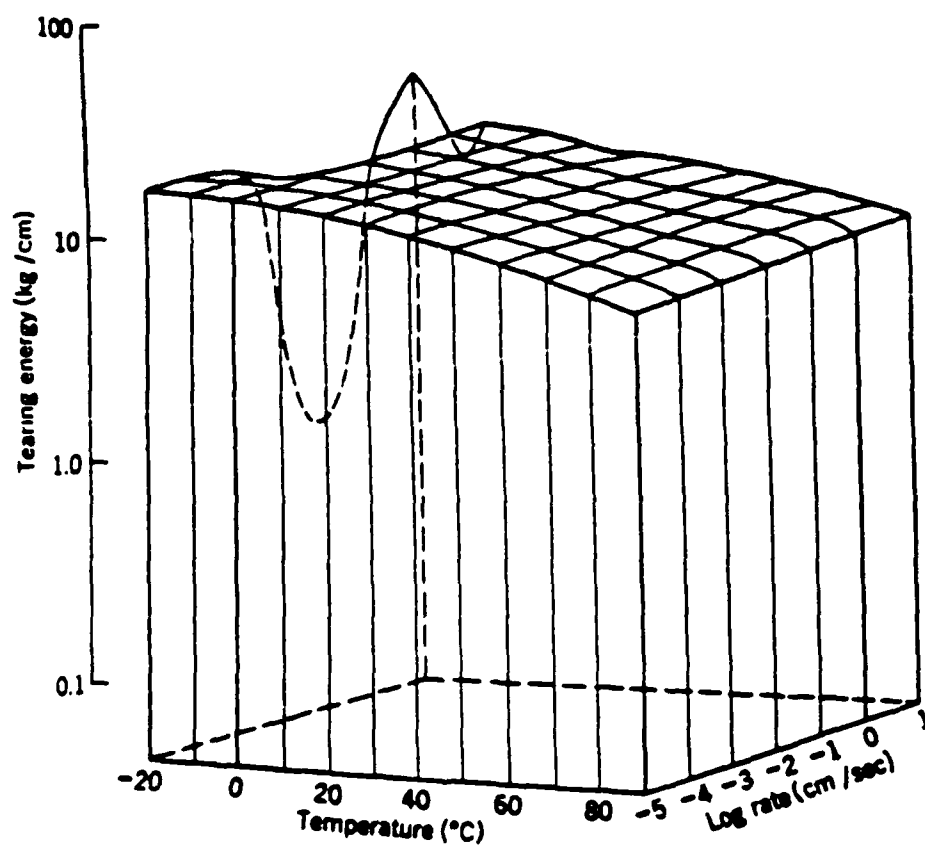
(c) Natural gum rubber vulcanizate.

Figure 1.3: Tearing energy surface for an SBR gum vulcanizate and its dependence on the temperature and the rate of tearing.
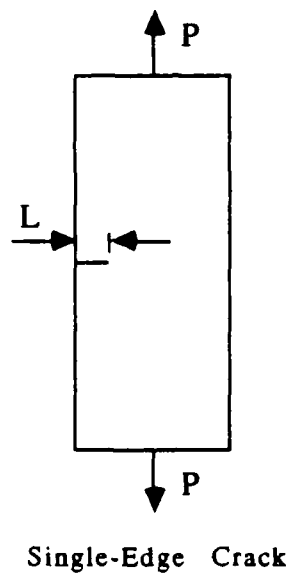
Single-Edge Crack

$$T_c = 2\frac{\pi}{\lambda_c^{1/2}}LW_c$$

λ_c = Extension ratio at onset of crack growth.

W_c = Strain energy density at onset of crack growth.

(a) Single-edge crack specimen.

Figure 1.4: Test geometries used to measure tearing energy
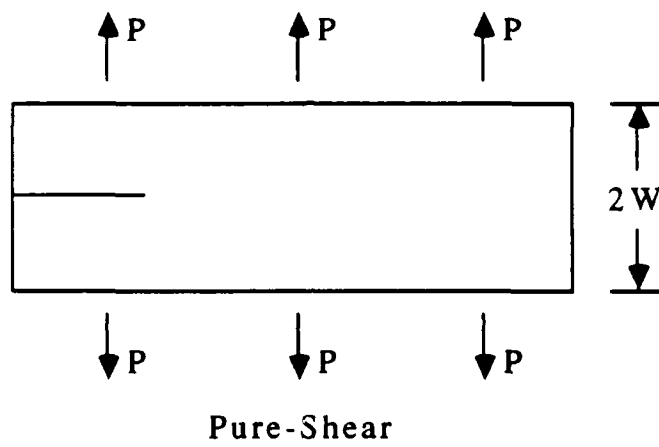
Pure-Shear

$$T_c = 2w W_c$$
$$2w = \text{Specimen width.}$$

(b) Pure-shear specimen.

Figure 1.4: Test geometries used to measure tearing energy.
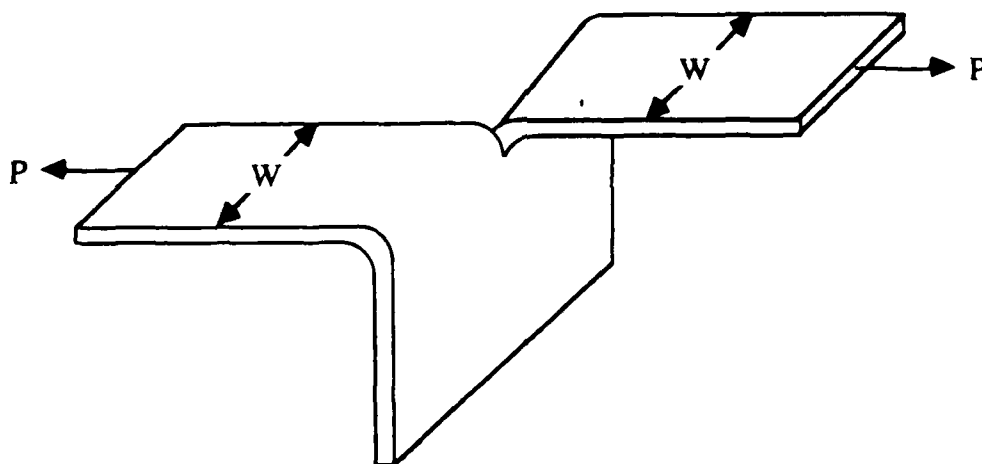
Trouser-Tear

$$T_c = \frac{2P_c\lambda_c}{h} - 2wW_c$$

P_c = Load at onset of crack growth.

h = Specimen thickness.

λ_c = Extension ratio at onset of crack growth in arms.

W_c = Strain energy density at onset of crack growth in arms.

(c) Trouser-tear specimen.

Figure 1.4: Test geometries used to measure tearing energy.

is an element along Γ. The equivalence of the J-integral to the tearing energy. equation (1.1), was proven by Chang [18]. The significance of both the J-integral and the tearing energy in nonlinear elasticity is that they are fracture characterizing parameters. Experimentally measured far from the crack tip, the value of the tearing energy shows a one to one correspondence with the strain distribution at the tip of a thin notch of arbitrary width [19].

1.5 Crack Propagation

The failure mode in thin elastomer sheets has been well documented [8,9,2]. Failure initializes in a region of high stress concentrations with the enlargement of a flaw or the formation of a crack. The crack then grows at a constant or progressively increasing rate until a critical instability occurs. The test specimen ultimately fails by rupture normal to the maximum principal stress. The size of naturally occurring flaws which govern the fracture process is estimated as $\sim 10^{-3}$ cm [20] and their presence under deformation causes local rupture of isolated molecules or crosslinks.

As natural rubber deforms, molecular chain alignment and crystallization begins when $\lambda > 3$ [9]. These mechanisms enhance crack tip blunting and retard crack growth. Other mechanisms which decrease the amount of energy available for crack propagation, discussed previously, may also be present.

Under monotonic loading, crack propagation can be divided into three categories based on the magnitude of the tearing energy, T. Below T_0, 40 J/m^2 [8], no crack growth is found and elastic loading of the crack tip occurs without crack extension. Subcritical crack growth occurs when $T_0 < T < T_c$ and initiates by reorientation and slippage of molecular chains or void growth. Elastic loading continues but, due to crack extension, viscoelasticity and hysteresis influence the intensity of the crack tip field. Because subsequent material response is softer, subcritical crack growth is stable [11]. Finally, when T exceeds T_c, the crack extends by a large amount, several millimeters, ultimately leading to rupture.

In unfilled elastomers, steady or smooth crack propagation is typically observed, where crack propagation occurs directly in front of the crack, with smooth tear surfaces. As crack extension proceeds, small fluctuations in the load can be found, as shown in Figure 1.6, while the crack surfaces becomes increasingly rough.
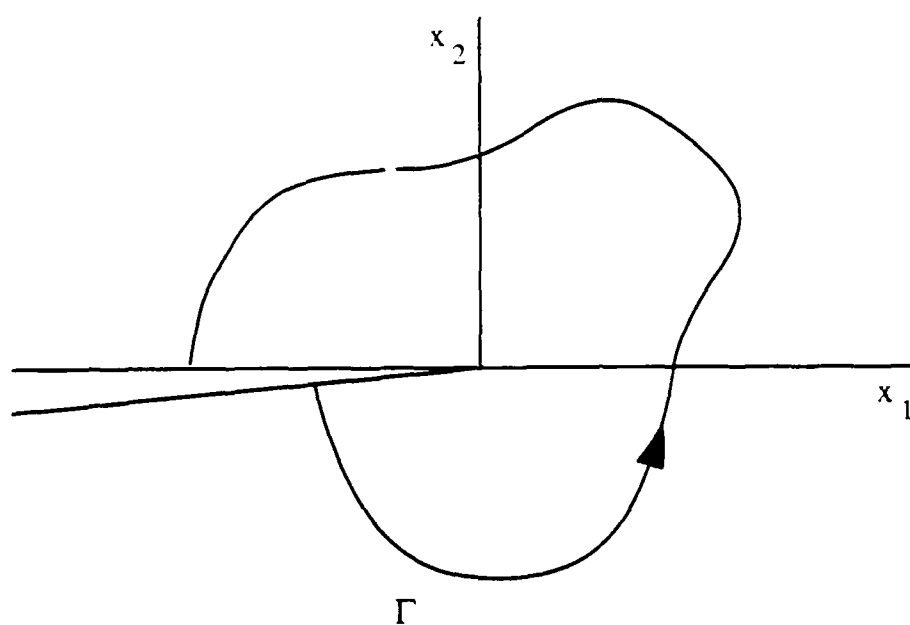
Figure 1.5: Evaluation of the J-integral.

1.5.1   The Effect of Fillers

Fine particulate fillers, such as carbon black, are commonly incorporated in rubber compounds to increase their tensile strength and tear resistance. Filler particles, of submicron diametral length, form aggregates which adhere to the elastomer. The reinforcing effects of filler particles are constrained to a range of deformation rates and temperatures, which are determined by the type of filler and elastomer compound. The magnitude of the reinforcing effect is influenced by the concentration of filler particles and volume concentrations of 0.3 to 0.5 typically produce optimal strength strength and tear resistance properties.

The effects of fillers on fracture behavior are significant. First, filled elastomers exhibit enhanced stress softening behavior, increasing the amount of dissipated energy and lessening the amount of energy available for crack propagation. When compared to the corresponding unfilled elastomer compound, both the tearing energy and the strain energy at break are higher for a filled elastomer. The strain energy at break can be divided into two components, that required for fracture and that consumed by stress softening effects. While the energy required for fracture is essentially the same for both a filled and the equivalent unfilled rubber compound, the energy consumed by stress softening effects is much greater in filled materials.

Failure processes in filled elastomers are different. Crack tip blunting is enhanced by filler reinforcement and, as the crack propagates, crack extension does not occur along a path but deviates at an angle away from the crack front and in severe cases, the crack can propagate in the load direction. This deviation has been attributed to hysteresis [21]. When crack extension occurs faster than the rate at which the stresses can readjust to changes caused by hysteresis, the crack will grow in the direction of maximum stress in a stationary stress field. After the crack deviates, crack growth is arrested and then is reinitiated perpendicular to the applied load.

The fracture surface of filled materials is rough and is characterized as knotty tearing. The load history is not smooth but discontinuous, with regular variations in load, Figure 1.6. Crack propagation is found at the maximum value of the load, while crack arrest occurs at the minimum value of the order of that found for smooth tearing of the unfilled elastomer. This type of crack propagation is termed slip-stick and is found in the same range of deformation rates and temperatures where filler reinforcement is present. Outside of this region, where the presence of filler particles no longer enhances tensile strength and tear resistance, tear behavior is smooth.

Micrographs of crack propagation in filled and crystallizing rubbers show that secondary branching has occurred, not only in the plane of the crack, but also to considerable depth on either side [9]. Secondary branching is attributed to rupture of molecular chains or entanglements and further reduces the amount of stored elastic energy in the crack tip region.

1.6 Cavitation

Cavitation is a failure process commonly found in elastomers. Under a critical value of a dilitant stress or hydrostatic tension, a pre-existing microvoid will suddenly expand elastically and will continue to grow catastrophically until it is large enough to relieve the hydrostatic tension. The vacuole is often formed near the surface of an inclusion which is well bonded to the elastomer material. While the elastomer has internally ruptured, it has not detached from the surface of the inclusion. Cavitation precedes tearing, although the relationship between cavitation and tearing is not understood. In tearing, strands of elastomer material stretch across the crack tip and, although not proven experimentally, it has been suggested that cavitation takes place ahead of the crack tip and that these strands are formed by material between cavities [11].

Cavitation should be distinguished from dewetting, which refers to the detachment of elastomer material from the surface of weakly bonded inclusions under load. In dewetting, vacuoles are found at the surface of the inclusion, whereas in cavitation, vacuoles are near the surface of the inclusion.

1.6.1 A Local Cavitation Criterion

A theoretical analysis of the cavitation process in an incompressible material has been considered by Ball [22]. For certain constitutive laws, an explicit formula for calculating the critical value of the hydrostatic tension, $\mathcal{P}_{crit}$, at cavitation was derived through the application of a hydrostatic tensile stress on the surface of a solid sphere. As this sphere undergoes a radial deformation, at $\mathcal{P}_{crit}$ it is energetically more favorable for a void to form than for the sphere to continue to deform radially.

Consider a solid sphere, with initial radius r_0, composed of an isotropic, homogeneous, and incompressible material. Characterizing this material is the strain energy function,

$$W = W(\lambda_1, \lambda_2, \lambda_3) \, , \tag{1.3}$$
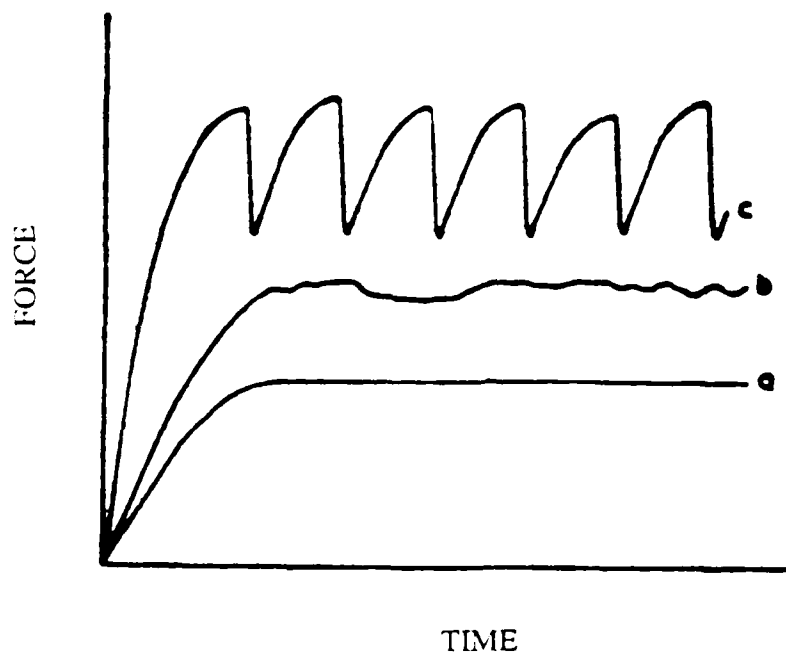
Figure 1.6: Load time curves demonstrating steady and stick-slip tearing for constant rate of extension of the trouser test specimen. From Greensmith, H.W. and A.G. Thomas, Rupture of rubber. III. "Determination of tear properties". *J. Poly. Sci.*, 18, (1955), p.193.

where λ_i are the principal stretch ratios. For an incompressible material,

$$\lambda_1 \lambda_2 \lambda_3 = 1 \ . \tag{1.4}$$

The principal Cauchy stresses, τ_{ij}, are denoted by

$$\tau_{ij} = \lambda_i \frac{\partial W}{\partial \lambda_i} - p \ , \tag{1.5}$$

given the pressure, p, introduced by the constraint of incompressibility.

A uniform tensile stress, $\mathcal{P}$, is applied along the outer surface, at radius r_0. The strain energy function representing this deformation can be expressed as $W(\lambda^{-2}, \lambda, \lambda)$. Initially the sphere does not deform due to incompressibility and spherical symmetry, but, as $\mathcal{P}$ is increased, it becomes energetically more favorable for a spherical cavity to form when

$$\mathcal{P}_{crit} = \int_1^\infty \frac{1}{\lambda^3 - 1} \frac{\partial W}{\partial \lambda} d\lambda \ . \tag{1.6}$$

This solution is based on the assumption that the Cauchy stress vanishes at the center of the sphere, requiring that

$$\int_\delta^\infty \frac{1}{\lambda^3 - 1} \frac{\partial W}{\partial \lambda} d\lambda \tag{1.7}$$

exists and is finite for $\delta > 1$. If the integral in equation (1.7) does not converge, then the critical value of the hydrostatic tension is infinity and cavitation in this material would not occur. In addition, the stress state must be one of hydrostatic tension as voids will not develop under hydrostatic compression.

Equation (1.6) represents a local cavitation criteria which can be applied to a crack tip stress field to predict the site of cavitation. Here, the hydrostatic tension is defined as

$$\mathcal{P}_{crit} = \tau_{ii}/3 \ . \tag{1.8}$$

Cavitation will occur at the location in front of the crack tip where $\mathcal{P}$ equals $\mathcal{P}_{crit}$.

For a Neo-Hookean material, W is expressed as

$$W = \frac{\mu}{2} \left(\lambda_1{}^2 + \lambda_2{}^2 + \lambda_3{}^2 - 3 \right) \ , \tag{1.9}$$

where μ is the shear modulus at infinitesimal deformations. When this strain energy function is substituted into equation (1.6), the critical hydrostatic tension at cavitation is

$$\mathcal{P}_{crit} = 2.5\mu \ . \tag{1.10}$$

Experimental and computational analysis have confirmed Ball's predictions in elastomer materials. Oberth and Bruenner [23] conducted cavitation experiments on polyurethane bars containing well bonded steel spheres, noting the critical loads at which cavitation, found near the poles of the spheres, occurred. A finite element analysis [24] of the test specimen confirmed that the maximum value of the hydrostatic stress is located near the poles of the spheres, and that, for a Neo-Hookean material, the maximum value of the hydrostatic pressure was 2.5μ at the critical loads reported by Oberth and Bruenner [23].

Similar findings for cavitation were reported for cavitation in thin cylinders [3]. At small values of the applied tensile stress, an audible *popping* sound was associated with cavitation and an approximate stress analysis showed that the limiting value of the hydrostatic tension was 2.5μ. Again, a finite element analysis [24] demonstrated that the state of stress at the center of the cylinder is nearly hydrostatic and that, when the local hydrostatic tension is 2.5μ, the numerically applied load is consistent with the experimentally load reported at cavitation. An experimental and computational study [25] of elastomer cubes under fatigue loading showed that voids were found in the experimental specimens at numerically predicted locations of maximum hydrostatic tension.

Experimental evidence also suggests that a thickness effect is present in the cavitation of elastomers. When the thickness is varied as an experimental parameter, test specimens with thicker geometries are associated with a limiting value of the hydrostatic tension, 2.5μ, for a Neo-Hookean material at cavitation, whereas for thin specimens, cavitation occurs at higher stresses [3,4].

The size and distribution of inclusions can also influence void formation. In these studies [4,26,27,28,29], larger applied loads at cavitation are associated with smaller inclusions, either cylindrical or spherical, but decrease and approach a limiting value as the size of the inclusion increases. In addition, when the distance between two inclusions was varied, larger loads are required for void formation between two closely spaced inclusions. As the distance between the the two inclusions increases, the applied load at cavitation again decreases to a limiting value, calculated at 2.5μ for a Neo-Hookean material.

From these cavitation studies, it can be concluded that void formation occurs at sites of maximum hydrostatic tension and that thickness influences the magnitude of the hydrostatic tension. Now it will be shown that, on the basis of linear elasticity, differences in triaxiality between the plane strain and plane stress crack tip fields exist and that the triaxial tension is larger under plane strain conditions. Consequently, cavitation should occur at a lower limiting value in thick specimens, i.e., in plane strain.

1.6.2   Plane Strain and the Effect of Thickness

In this section, a simplified model based on linear elasticity [1] will be used to discuss the transverse constraint found in fracture. This model will illustrate the effect of thickness in fracture and, although highly idealized, its main conclusions are applicable to elastomer materials.

Consider a bar of incompressible materials subjected to a tensile stress. The bar will strain in the longitudinal direction and contract in the transverse directions. For an incompressible material, the Poisson's ratio, ν, equals one-half and the transverse strain is one half the longitudinal strain under infinitesimal loading. If the bar is stretched to finite deformations by the stretch ratio λ, the principal stretch ratios, λ_i, become $(\lambda, 1/\sqrt{\lambda}, 1/\sqrt{\lambda})$.

In a thick plate containing a through thickness crack, high stresses and large transverse strains are found at the crack tip. Along the crack faces, though, the material is traction free and the transverse strain is absent. Away from the crack tip, the stresses are lower and the transverse strain is correspondingly smaller. At the crack tip in Figure 1.7, a thin roll of material wants to contract in the transverse direction, but the bulk of the material surrounding the tip will not allow this contraction to occur. The transverse strain remains zero. As a consequence of this constraint, there will be a tensile stress in the thickness direction. Here, the transverse direction is the x_3 direction and

$$\epsilon_{33} = 0 ,$$

$$\sigma_{33} = \nu(\sigma_{11} + \sigma_{22}) .$$

$$(1.11)$$

This condition is termed plane strain.

Now consider a thin plate of the same material containing a crack of equal size. Again, a tensile loading is applied in the longitudinal direction. Because the plate is thin, the length of the roll of material that wants to contract at the crack tip is smaller than its diameter. The material can easily contract and the transverse strain is nonzero. The material at the crack tip is not constrained so that there is no stress in the thickness direction and σ_{33} equals zero. This condition is plane stress.

The length of the roll of material that wants to contract equals the thickness of the plate and its diameter will be proportional to the loading, refering to Figure 1.8. In plane strain, the thickness is large compared to the diameter of the roll. Due to the variance of σ_{33} in plane stress versus plane strain, cracks respond

differently. In metals, the fracture toughness is higher in plane stress and depends on the thickness as shown in Figure 1.9. When the thickness is large enough for plane strain conditions to occur, the fracture toughness remains constant and is termed K_{1c} or the plane strain fracture toughness. If the diameter of the roll of contracting material equals the thickness of the plate, plane stress conditions are present. When this diameter is small, plane strain conditions are found because the transverse strain remains zero. The surrounding material prevents the material at the crack tip from contracting freely.

The hydrostatic tension, $\mathcal{P}$, is defined in linear elasticity as

$$\mathcal{P} = \frac{\sigma_{ii}}{3} .$$
(1.12)

The hydrostatic tension is larger in plane strain compared to plane stress because the σ_{33} stress component is nonzero. For a linear elastic incompressible material,

$$\mathcal{P} = \frac{1}{2}(\sigma_{11} + \sigma_{22}) \quad \text{(plane strain)},$$

$$\mathcal{P} = \frac{1}{3}(\sigma_{11} + \sigma_{22}) \quad \text{(plane stress)}.$$
(1.13)

At a given applied stress, σ, the hydrostatic pressure is higher in plane strain. If a cavitation criteria based on the hydrostatic pressure is considered, cavitation should occur first in plane strain. Thus, the plane strain condition represents a limiting condition for the onset of void growth.

Based on the premise that a thickness effect is present in the failure of metals, it is suggested here that a thickness effect also is present in the failure of elastomers. Preliminary evidence supporting this hypotheseis has been presented by the experiments on void formation in these incompressible, or nearly incompressible materials. A finite element study [7] of Mode I fracture in rubber sheets under identical loading was conducted with both plane strain and plane stress boundary conditions. Computed values of the J-integral were higher in plane strain when compared to those in plane stress. Thus, computational and experimental research indicate that a thickness effect may exist on a microscopic and a macroscopic level. It is the purpose of this investigation to experimentally determine if failure is different in plane strain, although the thickness effect may not be the same as that found in metals or other materials.
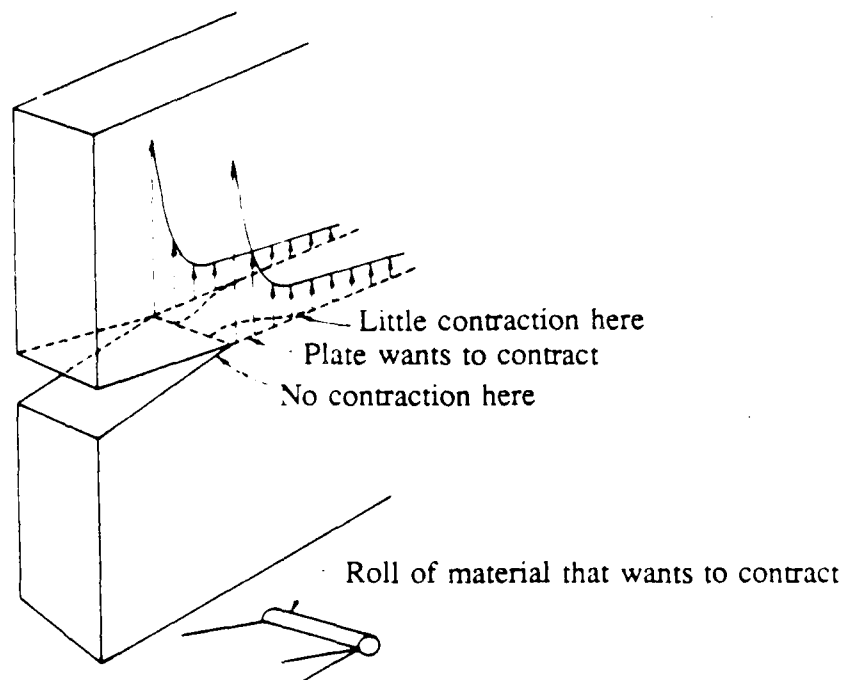
Figure 1.7: Roll of material contracting at crack tip.
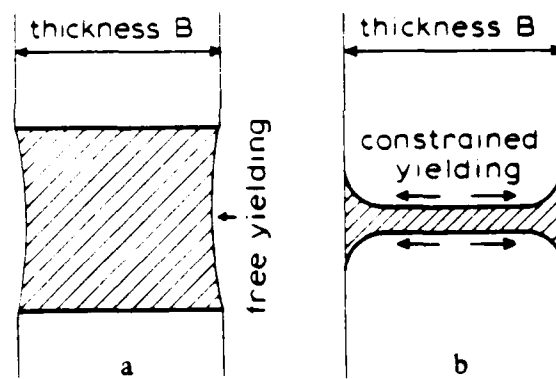
Figure 1.8: Free yielding in plane stress (a), constrained yielding plane strain (b).
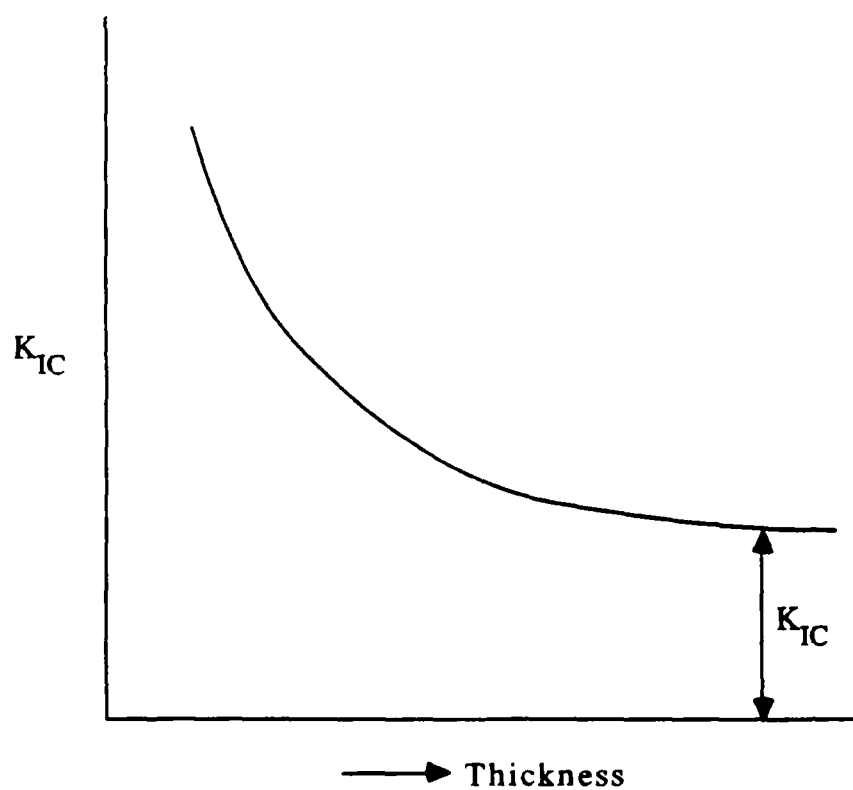
Figure 1.9: K_{Ic} versus thickness in metals.

Chapter 2

Computational Investigation

2.1 Objectives

The nonlinear asymptotic solution for a Mode I crack in plane strain will be examined in an incompressible material through a finite element analysis. Small scale nonlinearity, where the nonlinear mechanical crack tip field is confined to a small region surrounding the crack tip, will be assumed. The computational results will be compared to the nonlinear asymptotic solution derived by Knowles [5] and Stephenson [6] for a Mooney-Rivlin material. The accuracy with which finite element techniques can predict the nonlinear asymptotic field and the geometric scale, over which the nonlinear asymptotic field is present, will be determined.

The effect of the constitutive law upon the finite element results will be found using two forms of the Rivlin law: the linear representation of this law, known as the Mooney-Rivlin law, and a model which includes higher order terms. Although both forms of the Rivlin law accurately predict material behavior at small to moderate deformations, the Mooney-Rivlin form, in contrast to the higher order model, underestimates stresses at large deformations. As large deformations are found at the crack tip, the differences found in the nonlinear asymptotic field due to the choice of a constitutive model can become significant when relating computational results to physically observed material behavior. Finally, criteria for void nucleation in incompressible materials [22], will be examined through the finite element results and a micromechanical failure model [30] to predict the location of void nucleation in the nonlinear crack tip field.

35

2.2   A Mode I Crack and the Linear Asymptotic Field

Consider a body containing a through thickness stationary crack as in Figure 2.1. Under Mode I loading, a tensile stress, σ, is applied normal to the plane of the crack. The faces or surfaces of the crack are traction free while the dominant displacements along the crack face are normal to the plane of the crack. No thermal or body forces are assumed to be present. A cartesian coordinate system is introduced at the tip of the crack in the undeformed body, as shown in Figure 2.2, where polar coordinates (r, θ) can be defined as

$$x_1 = r \cos(\theta) \quad , \quad x_2 = r \sin(\theta) \; . \tag{2.1}$$

The linear elastic asymptotic stress, as $r \to 0$, is

$$\sigma_{ij} = \frac{K_I}{\sqrt{2\pi r}} f_{ij}(\theta) \tag{2.2}$$

where nominal stresses are denoted by, σ_{ij}, assuming infinitesimal linear elasticity. The stress intensity factor, K_I, is a function of the crack length, the applied stress, σ, and the geometry of the body so that the influence of these quantities is found through K_I. The amplitude of the mechanical crack tip stress field is characterized by K_I in that two bodies of the same material, with cracks of different length and different applied loads, will have identical mechanical crack tip stress fields, equation (2.2), if their stress intensity factors are equal. For an infinite plate containing a centrally located crack of length $2L$, shown in Figure 2.3, the stress intensity factor is

$$K_I = \sigma\sqrt{\pi L} \tag{2.3}$$

Written out explicitly, the in-plane stresses and displacements u_i (Williams,[31]) in equation (2.2) are

$$\sigma_{11} = \frac{K_I}{\sqrt{2\pi r}} \cos\frac{\theta}{2} \left(1 - \sin\frac{\theta}{2}\sin\frac{3\theta}{2}\right) + o\left(r^{1/2}\right) \; ,$$

$$\sigma_{22} = \frac{K_I}{\sqrt{2\pi r}} \cos\frac{\theta}{2} \left(1 + \sin\frac{\theta}{2}\sin\frac{3\theta}{2}\right) + o\left(r^{1/2}\right) \; ,$$

$$\sigma_{33} = \frac{K_I}{\sqrt{2\pi r}} \cos\frac{\theta}{2} \cos\frac{3\theta}{2}\sin\frac{\theta}{2} + o\left(r^{1/2}\right) \; , \tag{2.4}$$

$$u_1 = \frac{K_I}{\mu}\sqrt{2\pi r} \cos\frac{\theta}{2}\left(1 - 2\nu + \sin^2\frac{\theta}{2}\right) + o\left(r^{1/2}\right) \; ,$$

$$u_2 = \frac{K_I}{\mu}\sqrt{2\pi r} \sin\frac{\theta}{2}\left(2(1 - \nu) - \cos^2\frac{\theta}{2}\right) + o\left(r^{1/2}\right) \; .$$

2.3   The Nonlinear Asymptotic Field

In the deformed configuration, Figure 2.4, a new coordinate system is introduced at the crack tip such that the deformed coordinates, y_i, are defined in terms of the undeformed configuration as

$$y_i = x_i + u_i \ , \ \text{ or } \ y = Fx \ , \tag{2.5}$$

given the displacement field, u_i, and the deformation gradient, F_{ij}.

Knowles [5], in conjunction with Sternberg, derived the nonlinear asymptotic solution for a Mode I crack in an incompressible material, based on the Mooney-Rivlin constitutive model and assuming finite elasticity while Stephenson [6] expanded this asymptotic crack tip field to include higher order terms. Their method of solution, the formulation and resolution of a nonlinear eigenvalue problem, is presented in Appendix-A.

The Mode I plane strain asymptotic solution [5], for a Mooney-Rivlin material is

$$\tau_{11} \sim \frac{\mu}{2}b(1 - \cos\theta) \ ,$$

$$\tau_{22} \sim \frac{\mu}{2}a^2 r^{-1} \ ,$$

$$\tau_{12} \sim \frac{\mu}{2}abr^{-1/2}\sin\frac{\theta}{2} \ , \tag{2.6}$$

$$y_1 \sim br\sin^2\frac{\theta}{2} + \frac{1}{a}r^{3/2}\left(2\cos\frac{\theta}{2} - \frac{2}{3}\cos\frac{3\theta}{2}\right) \ ,$$

$$y_2 \sim ar^{1/2}\sin^2\frac{\theta}{2} + r^{3/2}\left(d\sin\frac{3\theta}{2} - \frac{b^2}{2a}\sin\frac{\theta}{2}\right) \ ,$$

where the Cauchy stresses, τ_{ij}, and the deformation field, y_i, are referenced to the undeformed polar coordinate system (r,θ) at the crack tip, and a, b, and d refer to load amplitude constants. When comparing the nonlinear asymptotic solution, equation (2.6), to the linear elastic crack tip field, equation (2.4), the most significant difference is that only τ_{12} and y_2 are functions of the square root of r. τ_{22} dominates the stress field and possesses the most singular term, $1/r$, but it is not a function of angular extent, depending only on radial distance from the crack tip. In contrast, τ_{11} is determined solely on angular extent and, for a given angle, remains constant with increasing distance from the crack tip. Only τ_{12} is a function of both $r^{-1/2}$ and θ, similar to the linear elastic shear stress.

Both y_1 and y_2 are functions of both r and θ, while y_1 is directly proportional to r. Along the crack front ($\theta = 0$ degrees) and the crack face ($\theta = 180$ degrees), the y_1 coordinate equals the x_1 coordinate, a consequence of incompressibility ($\nu = 0.5$) as the linear elastic displacement, u_1, also vanishes at these angles.

2.4 Small Scale Nonlinearity

In a body of nonlinear incompressible material containing a crack, it is assumed that the linear elastic stress field, equation (2.5), can be found in a region around the crack tip, shown in Figure 2.5, if the applied loads are sufficiently small, i.e., only small geometry changes are present and material behavior approaches linear elasticity[32,17]. These conditions are physically violated as $r \to 0$. The radius R^* will define a boundary such that, when $r > R^*$, small geometry changes and linear elasticity are appropriate assumptions. This region is termed K-dominant because the value of the applied stress intensity factor will determine the amplitude of the triaxial stress field. The size of this region is small compared to the crack length and the overall geometry of the body.

This K-dominant region encompasses a smaller nonlinear region much closer to the crack tip, $r < R^*$, called the fracture process zone, where cavitation can be found. Finite deformations are now present and it is assumed that the nonlinear asymptotic crack tip stress field (Knowles[5] and Stephenson[6]) in equation (2.6) will be located here. As $r \to R^*$, the stresses gradually change from the nonlinear elastic asymptotic field to the linear elastic field.

The radius R^* will be arbitrarily but plausibly defined in terms of the deformation gradient, F_{ij}. Along R^*,

$$|F_{ij} - \delta_{ij}| \sim 0.1 .$$
(2.7)

When $r \ll R^*$, deformations will be large and the nonlinear asymptotic field is present while, for $r \gg R^*$, the deformation gradient will be small and the linear elastic asymptotic field will prevail.

Under the conditions of small scale nonlinearity, the energy release rate is equivalent to the J-integral, or

$$J = \frac{K_I^2 (1 - \nu^2)}{E} .$$
(2.8)

where E is the Young's modulus. Within the methodology of linear elastic fracture mechanics, it is assumed that crack extension occurs at critical values of K_I and J_I, termed K_{IC}, the fracture toughness, and J_{IC}.

Small scale nonlinearity is analogous to small scale yielding [32,17] in elastic-plastic materials in that the region of nonlinearity around the crack tip is sufficiently small compared to the crack length and the overall geometry of the body. Where the linear elastic asymptotic field can be found, the conditions of small geometry change and linear elasticity are also met. However, in small scale yielding, it is possible for the K-dominant region to surround another region which is closer to the crack tip where the material behavior is plastic, violating the assumption of

linear elasticity, and yet still have small geometry changes while, much closer to the crack tip, both large geometry changes and plasticity will be present. In small scale nonlinearity, though, both assumptions, linear elasticity and small geometry changes are violated at approximately the same radius, R^*.

One of the load amplitude constants, a, in the nonlinear asymptotic solution can be found for a centrally located crack in an infinite plate, Figure 2.3, in terms of the applied stress, σ. Under small scale nonlinearity, the energy release rate, equation (2.8), is equivalent to the J-integral, equation (1.2), which is evaluated from the nonlinear asymptotic field in equation (2.6). The details of this calculation are shown in Appendix-B, and

$$a = \frac{\sigma}{\mu}\sqrt{L} \ . \tag{2.9}$$

The magnitude of a will increase with the applied stress, σ, but is also a function of the shear modulus and the crack length.

2.5 Problem Description

Consider a thick infinite plate of incompressible material containing a through-thickness crack under Mode I loading. In this computational investigation, a finite element analysis of the crack tip region, modelled as a circular plate shown in Figure 2.6, was performed. Consistent with small scale nonlinearity, the linear elastic asymptotic solution, was applied along the outer radius, L, of the circular plate. Two forms of the Rivlin constitutive law, the first and third order invariants were used to predict material behavior.

Before conducting the nonlinear finite element analysis, the numerical model was tested by verifying the accuracy of the linear elastic asymptotic field close to the crack tip at sufficiently small loads and by determining the geometric size scale which would satisfy St. Venant's principle, i.e., the crack tip stress field is independent of the type of applied kinematic constraint, consistent nodal point forces or displacements.

2.6 Computational Procedures

The analysis was performed using the finite element code, ABAQUS [33] in which selected numerical procedures were suitable for both nonlinear materials and geometry. A plane strain quadratic element designed specifically for incompressible

material behavior was chosen where the pressure field, associated with the constraint of incompressibility, is independently interpolated and coupled to the displacement solution as a Lagrange multiplier. The element is considered a mixed formulation element because the equilibrium equations and compatibility conditions are numerically solved from both displacement and stress variables. The value of the J-integral was computed using the domain integral method [34], which is equivalent to virtual crack extension [35] in two-dimensional problems.

2.7 Constitutive Models

Rubber and elastomers are classified as hyperelastic or nonlinear elastic materials, capable of elongations up to 800% prior to failure. Due to the large deformations found in these materials, constitutive laws from linear elasticity or linear viscoelasticity, which are based on equilibrium and time dependent properties under infinitesimal deformations, cannot be used to predict material response under large loads.

Many constitutive laws for rubber materials are based on a molecular theory [36,11] where elastomers are modelled as a network of freely joined molecular chains which are allowed to pass through each other without hindrance. These chains deform under load and the resulting stress is related to the energy change of the network. Different constitutive theories based on this assumption include Gaussian, phenomenological, viscoelastic and kinetic theories. The Gaussian model and one specific phenomenological model, the Rivlin law, will discussed in greater detail below.

Both the Gaussian and the Rivlin laws model the behavior of an ideal elastomer material in which purely elastic deformations are mechanical and completely reversible under isothermal conditions. The material is assumed to be initially isotropic, homogeneous, and incompressible. The significance of the word *initial* stems from nonhomogenities, such as the localized crystallization of natural rubber, which can be found under small loads and disappear upon load removal. Of course, when the load is significantly large, crystallized regions exhibit hysteresis and material behavior is now irreversible. In addition to hysteresis, internal friction between molecules and permanent set are also departures from the ideal finite elasticity in which these theories are based, although static loading conditions can minimize the effect of internal friction.
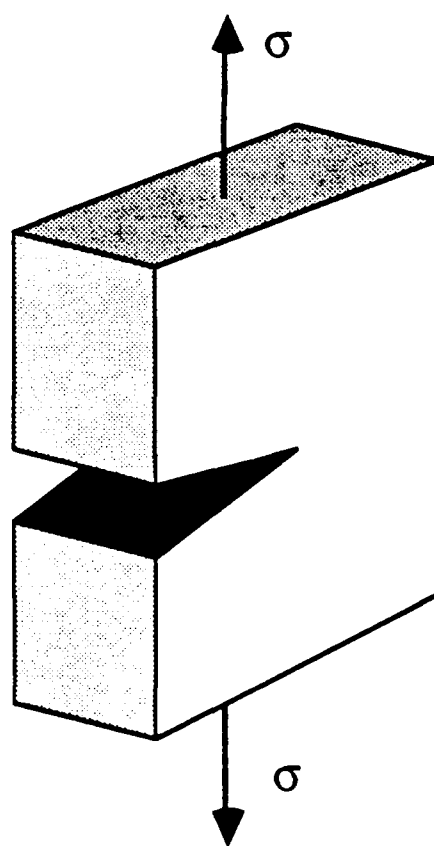
Figure 2.1: A Mode I crack.
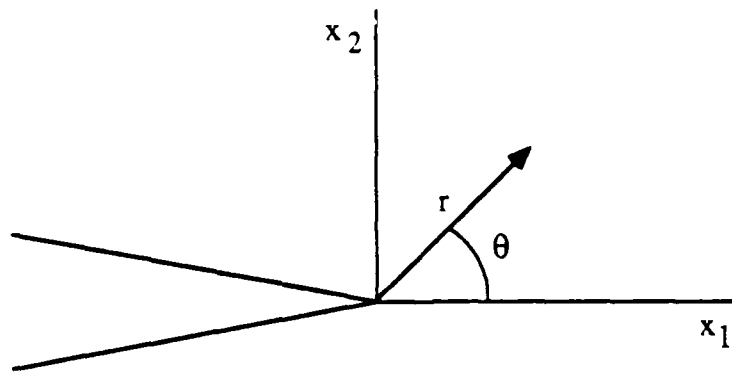
Figure 2.2: Orientation of the crack in the undeformed coordinate system.
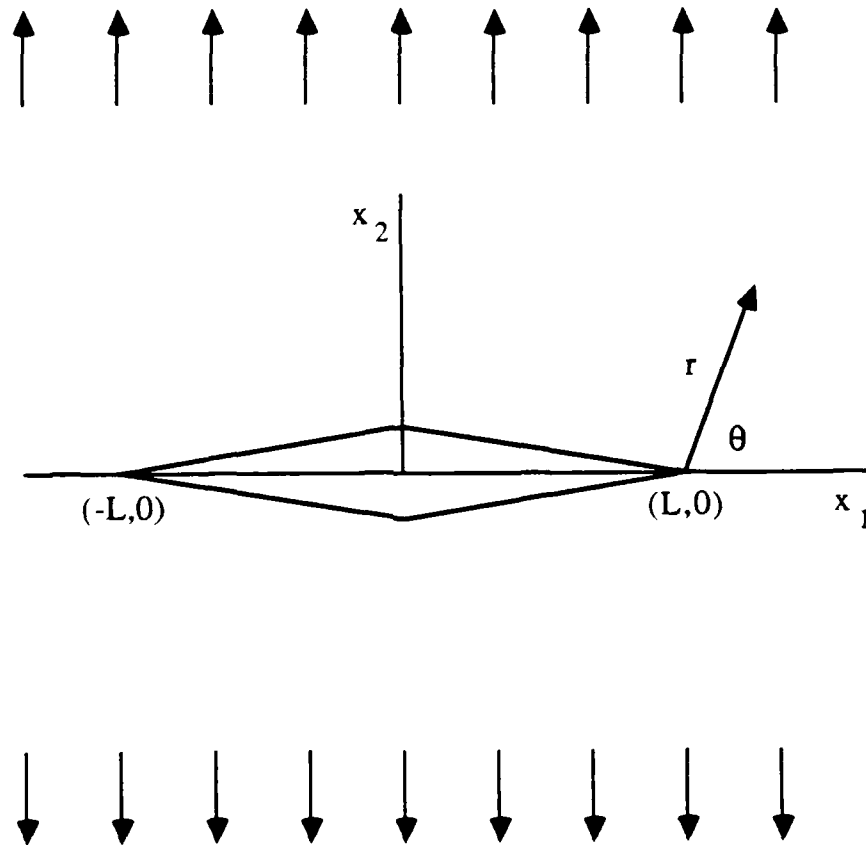
Figure 2.3: A center crack in an infinite plate.
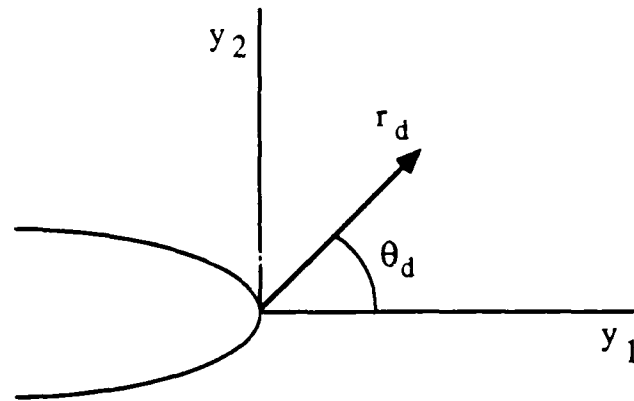
Figure 2.4: Orientation of the crack in the deformed configuration.
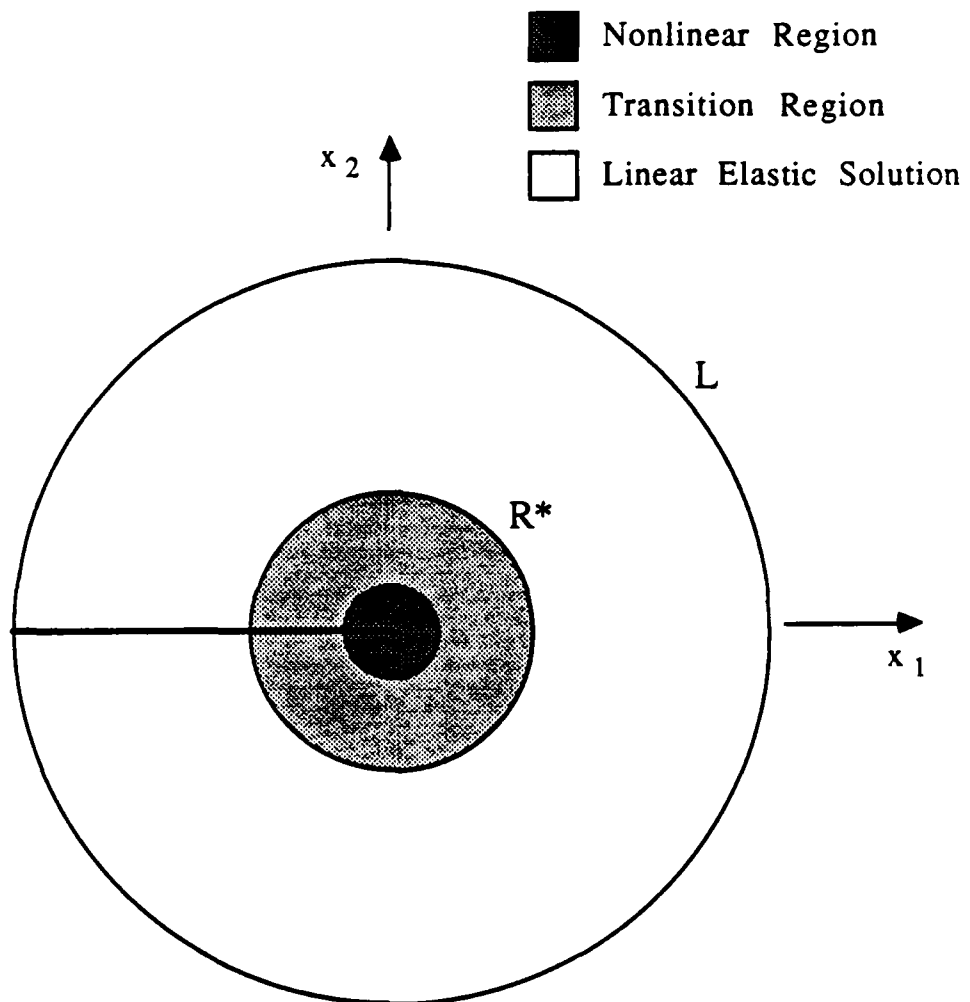
Figure 2.5: Small scale nonlinearity.
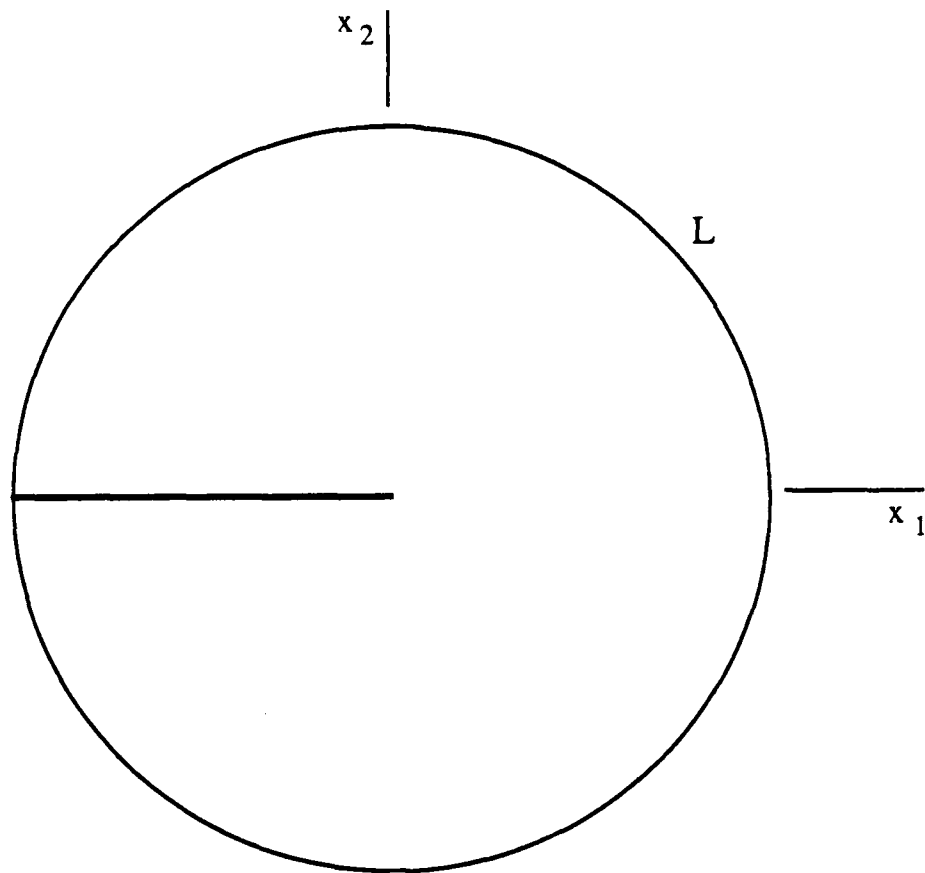
Figure 2.6: A through thickness crack in an infinite plate.

Strain energy functions, W, representing these constitutive laws are developed in terms of the strain invariants, I_i,

$$
\begin{aligned}
I_1 &= \lambda_1^2 + \lambda_2^2 + \lambda_3^2 \ , \\
I_2 &= \lambda_1^2\lambda_2^2 + \lambda_2^2\lambda_3^2 + \lambda_1^2\lambda_3^2 \ , \\
I_3 &= \lambda_1^2\lambda_2^2\lambda_3^2 \ ,
\end{aligned}
\tag{2.10}
$$

which are defined by the stretch ratios, λ_i, the positive square roots of the eigenvalues of the right stretching tensor. The third strain invariant equals one as a consequence of incompressibility.

The Gaussian constitutive law assumes a statistical distribution of the length of the molecular chains in their undeformed state and that the undeformed length is much less than the fully extended length of the molecular chain in its deformed state. The strain energy function characterizing this material response is the Neo-Hookean law

$$
W = C\,(I_1 - 3) \ ,
\tag{2.11}
$$

where the single material constant, C, is proportional to μ and can be defined in terms of the molecular weight, M, the number of subchains between crosslinks, N, the molecular weight of the subchains, M_e, and the density of the elastomer, ρ_p, by

$$
C = \frac{\mu}{2} = NkT_t = \rho_p RT_t \frac{(1 - 2M_e/M)}{M_e} \ .
\tag{2.12}
$$

Here, k denotes the Boltzmann constant, T_t is the absolute temperature, and R represents the universal gas constant. This theory applies when the strains are not too large, i.e., strains do not approach the limiting deformability of the molecular network. When a significant number of chains becomes fully extended, this theory is no longer valid, as shown in Figure 2.7 [36]. At moderate deformations, the actual nominal stresses are less than predicted stresses while at large deformations, the actual nominal stresses are greater than predicted values, a consequence of material behavior deviating from the ideal theory.

In the Rivlin constitutive model [37], the strain energy function, W, is expressed as a function of the strain invariants in the form of a doubly infinite series, or a Taylor expansion around the undeformed state of the material, as

$$
W = \sum_{i=0}^{n} \sum_{j=0}^{n} C_{ij}(I_1 - 3)^i (I_2 - 3)^j \ ,
\tag{2.13}
$$

where the material constants are C_{ij}. For the strain energy to vanish when the material is undeformed, the term C_{00} must equal zero. Equation (2.13) is the most general form of a phenomenological constitutive equation for the equilibrium of an

ideal hyperelastic material. For sufficiently small deformations, the terms in this expansion, $(I_1 - 3)$ and $(I_2 - 3)$, are small and of the same order in magnitude, and consequently, the linear terms in W, regardless of the additional higher order terms included in W, should approximate material behavior. When a linear relationship exists between the shearing force and the amount of simple shear, γ, Rivlin [38] found that W could be valid even at large deformations if the assumptions of an ideal incompressible material are met in the undeformed state.

The linear form of equation (2.13) is referred to as the Mooney-Rivlin material law, stated as

$$W = C_{10}(I_1 - 3) + C_{01}(I_2 - 3) \ . \tag{2.14}$$

The material constant C_{01} is related to the number of permanent chemical crosslinks and the strength of temporary intermolecular interactions caused by crystallites or molecular entanglements but is independent of swelling while the second material constant, C_{01}, decreases with swelling and repeated extension, representing the magnitude of transient intermolecular interactions. The flexibility of the molecular chains and their ability to spontaneously crystallize increases with the ratio of C_{01}/C_{10} [11]. Finally, at infinitesimal deformations, these material constants are related to μ by

$$\mu = 2(C_{10} + C_{01}) \ . \tag{2.15}$$

In simple extension, the nominal stress, σ, is expressed as

$$\sigma = \left(\lambda - \frac{1}{\lambda^2}\right)\left[\frac{\partial W}{\partial I_1} + \frac{1}{\lambda}\frac{\partial W}{\partial I_2}\right] \ , \tag{2.16}$$

for a given stretch ratio, λ, or

$$\sigma = \left(\lambda - \frac{1}{\lambda^2}\right)\left[C_{10} + \frac{1}{\lambda}C_{01}\right] \ , \tag{2.17}$$

using the Mooney-Rivlin form of the strain energy. When equation (2.17) is rewritten as

$$\frac{\sigma}{(\lambda - 1/\lambda^2)} = C_{10} + \frac{1}{\lambda}C_{01} \ , \tag{2.18}$$

a linear relationship between the left hand side and $1/\lambda$ is found where the slope of the straight line is C_{01} and the sum of the two material constants, $(C_{10} + C_{01})$, is the y-intercept at $\lambda = 1$. This graph is referred to as a Mooney plot, shown in Figure 2.8 for a vulcanized natural rubber. At moderate deformations, $0.45 > 1/\lambda > 0.9$, a linear relationship is found and deviations outside this region are attributed to experimental error $(1/\lambda > 0.9)$ and crystallization $(1/\lambda < 0.45)$. Rivlin [38] notes that material constants obtained using the linear portion of the Mooney plot do not accurately predict material behavior at large

deformations, $\lambda > 2.2$, or under other types of deformations such as pure shear, compression, and simple torsion. Even though the Mooney-Rivlin constitutive model does not provide a self-consistent model for the behavior of rubber under general deformations, it is still commonly used because many tensile engineering applications for rubber are confined to $\lambda < 2.2$.

To obtain improved values of C_{01} and C_{10}, more than one type of deformation behavior, i.e., simple extension and compression, are used and a typical Mooney plot showing both types of deformations is provided in Figure 2.9.

James, Green, and Simpson [39] suggested that the phenomenological expression of the strain energy in equation (2.13) should be simply treated as a form of a regression analysis where the material constants become mathematical constants without physical meaning. From a biaxial extension experiment, which models general deformation behavior, suitable constants can be obtained to predict material behavior in a regression equation containing sufficient terms. The success of the regression analysis is then evaluated by the degree to which other forms of deformation behavior such as simple extension can be predicted. Using this approach for a natural rubber, James, Green and Simpson [39] showed that this approach not only models simple deformation behaviors but also more complex engineering problems such as the inflation of rubber membranes and tubes.

In this computational investigation, a crack analysis will be performed under plane strain conditions, where I_1 and I_2 are equal, as shown in Appendix A. Two material laws were used to model the Mode I nonlinear asymptotic solution. The Mooney-Rivlin law, $(n = 1)$ in equation (2.13) was chosen because the incompressible nonlinear asymptotic solution [5,6] is based on this constitutive law. In plane strain, this law is identical to the Neo-Hookean model, or

$$W = (C_{10} + C_{01})(I_1 - 3) \ , \tag{2.19}$$

where the material constants,

$$\frac{C_{10}}{\mu} = 0.45 \ \text{and} \ \frac{C_{01}}{C_{10}} = 0.1 \ , \tag{2.20}$$

represented typical experimental values.

To determine the effect of higher order terms, which would more accurately model material behavior at high extensions, on the nonlinear asymptotic solution, the third order invariant $(n = 3)$ of the Rivlin law, equation (2.13),

$$\begin{aligned} W = \ & (C_{10} + C_{01})(I_1 - 3) \\ & + (C_{11} + C_{20} + C_{02})(I_1 - 3)^2 \\ & + (C_{21} + C_{12} + C_{30} + C_{03})(I_1 - 3)^2 \end{aligned} \tag{2.21}$$

was selected given the material constants provided by James, Green, and Simpson [39] as

$$C_{10}/\mu = 0.45 \quad ; \quad C_{01}/C_{10} = 0.10$$

$$C_{11}/C_{10} = -8.4 \times 10^{-3} \quad ; \quad C_{20}/C_{10} = -5.7 \times 10^{-3}$$

$$C_{02}/C_{10} = 5.0 \times 10^{-4} \quad ; \quad C_{21}/C_{10} = 3.9 \times 10^{-4}$$

$$C_{12}/C_{10} = -6.9 \times 10^{-5} \quad ; \quad C_{30}/C_{10} = 3.4 \times 10^{-4} \tag{2.22}$$

$$C_{03}/C_{10} = 3.4 \times 10^{-6}$$

The third order invariant includes all linear, second order and third order terms. The second order invariant ($n = 2$) was not chosen because it did not accurately predict tensile stresses at large strains.

Nominal stress strain curves, normalized by μ, are shown in Figure 2.10 and demonstrate that, at small to moderate deformations, $\lambda < 4.0$, the two constitutive models show similar stresses but at larger deformations, the Mooney-Rivlin law ($n = 1$) underestimates experimentally determined nominal stresses while the higher order constitutive law ($n = 3$) more accurately predicts experimental behavior.

The constitutive law, equation (2.13), was based on the assumption that, at sufficiently small deformations, linear behavior is observed in simple shear where the deformation behavior can be expressed as

$$\lambda_1 = \lambda \ , \quad \lambda_2 = 1 \ , \quad \lambda_3 = \frac{1}{\lambda} \ . \tag{2.23}$$

The amount of simple shear, γ, is the F_{12} term in the deformation gradient or

$$\gamma = \lambda - \frac{1}{\lambda} \ , \tag{2.24}$$

where

$$F = \begin{bmatrix} 1 & \gamma \\ 0 & 1 \end{bmatrix} . \tag{2.25}$$

For an incompressible material, it can be easily shown that I_1 equals I_2, denoted in terms of λ by

$$I_1 = I_2 = \lambda^2 + \frac{1}{\lambda^2} + 1 \ . \tag{2.26}$$

The strain energy functions for $(n = 1)$, equation (2.4), and $(n = 3)$, equation (2.21), become

$$W = \tfrac{1}{2}\mu\gamma^2 \qquad\qquad (n = 1);$$

$$
\begin{aligned}
W = \ & 2\,(C_{10} + C_{01})\,\gamma^2 \\
& +4\,(C_{11} + C_{20} + C_{02})\,\gamma^4 \qquad (n = 3), \\
& +6\,(C_{21} + C_{12} + C_{30} + C_{03})\,\gamma^6
\end{aligned}
\qquad (2.27)
$$

while the shear stress, σ_{xy} is expressed as

$$\sigma_{xy} = \mu\gamma \qquad\qquad (n = 1);$$

$$
\begin{aligned}
\sigma_{xy} = \ & 2\,(C_{10} + C_{01})\,\gamma \\
& +4\,(C_{11} + C_{20} + C_{02})\,\gamma^3 \qquad (n = 3), \\
& +6\,(C_{21} + C_{12} + C_{30} + C_{03})\,\gamma^5
\end{aligned}
\qquad (2.28)
$$

Equation (2.28) shows that, for $(n = 1)$ a linear relationship between the shear stress and γ is found at all deformations but for $(n = 3)$, a linear relationship will be found only at small deformations when the linear terms dominate the solution. As γ increases, the higher order terms will become increasingly more important and this is shown graphically in Figure 2.11. When $\gamma < 3$, the differences in the shear stress between the two constitutive models are small, but at $\gamma > 3$. the graph for $(n = 3)$ is no longer linear and large differences between the shear stresses are found between these two models. For both constitutive models, μ can be determined as twice the sum of the material constants or

$$\frac{\mu}{2} = \sum_{i=0}^{n}\sum_{j=0}^{n} C_{ij} \, , \qquad (2.29)$$

In modelling material behavior, there exists a region surrounding the crack tip where non-ideal hyperelastic material behavior is present due to crystallization and viscoelasticity, and in this region, the nonlinear asymptotic solution [5,6] predicts that λ and W become infinite as $r \to 0$, which is not physically realistic. Therefore, there is a limit to the region where the asymptotic solution and strain energy are valid as the radius from the crack tip vanishes and continuum mechanics no longer applies. Alternative constitutive models based on viscoelastic and molecular theory, such as Halpin and Bueche [10], could prove extremely useful in predicting material behavior when non-ideal hyperelastic material behavior is present, although these models were not explored in this investigation.
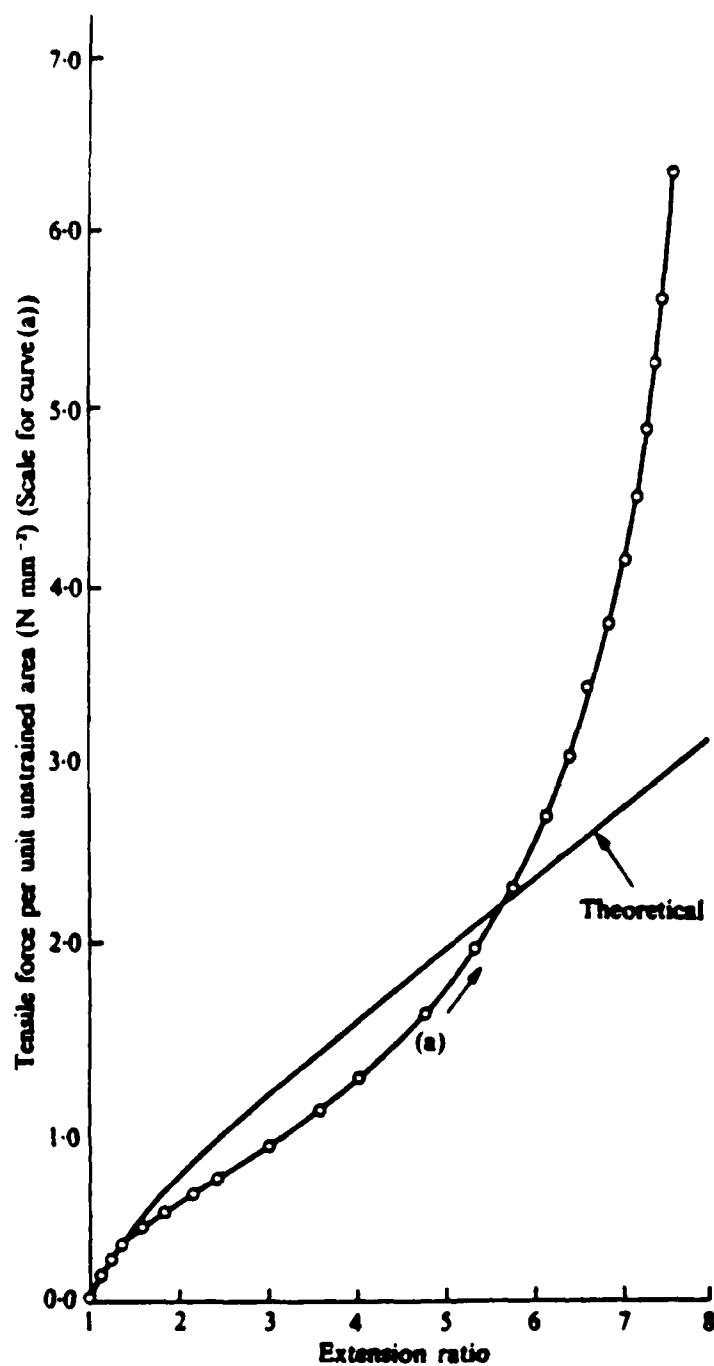
Figure 2.7: Comparison of experimental and theoretical predictions from Gaussian theory. From: Treloar, L.R. The physics of rubber elasticity. *Clarendon Press, Oxford*, (1958), p. 87.
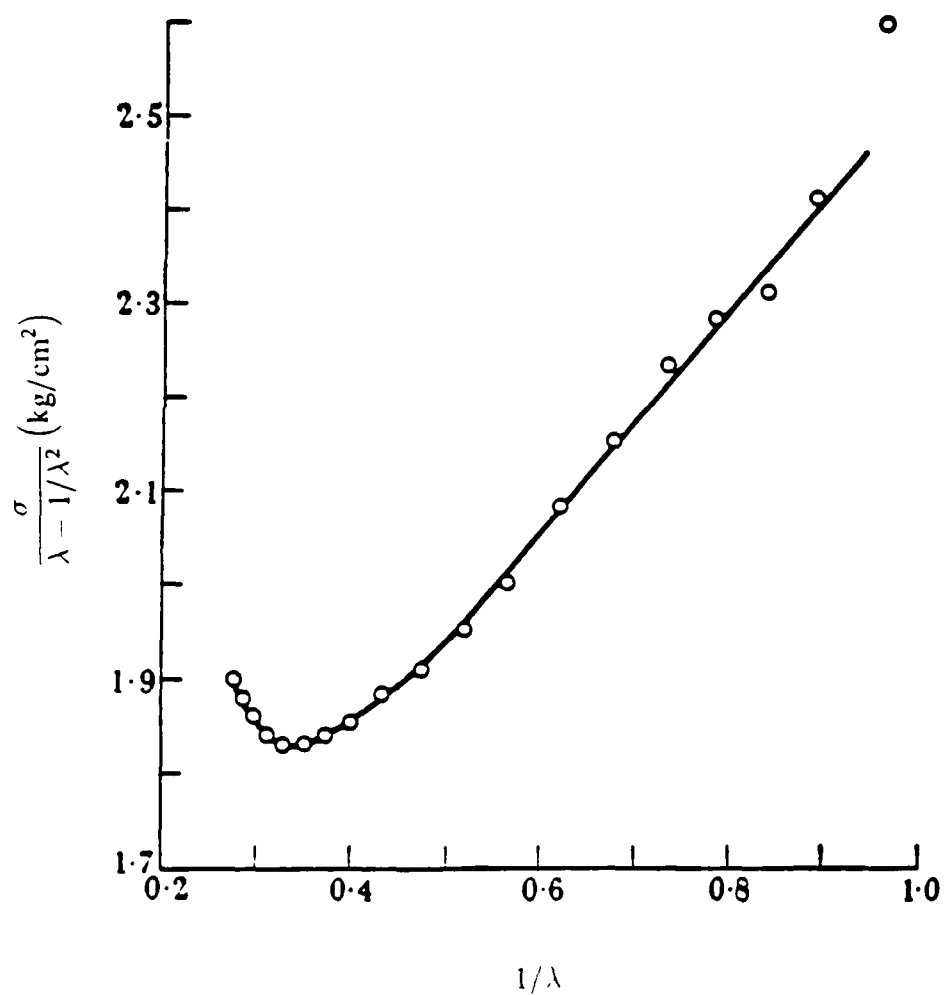
Figure 2.8: Mooney plot using simple extension data only. From: Rivlin, R.S. and Saunders, D.W Large deformations of isotropic materials. VII. Experiments on the deformations of rubber. *Phil. Trans. Roy. Soc.A.* **865** (243) (1951), p. 269.
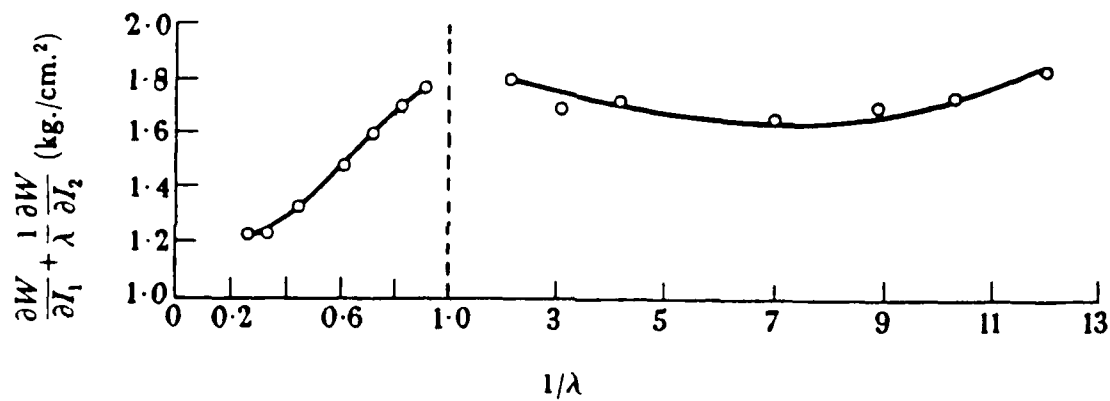
Figure 2.9: Mooney plot from simple extension and compression. From: Rivlin, R.S. and Saunders, D W. Large deformations of isotropic materials. VII. Experiments on the deformations of rubber. *Phil. Trans. Roy. Soc.A.* **865** (243) (1951), p. 274.
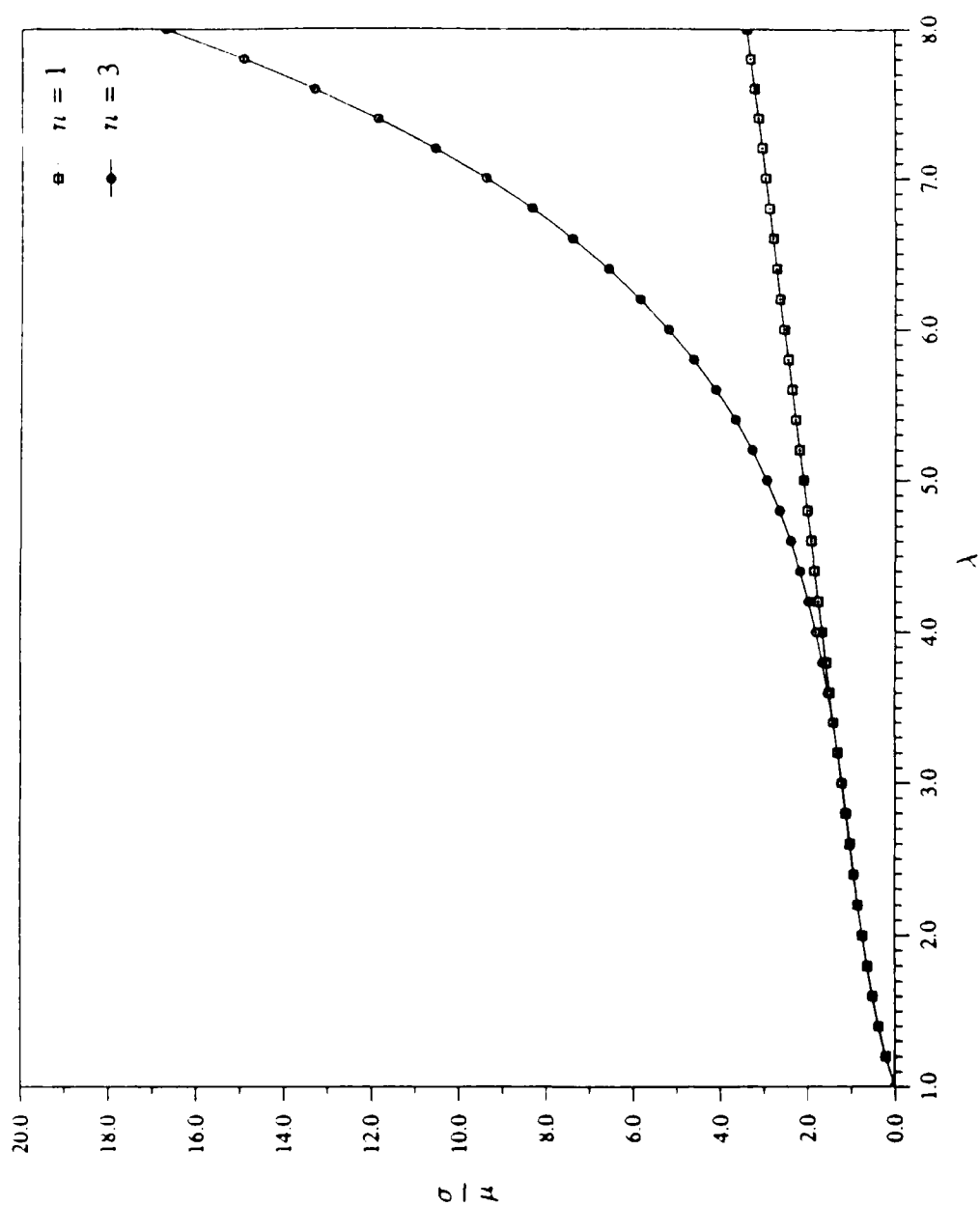
(a) At large deformations, $\lambda \leq 8$.

Figure 2.10: Normalized nominal stress strain curve for Mooney-Rivlin material ($n = 1$) and third order strain invariant ($n = 3$).
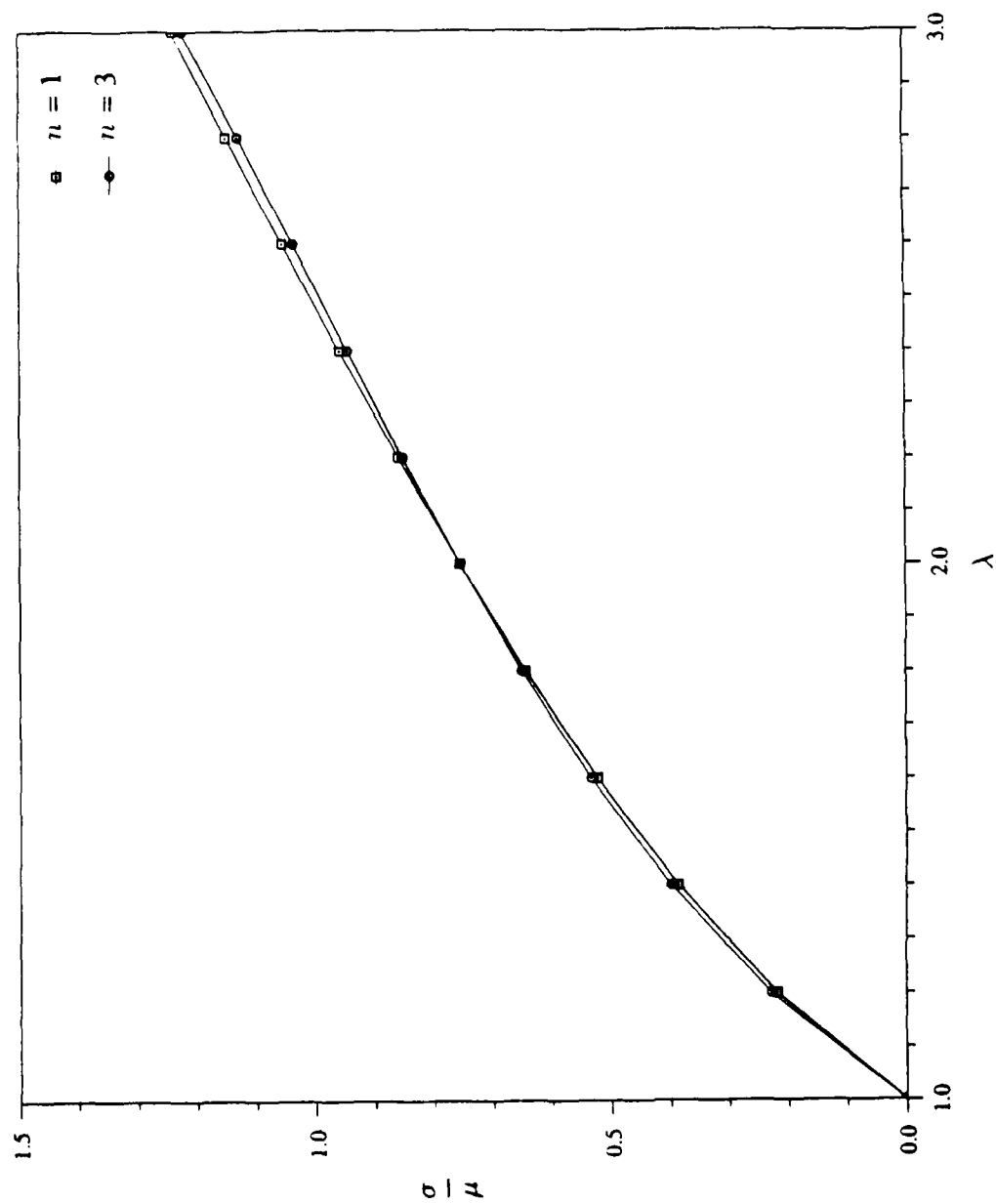
(b) At small deformations, $\lambda \leq 3$.

Figure 2.10: Normalized nominal stress strain curve for Mooney-Rivlin material ($n = 1$) and third order strain invariant ($n = 3$).

(a) At large γ.

Figure 2.11: Normalized shear stress versus γ.

Amount of Shear, γ

$\square$ $n = 1$

$n = 3$
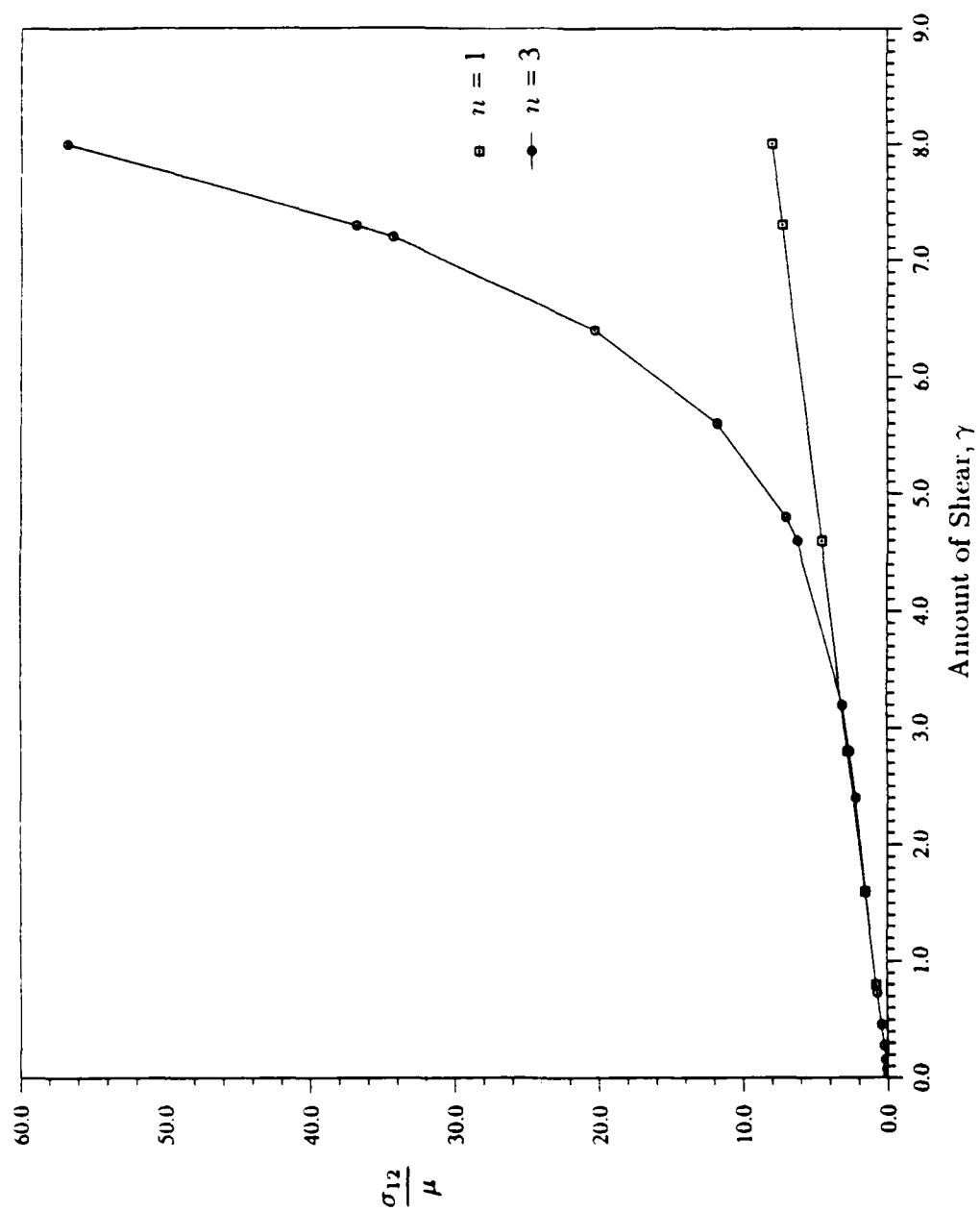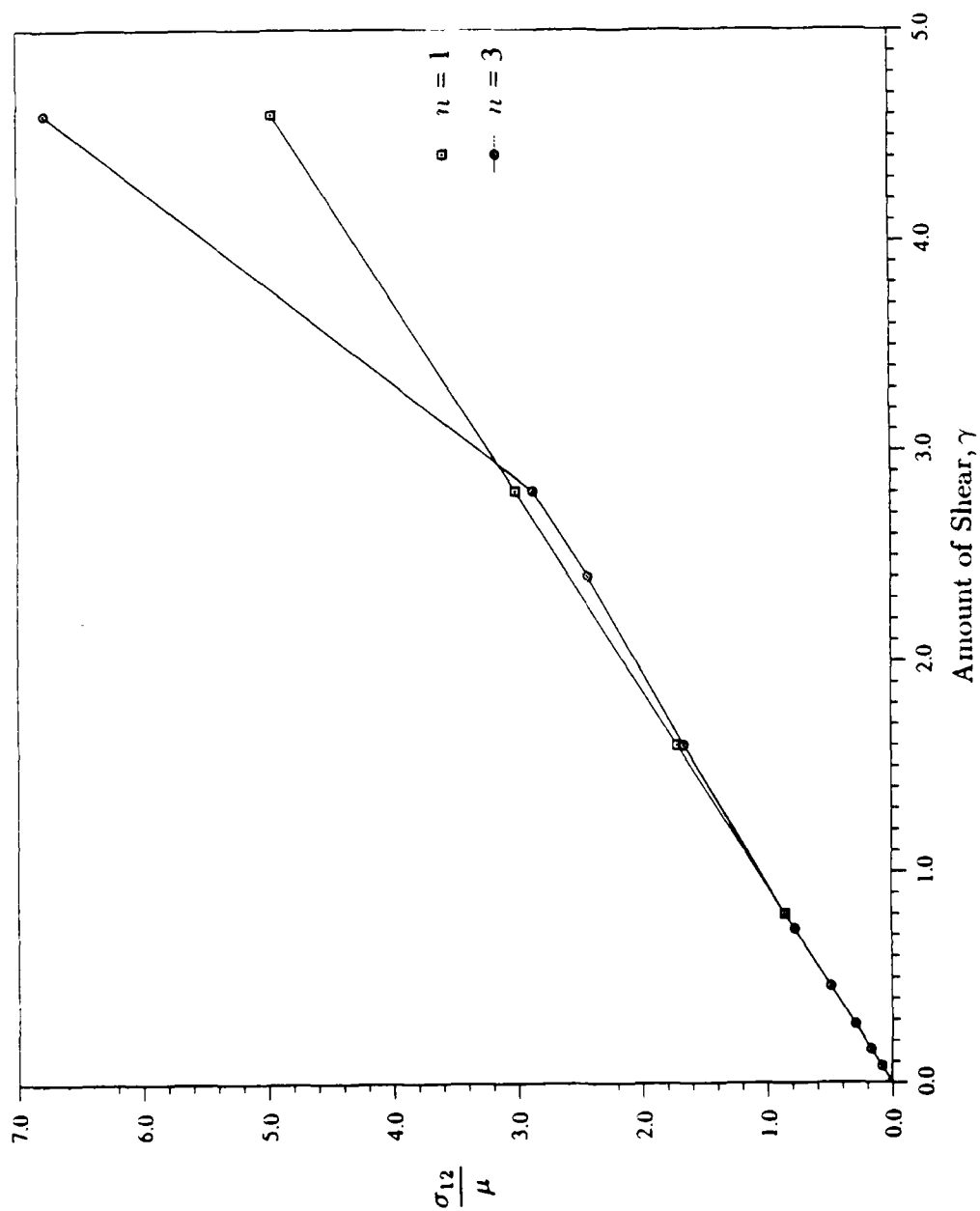
(b) At small γ.

Figure 2.11: Normalized shear stress versus γ.

2.8 Computational Model

Only the top half of the crack tip region, Figure 2.12, is required for finite element discretization since the problem has reflective symmetry about the x-axis. The crack length, L, equals the radius of the semi-circle. The finite element mesh contains two regions. A coarse mesh surrounds the crack tip. Enclosing this coarse region is a refined mesh where more accurate crack tip field quantities may be found. Both the coarse and the refined regions contain rings of eight noded isoparametric quadrilateral elements. Within a ring, all elements have equal angular extent and the same radial length.

The coarse region in Figure 2.13 contains four rings and extends to $10^{-6}L$. The first ring is constructed of three elements of length $10^{-9}L$. In each subsequent ring, the number of elements is doubled so that the fourth ring contains twenty-four elements. Element lengths in the remaining three rings of the coarse mesh were biased, such that, along a radius extending from the crack tip, the elements are equally spaced on a logarithmic scale from $10^{-9}L$ to $10^{-6}L$. Along each ring, nodal displacements are constrained to enforce compatibility. The surrounding refined mesh is shown in Figure 2.14. All thirty-six rings in this region are constructed of twenty-four elements. Again, the element length increases with radial distance from the crack tip with reference to a logarithmic size scale. Six rings of elements, equally spaced on a logarithmic scale, are contained within a decade unit of crack length, $10^{-m+1}L$ to $10^{-m}L$, where m ranges from 5 to 0. The refined mesh extends from $10^{-6}L$ to L. The entire mesh contains 2850 nodes, with two kinematic degrees of freedom at each node and an additional pressure degree of freedom at the corner nodes. Constructed from 909 elements, the coarse mesh is composed of 45 elements while the refined mesh contains the remaining 864 elements.

One of the assumptions of small scale nonlinearity is that, for sufficiently small loads, linear elasticity would be approximated throughout the crack tip region and that the nonlinear elastic asymptotic crack tip field would evolve when the load was increased. In addition, because the linear elastic asymptotic field is applied as an applied displacement field, it became necessary to determine a value of ν which approximates the behavior of a Mooney-Rivlin material under infinitesimal loads.

First, ν was determined by applying a Mode I linear elastic field as consistent nodal point forces to the outer boundary and comparing the computational results at the crack tip for a linear elastic material to those obtained from an *equivalent* Mooney-Rivlin material, i.e., equal shear moduli at infinitesimal deformations, under identical loading where the value of the stress intensity factor, $K_{I\,applied} = 80\,\text{kPa-m}$, was small enough so that the maximum engineering strain was 0.1. The material

properties of the linear elastic material were modified by varying ν and the finite element analysis was repeated. When $\nu = 0.4999$, the crack tip stress fields for the linear elastic material and the Mooney-Rivlin material agree within two or more digits of accuracy, but when ν is decreased, the two stress fields are only of the same order of magnitude.

The adequacy of the mesh was then verified by comparing the finite element results to the linear elastic asymptotic field. On the basis of equation (2.4), stresses were normalized by a characteristic length, $K_{I \, applied}/\sqrt{2\pi r}$, at different radial distances and then compared to the theoretical solution. Shown in Figure 2.15 as a function of angle, θ, around the crack tip, the greatest differences between the computational stresses and linear elastic theory are found along the radius closest to the crack tip for σ_{11} and σ_{22}. Along an arc of radius of $10^{-6}L$, the numerical solution agrees with theoretical predictions. Closer to the crack tip, small differences between theory and the numerical solution are present and are attributed to hydrostatic pressure. The numerical values of shear stress, σ_{12}, agree with linear elastic theory at all radii. Calculated values of the J-integral were within one percent of the applied value of the J-integral, equation (2.8).

Even though the mesh is coarse at the crack tip, accurate stresses were obtained because this mesh was designed to equalize the error in the element energies surrounding the crack tip. A mesh pattern, considered optimal in that the error in the element energies is equally distributed, was designed by Fried and Yang [40] under the following assumptions: (1) the form of the strain energy is quadratic, i.e., under small displacement theory and linear elasticity; (2) the displacement field will be interpolated with polynomial functions, as in the finite element method; and (3) the displacement field is of the order r^η, where $0 < \eta < 1$. This approach has proven useful in constructing near tip optimal meshes for linear elastic crack tip problems [41]. In this computational analysis, only $u_2 \sim r^\eta$ where $0 < \eta < 1$, based on equation (2.6), and consequently the strain energy is only approximately quadratic. However, the Fried and Yang approach is likely to be better than a uniform mesh pattern and, in the linear elastic region, will equally distribute the error in the element strain energies. To determine the actual error distribution in the nonlinear region, an error analysis based on the asymptotic field and the energy expansion is necessary, but is beyond the scope of this investigation. Finally, when the coarse mesh around the crack tip was further refined, the crack tip elements everted when the maximum strain exceeded 0.2.

A coarse mesh containing twenty-two rings of elements was constructed to identify the appropriate geometry for this problem. The mesh design was similar to the refined mesh in that the elements within a ring were of equal angular extent and radial length and that the element lengths along a radius emanating from the crack tip were biased with reference to the logarithmic scale described previously.

In two separate analyses, the effect of the type of boundary conditions (point forces versus displacements) on the small scale nonlinearity solution was determined. The Mode I linear elastic field was applied as consistent nodal point forces, calculated by integrating the Mode I stress field, equation (2.4), along the surface $r = L$. The value of K_I was gradually increased until $R^* \sim 10^{-4}L$. In the same manner, the Mode I linear elastic displacement field ($\nu = 0.4999$), given as

$$u_1 = \frac{K_I}{\mu}\sqrt{2\pi r}\cos\frac{\theta}{2}\left(1 - 2\nu + \sin^2\frac{\theta}{2}\right) + o\left(r^{1/2}\right) \ .$$

$$(2.30)$$

$$u_2 = \frac{K_I}{\mu}\sqrt{2\pi r}\sin\frac{\theta}{2}\left(2(1 - \nu) - \cos^2\frac{\theta}{2}\right) + o\left(r^{1/2}\right) \ .$$

was nodally enforced along the surface $r = L$. Due to convergence difficulties, the linear elastic field for $\nu = 0.4999$ could not be directly applied. The finite element solution was obtained in a two step process, refer to Figure 2.16. First, the displacement field for $\nu = 0.49$ was applied along the surface $r = L$, and the magnitude of K_I was increased to the desired value, K^*. Next, the displacement field for $\nu = 0.4999$ was applied to the intermediate results so that the displacement boundary conditions changed from $u(K^*, \nu = 0.49)$ to $u(K^*, \nu = 0.4999)$. Again, the value of K_I was increased until $R^* \sim 10^{-4}L$. Here, the value of ν is treated as a parameter in the displacement boundary conditions rather than a variable material property. The two step process will not affect the computational results because the elastomer material is nonlinear elastic and consequently, the load/material path is irrelevant.

The effect of the boundary condition type is shown in Figures 2.17 and 2.18. As the radius of the transition region, the magnitude of the applied value of the stress intensity factor, and the resulting value of the J-integral increase, the solution accuracy, measured by the numerically calculated value of the J-integral, decreases. The value of the numerically computed J-integral increases with the magnitude of the stress intensity factor when displacement boundary conditions are used in contrast to the computational results when consistent nodal point forces are applied. Regardless of the type of the applied boundary condition, the numerical value of the J-integral is path independent at radii exceeding $10^{-7}L$, shown in Figure 2.19. Based on St. Venant's Principle and under the assumptions of small scale nonlinearity, the mesh geometry must be sufficiently large to ensure that the leading term of the applied linear asymptotic field, equation (2.4), is dominant and that the higher order terms do not contribute significantly to the crack tip stress field. These conditions will be satisfied if R^* is extended only to $10^{-5}L$, assuring that the finite element solution is independent of the type of boundary condition that is applied and that the numerical value of the J-integral will be within five percent of the applied value. Stress fields from both types of

boundary conditions were compared when the radius of the transition region was $10^{-5}L$. The stresses were found to be independent of the boundary conditions as the stress field obtained from the displacement boundary conditions agreed with those obtained from the traction boundary conditions within one percent.

The finite element results for the nonlinear analysis were made using the refined mesh described previously. Loading were applied as consistent nodal point forces. The value of the stress intensity factor, K_I, was increased until $R^* = 10^{-5}L$. Computed values of the J-integral at radii exceeding $10^{-6}L$, where the refined mesh begins, were within five percent of the applied value for both constitutive models. For the Mooney-Rivlin material $(n = 1)$, the analysis was continued until the elements at the crack tip began everting. However, for the third order invariant material $(n = 3)$, numerical difficulties were encountered upon load application. To circumvent the problem of the crack tip elements everting, three nodes along the first ring of elements at $\theta = 0$, $\pi/2$, and π were constrained to move in the x-direction only, while the remaining nodes along this ring are constrained only to enforce compatibility, as shown in Figure 2.20. These kinematic constraints allow material flow around this small nucleus of material of radius $10^{-9}L$ in the coarse mesh region and have a negligible effect on stresses in the refined mesh region, which begins at $r = 10^{-6}L$ and where the nonlinear asymptotic solution will be found.

2.9 Results

A computational investigation of Mode I plane strain fracture of an elastomer material was performed under the conditions of small scale nonlinearity Two finite element analyses were performed, one using the Mooney-Rivlin material, equation (2.14), referred to here as $(n = 1)$, while the second analysis was based on the third order invariant of the Rivlin constitutive law, equation (2.21), which will be denoted as $(n = 3)$.

Prior to examining the mechanical crack tip fields, the adequacy of the geometric scale and the path independence of the J-integral will be shown as the magnitude of R^* increases. The effect of the additional kinematic constraint on λ when $(n = 3)$ will be shown. The region of dominance of the nonlinear elastic crack tip field, as determined by the stresses and displacements, will be investigated and crack tip field quantities are compared to the nonlinear asymptotic solution of Knowles and Sternberg [5]. Stresses and deformation fields are normalized by the *characteristic length* represented by $(J_{applied}/\mu)$, where $J_{applied}$ is referenced to the the applied value of K_I along the surface $r = L$ through equation (2.8).

Boundary Conditions

Mode I Linear
Elastic Solution

Traction free
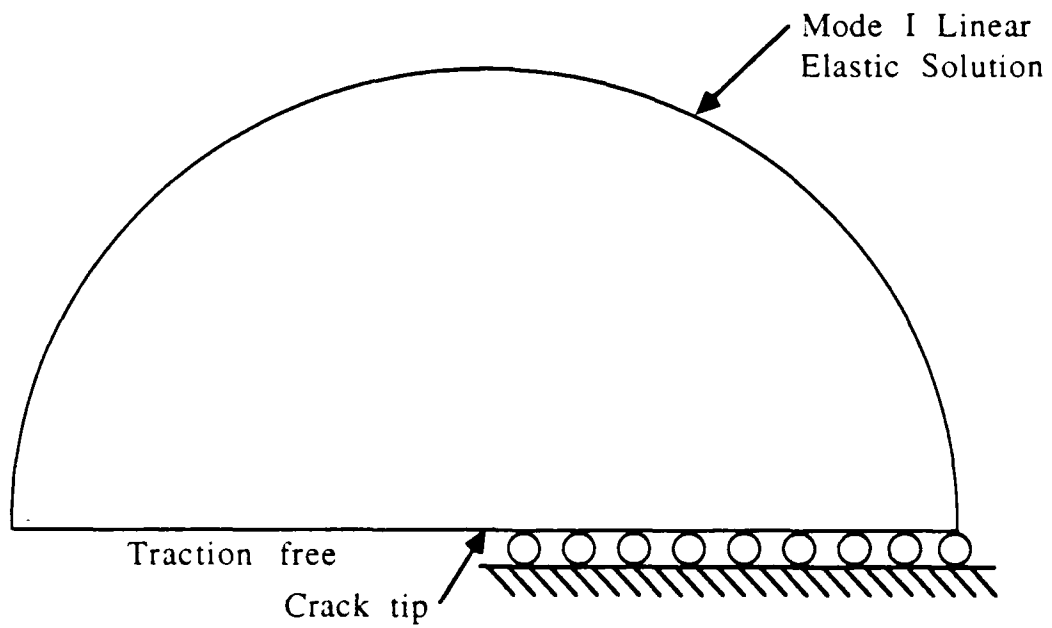
Crack tip

Outer Radius, L

Radius of Nonlinear Region, $R^* = 10^{-5}L$

Figure 2.12: Model of crack tip with boundary conditions.
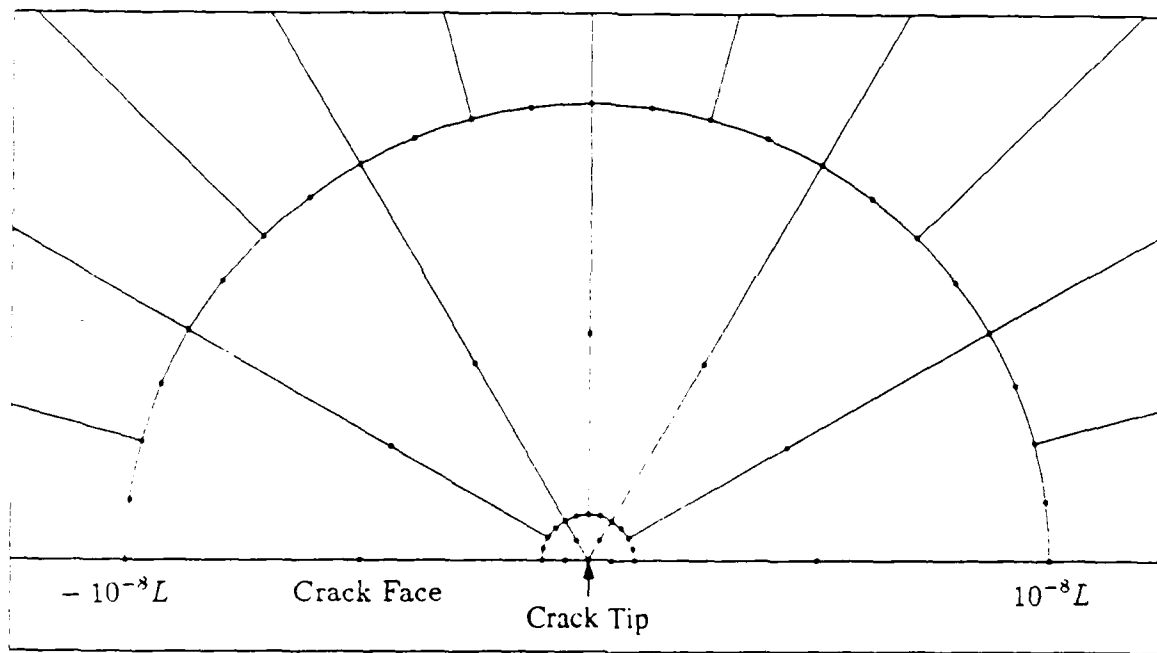
(a) Rings 1 and 2.

Figure 2.13: Coarse crack tip region.

$-10^{-6}L$ Crack Face $10^{-6}L$
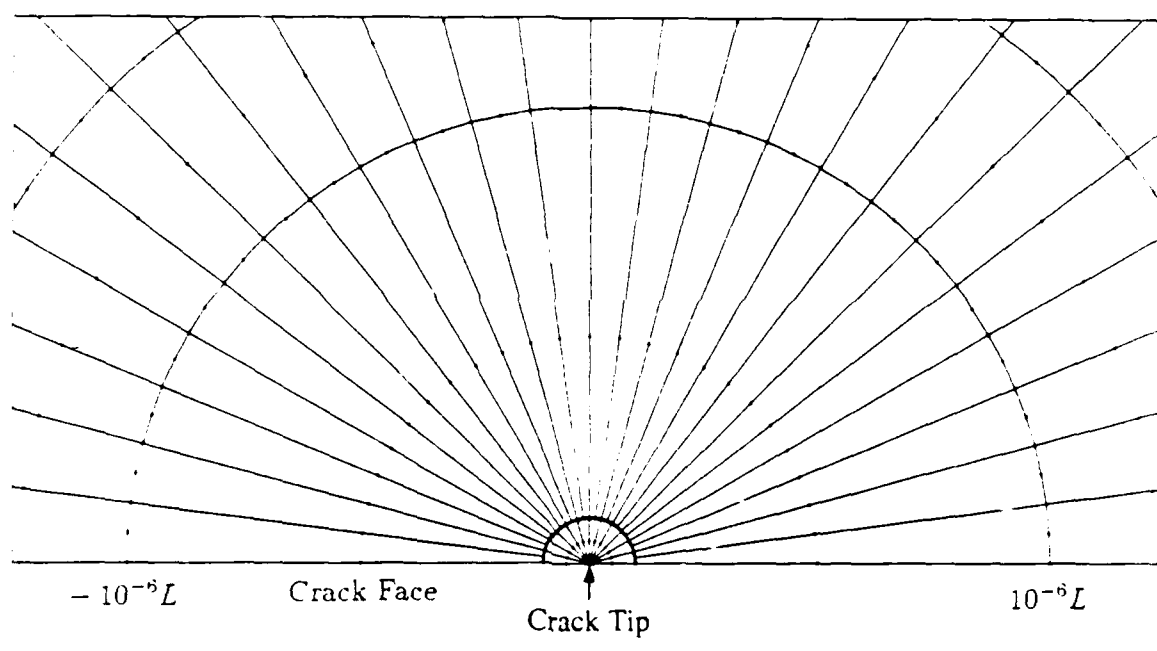
Crack Tip

(b) Rings 3 and 4.

Figure 2.13: Coarse crack tip region.
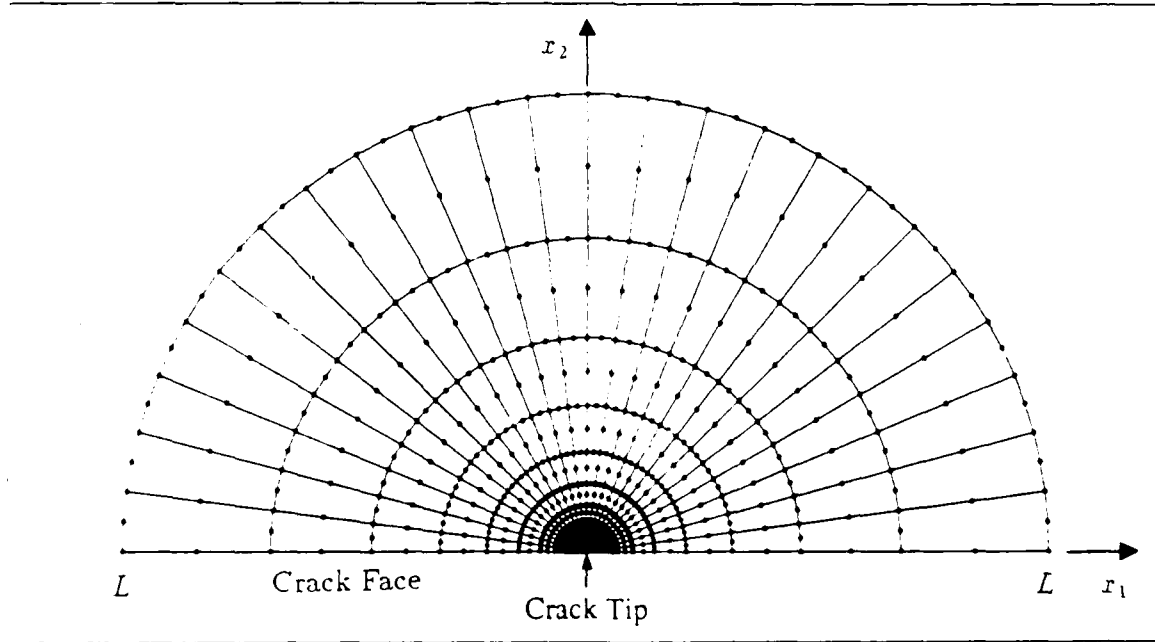
Figure 2.14: Refined mesh surrounding coarse mesh and crack tip.
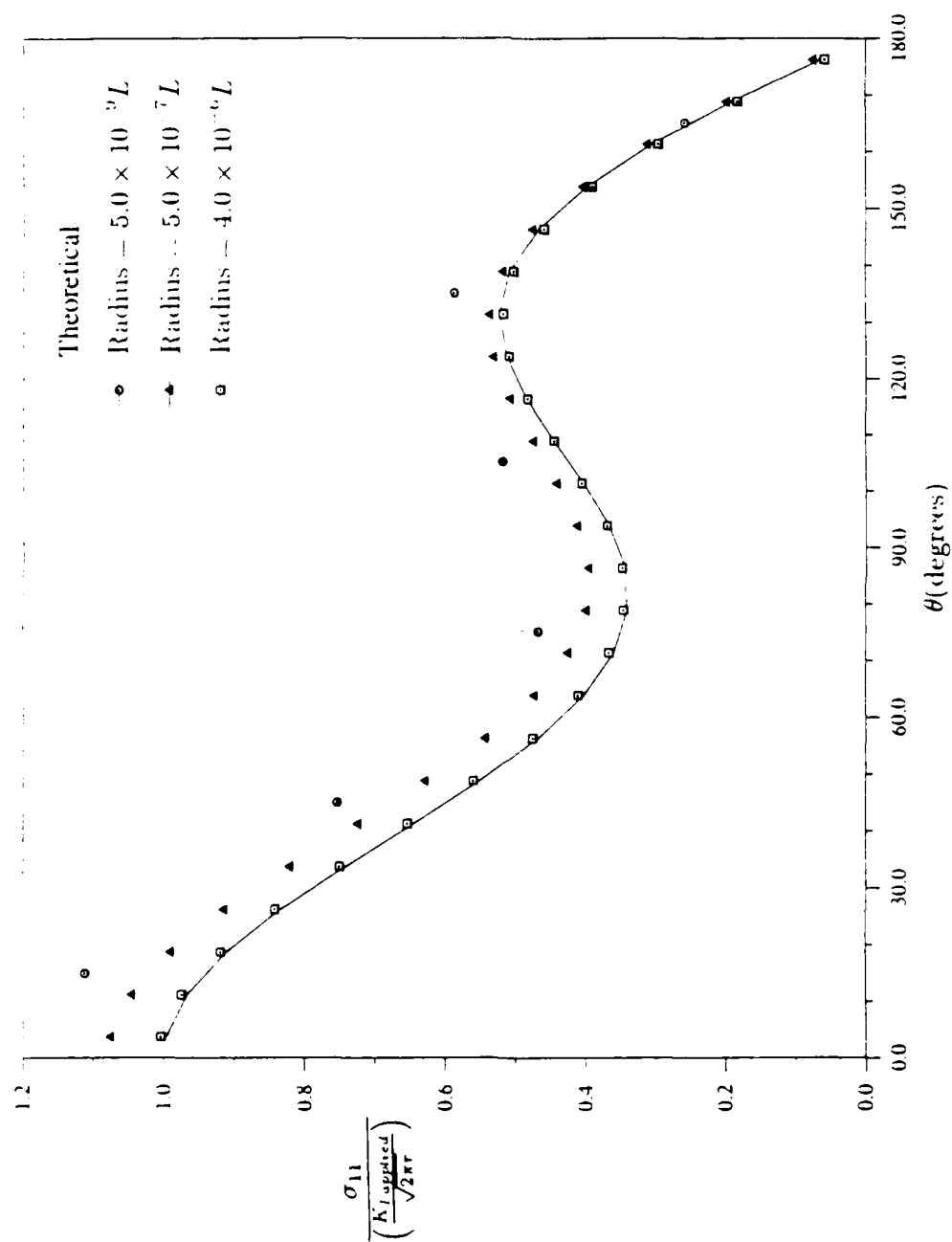
(a) Finite element results for σ_{11}, compared to linear elastic theory.

Figure 2.15 Linear elastic solution.
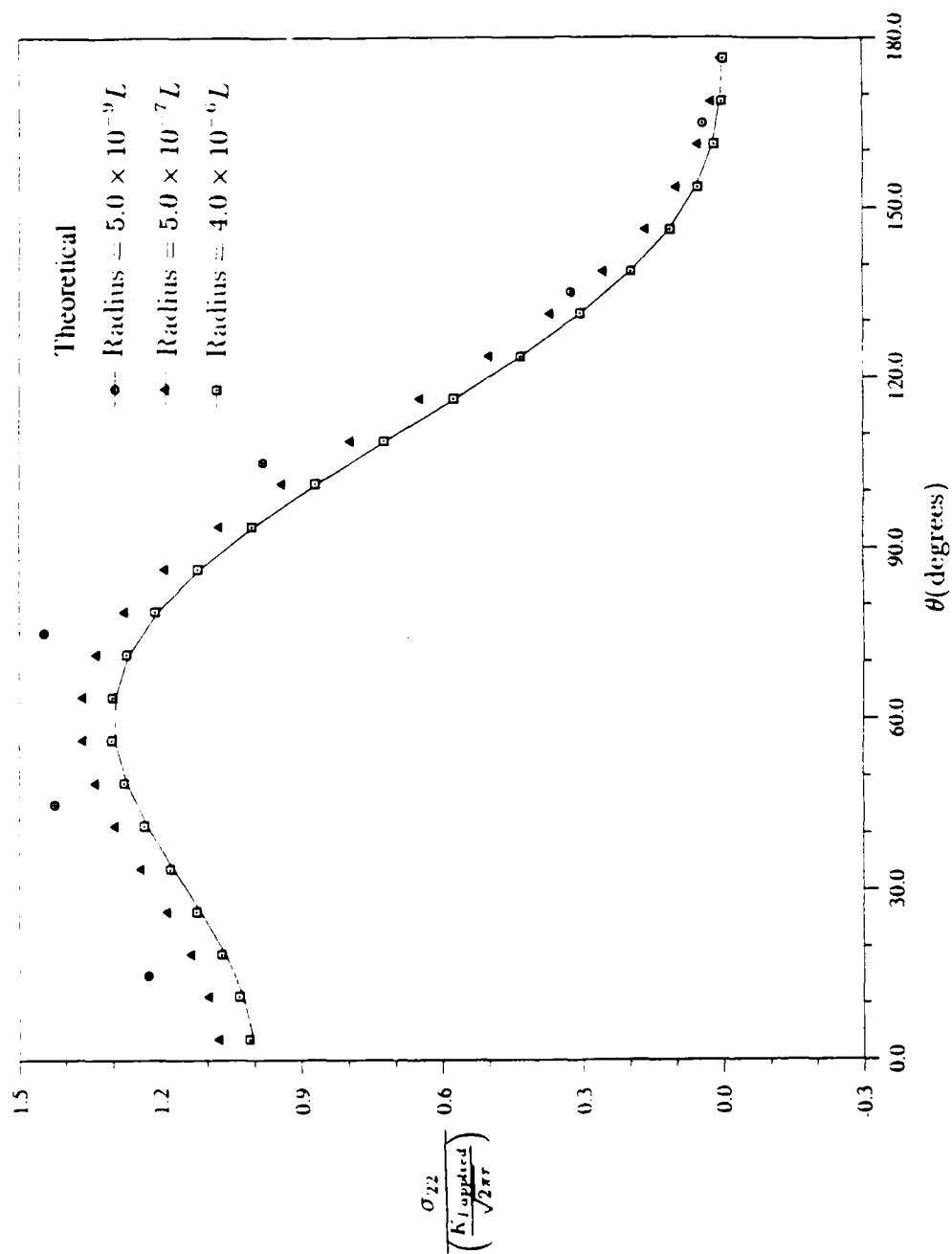
(b) Finite element results for σ_{22}, compared to linear elastic theory.
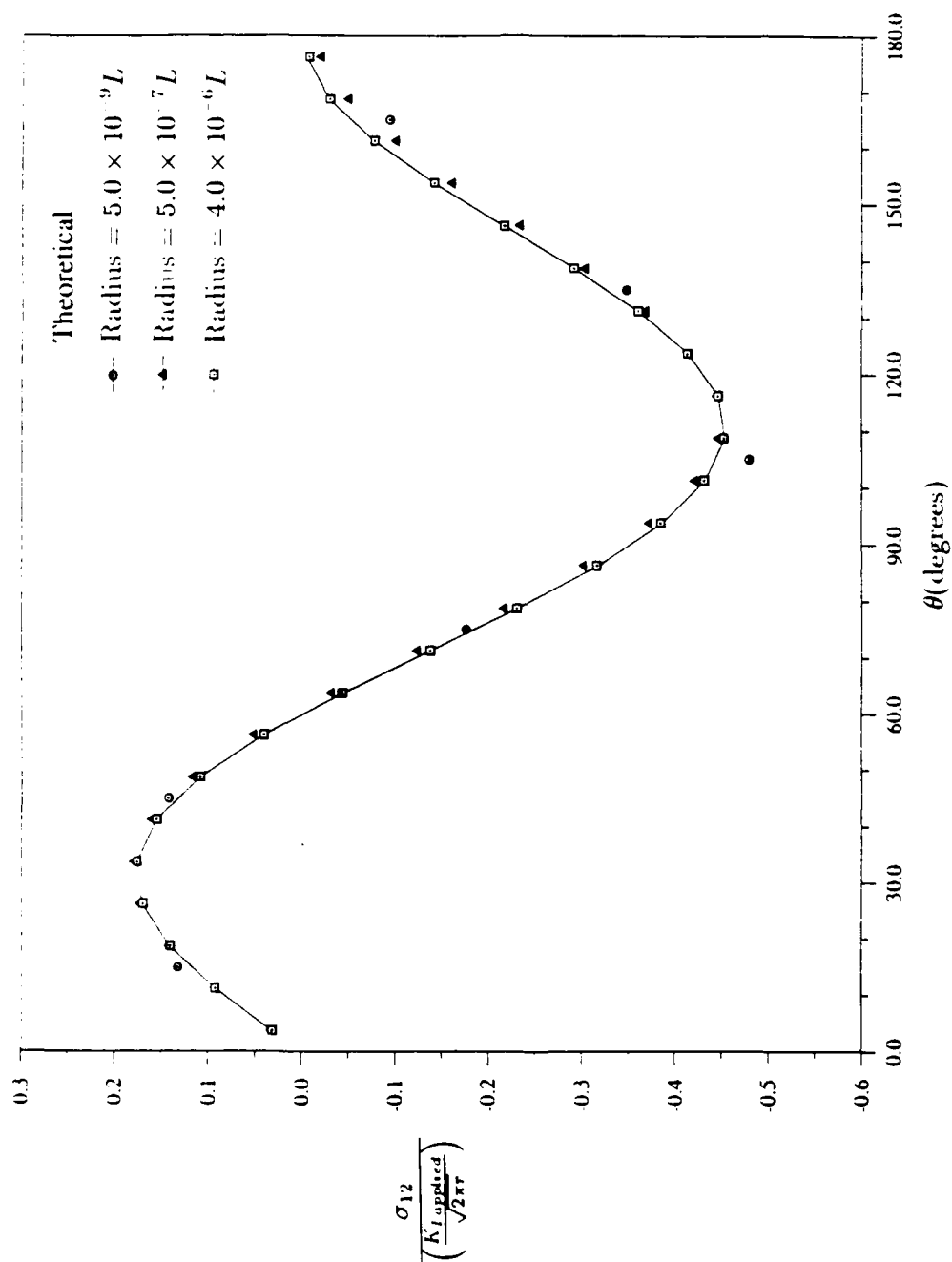
Figure 2.15: Linear elastic solution.

(c) Finite element results for σ_{12}, compared to linear elastic theory.

Figure 2.15: Linear elastic solution.

$$\frac{K_{I\,applied}}{\mu\sqrt{L}} \times 10^{-5}$$

4.7

2

1

0.49   0.4999

ν
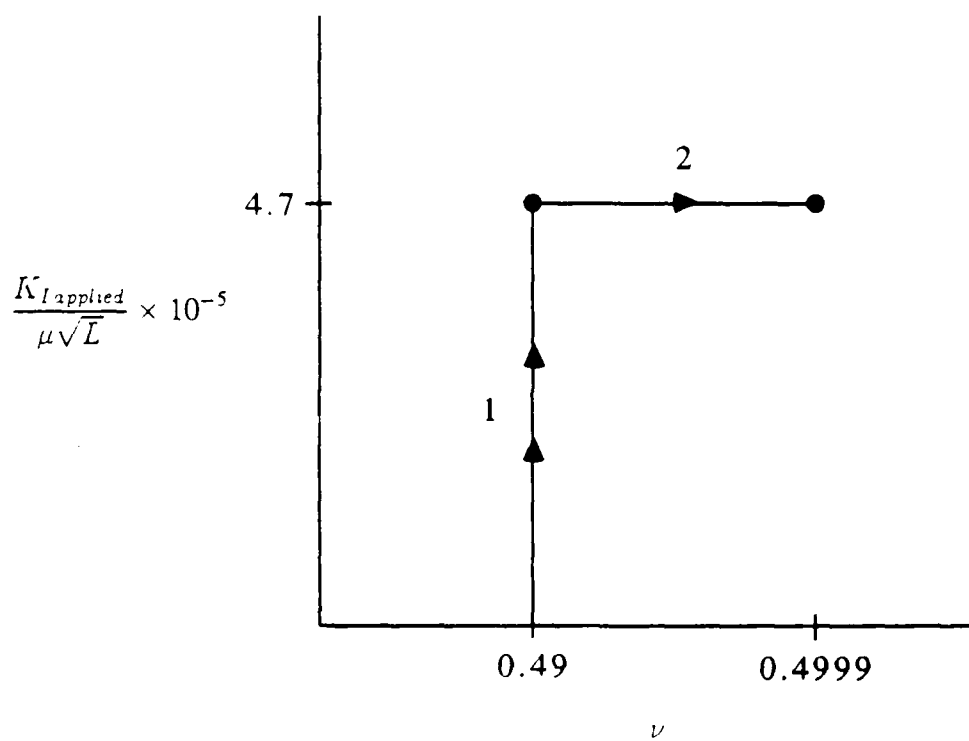
Figure 2.16: Parametric two step process used to obtain finite element solution when applied displacements are used.
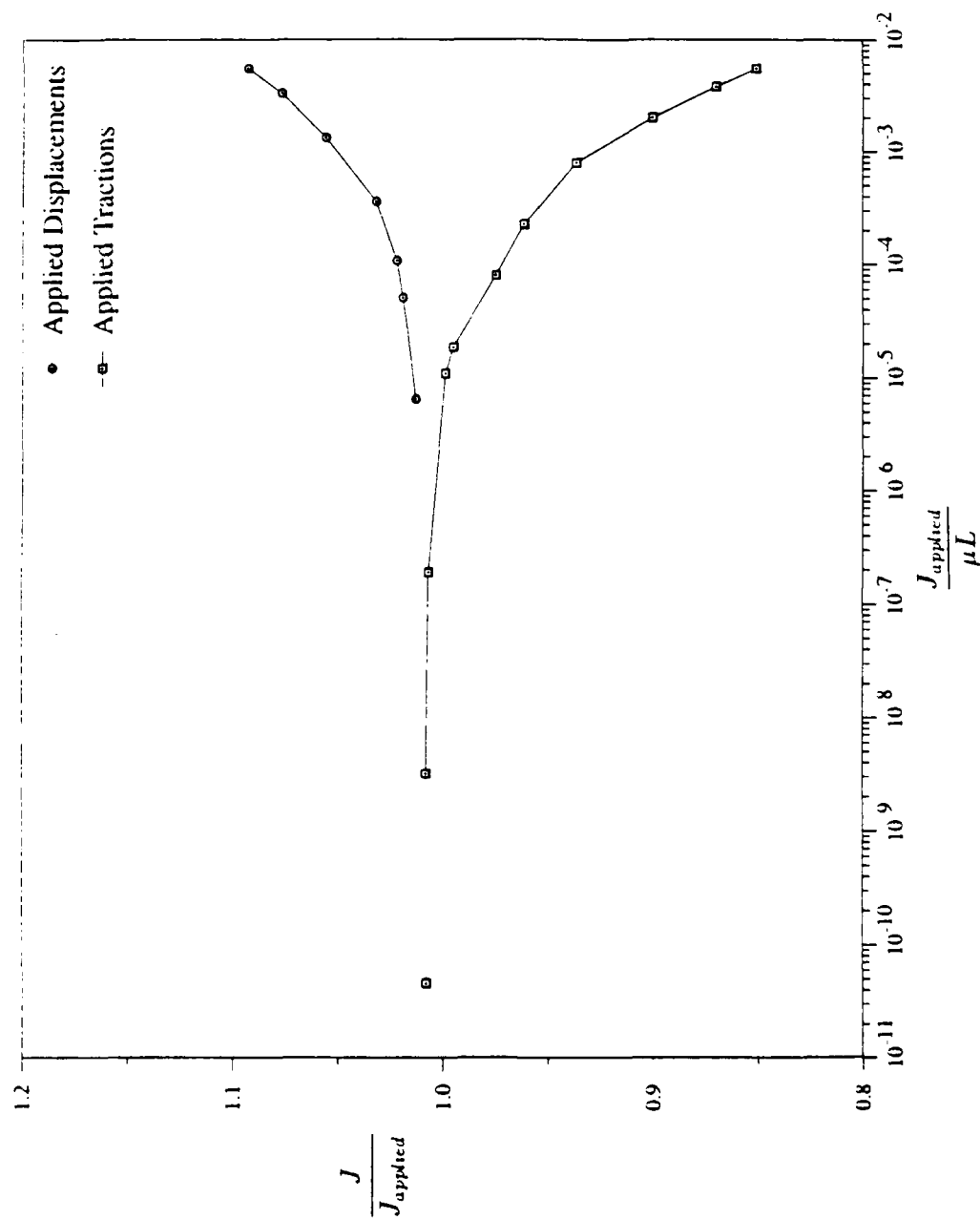
Figure 2.17: Effect of boundary condition type on numerically obtained values of the J integral along $r = 1.2 \times 10^{-6}$ L.
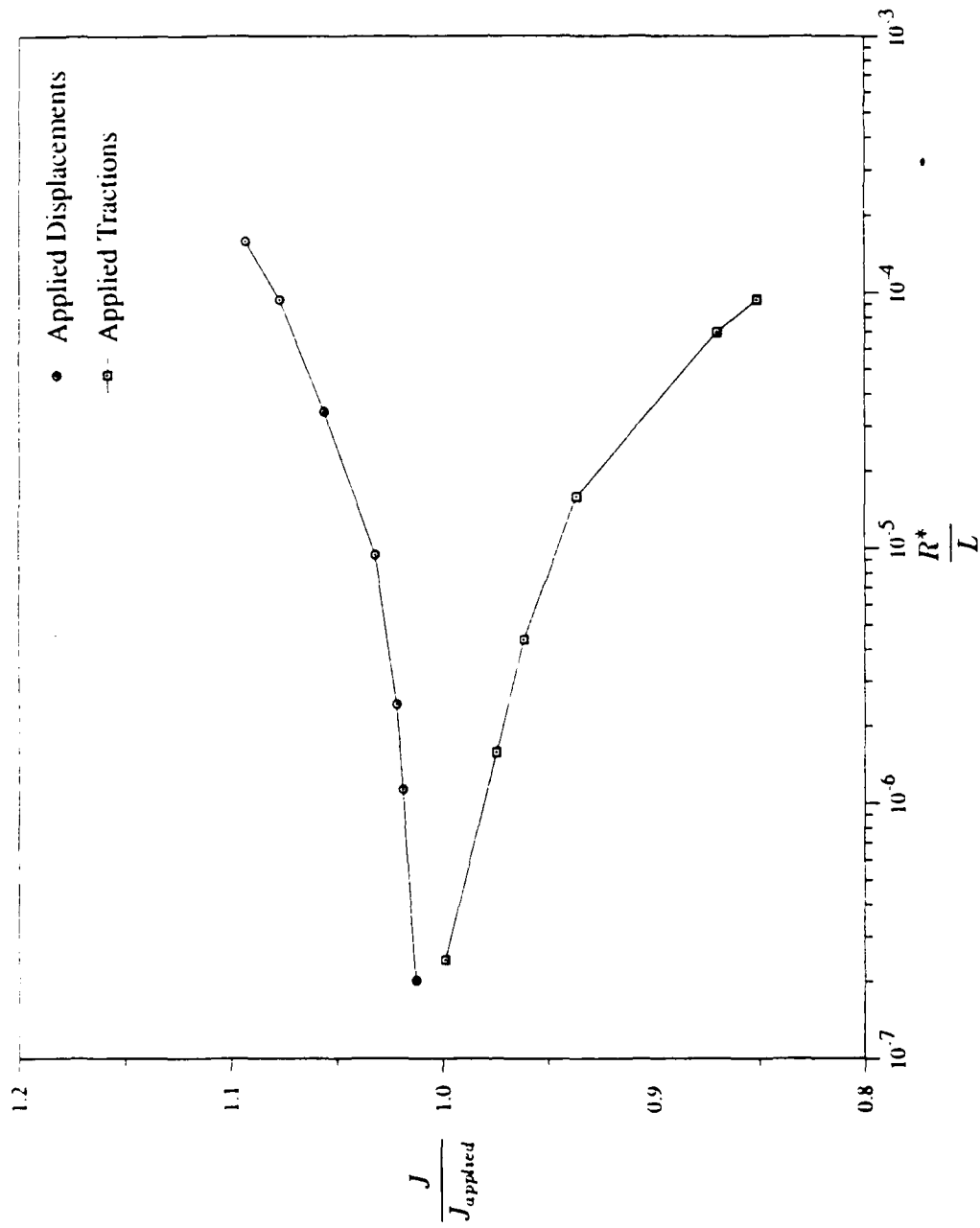
Figure 2.18: Effect of boundary condition type on R^* along $r = 1.2 \times 10^{-6} L$.
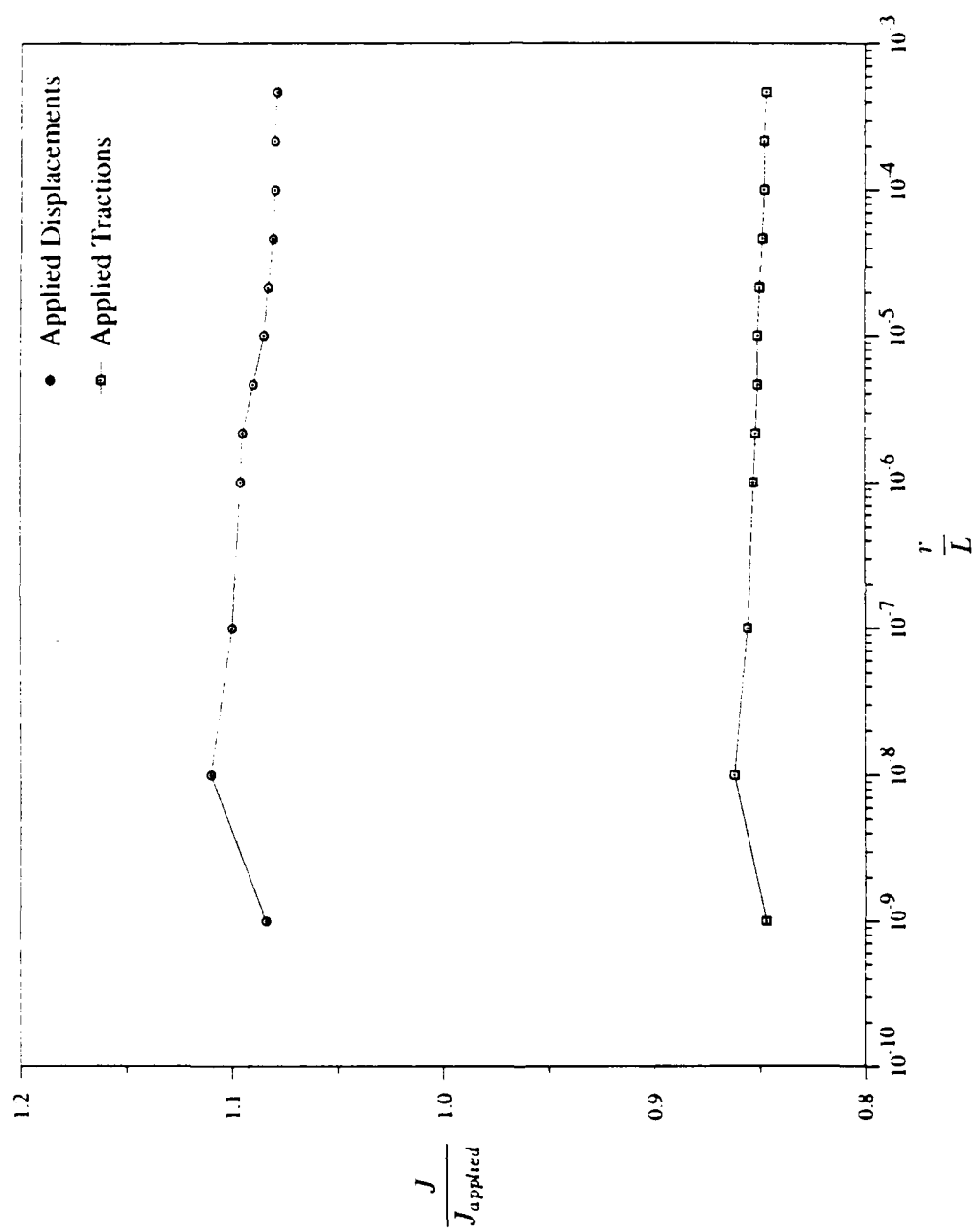
Figure 2.19: Path independence of the J integral for $J_{applied} = 0.023$ MPa m.
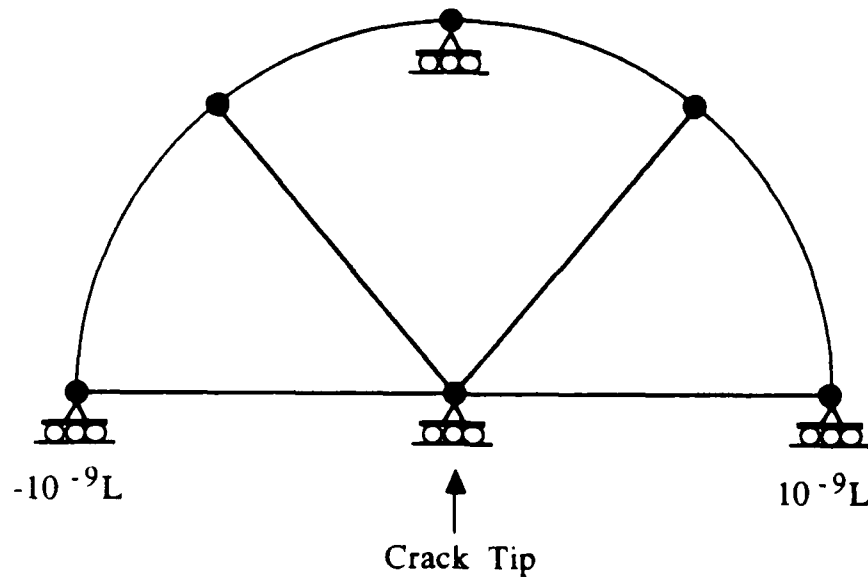
Figure 2.20: Additional finite element kinematic constraints imposed for third order invariant of material law ($n = 3$).

The nature of the nonlinearities, material and kinematic, will be described through contours of the deformed crack tip. Finally, the hydrostatic pressure field in front of the crack will be examined and Ball's failure criteria [22] will be applied to predict the location of cavitation in front of the crack. Using the failure model of Rice and Johnson [30], this prediction will be related to the microstructure of the material.

2.9.1 Geometric Scale

This finite element mesh was designed to ensure that the crack tip stress field is independent of the type of boundary condition (point forces versus displacements) that is applied. To verify that the appropriate geometric scale is maintained, the accuracy of the computed J-integral is shown as a function of R^* and $J_{applied}$, that magnitude applied along $r = L$, in Figures 2.21 and 2.22. Because the geometric scale was maintained for both material laws, only the results for $(n = 3)$ are presented. The geometric scale for this mesh was appropriate as the numerical values of the J-integral are within five percent of applied values at all load levels.

The magnitude of R^* increased linearly with $J_{applied}$ as found in Figure 2.23 ($n = 1$) and 2.24, ($n = 3$) or

$$ R^* \times \frac{J_{applied}}{\mu} \quad \text{or} \quad R^* \times \left(\frac{K_{I\,applied}}{\mu} \right)^2 , \qquad (2.31) $$

similar to the size of the plastic zone in small scale yielding. In these numerical analyses, R^* was extended to $1.2 \times 10^{-4}L$ until the crack tip elements everted for $(n = 1)$, while R^* was allowed to reach $6.6 \times 10^{-4}L$ for $(n = 3)$ where the analysis was stopped because the limits of the geometric scale, defined by a five percent error in the numerical value of the J-integral, were attained. The region of dominance of the nonlinear elastic field is found throughout the first decade of elements closest to the crack tip in the refined mesh region for $(n = 1)$ but extends well into the second decade for $(n = 3)$.

2.9.2 Path Independence of the J-integral

The J-integral was within one percent of the mean value along all contours from $r = 10^{-6}L$ to $3.0 \times 10^{-3}L$, Figure 2.25, the largest radius at which the J-integral was evaluated, indicating the J-integral is path independent throughout the refined mesh region. Although the accuracy of the J-integral decreased with increasing load as shown in Figure 2.21, the maximum error in the computed J-integral was
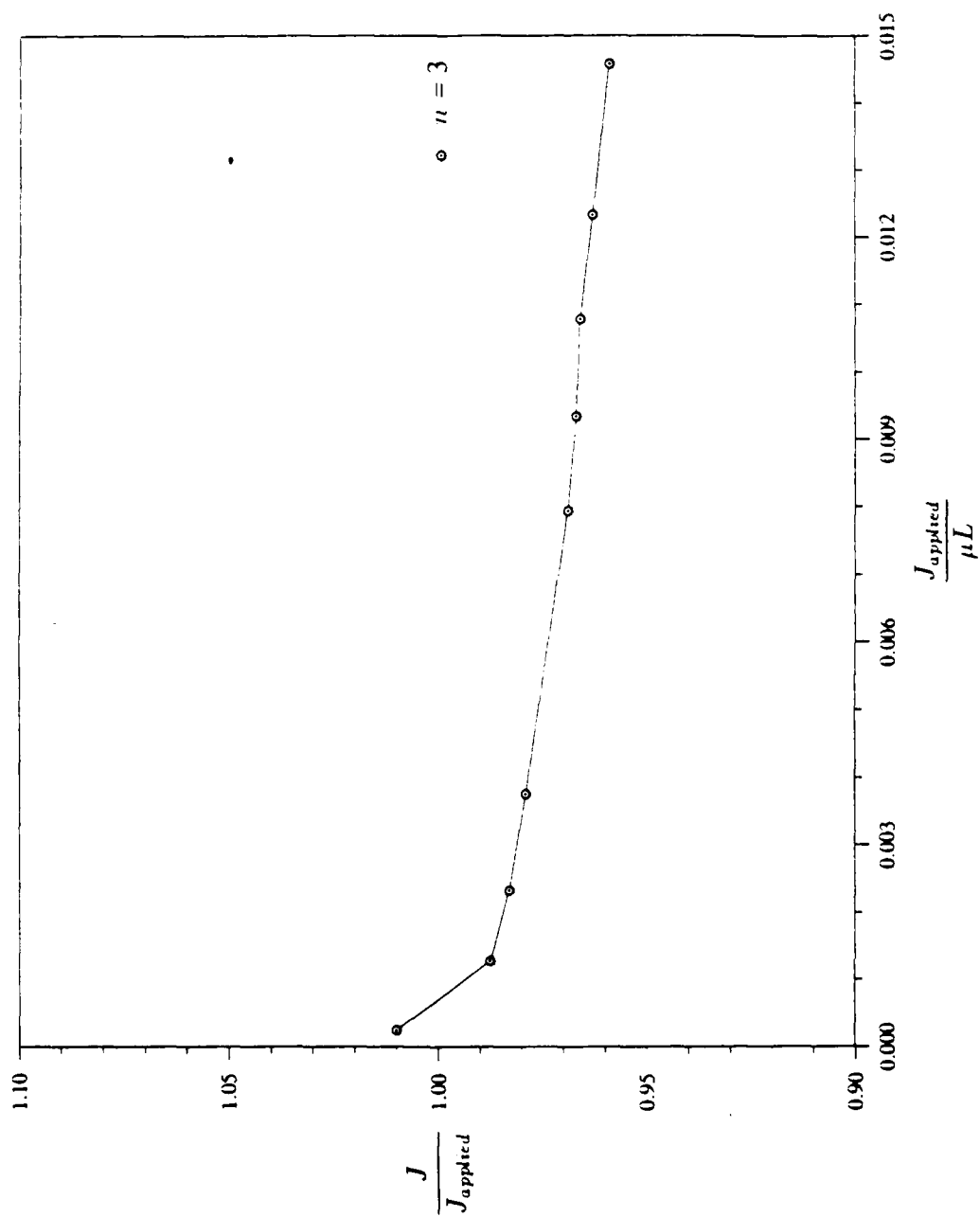
Figure 2.21: The accuracy of the J integral along $r = 2.0 \times 10^{-2}L$ as a function of $J_{applied}$
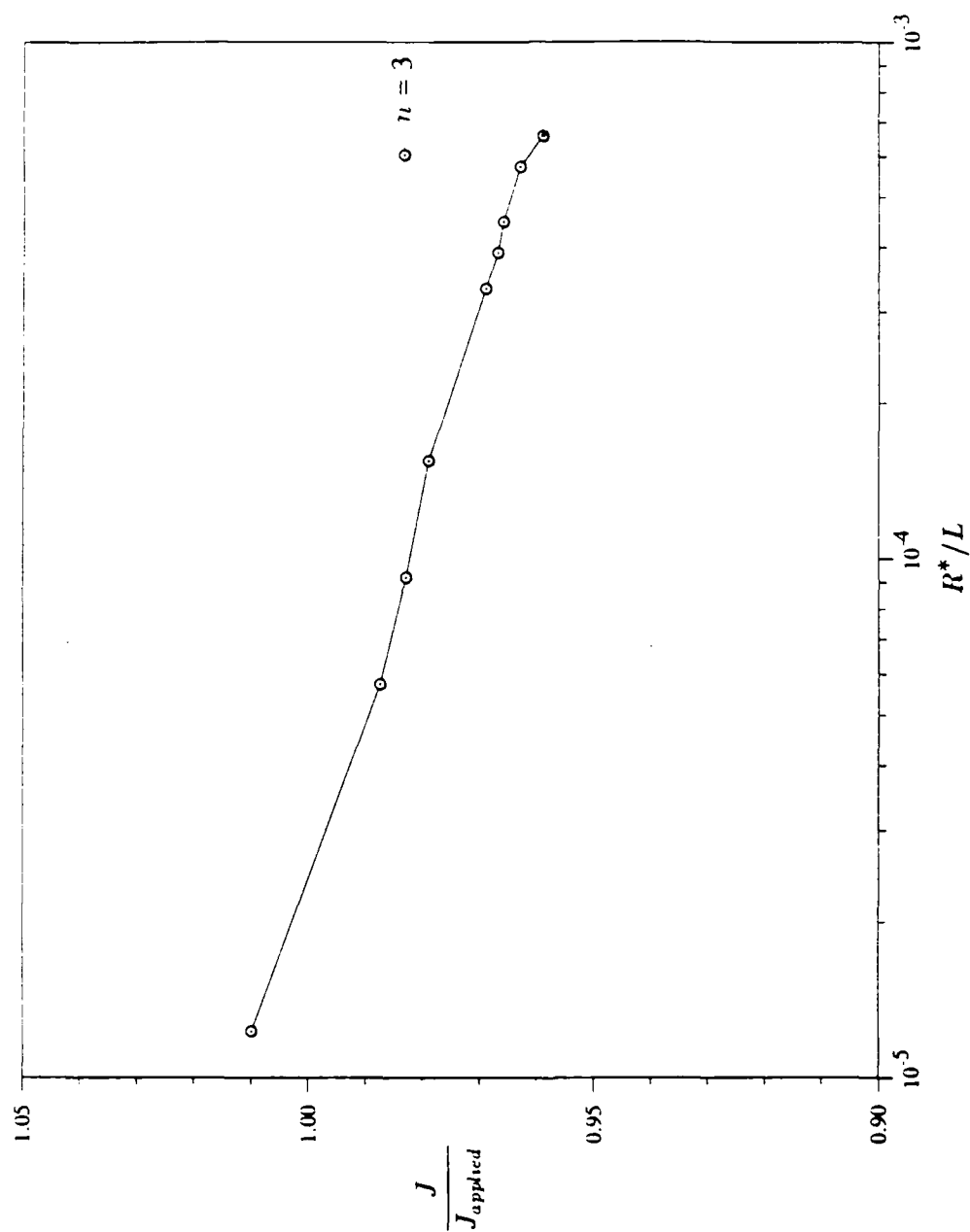
Figure 2.22: The accuracy of the J-integral along $r = 2.0 \times 10^{-2} L$ as a function of R^*.
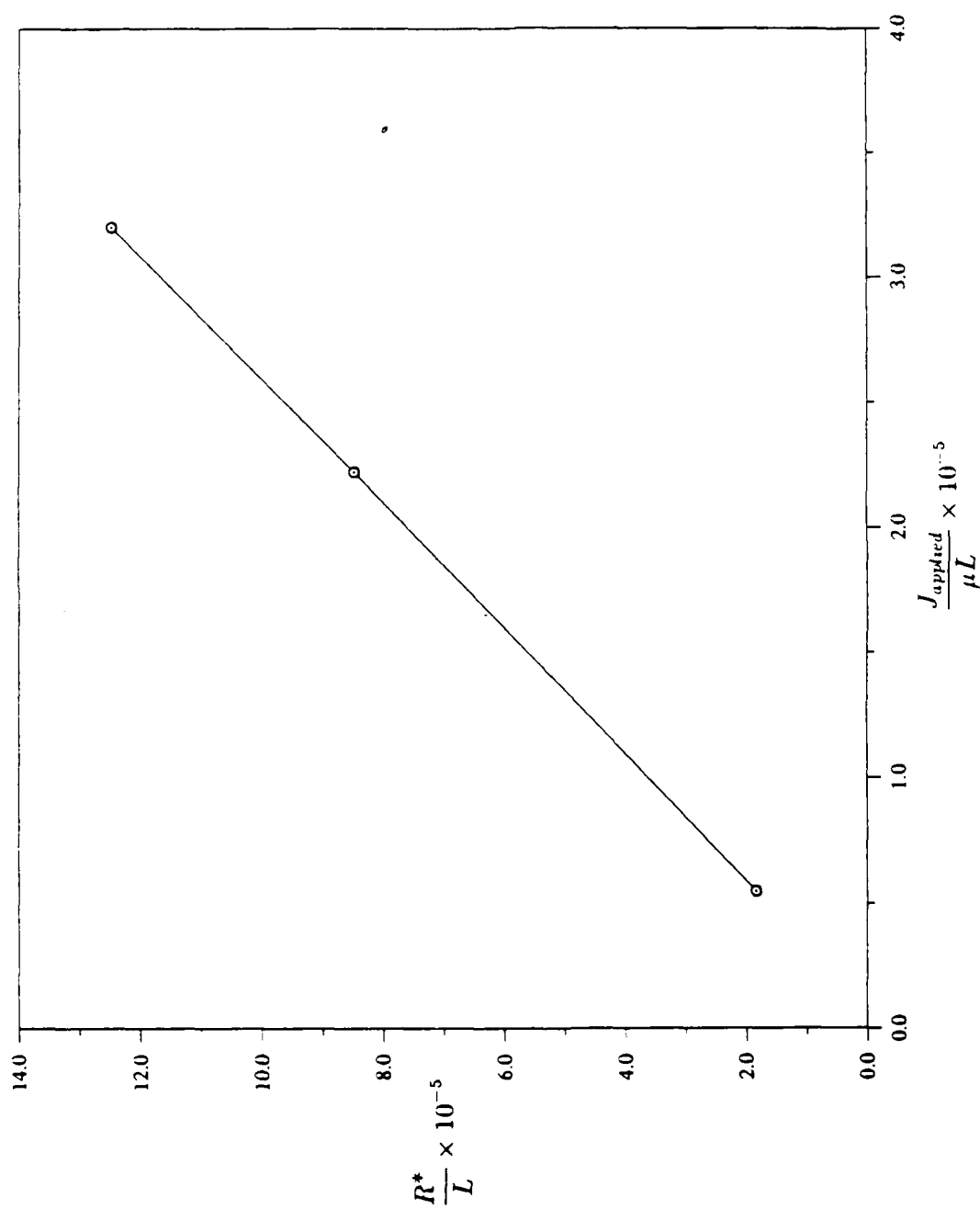
Figure 2.23: Increasing R^* with $J_{applied}$ for $(n-1)$.
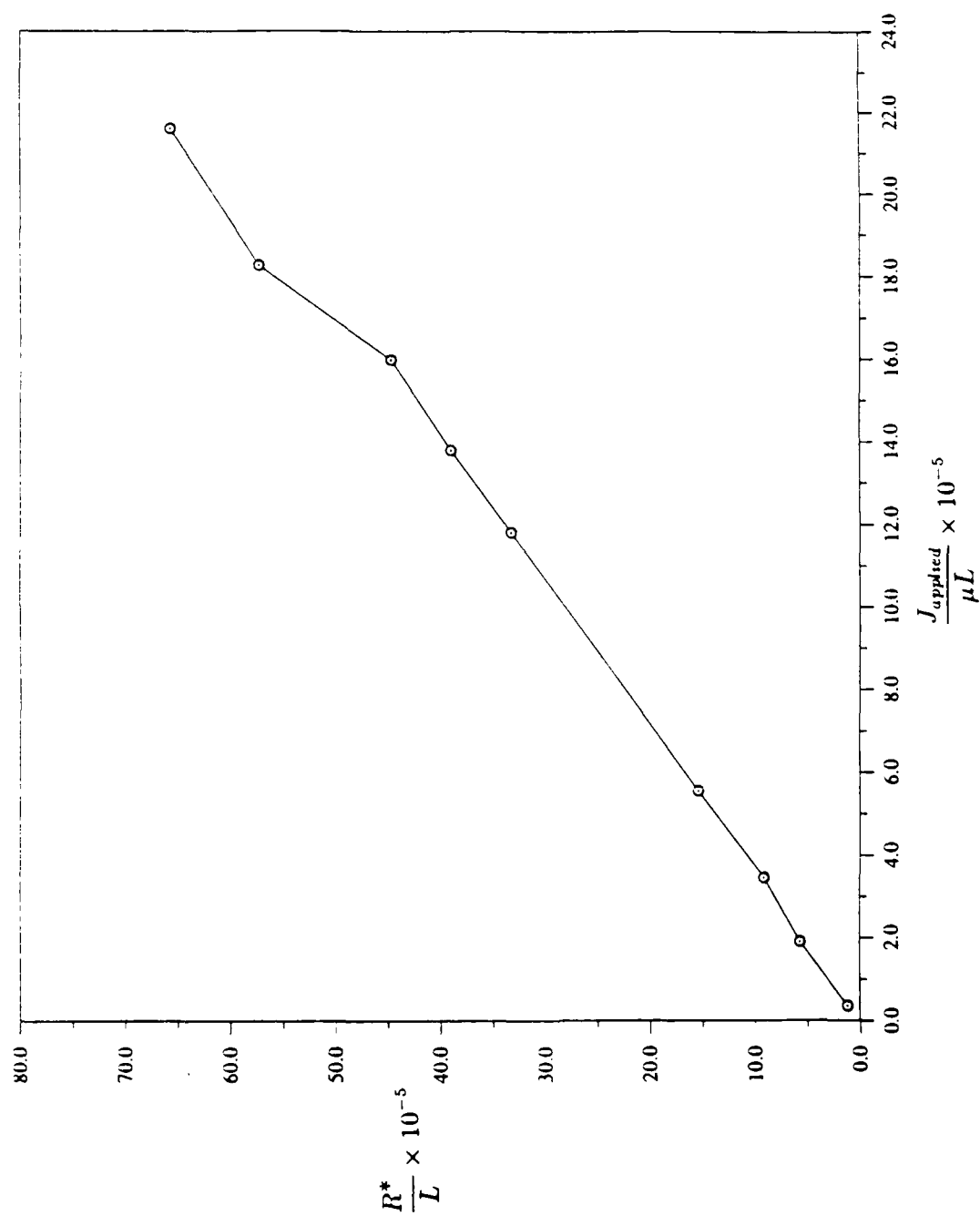
Figure 2.24: Increasing R^* with $J_{applied}$ for ($n = 3$).

two percent for $(n = 1)$ but increased to five percent for $(n = 3)$. In the analysis of the higher order constitutive model, the value of the J-integral evaluated along the crack front is small due to the kinematic constraints applied along the first ring of nodes, however, at contours away from the crack front, the magnitude approximates applied values.

2.9.3 Determination of Load Amplitude Parameters

In the Knowles and Sternberg solution [5], equation (2.6), there are three load amplitude parameters, a, b, and d. The load parameters, a and b, are associated with leading order terms in both the stress and deformation fields. The magnitude of a in small scale nonlinearity can be determined by direct evaluation of the J-integral, shown in Appendix-B, so that the remaining load parameters must be found from the numerical analysis. As $r \to 0$, the nonlinear asymptotic solution should dominate the computational results and the load parameter, b can be evaluated. To solve for b, the y_1 deformation field was considered. At $\theta = 180$, the y_1 deformation field, equation (2.6), becomes

$$y_1 \sim br \qquad (2.32)$$

However, for both material laws, b could not be found accurately because, as r vanishes, the value of b does not converge to an asymptotic limit although it is noted that

$$b \sim o(1) \qquad (2.33)$$

for both material laws. Similar results are found when an evaluation of b is attempted using τ_{11} and τ_{12}, equation (2.6), at $\theta = 90$, where

$$\tau_{11} \sim \frac{\mu}{2}$$

$$\qquad (2.34)$$

$$\tau_{12} \sim \frac{\mu}{2} \frac{ab}{\sqrt{r}}$$

The value of the amplitude constant d, associated with higher order terms in the y_2 component of the deformation field, also could not be obtained.

Although the load amplitude constant b is associated with leading order terms in the nonlinear stress field, these terms are not the dominant stresses as τ_{22} in equation (2.6) $\gg \tau_{11}, \tau_{12}$ and $y_2 \gg y_1$ as $r \to 0$, and, in finite element analyses, it is the dominant terms that can be found with the greatest accuracy.
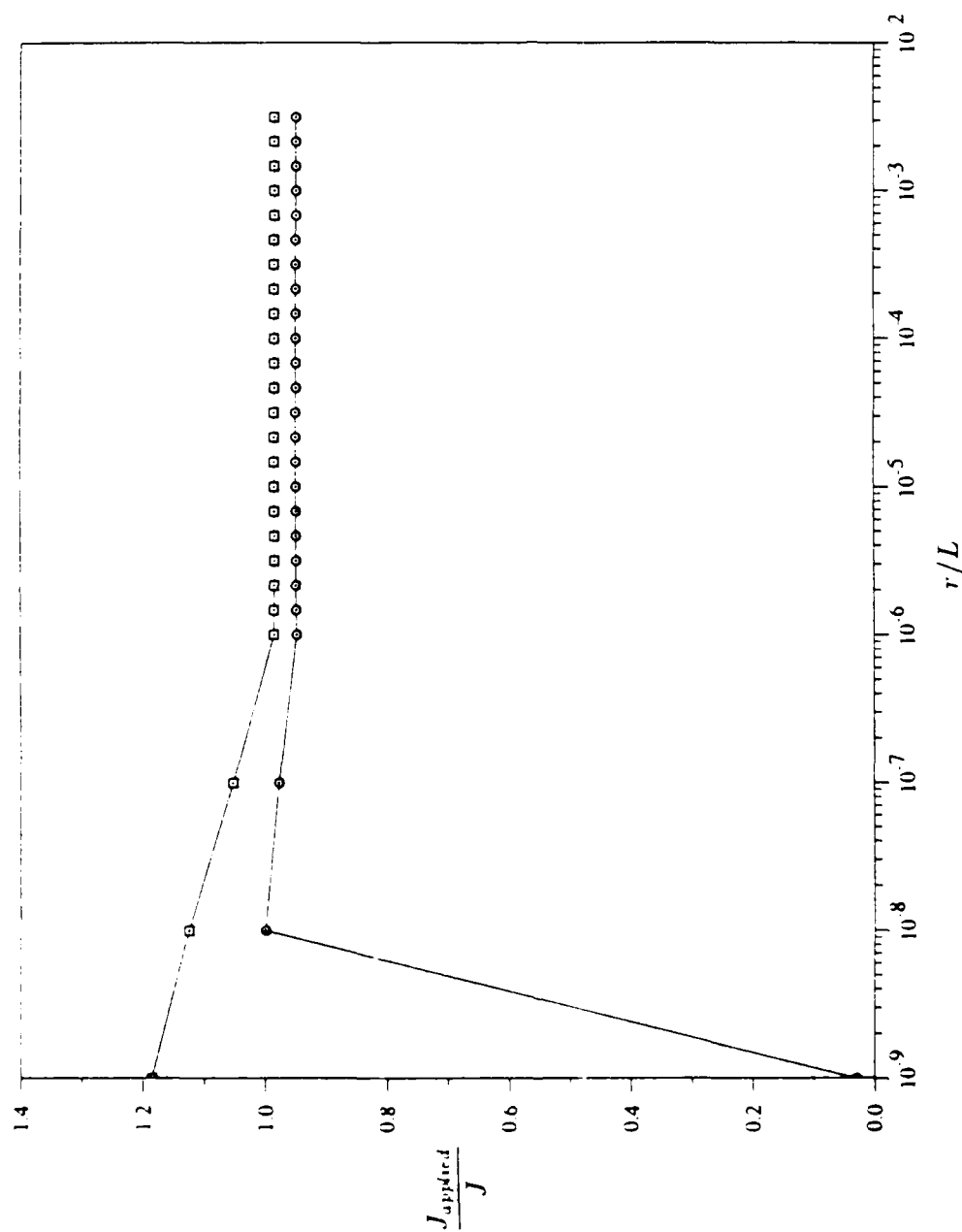
Figure 2.25: Path independence of the J integral at $J_{applied} = 0.016 \, MPa \, m(n = 1)$ and $0.257 \, MPa \, m(n = 3)$.

In Appendix-A, additional higher order terms, derived by Stephenson [6], are included in the nonlinear crack tip field. Because the value of the load amplitude constants b and d could not be determined, it was not attempted to evaluate the load amplitude constants associated with these additional terms.

2.9.4 Crack Tip Contours

As provided by Figure 2.26 and 2.27, the deformed crack surface is similar for both constitutive models where the radius of curvature close to the crack tip is $0.316(J_{applied}/\mu)$ for $(n = 1)$ and increases slightly to $0.319(J_{applied}/\mu)$ for $(n = 3)$, approximating that of the linear elastic solution $(\nu = 0.5), 0.318(J_{applied}/\mu)$. The crack tip opening displacement, measured at $(\theta_d = 135)$ from the crack tip, was $1.3(J_{applied}/\mu)$ for both $(n = 1)$ and $(n = 3)$.

2.9.5 λ Along the Crack Front

As a consequence of incompressibility,

$$I_3 = \lambda_1 \lambda_2 \lambda_3 = 1 \ , \qquad (2.35)$$

and plane strain,

$$\lambda_3 = 1 \ , \qquad (2.36)$$

the principal stretch ratios can be denoted as $(\lambda, 1/\lambda, 1)$. The value of lambda, Figure 2.28 and 2.29, is shown in front of the crack tip $(\theta = 0)$ for both constitutive models and is influenced by the additional kinematic constraint for $(n = 3)$. From the nonlinear asymptotic solution, $\lambda \to \infty$ as $r \to 0$. The presence of a square root singularity, i.e., $\lambda \propto r^{-1/2}$, consistent with the nonlinear asymptotic solution is detected for $(n = 1)$. However for $(n = 3)$, the kinematic constraint prevents λ from increasing as rapidly by removing the square root singularity at the crack tip and replacing it with a weaker singularity, $\lambda \propto r^{-1/5}$ as $r \to 0$. Close to the crack tip, λ increases slowly to a value of 10 at $x_1 = 5.0 \times 10^{-9} L$, the first ring of unconstrained nodes.

2.9.6 Crack Tip Stress Fields

Normalized contours of stress, found at the centroid of the element, versus undeformed radial distance from the crack tip are shown in Figure 2.30 through 2.35.
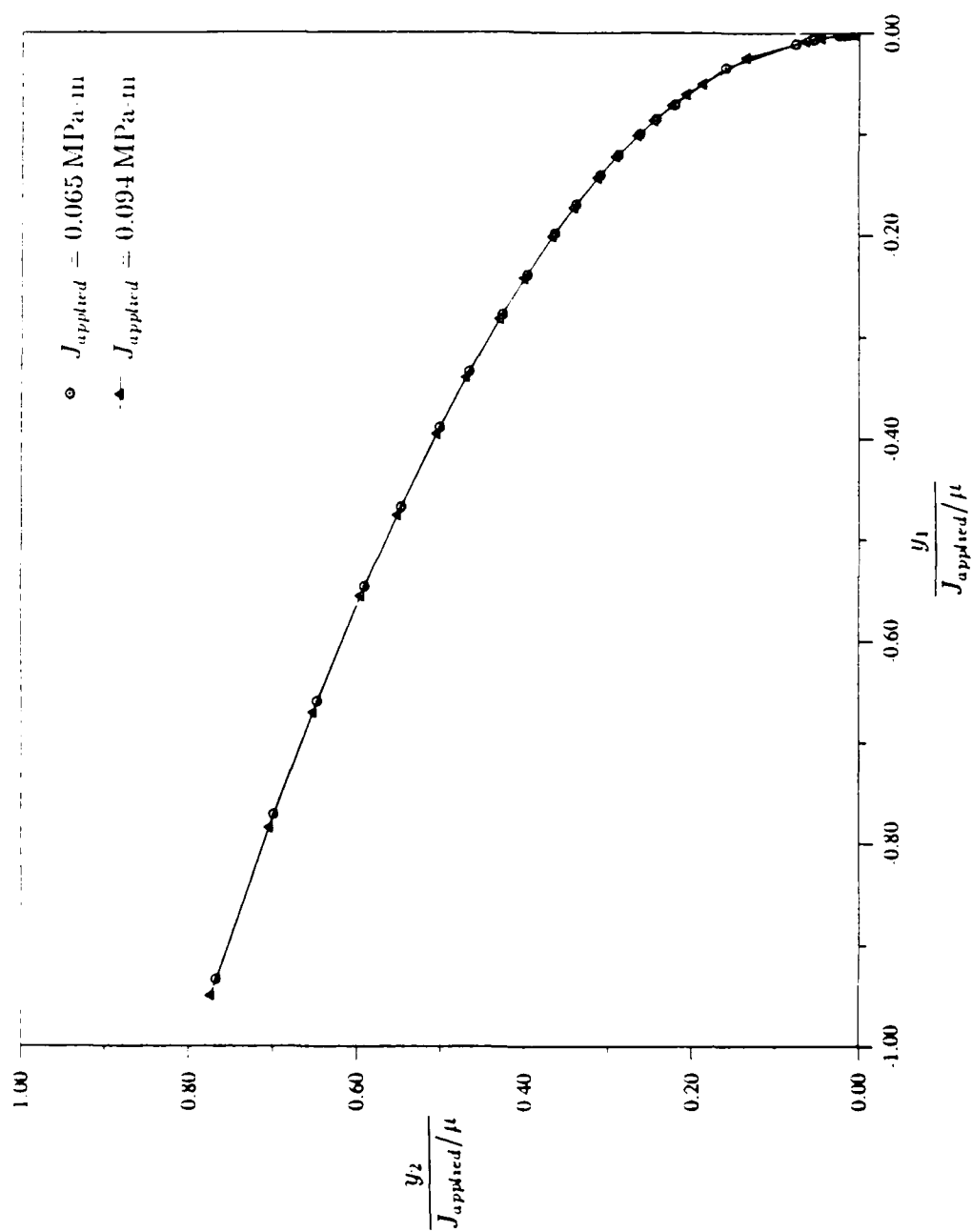
Figure 2.26: Crack tip contour for $(n = 1)$.
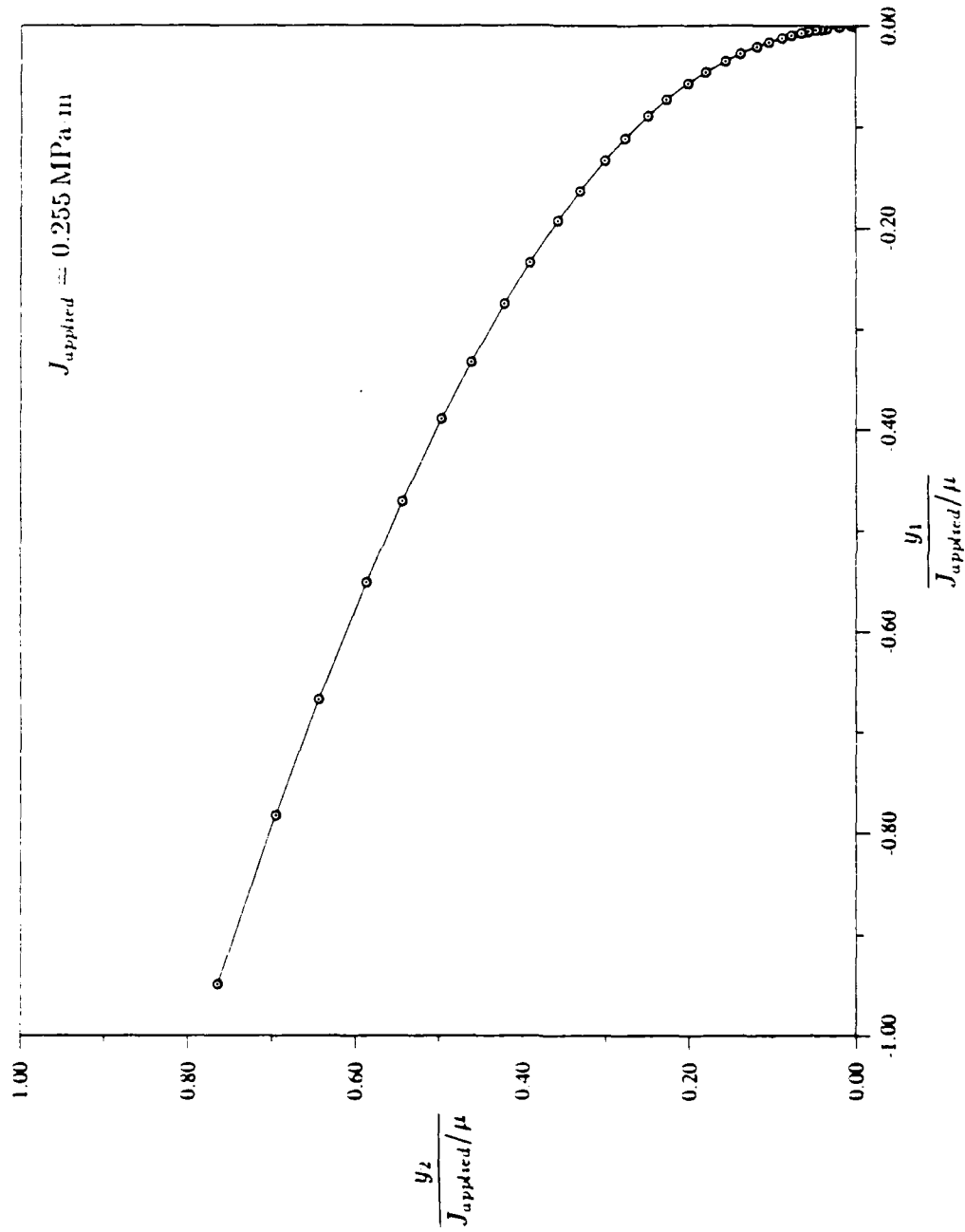
Figure 2.27: Crack tip contour for (n = 3).
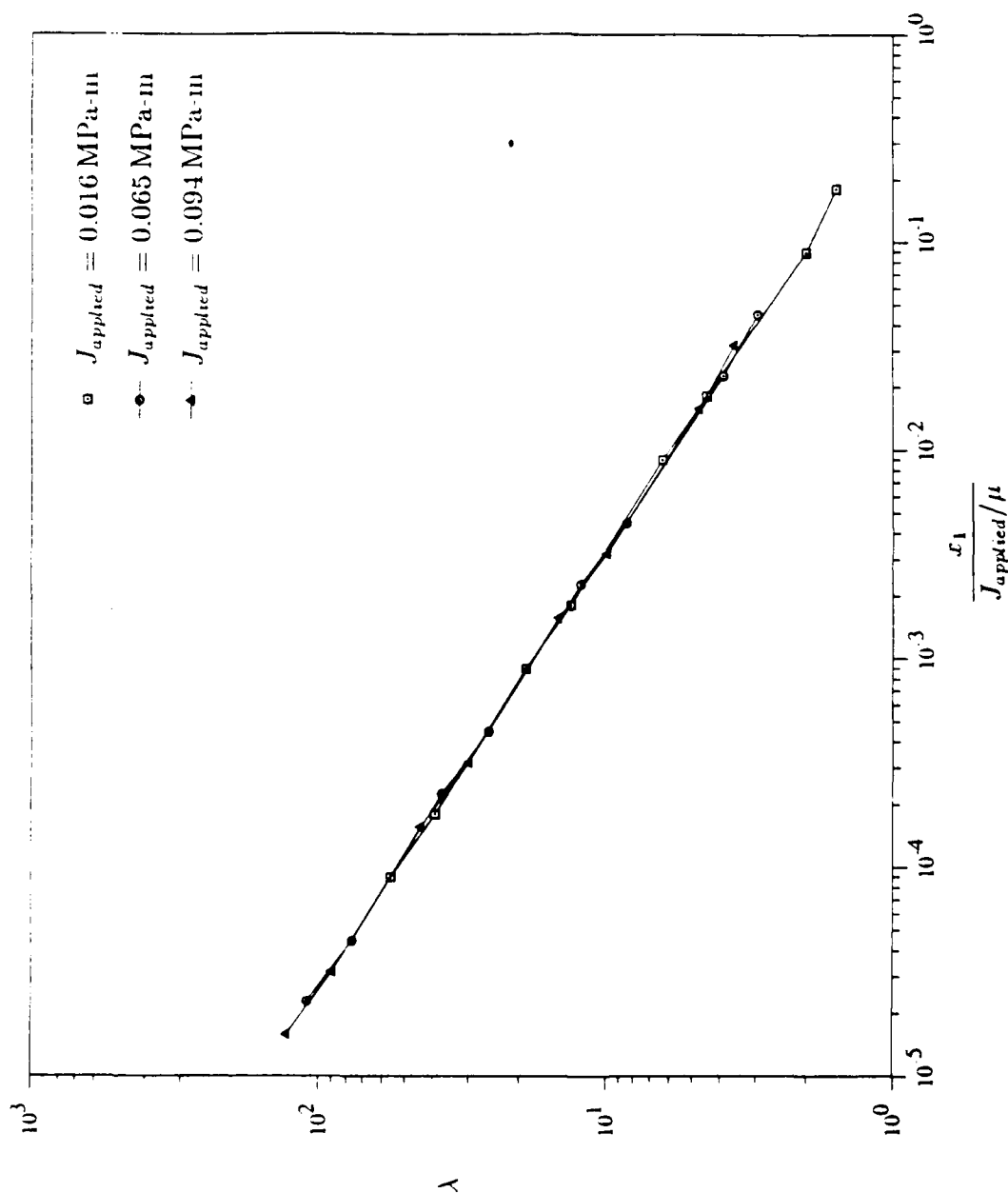
Figure 2.28: λ along the crack front for ($n = 1$).
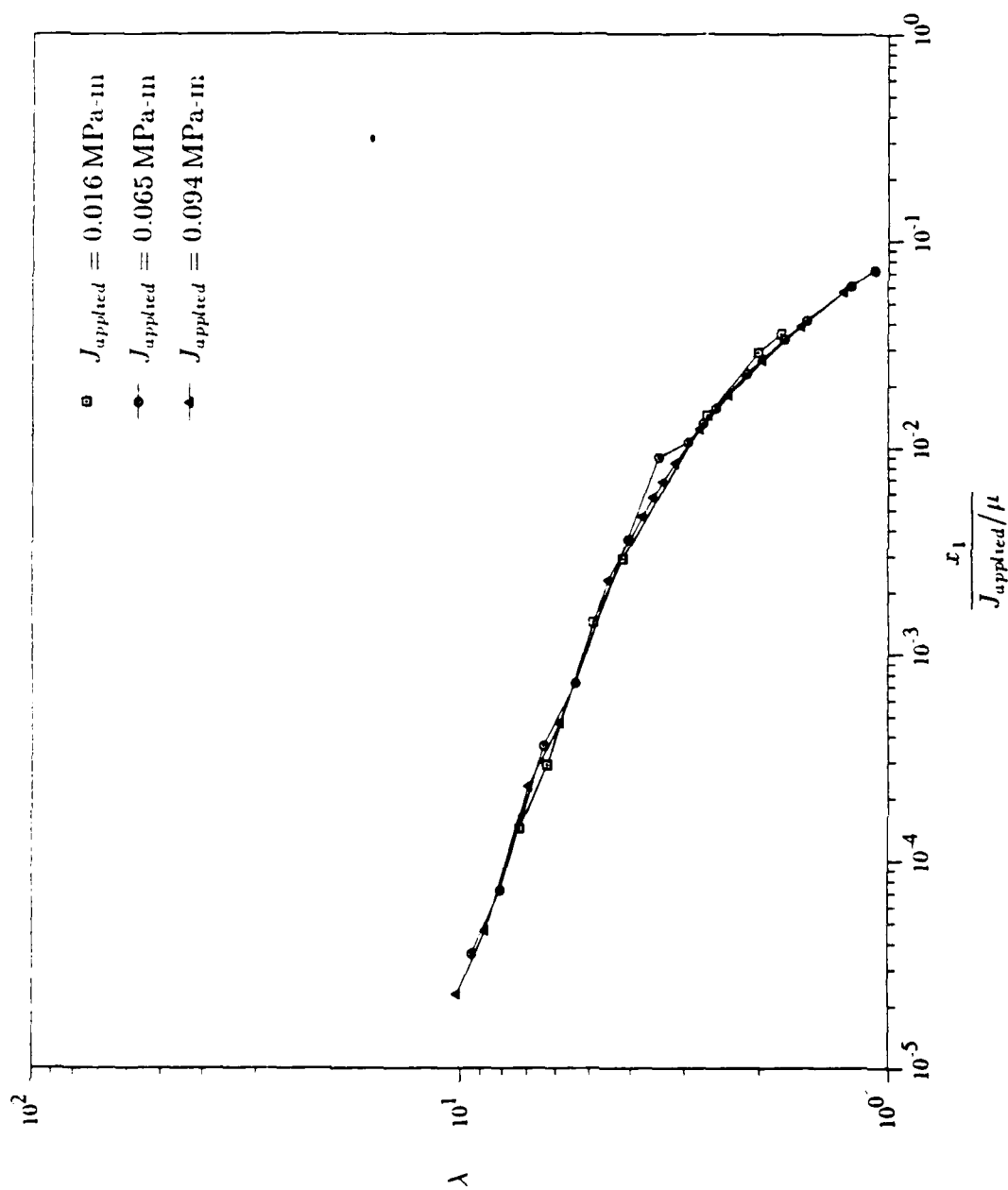
Figure 2.29: λ along the crack front for ($n = 3$).

Far from the crack tip, the stress field agrees with the applied linear elastic solution, but as the radius approaches the crack tip, a gradual change from the linear elastic solution to the nonlinear elastic solution occurs and close to the crack tip, the nonlinear solution is found. In terms of the characteristic length, the outer boundary of the nonlinear and transition region is located at a radius of $10^{-4}L$ in the undeformed configuration, well within the refined mesh.

The region of dominance of the nonlinear stresses is approximately the same for both material laws. The contours of τ_{22}/μ, Figure 2.30 and 2.31, clearly shows the transition from the linear to the nonlinear asymptotic solutions. Far from the crack tip, a square root singularity indicative of the linear elastic field is present, however, as $r \rightarrow 0$, the singularity of order r^{-1}, associated with τ_{22} in the nonlinear asymptotic field in equation (2.6), is found. Although results are presented only for $\theta = 71.25$, this behavior is representative of stresses evaluated at other angles. Results for τ_{12}, Figure 2.32 and 2.33, and τ_{11}, Figure 2.34 and 2.35, again demonstrate the presence of the linear elastic asymptotic solution far from the crack tip and the gradual change to the nonlinear elastic solution. The graphs of τ_{12} clearly show the transition to the nonlinear solution even though the order of the singularity is the same for both the linear and the nonlinear solutions and only the magnitude of the load amplitude constant differs. Close to the crack tip, τ_{12} reverts back to the linear elastic solution for $(n = 3)$, a possible consequence of the kinematic constraint which will be discussed below. The computational results for τ_{11} are the least accurate of the crack tip stresses. The Knowles and Sternberg solution [5] predicts that τ_{11} is a function only of θ, and that, at a given angle, the value of τ_{11} should approach a constant in the nonlinear asymptotic region. The finite element results show that τ_{11} begins to approach a constant for $(n = 1)$ but demonstrates some oscillatory behavior between the linear and nonlinear asymptotic fields for $(n = 3)$ as $r \rightarrow 0$. However, $\tau_{11} \ll \tau_{22}$, and, as stated previously, the numerical analysis will calculate τ_{11} with the least accuracy because it is the smallest stress component.

The effect of the constitutive model on the stress field was unexpectedly small as larger stresses around the crack tip were expected for the higher order material law $(n = 3)$. The higher order constitutive model predicts higher stresses when $\lambda > 4$, compared to the Mooney-Rivlin model $(n = 1)$, and, as r vanishes, λ should be much greater than 4. The additional kinematic constraint causes $\lambda \rightarrow \infty$ more slowly for $(n = 3)$, reducing the intensity of the stress field in the refined mesh. Consequently, the stress fields for $(n = 1)$ and $(n = 3)$ at a given radius are closer than would be predicted.
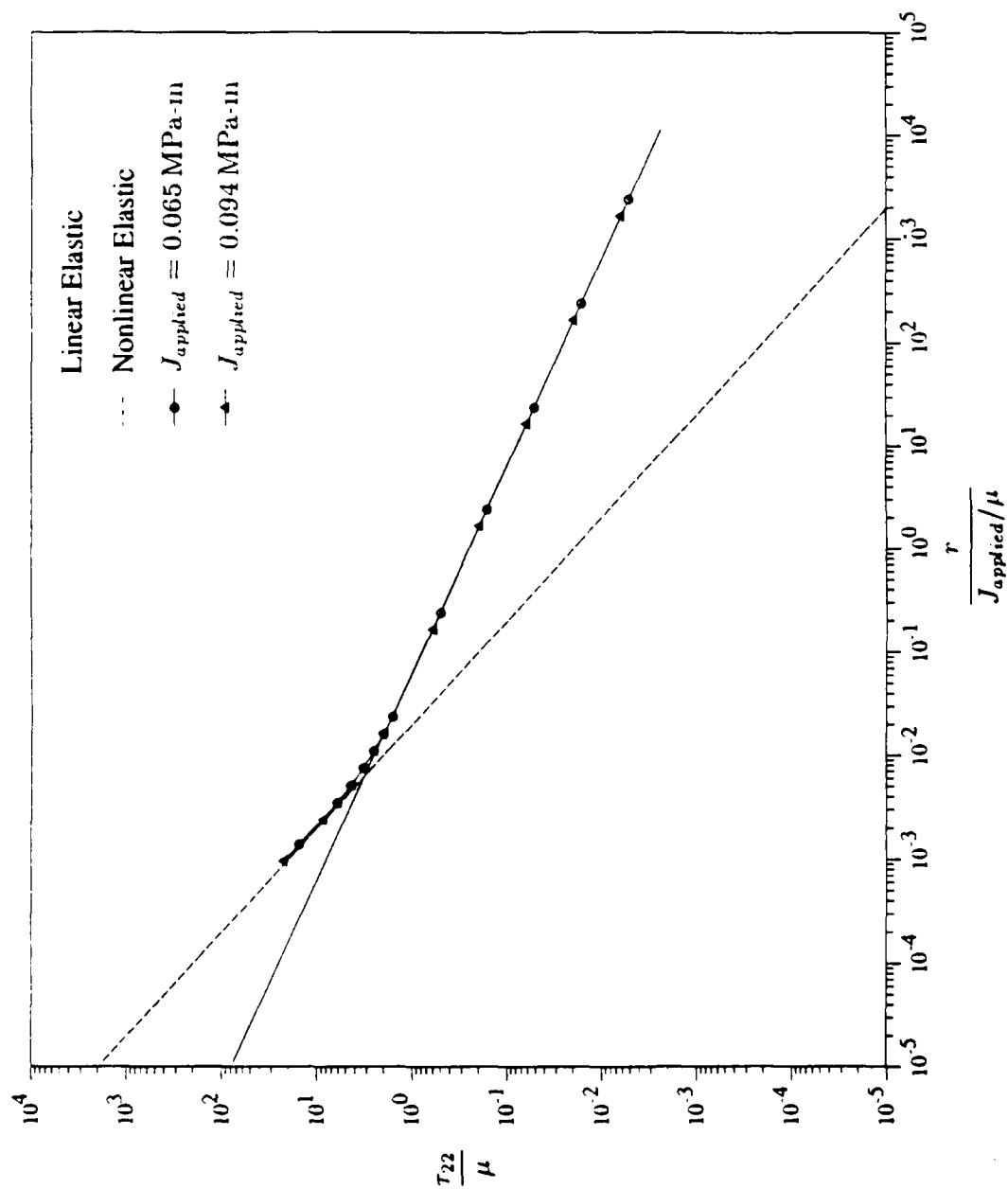
Figure 2.30. τ_{22} along $\theta = 71$ degrees for $(n = 1)$.
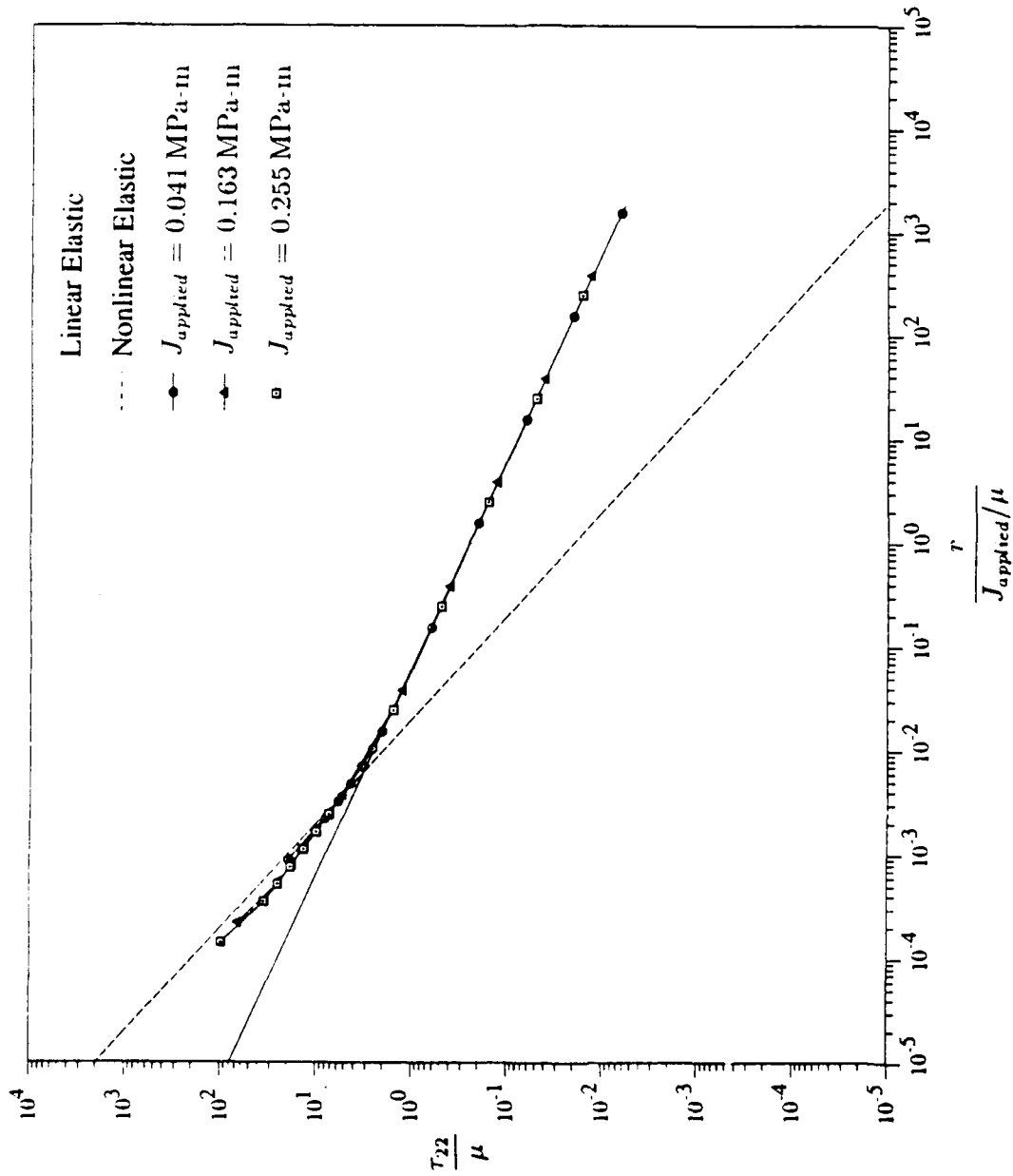
Figure 2.31: τ_{22} along $\theta - 71$ degrees for $(n - 3)$.
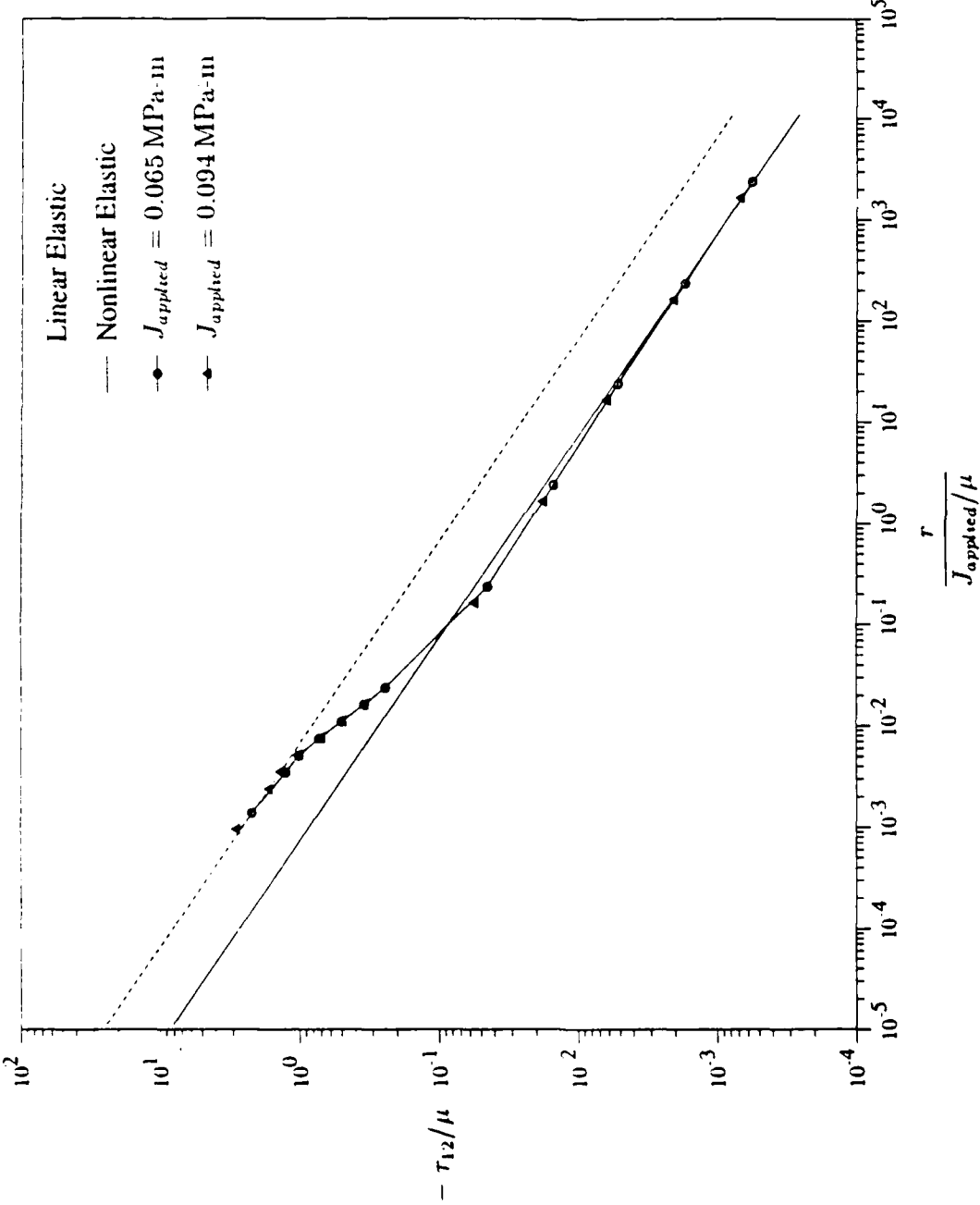
Figure 2.32: τ_{12} along $\theta = 71$ degrees for $(n = 1)$.
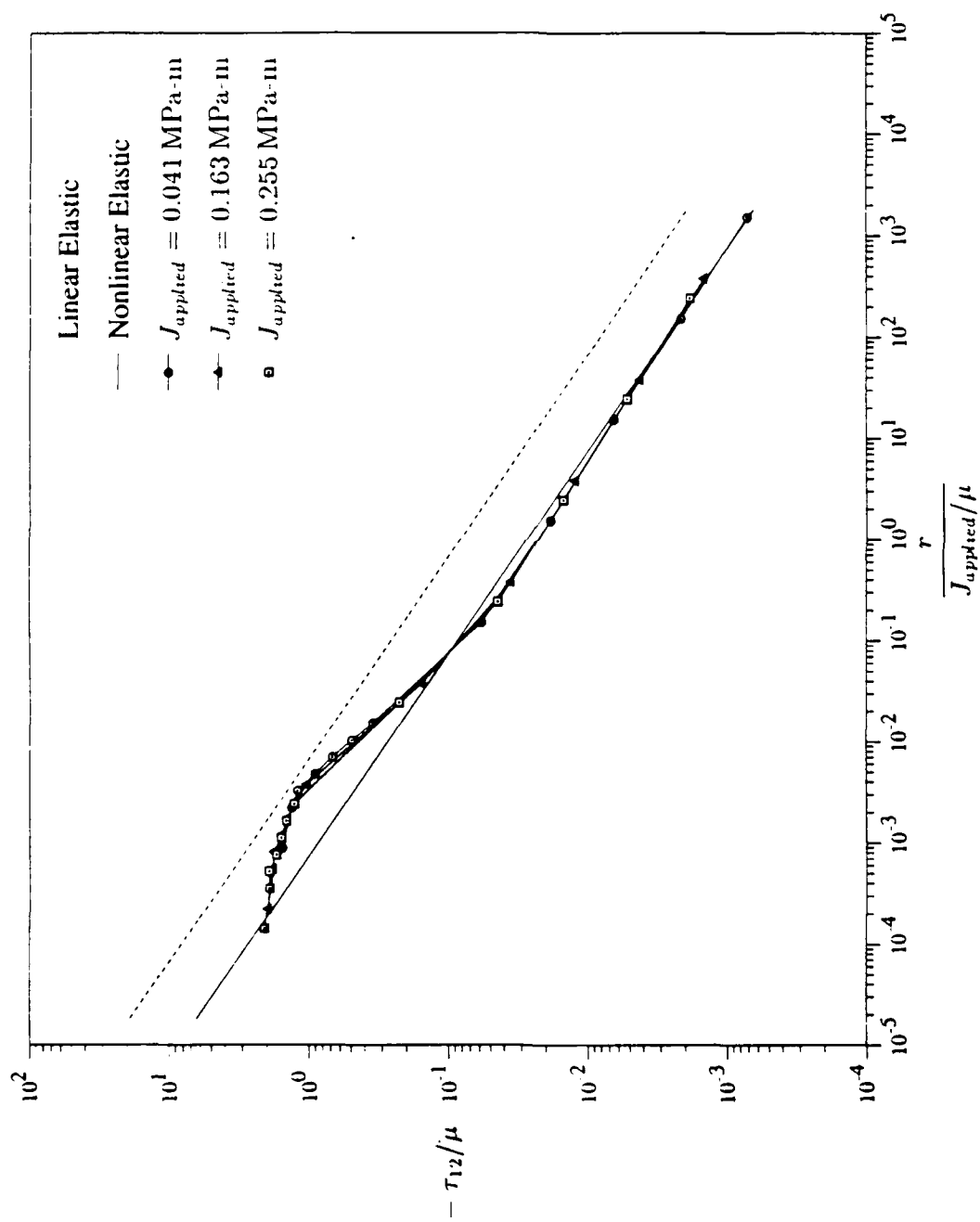
Figure 2.33: τ_{12} along $\theta = 71$ degrees for $(n = 3)$.
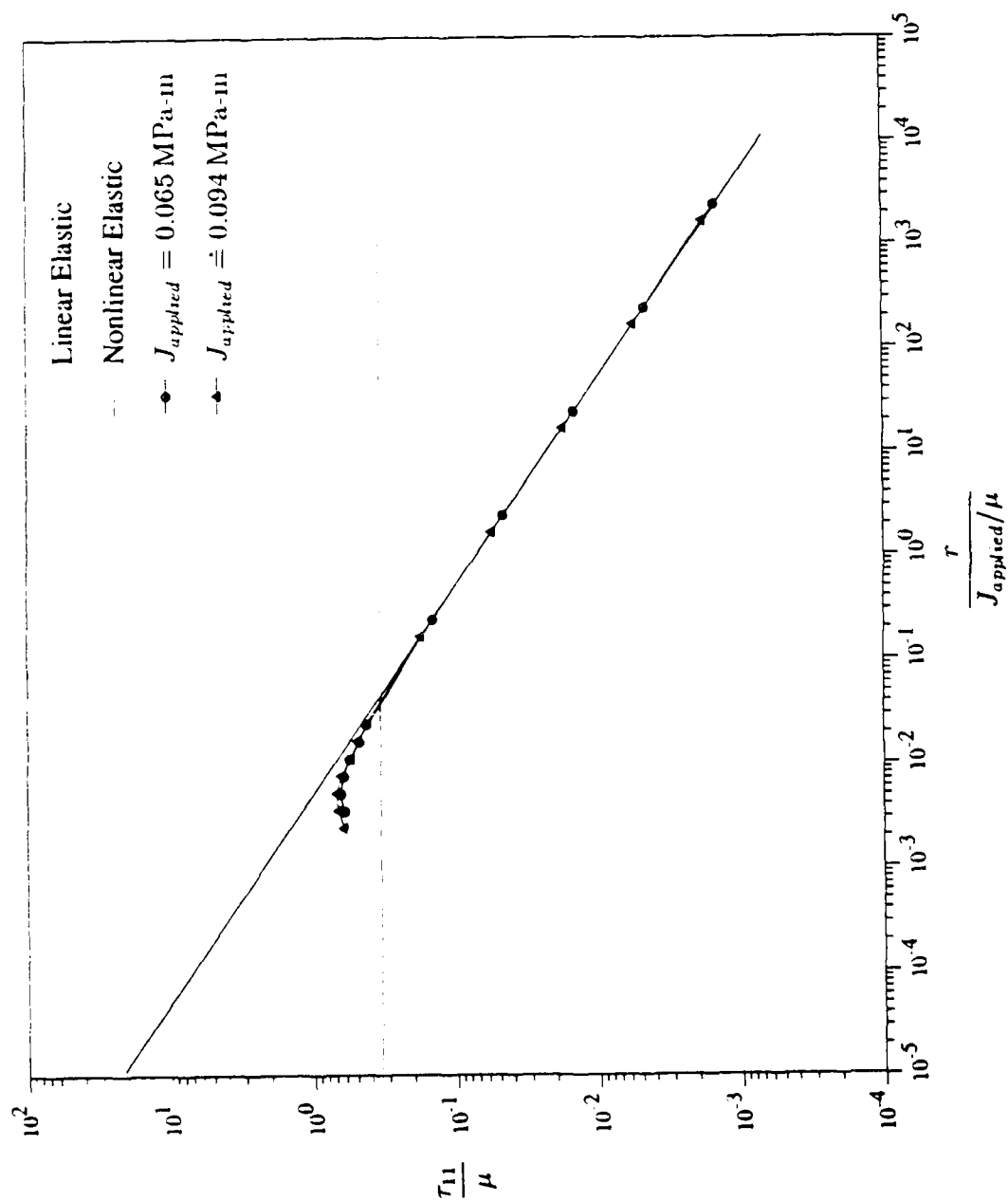
Figure 2.34: τ_{11} along $\theta - 71$ degrees for $(n-1)$.
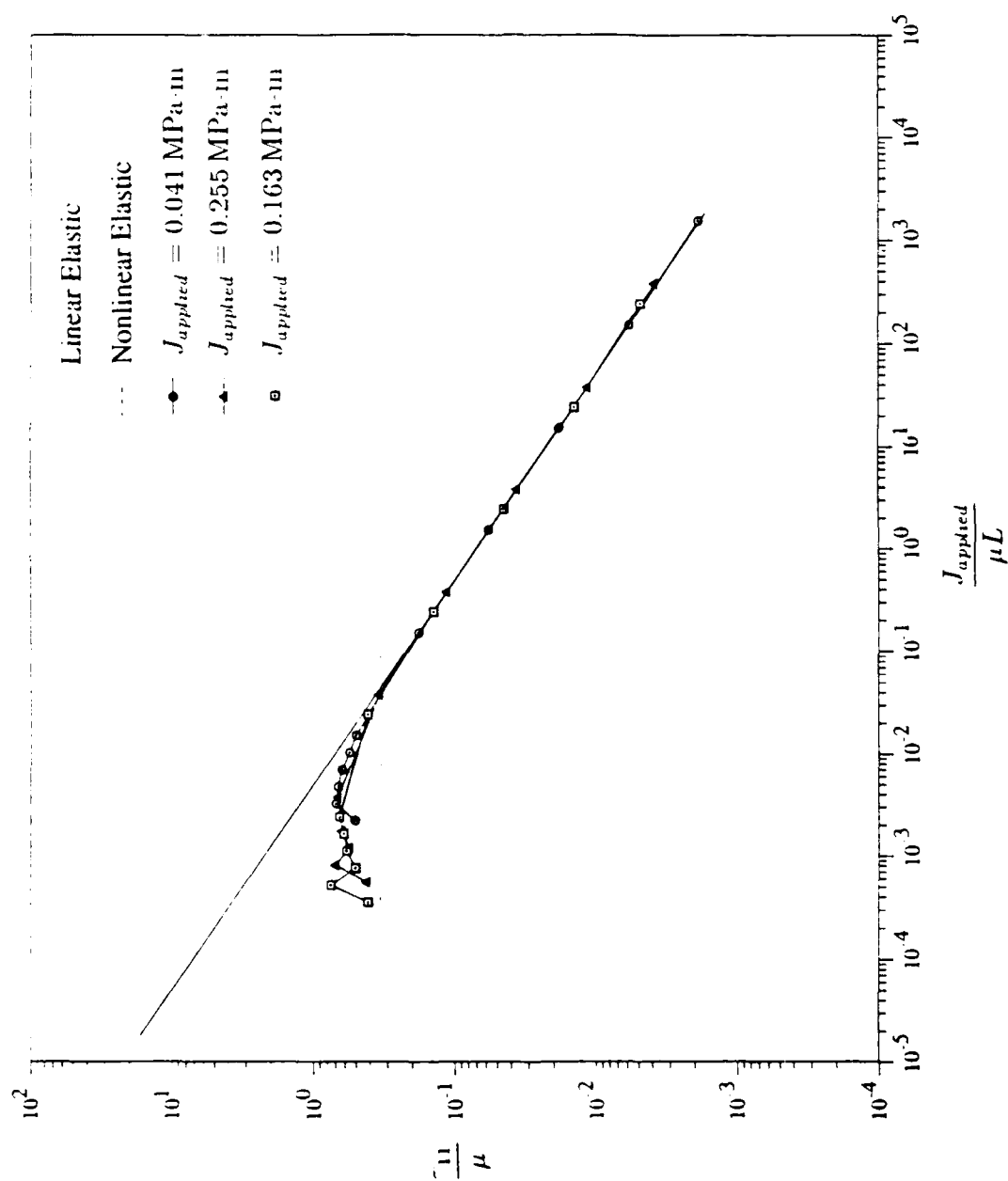
Figure 2.35: τ_{11} along $\theta = 71$ degrees for $(n = 3)$.

2.9.7 Characterization of the Nonlinear Crack Tip Region

From hyperelasticity, nonlinearity was previously defined in terms of the deformation gradient, F. If

$$|F_{ij} - \delta_{ij}| > 0.1 \ , \qquad (2.37)$$

nonlinear mechanical behavior is assumed. However, two types of nonlinearity can be found as deformations can be decomposed into a stretch and a rotation.

$$F = RU \qquad (2.38)$$

The right stretching tensor U is positive definite and symmetric and its principal values are denoted by the stretch ratios, λ_i, defining the amount of stretc' 'g in three mutually perpendicular directions. The tensor R is proper orthogonal and characterizes the rotation due to an angle, ϕ. Thus, the deformation gradient can be defined in terms of a rigid body rotation, given by the tensor, R, followed by a stretching denoted by U. Large values of λ_i represent the nonlinear material component of a deformation field while the kinematic component is given by the rotation angle, ϕ. Therefore, material and/or kinematic nonlinearities can be present. The sources of the nonlinearities associated with this small scale nonlinearity solution were examined from contours of λ_1 and ϕ, computed at the element integration points, made on the deformed configuration, (y_1, y_2) or (r_d, θ_d), normalized by the *characteristic length*, $(J_{applied}/\mu)$.

Material Nonlinearity

Nonlinear material behavior can be defined as

$$|\lambda - 1.0| > 0.1 \qquad (2.39)$$

Contours of $|\lambda - 1.0|$ are shown in Figure 2.36 and 2.37. For both constitutive models the radius of the nonlinear region is smallest in front of the crack tip at $\theta_d = 0$. This radius increases with the polar angle θ_d up to a value of $\sim 3.5(J_{applied}/\mu)$ at $\theta_d = \pi/2$. As θ_d is increased further and the crack surface is approached, the radius of the nonlinear region decreases. The size of the nonlinear region is approximately the same for both constitutive laws but the shape is different. The shape of the nonlinear region is elliptic for the third order invariant material law but is more circular for the Mooney-Rivlin law.
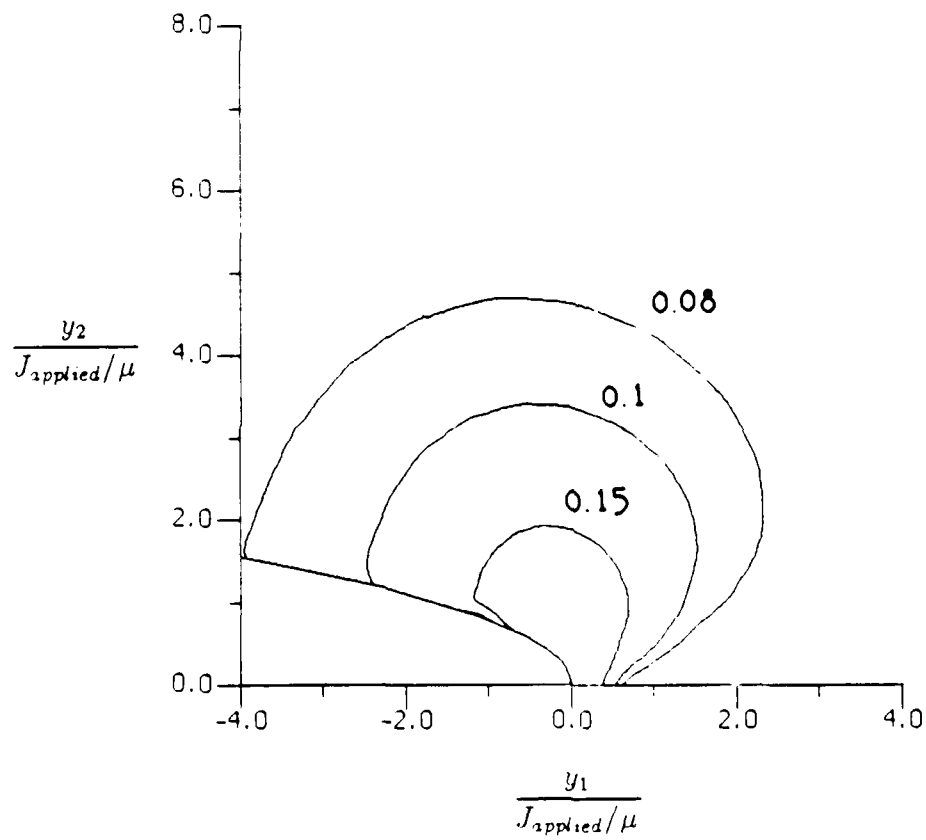
Figure 2.36: Contours of material nonlinearity in the deformed configuration for ($n = 1$).
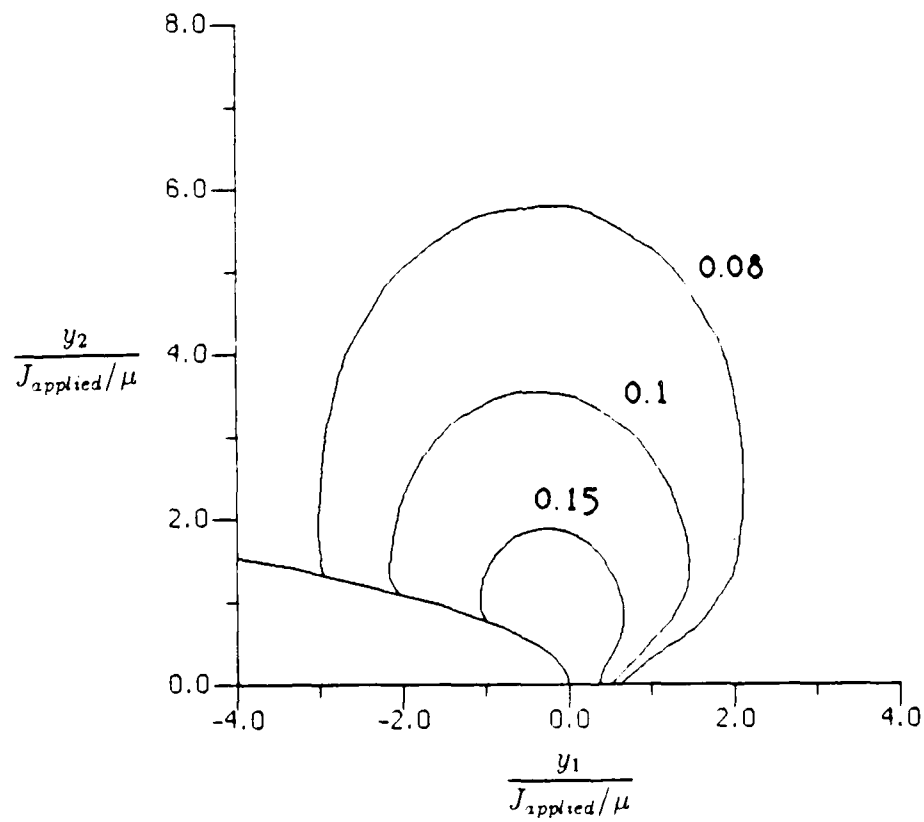
Figure 2.37: Contours of material nonlinearity in the deformed configuration for ($n = 3$).

Kinematic Nonlinearity

Rotations are considered large. i.e., representative of nonlinear elastic behavior. when

$$\varphi > 0.1 \; , \tag{2.40}$$

and contours of φ are presented in Figure 2.38 and 2.39. Here, the shape of the kinematic nonlinear region is approximately the same for both material laws but the size of the nonlinear region is much smaller for $n = 1$. This nonlinear region is located above and behind the crack tip and in front of the crack tip, $(\theta_d = 0)$, linear kinematic behavior or small rotations are found. Large rotations are present only above and behind the crack tip.

The nonlinear region around the crack tip can be characterized as follows. Large stretches and large rotations can be found in the immediate vicinity of the the crack tip and the size of this region in the normalized deformed configuration is independent of the constitutive law. It is surrounded by a second nonlinear region containing small stretches but large rotations, which is larger for $(n = 3)$ and extends to a radius of $15(J_{applied}/\mu)$, while the radius is $10(Japplied/\mu)$ when $(n = 1)$. Outside of this second nonlinear region, small rotations and small values of λ, representing linear elasticity and small geometry changes, are present.

In small scale nonlinearity, it was predicted that the assumptions of linear elasticity and small geometry changes would be violated at approximately the same radius. R^*, but the finite element results show that the region of kinematic nonlinearity extends further throughout the crack tip region when compared to that of material nonlinearity and that there exists an area of large geometry changes and linear elastic material behavior. The transition to small geometry changes and linear elastic material behavior in small scale nonlinearity is in contrast to small scale yielding, where the the linear elastic crack tip field can surround a region of small geometry changes and nonlinear material behavior closer to the crack tip and both kinematic and material nonlinearities are found as r vanishes. Thus, the transition region in small scale nonlinearity is characterized by large geometry changes and linear elastic material behavior while that in small scale yielding is defined by small geometry changes and nonlinear material behavior.

2.9.8 A Local Cavitation Criterion and the Rice-Johnson Failure Model

A theoretical criterion for cavitation [22] predicts that cavitation will occur when the triaxial tension ahead of the crack tip reaches a critical value, equation (1.6).
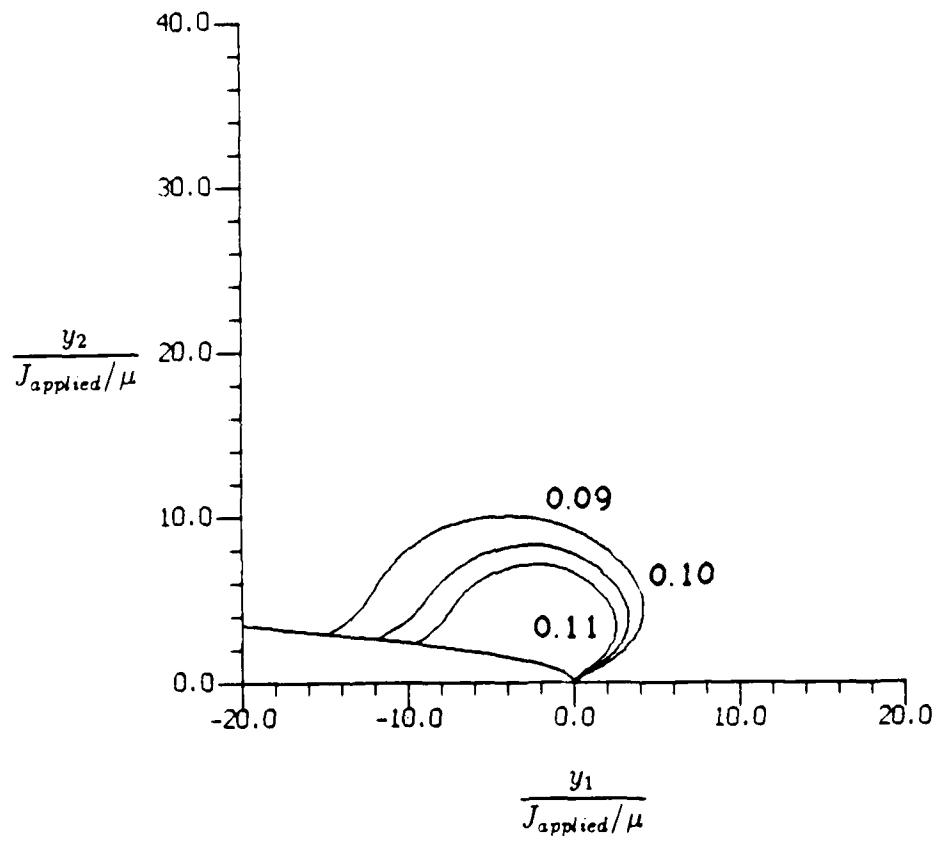
Figure 2.38: Contours of kinematic nonlinearity in the deformed configuration for $(n = 1)$.
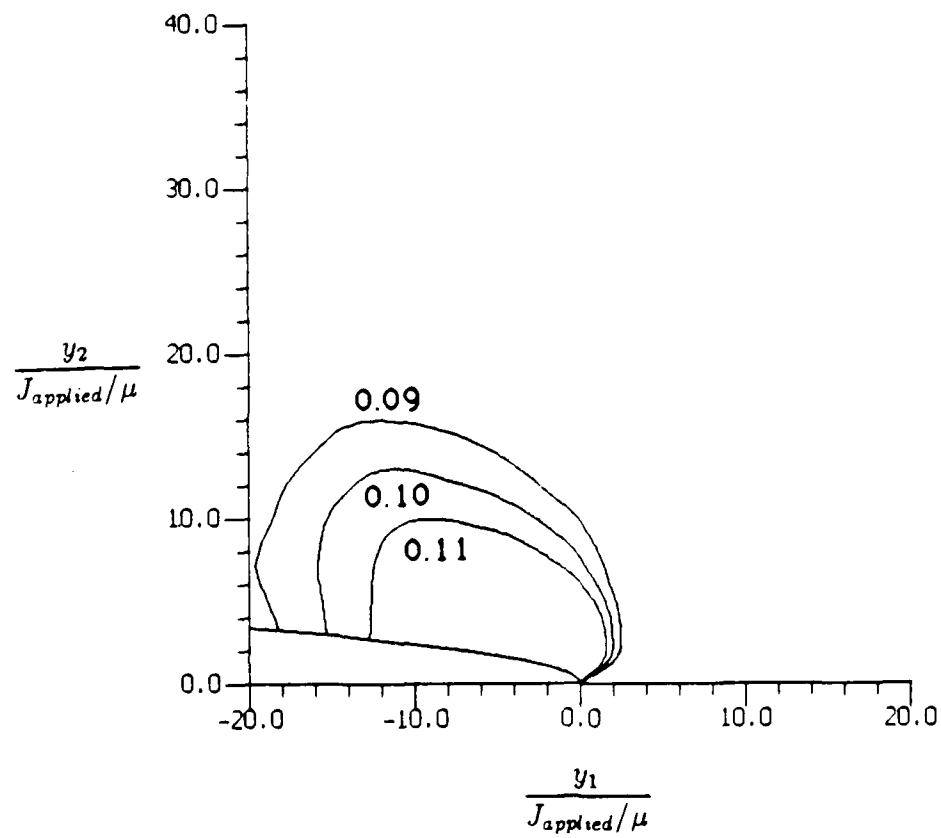
Figure 2.39: Contours of kinematic nonlinearity in the deformed configuration for $(n = 3)$.

For the Mooney-Rivlin model, this critical value, $\mathcal{P}_{crit}$, equals 2.5μ, however, when a higher order form of the Rivlin constitutive model is applied, the integral in equation (1.7) diverges. Consequently, Ball's cavitation criterion was applied only to the finite element analysis of ($n = 1$).

Cavitation was examined in front of the crack tip ($\theta = 0$) in the undeformed configuration, Figure 2.40. Here, far from the crack tip, the triaxial tension approximates that of the linear elastic solution while, close to the crack tip, it approaches that of the nonlinear elastic solution. $\mathcal{P}_{crit}$ is attained at $x_{1\,crit}/(J_{applied}/\mu) \sim 10^{-2}$, in the transition region between the linear elastic and the nonlinear elastic asymptotic solution. Contours of the triaxial tension in the deformed configuration are presented in Figure 2.41 for ($n = 1$) where $\mathcal{P}_{crit}$ in front of the crack tip is reached at $y_{1\,crit}/(J_{applied}/\mu) \sim 0.025$. Although Ball's cavitation criteria could not be directly applied when ($n = 3$), contours of the triaxial tension in the deformed configuration, Figure 2.42, are similar to those of ($n = 1$) and $\mathcal{P}_{crit}$ is found at approximately the same value of $y_1/(Japplied/\mu)$, indicating that the cavitation predictions based in the Mooney-Rivlin material law may have some limited validity when higher order forms of the Rivlin law are considered.

The failure model of Rice and Johnson [30] relates a localized fracture criteria to a critical microstructural distance, D, in front of the crack tip based on the mean particle spacing of the inclusions causing failure. In this analysis, the fracture criterion considered was the cavitation model discussed above while the inclusions causing localized cavitation of pre-existing microvoids were carbon black particles in a filled rubber. The assumption that carbon black influences cavitation is based on experimental evidence that microscopic tears in filled elastomers are associated with carbon black particles [42].

For a spherical particle, the mean particle spacing is

$$D = (\text{particle radius}) \times (\text{volume fraction})^{-1/3} , \qquad (2.41)$$

where the radius of aggregates of N330 carbon black particles is $0.25\mu m$ [42] and the volume fraction of carbon black in filled rubbers varies from 0.3 to 0.5. Here, D is approximately $0.2\mu m$. The failure model [30] predicts that

$$\frac{x_{1crit}}{J_{applied}/\mu} = N\frac{D}{J_{applied}/\mu} , \qquad (2.42)$$

given that N represents the number of mean particle spacings and $J_{applied}$ is the value of the J-integral at cavitation. The value of $x_{1crit}/(J_{applied}/\mu)$ is provided by the computational analysis as 0.01 and experimental data [16] measured:

$$J = 0.013\,\text{MPa-m} , \qquad (2.43)$$

where J is the applied value required for crack propagation in a natural rubber filled with N330 carbon black and $\mu \sim 2\text{MPa}$. When this data is substituted into equation (2.42), the value of N becomes 300 mean particle spacings in front of the crack tip. The value of N is high because J in equation (2.43) is that value required for crack propagation, and subcritical crack growth, $\sim 0.01\text{mm}$ [13], has already occurred. In this analysis, a critical cavitation event is predicted at a distance equal to the product of N and D, 0.006 mm, and approximates the amount of subcritical crack growth prior to crack propagation. However, the validity of Ball's criterion in the presence of material delamination, molecular alignment, and shear failure in front of the crack tip requires further examination. This local cavitation criterion may, in a practical sense, correspond to a subsequent initiation event, rather than the first onset of cavitation.

2.10 Discussion

The finite element results confirm the presence of the nonlinear elastic asymptotic field [5] at the crack tip although its region of dominance under small scale nonlinearity is small and show that a local cavitation criterion [22] can be applied to determine the site of cavitation in front of the crack tip.

The assumptions of small scale nonlinearity were met throughout the finite element analysis as determined by the accuracy of the J-integral with respect to the appropriate geometric scale. The relationship between the value of the J-integral and the applied stress intensity factor, $K_{I\,applied}$, equation (2.8), establishes the magnitude of R^*/L which represents a limiting condition for small scale nonlinearity. At sufficiently small loads, such that the maximum engineering strain is less than 0.1, the linear elastic crack tip field is accurately obtained throughout the mesh. However, as the applied load is further increased, the nonlinear elastic asymptotic field develops at the crack tip with increasing size and magnitude. It is located in the refined mesh region within the first decade of elements closest to the crack tip for ($n = 1$) and extends into the second decade for ($n = 3$). The range of dominance of the nonlinear elastic stress field increases linearly with the applied load. The J-integral was path independent throughout the refined mesh region and is most accurate at small loads. As the load increases, the error in the numerically computed J-integral approaches five percent, the maximum error allowed in this investigation under small scale nonlinearity

The value of R^* is small, $\sim 10^{-4}L$, and, at $r > R^*$, the plane strain linear elastic asymptotic solution is found. At $r < R^*$, the stress components agree with the nonlinear asymptotic solution, although the magnitude of the load parameters associated with nondominant terms could not be determined with accuracy. The
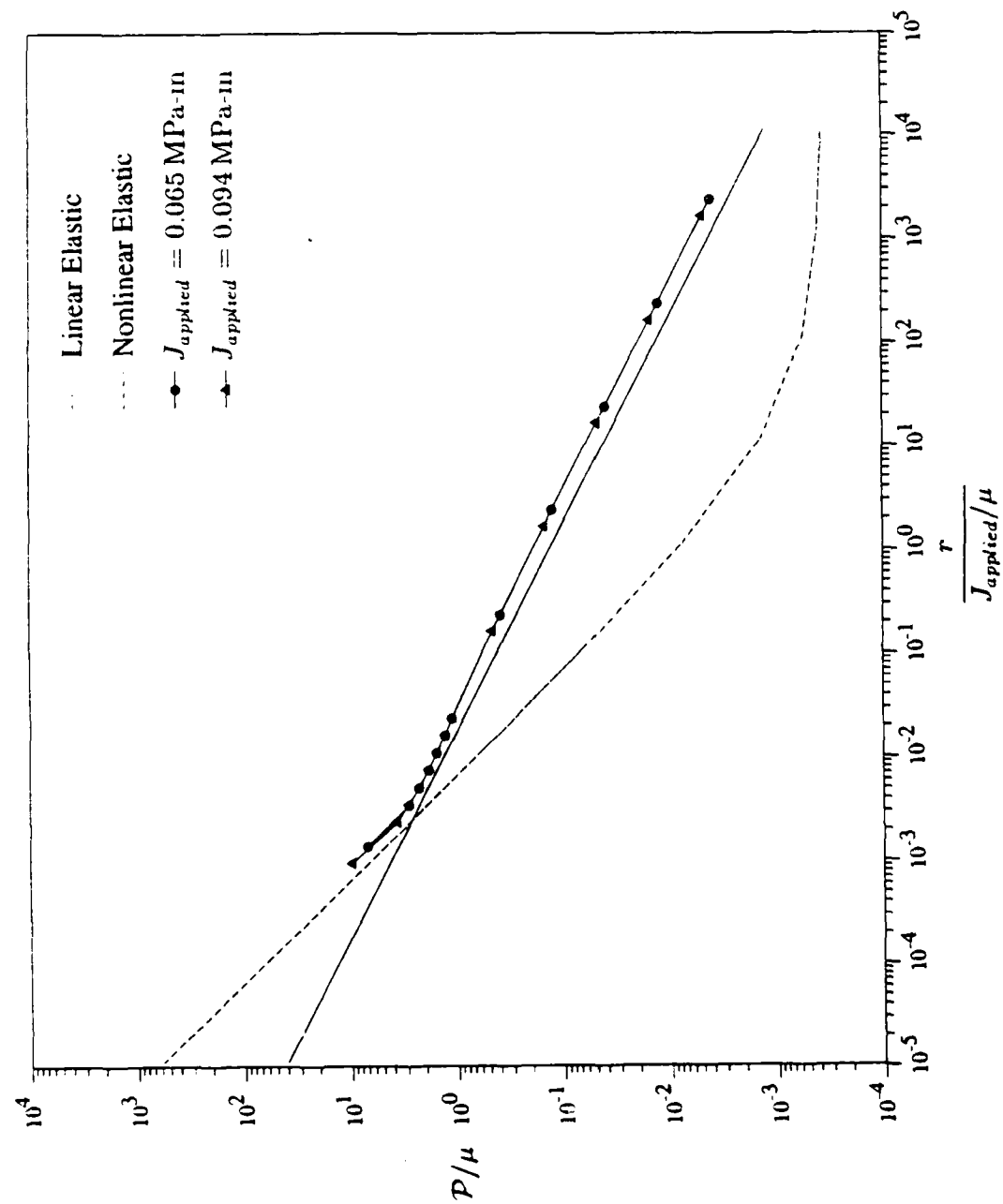
Figure 2.40: Triaxial tension along the undeformed crack front for ($n = 1$).
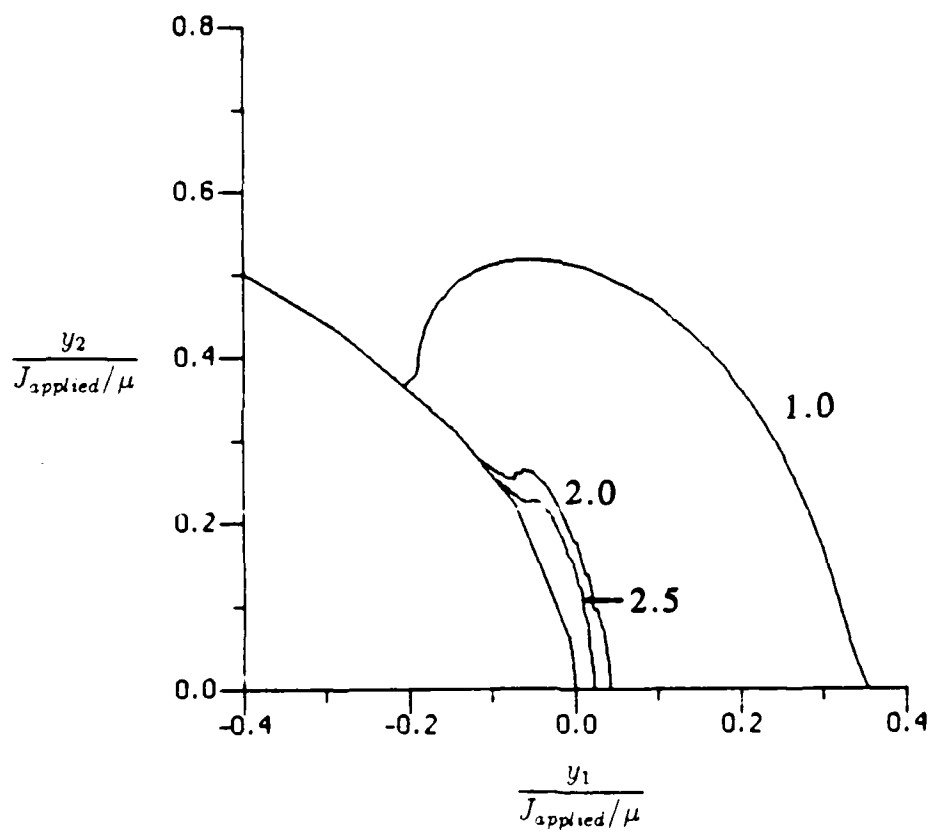
Figure 2.41: Contours of triaxial tension in the deformed configuration for $(n = 1)$.
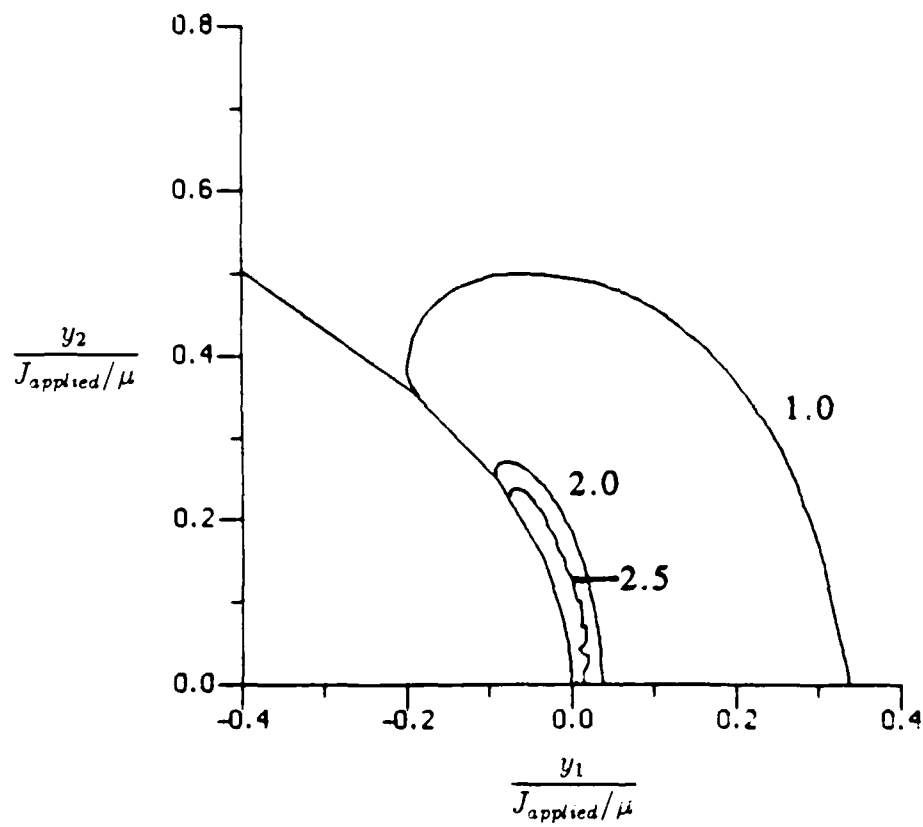
Figure 2.42: Contours of triaxial tension in the deformed configuration for ($n = 3$).

stress and deformation fields did not show any oscillatory behavior, except τ_{11} for ($n = 3$), but were smooth throughout the finite element mesh at all loads. Examination of the deformed crack tip surface in normalized coordinates for both constitutive laws showed that the radius of curvature at the crack tip, ρ, agreed with that from the linear elastic solution, $\sim 0.32(J_{applied}/\mu)$, and that the crack tip opening displacement was $1.3(J_{applied}/\mu)$, indicating the amount of blunting present.

The highly localized confinement of the nonlinear region and difficulties found with the determination of load amplitude constants, associated with nondominant terms in the nonlinear asymptotic field, were also reported by Ravichandran and Knauss [43] in their finite element analysis of a plane stress Mode I crack in a Neo-Hookean material. The plane stress nonlinear asymptotic solution [44] contains stress components with the same order of the singularity as the plane strain solution, $\tau_{22}, o(r^{-1})$, $\tau_{12}, o(r^{-1/2})$, and $\tau_{11}, o(1)$, but the angular functions differ. When compared to the plane stress solution, the region of dominance in plane strain is also small, $\sim 10^{-3}L$ when the far field loading is equivalent to $\lambda = 1.15$. In this investigation, λ far from the crack tip is approximately 1.01. The magnitude of R^* increases linearly with the applied load under both plane strain and plane stress conditions.

The effect of the constitutive model on the nonlinear crack tip field is small as the stress and deformation fields for both ($n = 1$) and ($n = 3$) are approximately the same. These differences are a consequence of the relative magnitude of the material constants and the additional finite element kinematic constraints applied to the ($n = 3$) analysis. The material constants, C_{01} and C_{10}, associated with linear terms in the Rivlin material law, are at least one order of magnitude greater than constants associated with the remaining terms, and as a result, the uniaxial stress strain curve approximates that of the linear form of the Rivlin law when $\lambda < 4$, as found in Figure 2.10. In addition, the kinematic constraint removes the square root singularity at the crack tip and allows λ to approach infinity more slowly as $r \rightarrow 0$, compared to the computational results for ($n = 1$). At a given distance in front of the crack tip, λ for ($n = 3$) $< \lambda(n = 1)$. Consequently, the magnitude of the stress fields located here are closer to each other in magnitude than would ordinarily be predicted. Because the square root singularity at the crack tip has been replaced by a weaker one, the nondominant stresses may not accurately reflect the nonlinear asymptotic solution, as demonstrated by the oscillatory behavior at τ_{11} and the return of τ_{12} to the linear elastic solution at small r.

A local cavitation criterion [22] determines that cavitation will occur when the triaxial tension is 2.5μ for a Mooney-Rivlin material. When this criterion is applied to the mechanical crack tip field, cavitation in front of the crack tip will take place in the transition region between the nonlinear and the linear asymptotic

fields for both constitutive models. Cavitation takes place ahead of the crack tip, at a critical length scale which is related to the microstructure of the material. In this investigation, the failure model [30] assumes that a critical cavitation event occurs when the value of the J-integral is that required for crack propagation and that carbon black aggregates in filled rubbers, rather than other impurities, has the strongest influence on the cavitation process. When a length scale defined by the mean particle spacing of carbon black aggregates is used, it is predicted that cavitation will occur at 0.006 mm ahead of the crack tip, which is consistent with experimentally reported values of subcritical crack growth. In this context, the local cavitation criteria has been applied, not to the first onset of cavitation but to a subsequent critical event.

Chapter 3

Experimental Investigation

3.1 Experimental Objectives

An experimental study of fracture of an elastomer is presented in this chapter. Because all ASTM standard and conventional test specimens for elastomers measure tear strength and tearing energy under plane stress conditions, a new test specimen was needed to investigate fracture in thick elastomer structures. To perform this experiment, a test specimen and testing apparatus were designed and manufactured to complete the following experimental objectives:

1. physically observe the Mode I fracture process in an elastomer containing a sharp crack under near plane strain conditions at large deformations,

2. determine the reproducibility of the material behavior,

3. determine the values of failure criteria such as the J-integral, fracture strength and crack mouth opening displacement (CMOD),

4. observe specimen geometry changes, and

5. determine the effect of crack length on the experimental results.

3.2 Specimen and Grip Design

There is no standard tear test specimen for *thick* rubber materials. Consequently, a test specimen and grips were designed to meet the experimental objectives listed

107

above. The test specimen had to be of sufficient thickness to maintain a plane strain condition along the crack front, i.e., the strains in the plane of the crack are zero at the crack front. Although an ideal plane strain condition cannot be achieved experimentally, limits on specimen thickness in metals can be determined under which the experimental measurement of J_{1c} is independent of thickness. It has been established, in metals under small scale yielding conditions, that the thickness should be fifteen times greater than the radius of the crack tip zone size. However, for elastomer materials, both the tolerance on the specimen thickness and the magnitude of the radius of the nonlinear crack tip zone has yet to be determined. A crack intersecting a lateral free surface is not in perfect plane strain because a traction free boundary condition is found there, as in Figure 3.1. With increasing distance from the free surface though, the boundary condition changes from plane stress to plane strain.

It is assumed here that the fracture resistance in elastomers, as measured by the J-integral, differs in plane strain compared to plane stress, so a test specimen containing significant plane stress regions must be avoided. In addition, to measure the value of the J-integral from a single test specimen, the nonlinear crack tip zone should be confined to the uncracked ligament region ahead of the crack and the test specimen geometry should have a single characteristic length scale referenced to the crack length, L. A short thick cylindrical test specimen, containing a deep crack , should satisfy these design criteria. An axisymmetric geometry provided another advantage in that a finite element analysis of a cylindrical test specimen is computationally easier to perform than a full three-dimensional finite element analysis of a specimen with a different geometry, such as a thick rectangular plate.

In the investigation of the specimen geometry restrictions, the height of the cylinder was also given important consideration. A crack would be introduced into the specimen at mid-height. The distance between the crack and the grips must be sufficiently large to validate the test accuracy, as Stacer [45,46] had shown that the distance between the grips and the crack for a constrained trouser test specimen influences the type of tearing (knotty versus smooth) observed. When the distance between the grips and the crack in a constrained trouser test specimen was large, knotty tear behavior was observed; when this distance was small, the knotty tear behavior was eliminated and smooth tearing was found. Higher values of the tearing energy are reported with knotty tearing, suggesting that small distances between the grips and the crack affects the failure process. Consequently, a final design criterion was to stabilize crack growth by using a short gage length..

The final specimen design was a short cylindrical dumbbell, 5.08 cm in height, H_{outer}, as shown in Figure 3.2. At both ends the diameter, D_{outer}, is 5.08 cm. In the middle of the specimen, there is a region where both the diameter, D_{inner}, and length, H_{inner}, equal 2.5 centimeters. The specimen is symmetric about its mid-

height, and a circumferential crack will be introduced along this line of symmetry. The diametral change from 5.0 centimeters to 2.5 centimeters was made smoothly by imposing a radius of curvature of 0.64 cm, thus eliminating sharp edges which could cause premature failure in areas other than the crack region. This specimen could be molded or machined from a molded cylinder.

The design specifications for the experimental grips are now presented. The grips must keep the specimen correctly aligned in the testing machine and must not introduce regions of high stress concentration along the contact surface between the specimen and the grips. Surface cracks or damage which would cause premature failure to the specimen should be avo   J. The grips must not obstruct observation of the fracture process and should not interfere with measurement of the CMOD and the diameter of the specimen during the test. The strength of the grips must be sufficient to prevent permanent deformation and, consequently, possible failure during a test. Their design should minimize the contribution of friction to the measured load. Finally, the grips must be reusable and easy to manufacture.

Two grips were needed, one for each end of the test specimen. As shown in Figure 3.3, each grip was composed of three pieces. The circular base plate had a diameter of 7.62 cm and is 0.64 cm thick. The end of the test specimen rested against this base. To hold the specimen in place, two identical semi-circular plates, of height 1.9 cm, surrounded each end of the specimen dumbbell shape. When joined together, these two plates formed a circle, of diameter 7.62 cm, containing a central circular hole with a 2.54 cm diameter. The inner core of the test specimen fits in this circular hole and the semi-circular pieces encompass the outer end of the dumbbell. A radius of curvature of 0.64 cm was introduced where the diameter changes from 2.5 centimeters to 5.0 centimeters on the inner side of each semi-circular plate. This follows the smooth transition between diametral changes in the undeformed test specimen geometry and avoids sharp edges which could lead to premature failure in the dumbbell test specimen, away from the crack region. Six fasteners connected the semi-circular plates to the base plate. The bolt heads protruded from the base plate but did not interfere with optical measurements taken during the experiment. Because the outer dumbbell portion of the specimen was encased in the grips, adhesives were unnecessary. Finally, the grip was attached to the clevis on the testing machine with a pin joint found on the base plate. The grips were made of medium strength steel to assure a stiff test apparatus.

To machine the test specimens, an additional set of grips were needed to hold the molded cylinder in the lathe. These aluminum grips are shown in Figure 3.4. Each grip held one end of the cylinder in a shallow cup of depth 0.32 cm. The grip with the 10.2 cm shaft fit into the chuck. The second grip, a solid cylinder with

the shallow cup cut out at one end and a bore at the opposite end for attachment to the lathe. was 6.34 cm in diameter and 3.8 cm long. These grips kept the molded cylinder aligned in the lathe while the specimen was machined. Specimen preparation will be discussed in a later section.

3.3 Material Description

Test specimens were made from an experimental elastomer material, 15TP-14AX. Designed for use in U.S. Army tank track pads, the material is a cured triblend of natural rubber. styrene butadiene (SBR), and a polymerized polybutadiene (Taktene 220). Its complete composition is given in Table 3.1.

Natural Rubber, SMR-20	35.0
SBR Polymer, Philoprene 1609	35.0
Polybutadiene, Taktene 220	30.0
Zinc Oxide	3.0
Stearic Acid	1.5
ISAF, N220 Black	65.0
Sundex 790	4.0
Sunolite 100	1.5
Agerite Resin D	2.0
Santoflex 13	3.0
Sulfur	1.3
Santocure IPS	3.2
Santogard PVI	0.2

Table 3.1: Formulation for 15TP-14AX (in parts per hundred by weight).

The elastomer, filled with N220 carbon black, was cured for 40 minutes at 154° C. This material was obtained from the U.S. Army Belvoir Research. Development and Engineering Center in the form of molded circular cylinders which were 5.08 cm in both diameter and height. Tensile test sheets, used to make dumbbell tensile specimens for conducting stress strain tests. were also received.
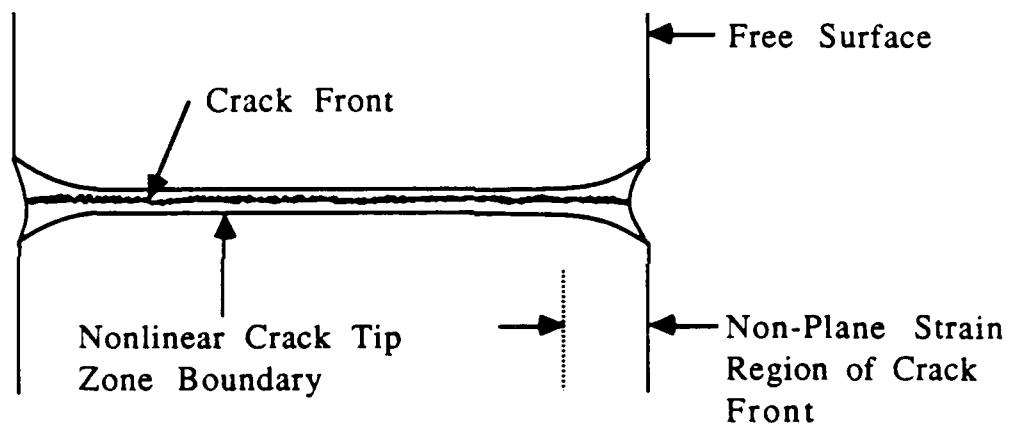
Figure 3.1: Plane strain and plane stress regions along crack front.
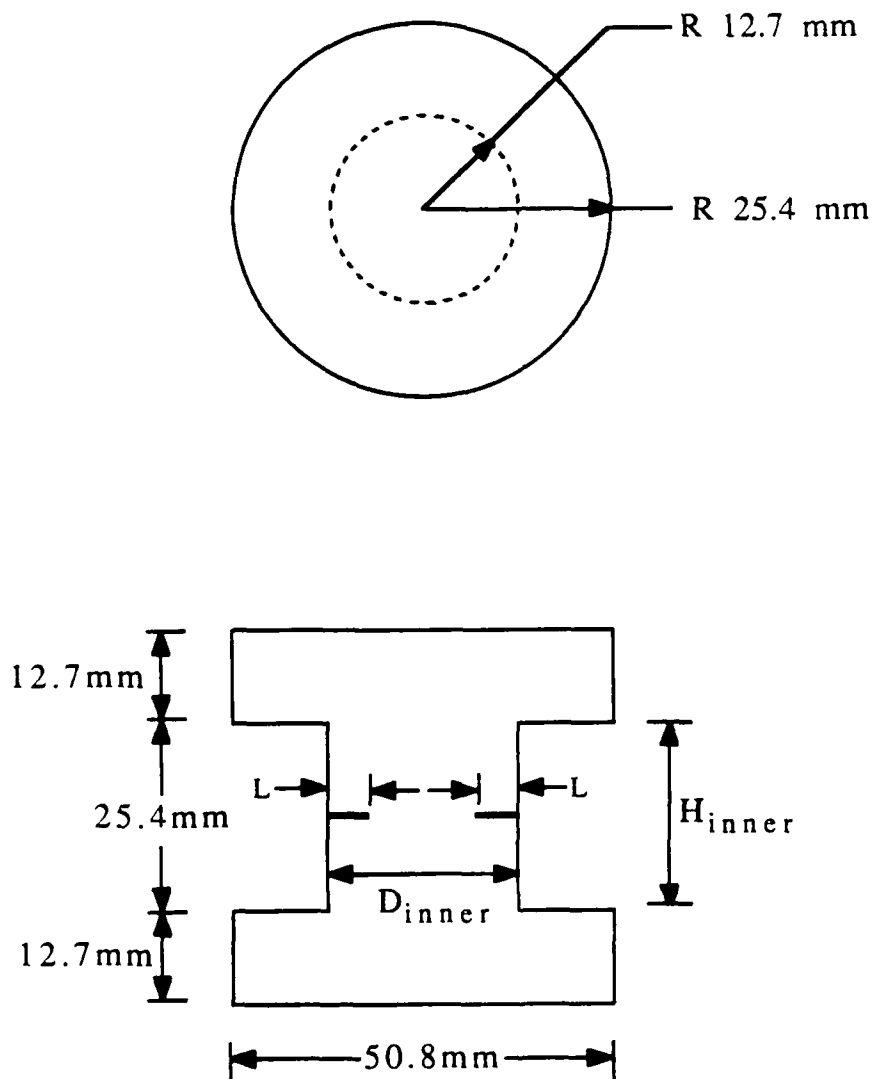
Figure 3.2: Test specimen geometry.
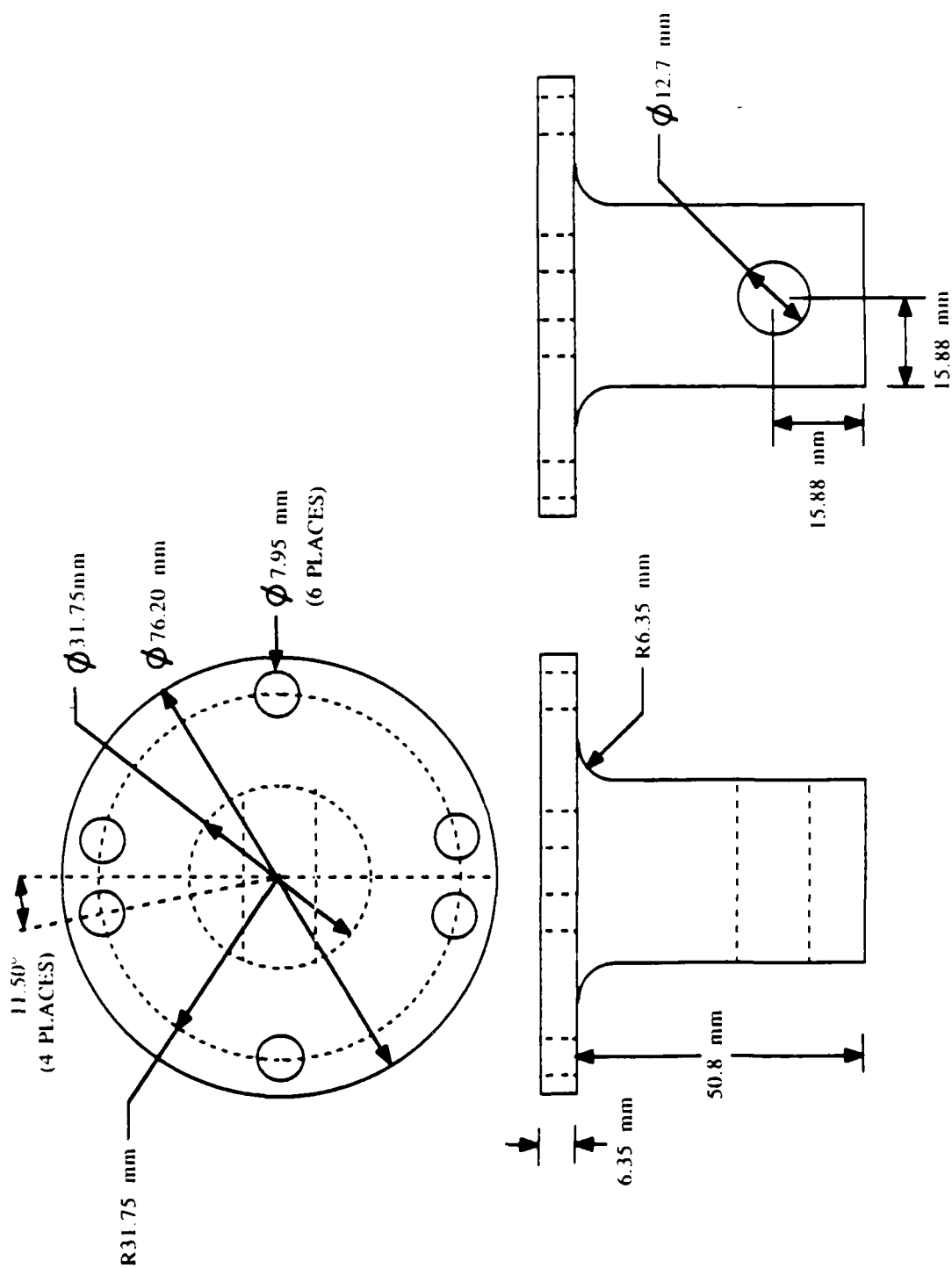
(a) Base plate.

Figure 3.3: Mechanical drawings for grips used in experiment.

11.50°
(2 PLACES)

R12.7 mm

R25.4 mm

R38.10 mm

R31.75 mm

A

A

6.35mm - 20 THD. x 12.7mm Deep
(3 PLACES)

12.70 mm

12.70 mm

19.05 mm

(b) Semi-circular plate.

Figure 3.3: Mechanical drawings for grips used in experiment.

R31.50 mm

R25.15 mm

R12.70 mm

3.18 mm

15.88 mm

R3.18 mm

101.60 mm
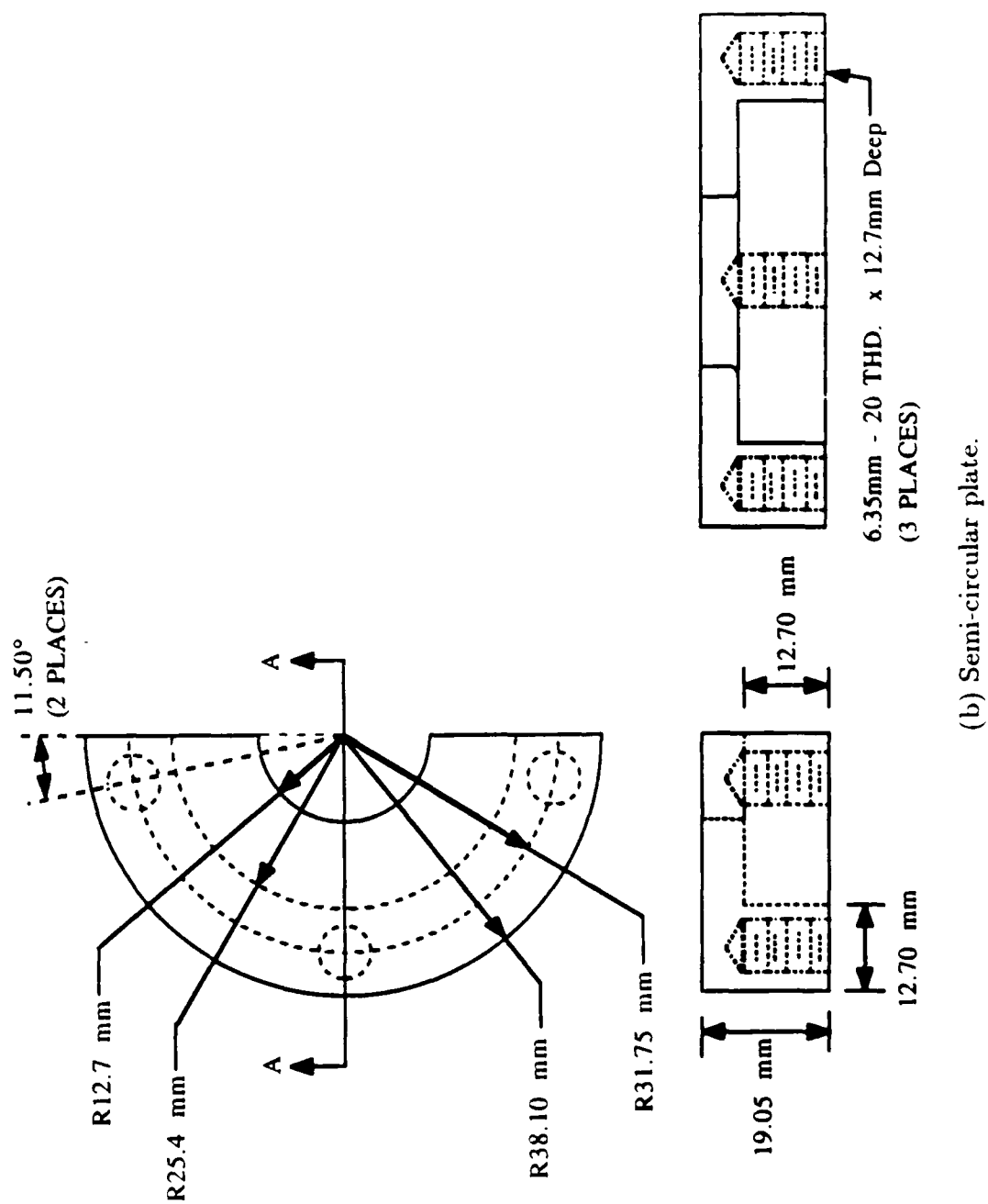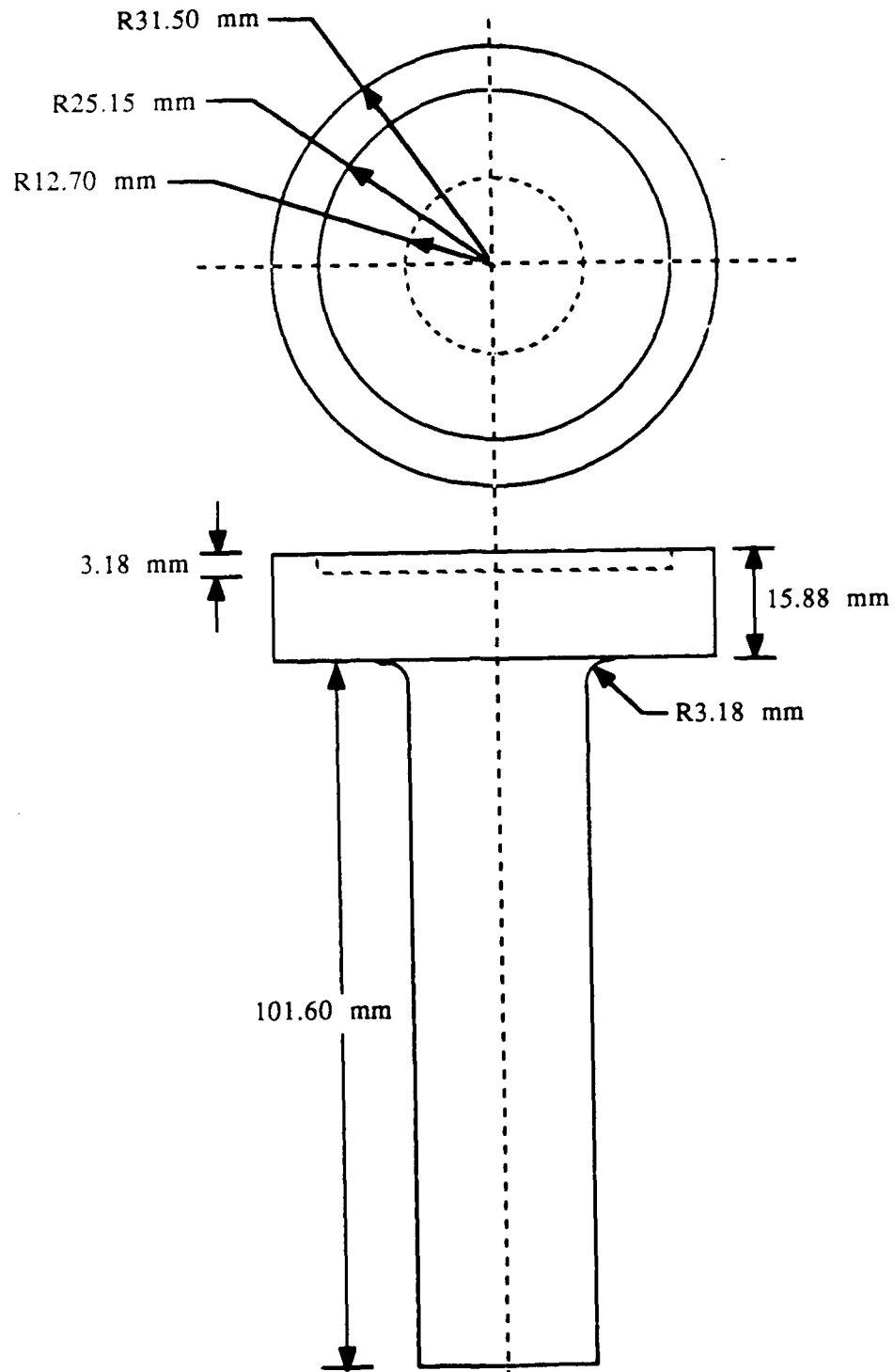
(a) Shaft piece.

Figure 3.4: Mechanical drawings for grips used in machining.

R31.50 mm

R25.15 mm

R3.66 mm

3.18 mm

38.10. mm

Counterbore to 6.35mm deep
60 degree angle included
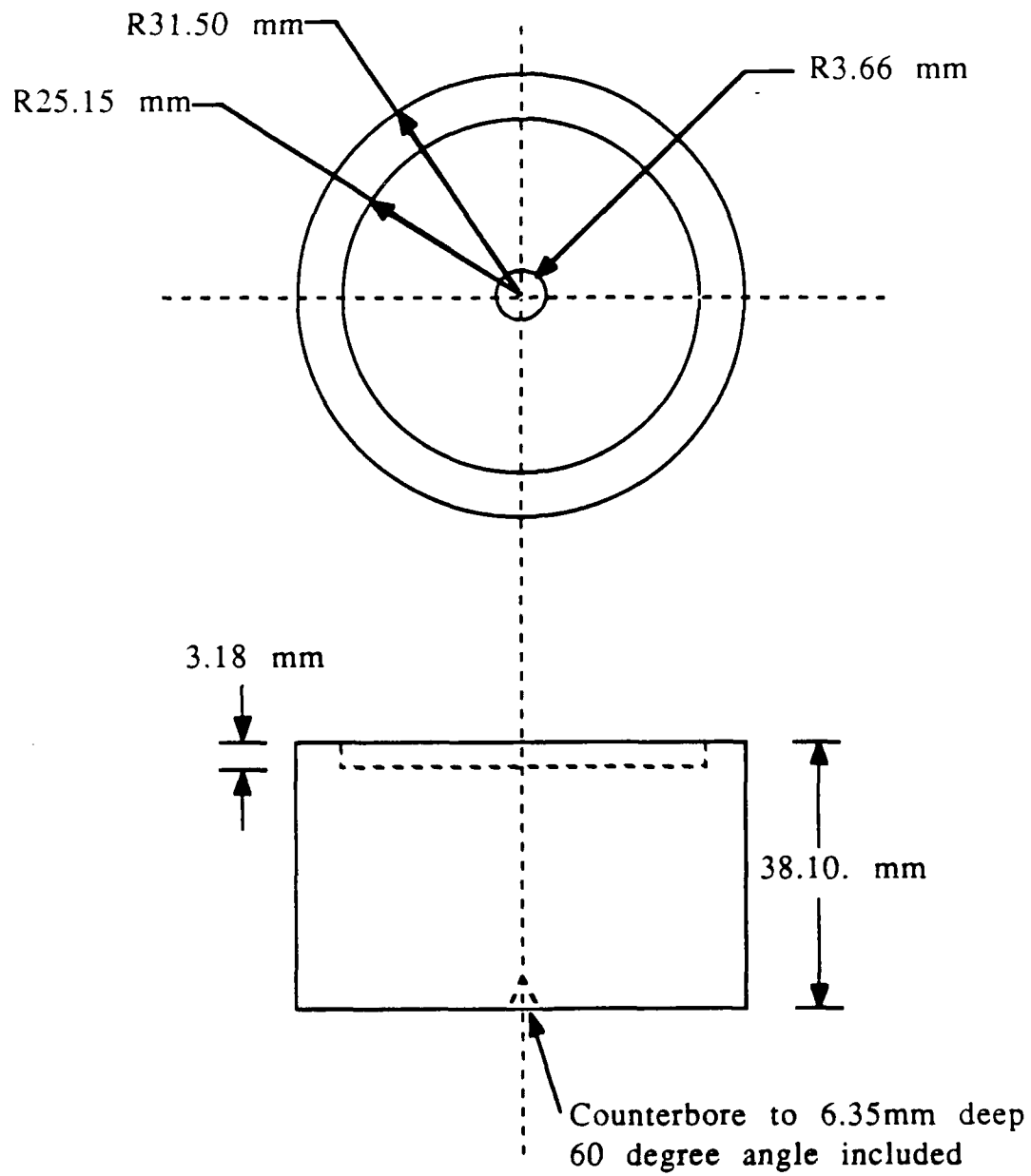
(b) Solid cylindrical piece.

Figure 3.4: Mechanical drawings for grips used in machining.

3.4   Material Properties

Uniaxial tensile tests were performed at a crosshead speed of 0.05 cm/minute at room temperature and a dumbbell tension test specimen geometry, as specified by ASTM D-412. Elongation was measured with an extensometer. The nominal stress strain curve is shown in Figure 3.5. At a given value of λ, each point on the stress strain curve represents the mean value of three standard ASTM D-412 tensile dumbbell test specimens. The breaking elongation and the nominal tensile strength are given in Table 3.2. When compared to material properties provided by Fort Belvoir, given in Table 3.3, all specimens met or exceeded the predicted λ_{break} of 4.4, and the average value of the nominal tensile strength, 17.9 MPa, was within ten percent of the predicted value of 19.7 MPa.

Specimen	λ_{break}	Tensile Strength (MPa)
1	4.4	16.1
2	4.5	17.3
3	4.7	20.2
Average	4.5 ± 0.2	17.9 ± 2.1

Table 3.2: Breaking elongation and nominal tensile strength from uniaxial tension tests.

Original Properties	
Tensile Strength, MPa	19.7
300% Modulus, MPa	9.97
Elongation, λ_{break}	4.40
Hardness, IRHD	73
Bashore Rebound, %	35
Specific Gravity	1.1294
Cure, minutes/°C	40/154

Table 3.3: Material properties of 15TP-14AX.

As in Figure 3.6, one specimen was loaded to an elongation of 250% and then unloaded. Upon unloading, the value of the nominal stress was reduced for a given value of λ. This loading-unloading curve demonstrated this material's viscoelastic behavior. Hysteresis, or energy dissipation in a load deformation cycle, was

evident. Material characterization studies [47] determined that the bulk modulus for this elastomer is 362 MPa.

3.5   Specimen Preparation

The test specimens were fabricated from the molded circular cylinders received from Fort Belvoir, and subsequently, the removal of a large amount of material from the mid-outer surface was required. The bulk of this material was cut from the cylinder using a tungsten carbide cutter on a lathe. When mounting the cylinder in the lathe with the grips in Figure 3.4, care was taken to avoid loading the cylinder in compression. The final dimensions of the test specimen were obtained by grinding, which also smoothed the surface and removed small cuts made by the carbide cutter. A glycol slurry was used periodically throughout fabrication to minimize heat buildup in the cylinders.

During the manufacturing process, differences in material behavior were observed. Two of the cylinders cut easily, and thin strips of elastomeric material were easily removed with the carbide cutte Little or no detectable heat buildup was present so that the glycol slurry was unnecessary. The remaining cylinders were more difficult to cut as the carbide cutter removed only shreds of material. Heating in these cylinders was observed, requiring the use of the glycol slurry. Heat buildup could be easily monitored because the heat was associated with a characteristic odor. When the odor was detected, machining stopped and the glycol slurry was applied. After the cylinder was again at room temperature, machining resumed. As the cylinders were molded from the same batch of elastomeric material, these differences represent within batch nonhomogenities, possibly from nonuniform curing conditions [9]. The test specimens were marked to distinguish those which machined easily, designated *M-*, from those, labelled *S-*, which were more difficult to cut.

The next step was to notch the test specimens. A sharp circumferential crack was made at the mid-height of the test specimen using an X-acto knife mounted on a lathe. The specimen was again placed on the lathe, care being taken not to load the specimen in compression. Liquid Ajax dish detergent was applied as a lubricant to facilitate the cutting process. The knife blade was inserted into the specimen and then the specimen was slowly rotated by hand to make a circumferential cut.

Small notches can be easily made following this procedure, but deep notches proved more difficult. A sharp blade can be used to introduce a deep crack but, as the specimen was rotated, the cutting blade bent. The use of fresh blades and
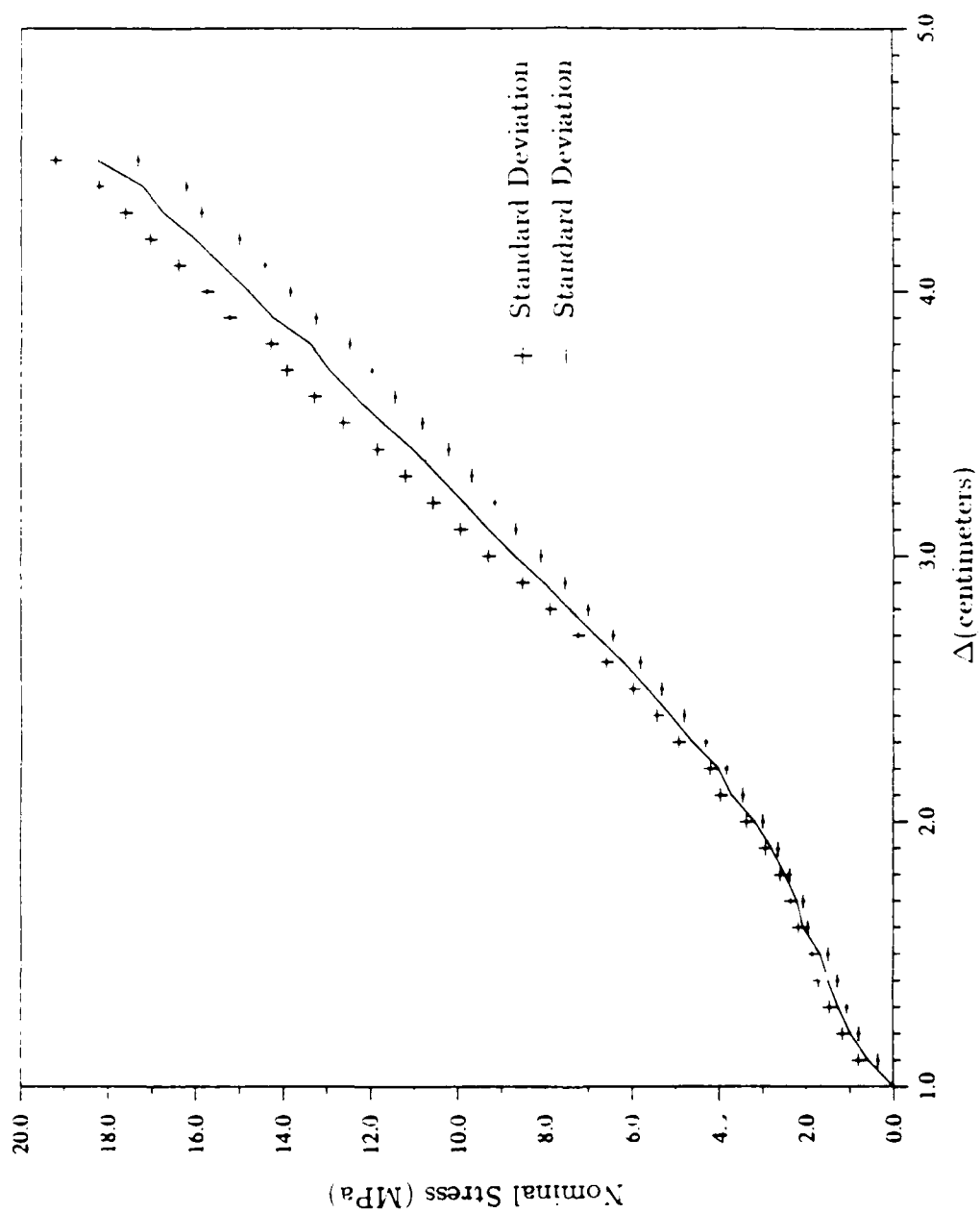
Figure 3.5: Nominal stress strain curve.
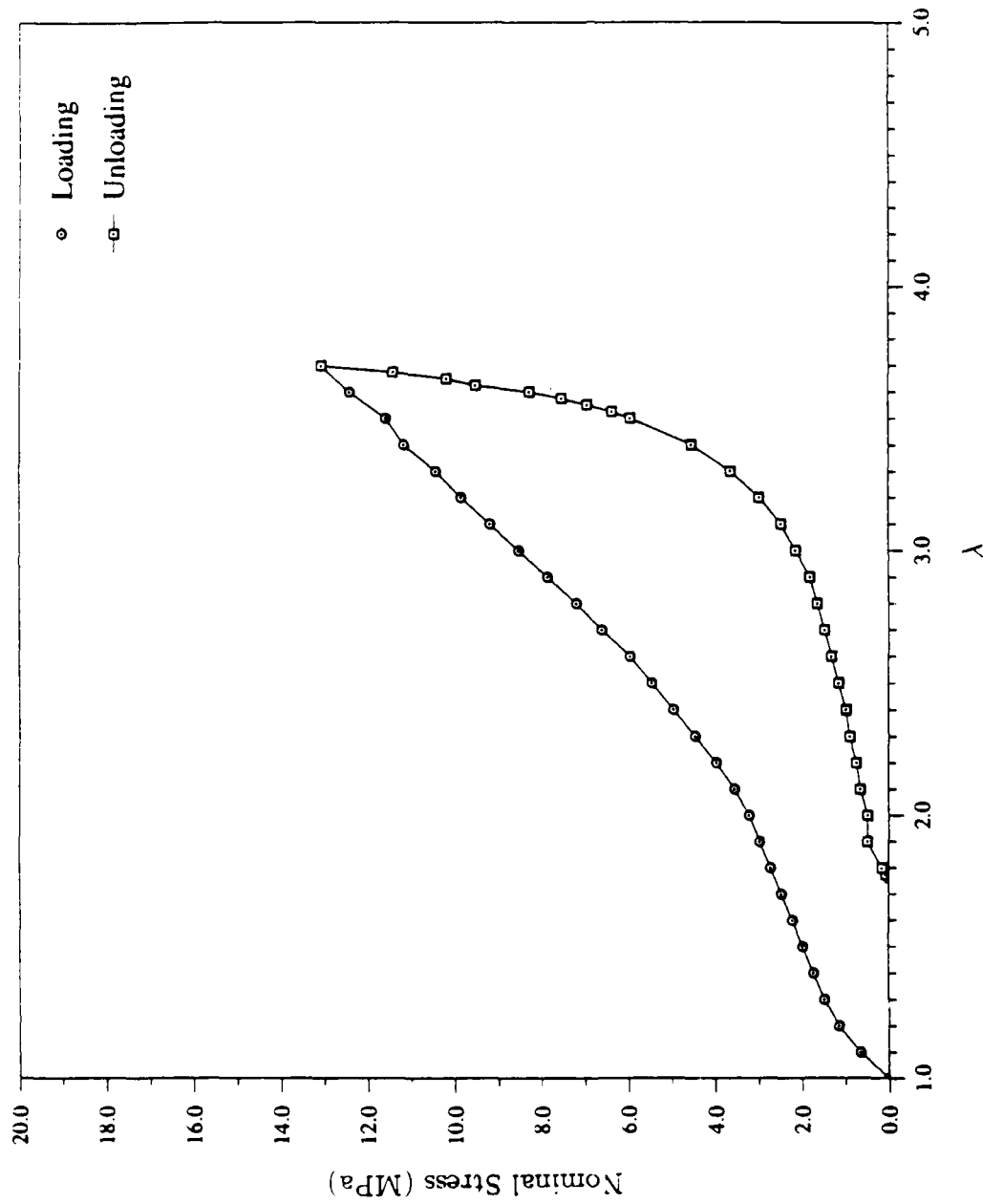
Figure 3.6: Nominal stress strain curve showing the effect of unloading.

liquid detergent did not alleviate this problem. The bending of the the cutting blade was attributed to friction between the thin steel blade and the elastomer material. As the specimen was rotated, the elastomer material pulled on the thin blade and caused it to bend because the liquid detergent was unable to penetrate the full depth of the crack and completely remove the friction present. Consequently, deep cracks were made by initiating a small circumferential cut of length 0.13 cm. Then, while the test specimen was slowly rotated, the crack size was increased to the desired length through increments of 0.13 cm. This procedure enabled the liquid detergent to penetrate deep into the crack, making the specimen easier to cut. Difficulties in making the notches were observed on both types of specimens, i.e., those that were easy to machine and those that were not.

Notch lengths, L, ranged from 0.508 to 0.671 cm. These lengths were considered sufficiently deep to confine the region of nonlinearity from the notch to the uncracked ligament length. A crack length of 0.560 cm was introduced into two S-specimens to check specimen preparation techniques by determining the accuracy of L and to verify the reproducibility of the experiment.

Final specimen dimensions, including L, were provided in Table 3.4 The diameter was measured at the mid-height of the specimen. The uniformity of the inner diameter along H_{inner} was determined in specimens M-2, S-3, and U-1 by measuring this diameter at three different locations. Specimen U-1 represented a prototype on which to test specimen manufacturing and experimental procedures. Ths specimen was made from a carbon black filled, track pad candidate elastomer material which had been tested statically in compression, but its precise material composition and strain history remained unknown. Because this specimen was fabricated by an experienced machinist, D_{inner} was more uniform throughout the length, H_{inner}, resulting in a lower tolerance on D_{inner}. Specimen M-1 contained a double notch, caused by the bending of the X-acto blade when the notch was made.

The test specimens were then cleaned with water in an ultrasonic cleaner, removing any liquid detergent and residual debris present along the crack surface. To better observe the fracture process, two visual aids, a white penetrant and a white ink, were applied to several test specimens after verifying on scrap 15TP-14AX material that these visual aids would not damage the test specimen or cause premature failure during experimental testing. A white penetrant was applied to the crack surfaces of specimen S-1 to record the location of the crack tip. To better visualize diametral changes during the experiment, white opaque ink was sprayed on specimens M-2, S-3, and U-1 away from the crack region. After applying masking tape to the outer surface encompassing the notch, ink was sprayed on these specimens and allowed to dry.

3.6   X-Ray Analysis of Notched Specimens

To check for the presence of impurities and voids, an x-ray analysis of the notched test specimens was performed prior to experimental testing. All specimens contained randomly spaced, spherical inclusions. The diameter of these inclusions was typically 0.2 mm, although some larger inclusions, of diameter 0.4 mm, were found. The *M-* and *S-* specimens both contained the same average number of inclusions per unit volume, $0.14\,mm^3$. Cylindrical inclusions of diameter 0.2 cm and length 1.0 mm, were also found in specimens *U-1* and *S-1*. In specimen *M-2*, a crescent shaped inclusion, approximately 1.4 mm long and 0.2 mm across, was located near the centerline of the specimen. All of these inclusions were more dense than the elastomer material surrounding them, although their exact composition remains unknown. This analysis did not detect any voids. Finally, the crack width was measured as 0.1 mm in all specimens.

3.7   Experimental Procedure

All specimens were tested in an Instron machine Model TTDL under displacement control at room temperature. A crosshead speed of 0.05 cm/minute was used for the double notched specimen, but the crosshead speed was increased to 0.13 cm/minute for the remaining specimens. The load history was monitored both autographically and digitally. Optical measurements of the CMOD, defined as the separation distance between the top and bottom crack surfaces along the outer radius of the specimen, were taken. Geometry changes were documented with a 35 mm camera and a videocamera. Photographs of the specimens were taken at close range to note details of the fracture process while the videocamera recorded overall geometry changes. From the videotape of the experiment, diametral changes in the test specimens were measured along the top grip.

All specimens were loaded to tensile failure. White opaque ink was sprayed on the deformed crack tip region of Specimen *S-2*, at a crosshead displacement, Δ, of 2.5 cm. The specimen was immediately unloaded at a crosshead speed of 0.13 cm/minute and then reloaded to tensile failure 24 hours later. This procedure was performed to identify the surface area present at $\Delta = 2.5$ cm, and then to determine the effect of unloading and reloading on that area.

3.8 Results

Failure occurred at large deformations and was characterized by material tearing in front of the blunted crack tip region and small amounts of slow, stable crack extension until rupture. The tearing process consisted of two distinct yet related phenomena, delamination and crack extension. Along a radius, $R_{inc} = D_{inner}/2 - L$, as shown in Figure 3.7, localized material failure was identified in two separate regions. Delamination was present between the fabricated crack surfaces, in contrast to crack extension which was found above and below the crack surface. Both phenomena were associated with failure normal to the crack surface, in the direction of the applied load.

This fracture process will be discussed qualitatively and quantitatively. Failure will be examined from the load and CMOD histories and through criteria such as nominal fracture strength and the values of the CMOD and the J-integral at failure. First, a detailed description of the tearing process observed in all specimens is given below.

3.8.1 Description of the Tearing Process

A characteristic failure process was observed at each of three stages of deformation: (1) upon initial loading of the specimen, (2) at moderate levels of deformation, where the crosshead displacement, Δ, was approximately between 1.8 cm and 3.6 cm, and (3) at large deformations, or when $\Delta > 3.6$ cm. Each of these stages is illustrated in Figure 3.7 and is referenced to Figure 3.7(a) in the undeformed configuration. Common features to each of these stages included parabolic, asymmetric blunting of the fabricated crack (point m), visible separation of the original crack surfaces into an upper and lower crack surface connected by an inner core of elastomeric material (point n), and material failure, leading to delamination (point o) and crack extension (point p). Here, delamination refers to the separation of material along the outer surface of the inner core, where the radius is R_{inc}. Points (m) through (o) are also labelled on the photographs of the deforming specimens, Figures 3.8 thru 3.10.

At small values of Δ, the specimen had sufficiently deformed such that new surface area, distinguished by its lighter color (due to reflection) in Figure 3.8(a), was exposed near the crack tip region. It was evident that, at the crack tip, localized material failure had taken place, i.e., $\lambda > \lambda_{break}$. The original crack surface had already separated into upper and lower surfaces connected by an inner core of material. The surface area of the inner core was smooth. Delamination at this stage, found along the mid-height of the deformed specimen, was initialized by the

formation of ellipsoidal holes, point (o) in Figure 3.7(b) and Figure 3.8(b), where the major axis was in the direction of the applied load, followed by material separation around these holes. Following material separation, the torn surface resembled rounded saw-toothed segments and retracted back towards the original crack surface, creating a base or ridge of elastomeric material at R_{inc}. Both the size of the segments and the height of the ridge were small. As evidenced by Figure 3.8(c), delamination, point (o), and material retraction, point (q) took place gradually around the circumference of the inner core. The material did not retract symmetrically about the mid-height, i.e., material along the top half of the specimen might still be moving up towards the top of the specimen while the material at the bottom was already at the ridge. By the end of this stage of deformation, the newly exposed material surface along the inner core was no longer smooth, for thin vertical strands of material connected the upper and lower fabricated crack surface.

In the next stage of deformation, the tearing process was magnified in size, refer to Figure 3.7(c) and Figure 3.9. The length of the inner core, the size of the ellipsoidal holes, and the size of the ridge of retracted material gradually increased, becoming wider and more visible. Two sets of vertical strands along the inner core were apparent, running from above and below the original crack surface and joining at the mid-height of the deformed specimen in small jagged saw-toothed segments. Tearing was initiated from the separation of these segments around ellipsoidal holes. Where the material had begun to retract, the location, at which delamination would next occur, point (r) in Figure 3.9(b), could be predicted by tiny jagged edges on the new surface area. Again this delamination process was neither simultaneous around the circumference nor was it symmetric about the mid-height.

By the final stages of deformation, referred to in Figure 3.10 and Figure 3.7(d), the initially small inner core had grown to almost 2.5 cm long and blunting of the outer radius, $D_{inner}/2$, point (s) in Figure 3.10(a), could be found. Strands of rubber extended proportionally longer over the inner core, i.e., more than half of the inner core's length, increasing the size of the saw-toothed segments. Delamination initiated from ellipsoidal holes found throughout the surface of the inner core. However, the holes became smaller and the separated material peeled back, point (t) in Figure 3.10(b), instead of slowly pulling back, towards a vertical edge of the specimen.

Crack extension in the direction of the applied load was detected visually and physically. The proposed model for crack extension is provided in Figure 3.7, showing schematically that asymmetric crack extension occurred above and below the original crack surfaces.

Visual evidence of crack extension in the direction of the applied load, is shown by point (u) in the sequence of photographs in Figure 3.11. Elastomer material between the two notches along the inner core was extended with increasing load. Figure 3.11(a). Along the lower middle and right side of the deformed specimen in Figure 3.11(b), newly exposed surface material between the original surfaces of the second lower notch is distinguished by its lighter color and extends out and away from the inner core. Visual observation of specimen *S-2* just prior to failure also verified this conclusion. The inner core of this specimen, at $\Delta = 5.3$ cm, separated from the material surrounding it along the bottom edge. The inner core extended deep into the lower section of the specimen and it could be seen that only the inner core connected the bottom portion of the specimen to the top.

At failure, the specimen broke into two pieces, a male and a female. The male piece was not consistently associated with either the top or bottom grip, as shown in Table 3.5, and was characterized by a plug, located in the center of the specimen, which extended outward and upward. The height of the plug, listed in Table 3.5 for each specimen, was approximately 0.5 cm and, for a given material type decreased slightly with increasing crack length. The surface at the top of the plug was smooth, resembling a glassy fracture surface. Micrographs showing the saw-toothed segments are provided in Figure 3.12, in which point (c) locates the fabricated crack surface. In the male piece, Figure 3.12(a), the saw-toothed segments, point (e) were found at the base of the plug, point (d), and could be matched to similar segments surrounding the perimeter of the cavity in the female piece. The female piece, Figure 3.12(b) contained a large cavity, point (f), in its center. Encompassing the perimeter of this cavity were several layers of crosshatched material which extended down into the cavity. The layer closest to the original crack surface, point(g), was thinnest and had the smallest saw-toothed segments while the layer furthest away from the original crack surface, point (h), was thickest with the largest saw-toothed segments.

There were usually two layers of saw-toothed segments surrounding the perimeter of the cavity or plug, but the number of layers for a given specimen varied from one to four, as tabulated in Table 3.6. Multiple layers were a consequence of increased specimen elongations and did not occur simultaneously, as evidenced by the existence of only two layers of crosshatched material found in specimen *U-1*, which failed prematurely. The number of torn surface layers was independent of material type and crack length.

Although successive layers of saw-toothed segments were visibly larger and thicker, it was difficult to quantify these dimensions because the tips of the saw-toothed segments curled over the previous layer of torn material, making measurements inaccurate. The failed specimen pieces were not sectioned at this time to quantify the observed size changes in the crosshatched layers.

Specimen	Crack Length (cm)	Height (cm)	Inner Height (cm)	Inner Diameter at Mid-Height (cm)	Mean Inner Diameter (cm)
M-1	0.508	4.989	2.385	2.296	-
M-2	0.638	5.009	2.423	2.360	2.418 ± 0.053
S-1	0.559	5.077	2.524	2.324	-
S-2	0.559	5.039	2.472	2.367	-
S-3	0.615	5.037	2.520	2.197	2.227 ± 0.048
U-1	0.671	4.826	2.168	2.474	2.510 ± 0.030

Table 3.4: Initial measurements of test specimens.

Specimen	Plug Location	Height(cm)
S-1	bottom	0.526
S-2	top	0.441
S-3	top	0.422
M-1	bottom	0.597
M-2	bottom	0.527
U-1	bottom	0.549

Table 3.5: Plug height and location in grips at failure.

Specimen	Number of Layers
M-1	1 - 4
M-2	2 - 4
S-1	1 - 3
S-2	1 - 4
S-3	1 - 4
U-1	1 - 2

Table 3.6: Number of torn surface layers.

Specimen	Layer	Distance (mm)
M-1	1	0.10
	2	1.00
M-2	1	0.06
	2	0.20
	3	0.40
	4	0.80
S-2	1	0.08
	2	0.50

Table 3.7: Distance between torn surface layers and the fabricated crack tip.

The distance between a torn surface layer and the fabricated crack tip increased with elongation, as shown in Table 3.7 for specimens *M-1*, *M-2*, and *S-2*. The thinnest and closest layer was approximately 0.1 mm away from the fabricated crack tip while the furthest and largest layer was 0.5 to 1.0 mm away from the tip.

Rupture occurred when crack extension reached a critical value, above or below the original crack surface. The specimen then broke into two pieces, creating a male piece from the deformed inner core and a female from the remaining specimen, where ruptured had initiated. Finally, by mating the ruptured specimen pieces, the fracture process can be referenced to the undeformed configuration in Figure 3.13. A small layer of torn surface area, representing the saw-toothed

segments, was located near the fabricated crack tip, the result of delamination and crack extension during the first stage of tearing. The size of each successive layer and the distance between layers increased with specimen elongation, each successive layer undercutting the previous one.

Localized material failure in the load direction had been identified in two separate regions. Material failure associated with delamination was found between the fabricated crack surfaces, along the surface of the inner core. The occurrence of material failure above and below the original crack surface led to increasing increments of stable crack extension and ultimate rupture of the test specimen.

3.8.2 Quantitative Results

Quantitative results such as the load and CMOD histories were referenced to the experimentally measured crack length, L_e. After rupture, the true crack length was measured by averaging two values of L_e found along a diameter in the female piece and was found to be within three percent of the intended crack length, shown in Table 3.8. The deviation between intended and experimental crack length was attributed to the difficulties in fabricating the notch, discussed previously. Because the inner and outer diameters of the cylindrical dumbbell specimen were not precisely concentric due to specimen manufacturing techniques, L_e varied by ~ 0.02 cm along a diameter. The differences in crack length between specimens *S-1* and *S-2* are large enough to expect that the load and CMOD histories for these specimens will not be the same and consequently, the reproducibility of the results could not be checked.

3.8.3 Nominal Fracture Strength, λ, and CMOD at Failure

When examining data at failure, the material type, crack length, and experimental history associated with each specimen must also be considered, and they are listed in Table 3.9. To determine the effect of damage on the load and CMOD, specimen *S-1* was damaged by applying nail polish to the deformed inner core at $\Delta = 3.6$ cm, and subsequently, a basis for distinguishing specimen damage versus experimental variation in measurements was developed for the remaining specimens. Specimen *S-2* had undergone a load deformation cycle as part of the experiment and, like specimen *U-1*, was not a virgin specimen when it was loaded to failure. Finally, specimen *M-1* contained a double notch.

(a) Undeformed configuration.
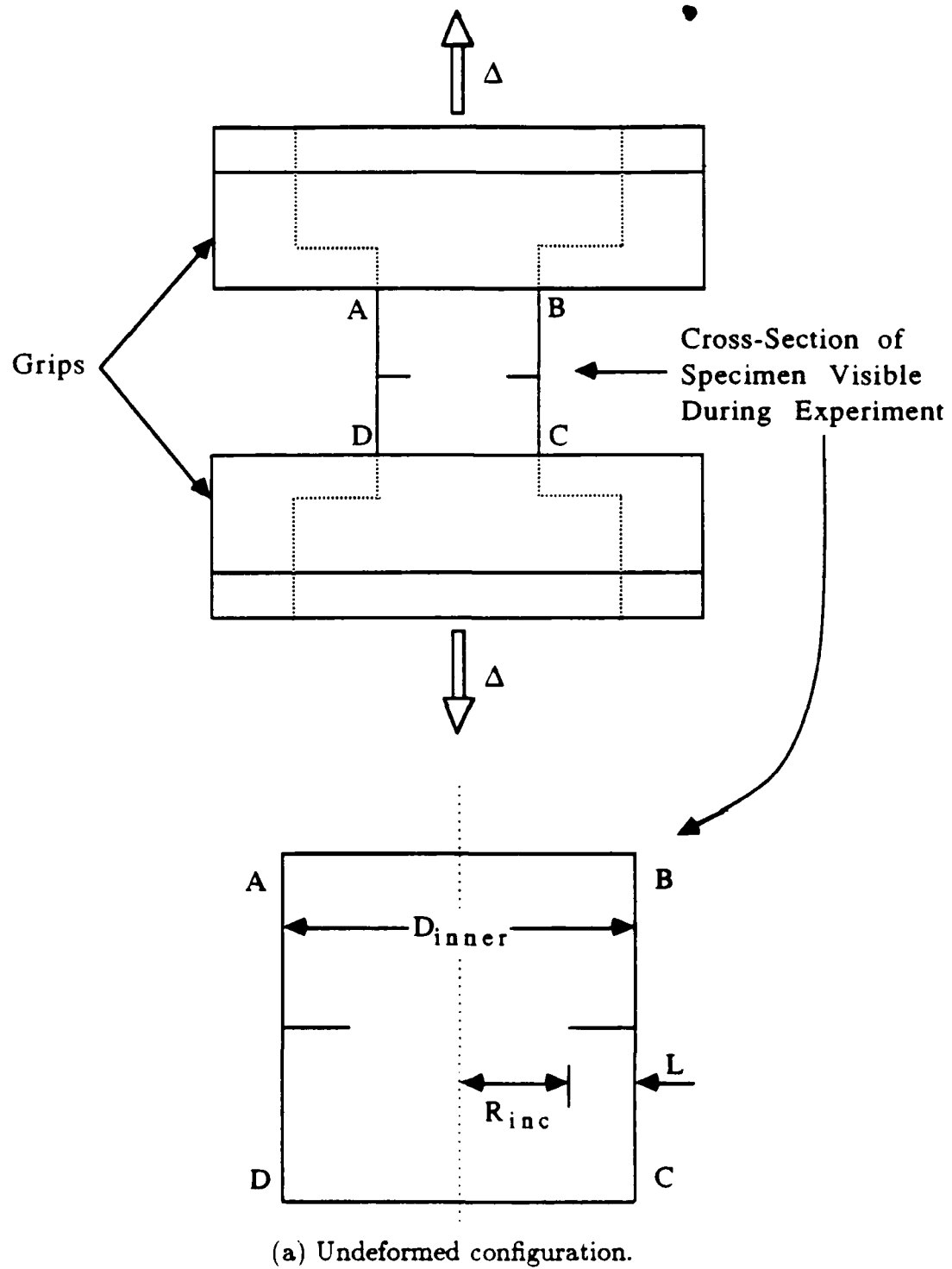
Figure 3.7: A cross-sectional view of the three stages of tearing.
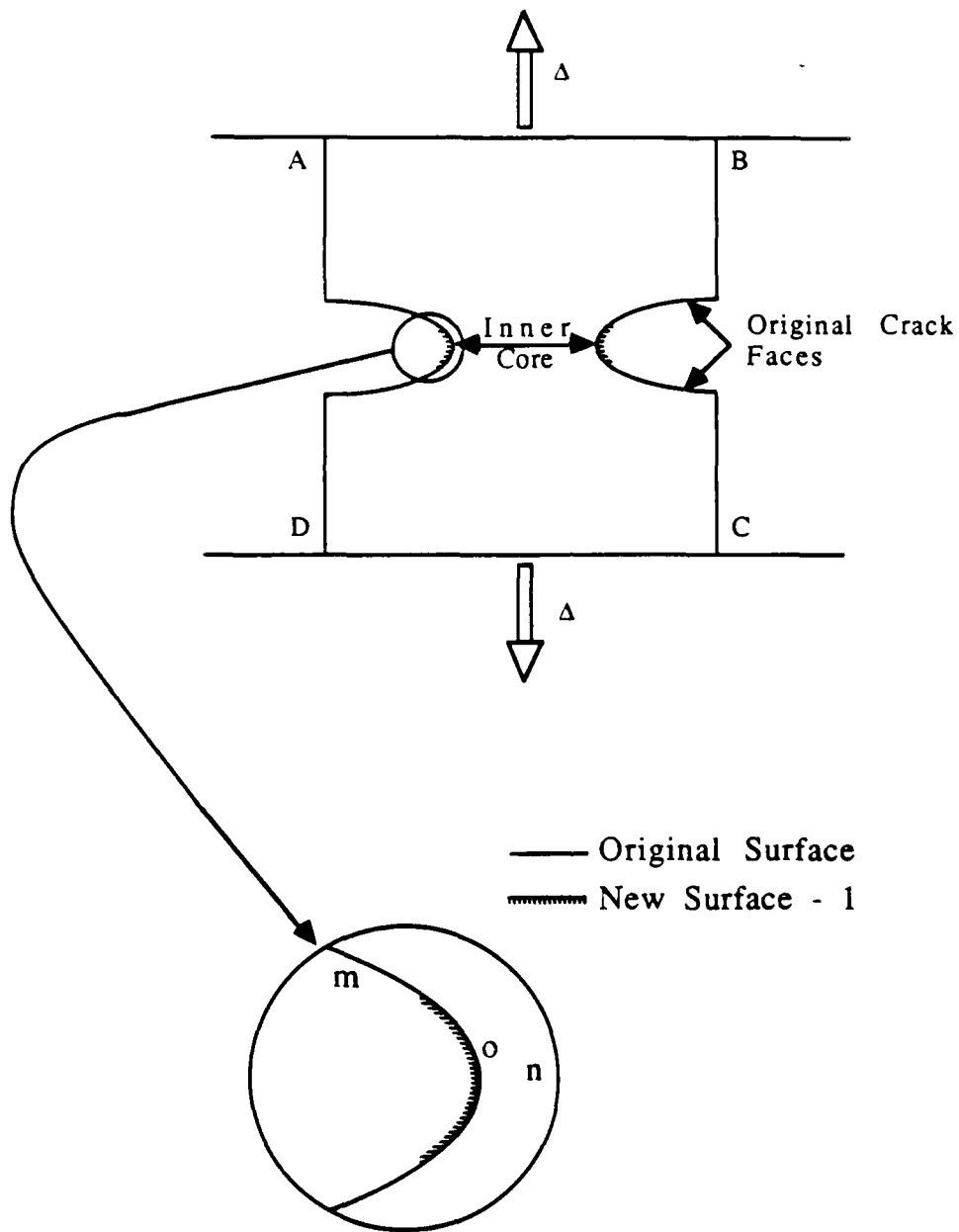
(b) Low values of Δ.

Figure 3.7: A cross-sectional view of the three stages of tearing.
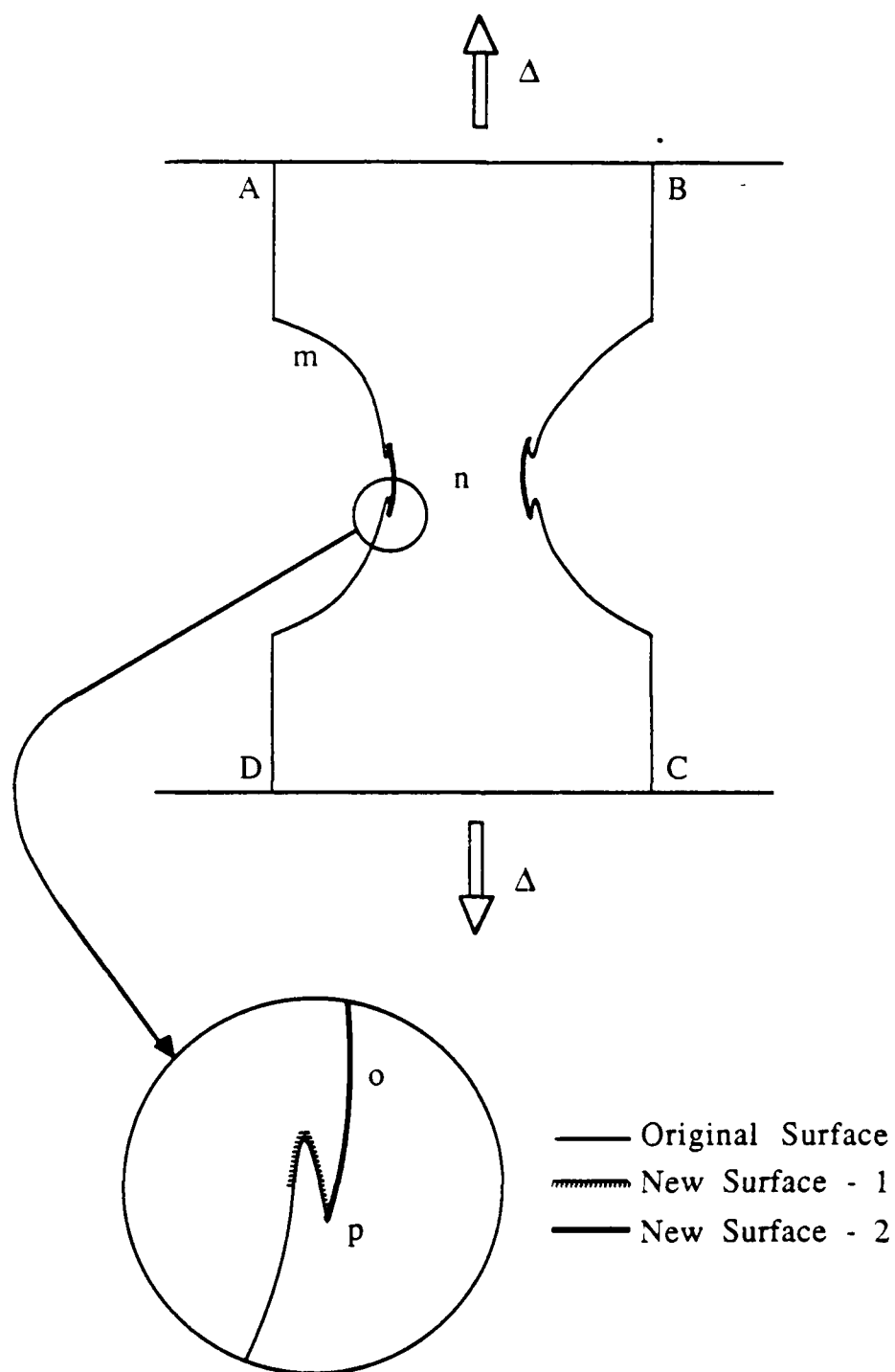
(c) Moderate values of Δ.

Figure 3.7: A cross-sectional view of the three stages of tearing.

(d) High values of Δ.
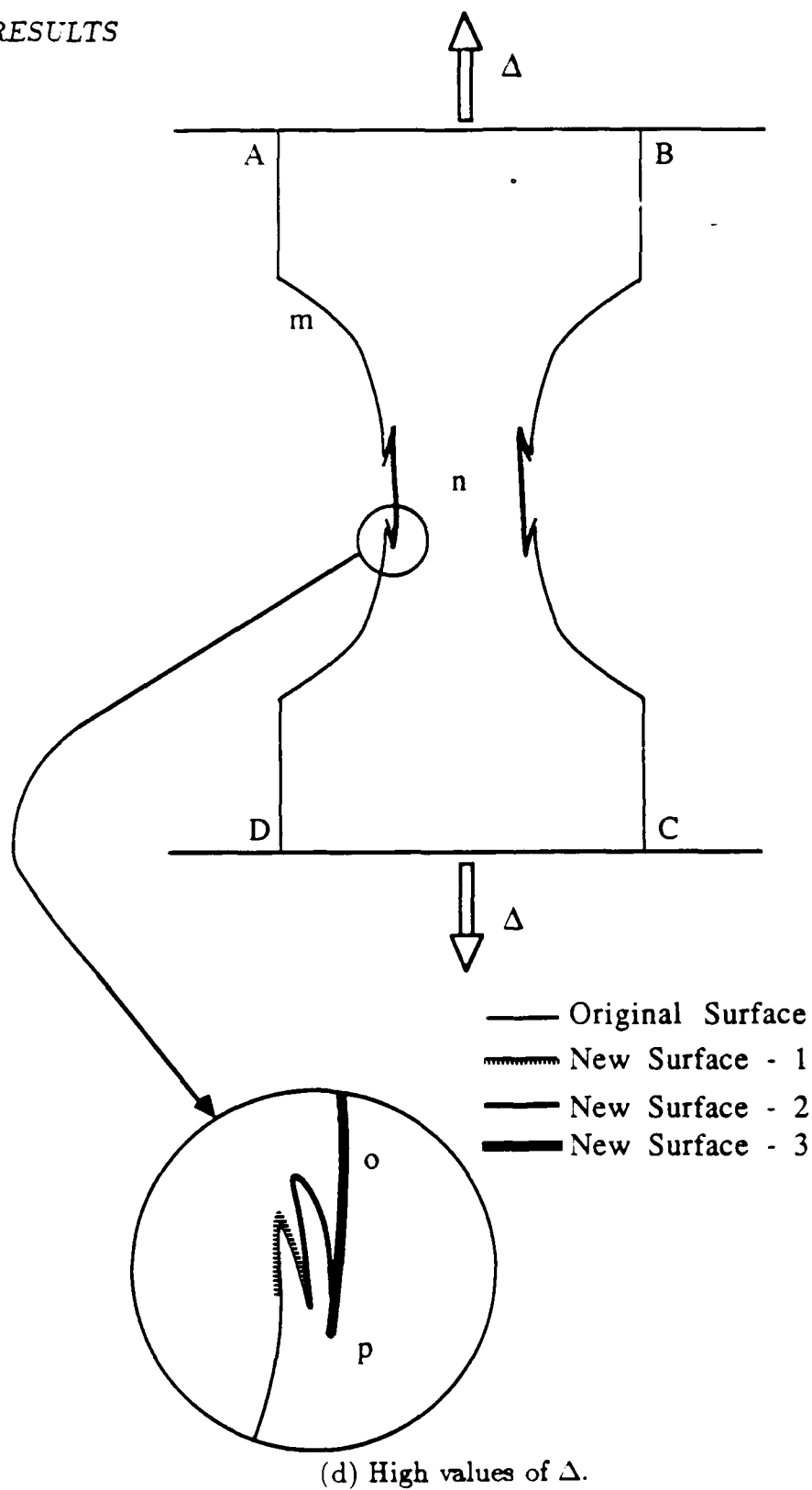
Figure 3.7: A cross-sectional view of the three stages of tearing.
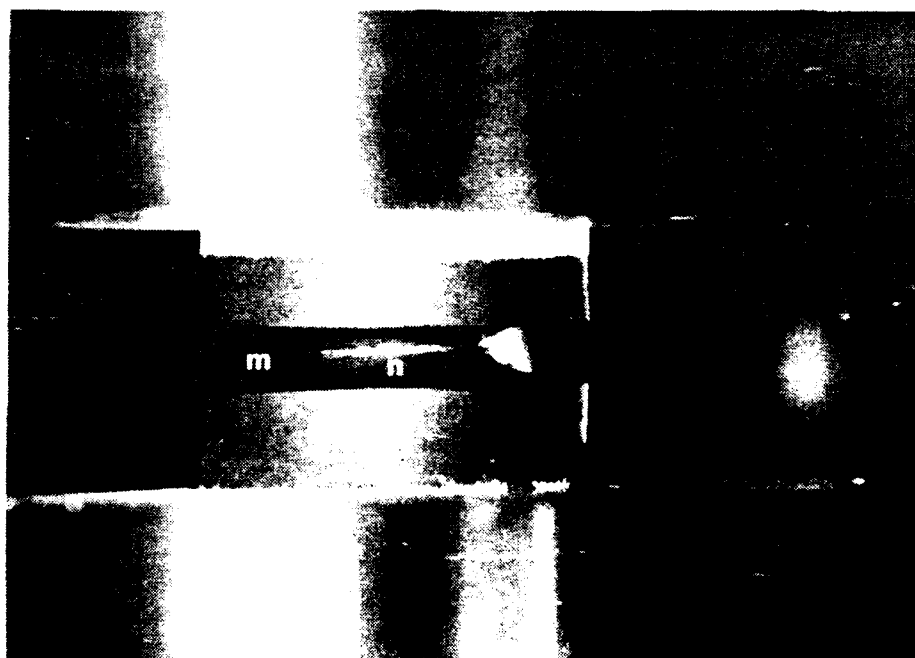
(a) Material separation, $\Delta = 0.64$ cm.

Figure 3.8: Tearing at low values of Δ in specimen *U-1*.
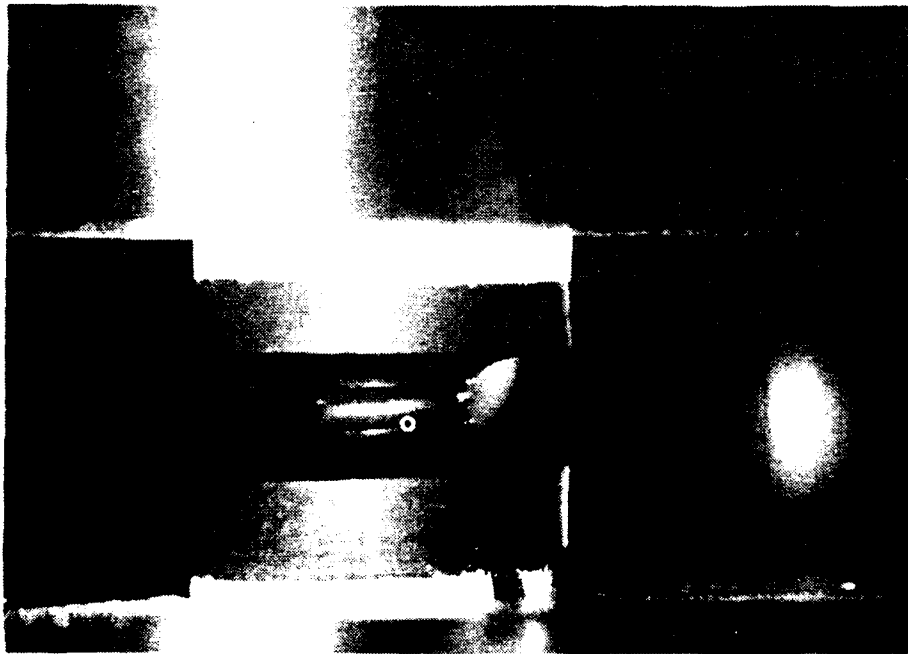
(b) Ellipsoidal holes at mid-height. $\Delta = 1.44$ cm.

Figure 3.8: Tearing at low values of Δ in specimen U-1.
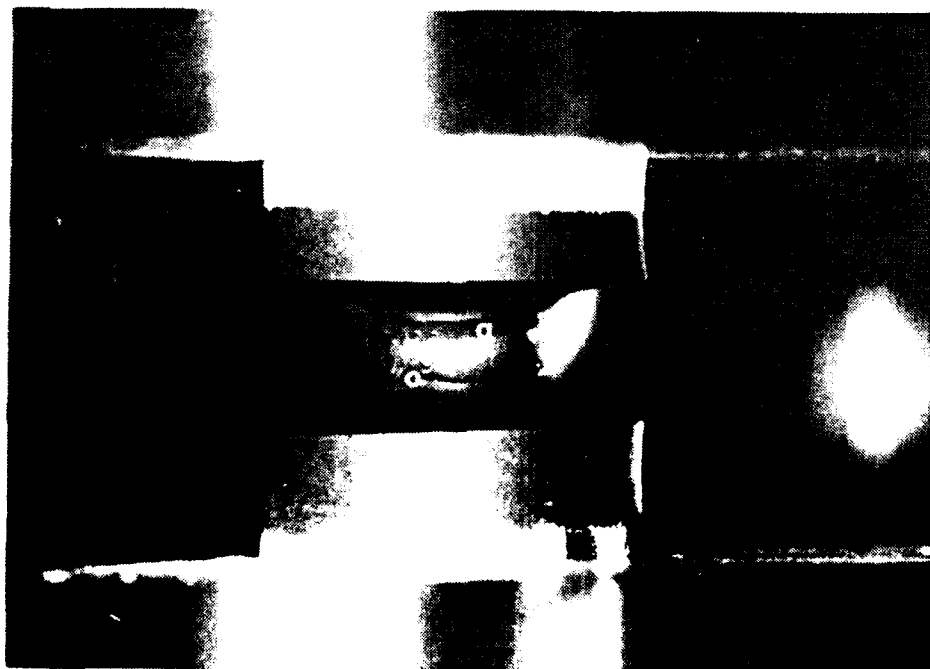
(c) Material retraction, $\Delta = 1.65$ cm.

Figure 3.8: Tearing at low values of Δ in specimen *U-1*.
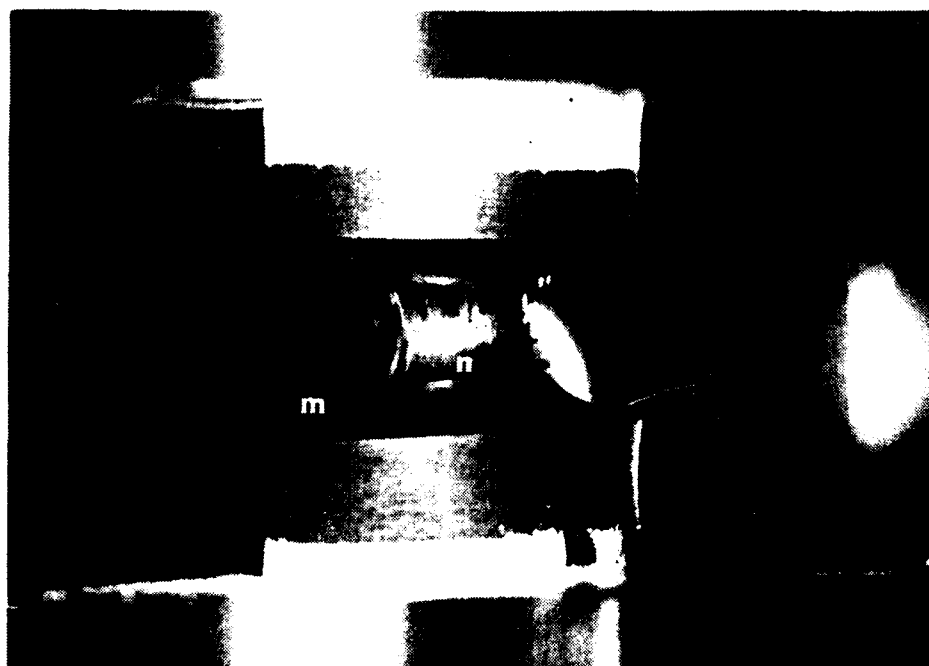
(a) Two sets of vertical strands joined at mid-height in specimen *U-1*, $\Delta = 2.0$ cm.

Figure 3.9: Tearing at moderate values of Δ.
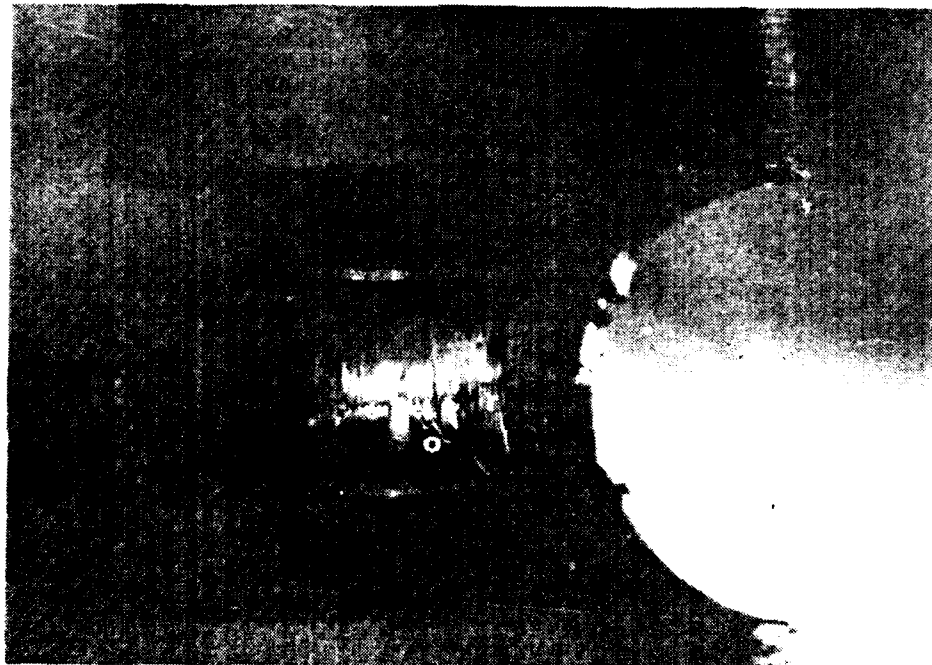
(b) Material retraction in specimen *S-1*. $\Delta = 3.0$ cm.

Figure 3.9: Tearing at moderate values of Δ.

(a) Blunting of the radius, $D_{inner}/2$, $\Delta = 5.1$ cm.

Figure 3.10: Tearing just prior to fracture in specimen S-2.

(b) Tears towards original crack surface, $\Delta = 5.6$ cm.

Figure 3.10: Tearing just prior to fracture in specimen *S-2*.

(a) Elastomer material between the two notches separating at mid-height.

Figure 3.11: Crack extension in specimen *M-1*, the double notched specimen.
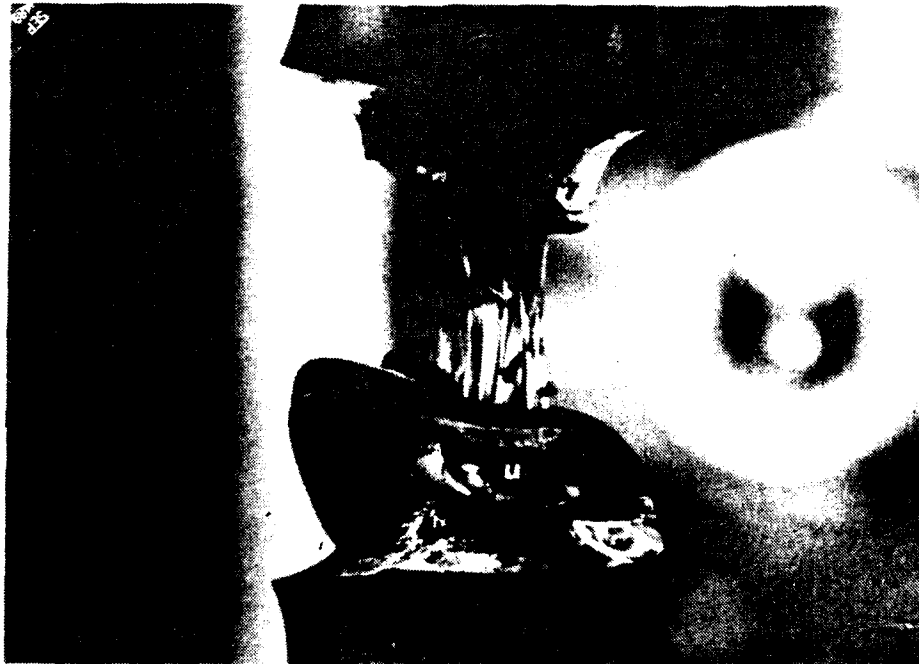
(b) Separated material has retracted downward and crack extension is indicated by the light material, extending outward, along the lower notch in the mid-right section of the deformed specimen.

Figure 3.11: Crack extension in specimen *M-1*, the double notched specimen.
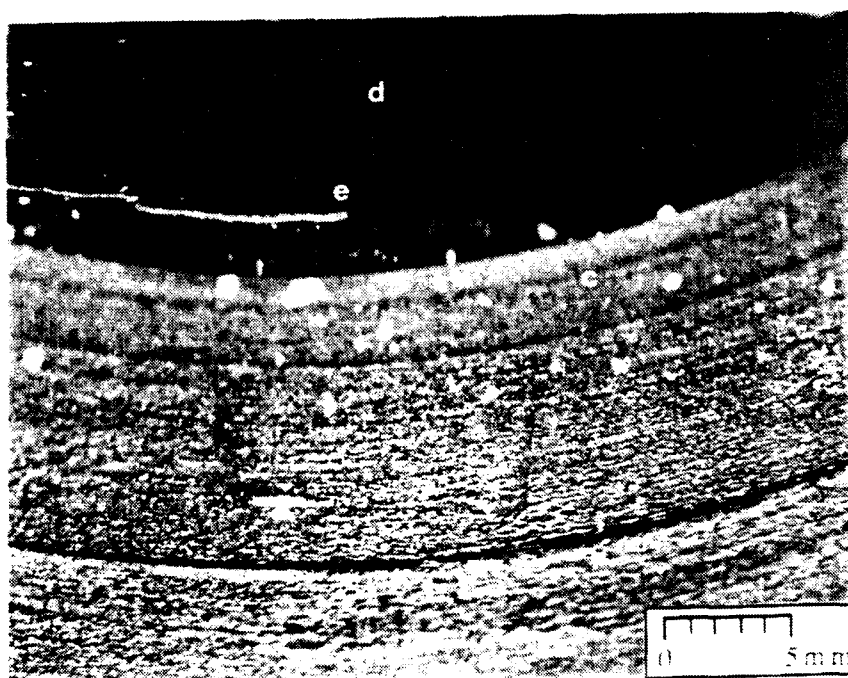
(a) Male piece, specimen S-2.

Figure 3.12: Micrographs at 30X of fractured specimens.
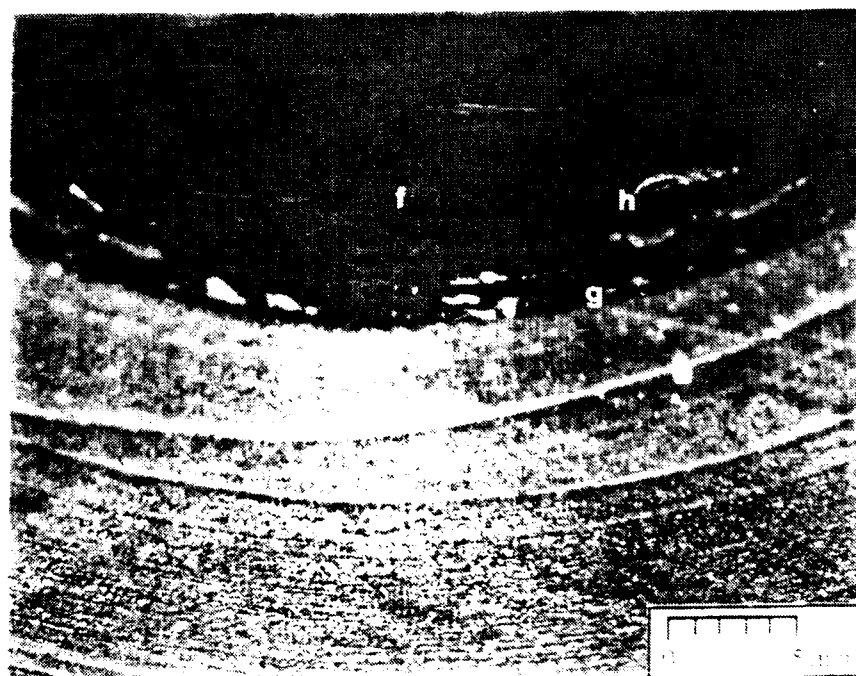
(b) Female piece, specimen *S-3*.

Figure 3.12: Micrographs at 30X of fractured specimens.
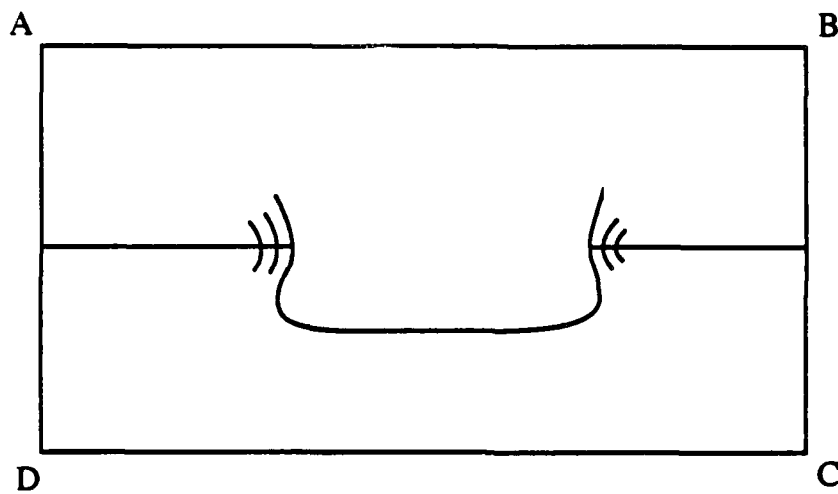
Figure 3.13: Material failure schematically referenced to the undeformed configuration.

Specimen	Crack Length (cm)		% Difference
	Experimentally Measured	Intended	
M-1	0.518	0.508	-2.0
M-2	0.634	0.637	0.5
S-1	0.547	0.560	2.0
S-2	0.576	0.560	-3.0
S-3	0.606	0.615	1.5
U-1	0.658	0.670	2.0

Table 3.8: Experimental and predicted crack length.

Specimen	Crack Length (cm)	Nominal Fracture Stretch λ_f	Nominal Fracture Strength (MPa)	CMOD$_f$ (cm)	Experimental History
M-1	0.518	3.24	9.79	-	Double Notch
M-2	0.634	3.14	11.4	3.0	
S-1	0.547	3.00	9.10	2.5	Damaged
S-2	0.576	3.28	9.45	2.8	Load Deformation Cycle
S-3	0.606	3.27	11.9	2.5	
U-1	0.658	1.95	7.79	1.2	Unknown Strain History

Table 3.9: Nominal fracture strength, nominal fracture stretch, CMOD$_f$.

All specimens except for specimen *U-1* were extended for five centimeters at failure, corresponding to a nominal fracture stretch, λ_f, of 3.0, where

$$\lambda_f = \frac{\Delta_{break}}{H_{inner}} + 1 \ . \tag{3.1}$$

Results for individual specimens are provided in Table 3.9. Specimen *U-1* fit snugly into the grips and this may have precipitated premature failure. Also, because the strain history of this specimen is not well known, specimen *U-1* could have been damaged prior to testing.

Nominal stresses at fracture, σ_f, were defined as

$$\sigma_f = \frac{P_f}{A_0} \ , \tag{3.2}$$

given the load at fracture, P_f, and the undeformed cross-sectional area, A_0. Here, A_0 is based on the effective radius, R_{inc} (see Figure 3.7(a)). The results clearly demonstrated that undamaged virgin specimens containing a single circumferential crack failed at higher strengths, 11 MPa, when compared to the remaining specimens. Damage (specimen *S-1*), material softening (*S-2* and *U-1*), and the presence of a double notch (*M-1*) all reduced fracture strength to 9 MPa. The prediction that, for a given material type, σ_f would decrease with increasing crack length could not be verified because experimental histories prevent such comparisons. Within batch variations (*M-* versus *S-*) of the nominal fracture strength were not apparent. Values of σ_f and λ_f were less than the uniaxial tensile strength, 19.7 MPa, and λ_b, 4.4, for all specimens.

The value of the CMOD at fracture, $CMOD_f$, revealed differences due to material type. For the *S-* specimens, $CMOD_f$ ranged from 2.5 to 2.8 cm and appeared to be independent of crack length or damage, while the $CMOD_f$ was 3.0 cm for specimen *M-2*. CMOD measurements were not taken for specimen *M-1* due to mechanical difficulties.

3.8.4   Load History

Load histories or $P - \Delta$ curves, given in Figures 3.14 and 3.15 (tabulated in Appendix-C), were consistent with predictions that the load would soften with increasing crack length for a given material type and also demonstrated that material type has a strong influence on the load response. At small values of Δ, the load was similar for all specimens, but by $\Delta = 0.5$ cm, differences due to the crack length and material type were observed. As the specimens continued to elongate, the load increased linearly with Δ until the onset of rupture, which could

be predicted by a drop in load (*M*-specimens) or by a constant load (*S*-specimens). Differences in load histories due to material type (*M*- versus *S*- versus *U*-) were readily apparent as specimen *U-1* exhibited the highest material stiffness even though this specimen had the longest crack. For both the *M*- and *S*- specimens, the material response was softer with increasing crack length, however the load history for specimen *M-2* ($L = 0.634$ cm) was similar to that for specimen *S-1* ($L = 0.547$ cm), reflecting the effect of within batch variations observed during manufacturing. Damage in specimen *S-1* at $\Delta = 3.6$ cm was indicated by as a sudden fluctuation in load, followed by a softer material response, and failure could not be predicted by a change in the slope of the $P - \Delta$ curve. A small load fluctuation was found in specimen *M-2* at $\Delta = 4.2$ cm, however its source was unknown.

The load histories were more representative of smooth tearing, in contrast to slip-stick tear behavior, and its shape reflects that stable crack growth was present throughout the experiment as shown in Figure 3.16, where an experimentally obtained $P - \Delta$ curve is a composite of many load curves valid for stationary cracks with increasing length, L. Finally, although three stages of tear behavior were observed, they could not be distinguished on the experimental load histories by a change in slope. At both transitions regions between stages of tearing, $\Delta = 1.8$ cm and $\Delta = 3.6$ cm, the $P - \Delta$ curves remain linear.

3.8.5 CMOD Histories

CMOD histories, provided in Figure 3.17 and 3.18 (tabulated in Appendix-C), were essentially linear up to failure, except for specimen *S-1*. Rupture could not be predicted at large values of Δ by changes in the CMOD-Δ curves. These curves appeared independent of crack length over the rage of crack lengths tested, while significant differences in values of the CMOD due to material type were not apparent until $\Delta > 2.0$ cm, when the CMOD curve for specimen *M-2* became slightly stiffer than that for the *S*- specimens. For specimen *S-1*, the value of CMOD at a given value of $\Delta < 2.0$ cm was smaller than the other specimens and as Δ increased further, large fluctuations in the CMOD were observed at $\Delta = 4.0$ cm, due to damage, and at $\Delta = 0.5$ and 2.3 cm, smaller fluctuations, attributed to experimental error, were also present. These smaller fluctuations were not attributed to significant specimen damage because the load history for specimen *S-1* is smooth in these regions. The CMOD leveled off at $\Delta = 2.5$ cm prior to failure in this specimen. Similar to the load histories, the three stages of tearing, that were visually observed, could not be identified by changes in the CMOD versus Δ curves.
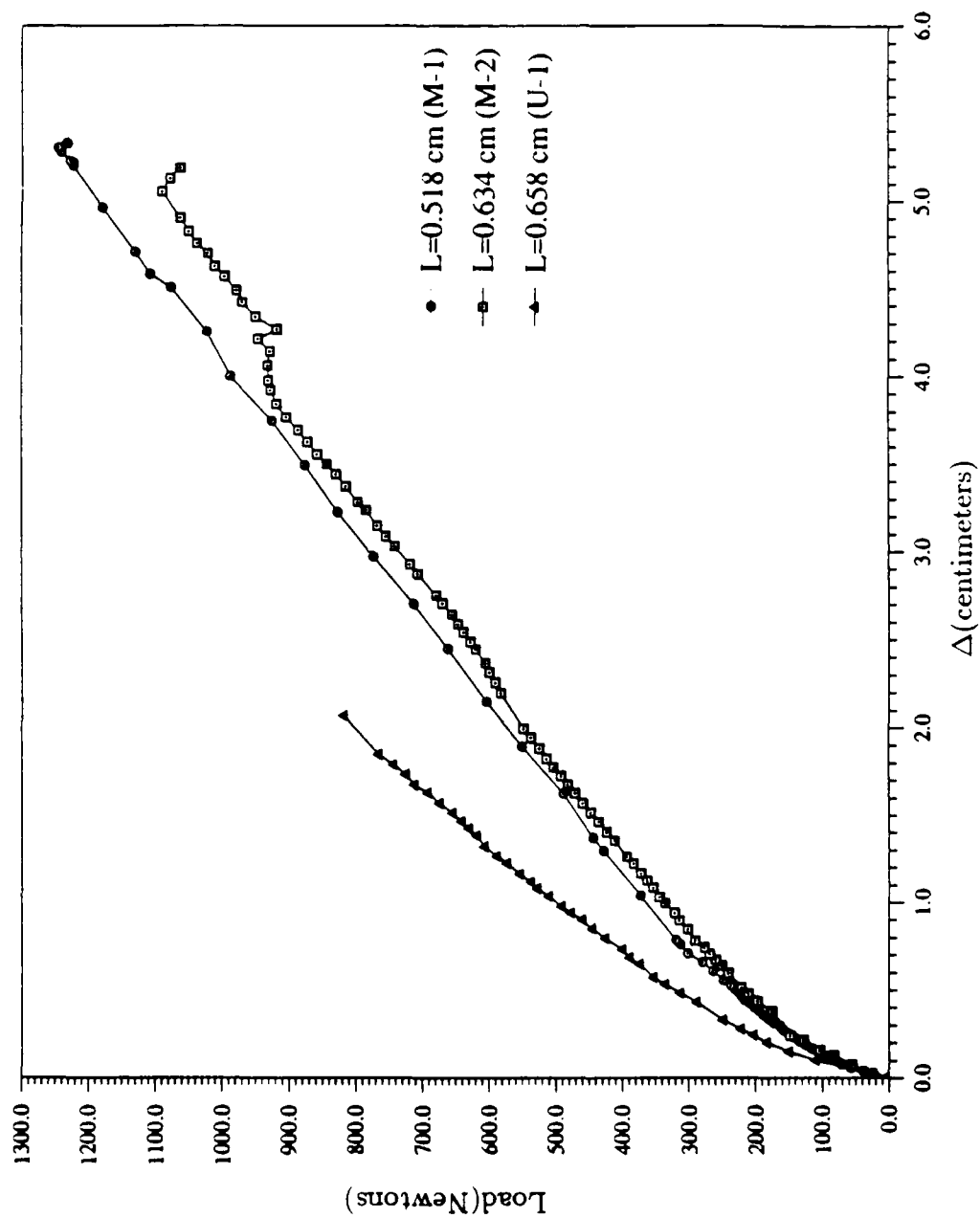
Figure 3.14: $P - \Delta$ curves for M- and U- specimens.
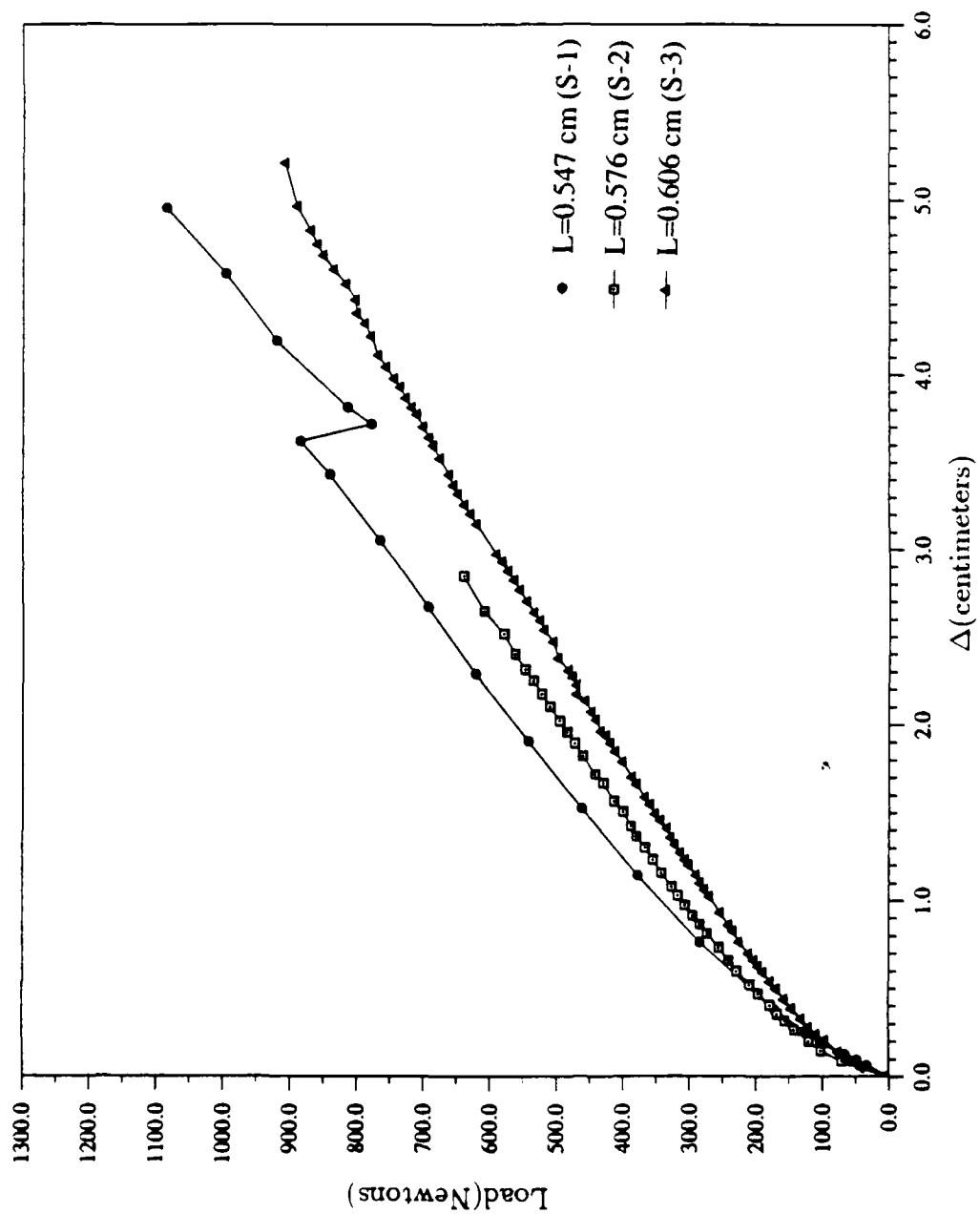
Figure 3.15: $P - \Delta$ curves for S- specimens.
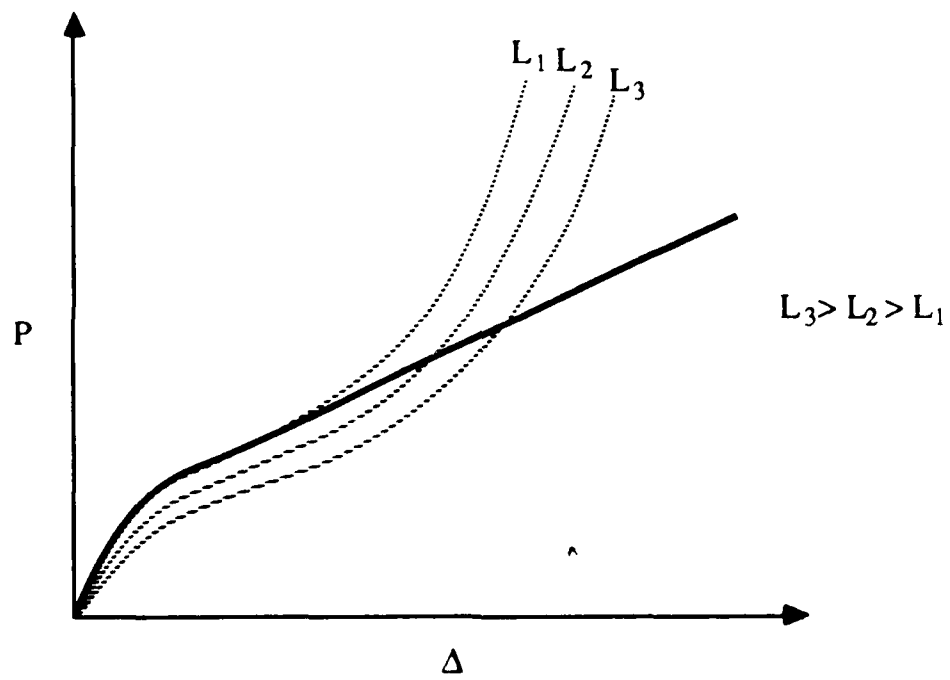
Figure 3.16: Composite $P - \Delta$ curve.
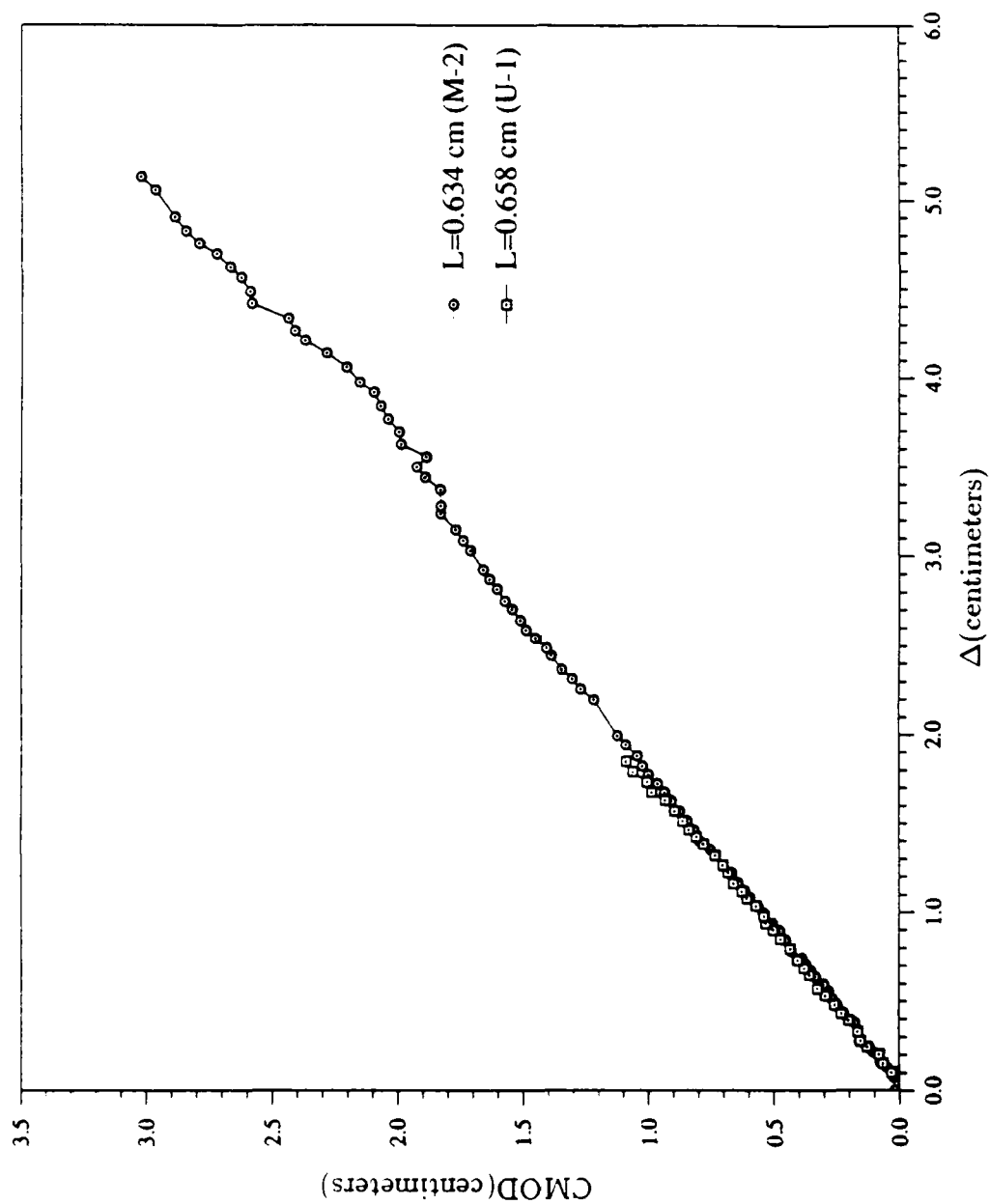
Figure 3.17: CMOD versus Δ for specimens *M-2* and *U-1*.
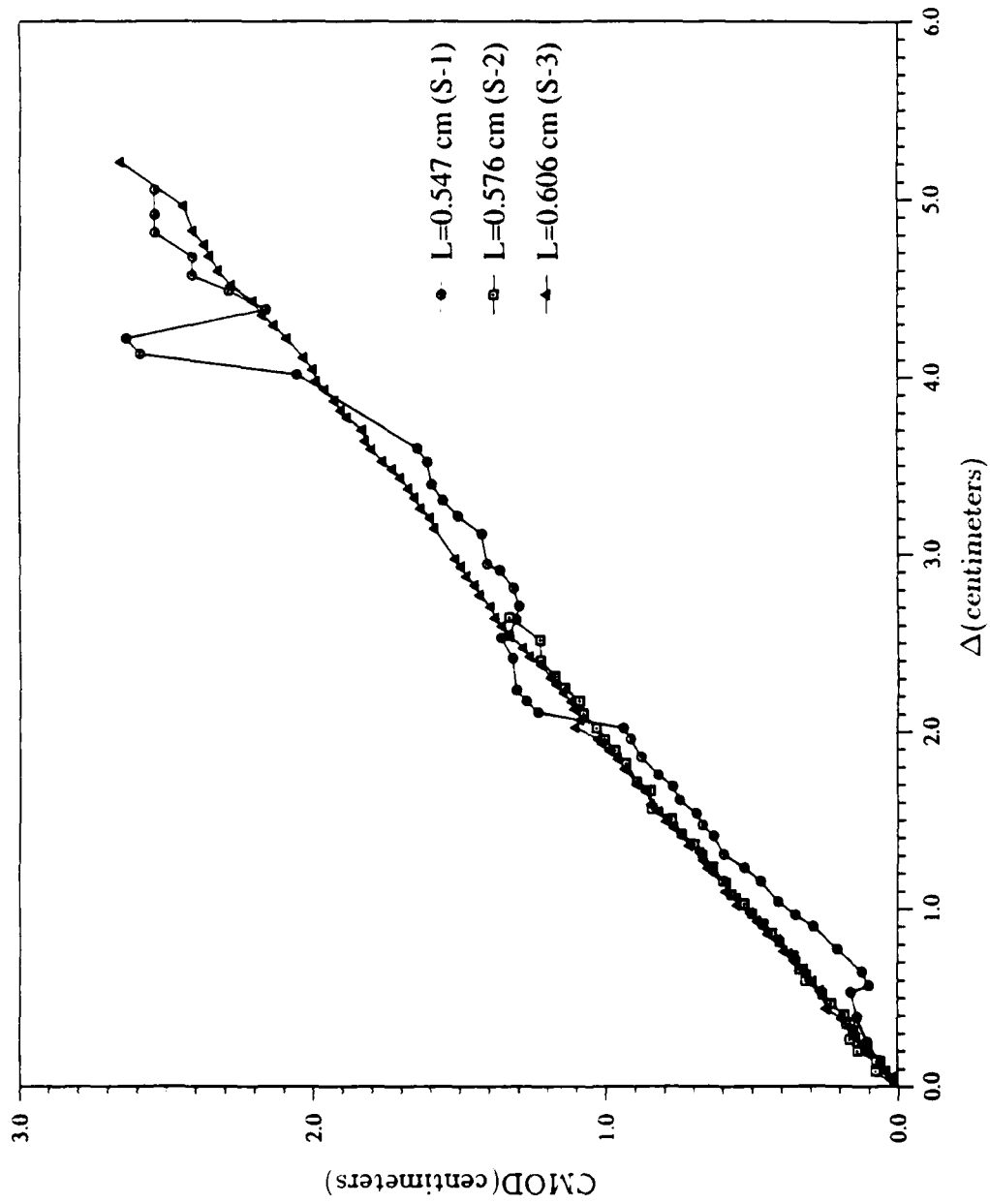
Figure 3.18: CMOD versus Δ for S- specimens.
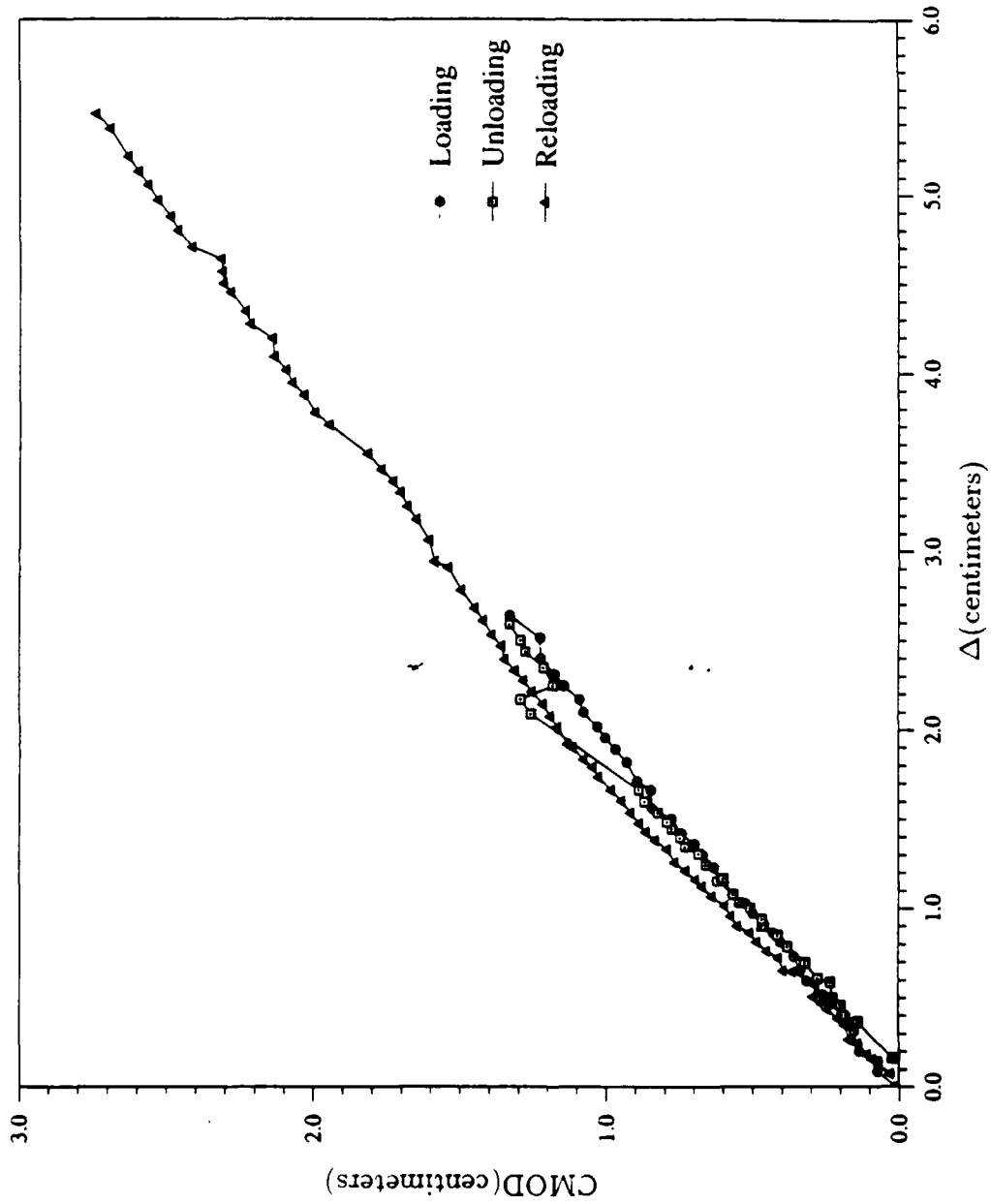
Figure 3.20: CMOD versus Δ for specimen *S-2* showing loading, unloading, and reloading.

a step size sufficient to provide three digit accuracy. The result of this integration, JdA versus Δ, is displayed in Figure 3.22 and, following a least squares fit, the value of JdA at $\Delta = 5.0$ cm was extrapolated as 7.5 Nm, corresponding to $J_f = 400kJ/m^2$ or, equivalently, a tearing energy, T_c of 200 kJ/m². This magnitude of T_c is higher than maximum values of 100 kJ/m² reported for filled natural and SBR rubbers [37,48] and is a consequence of the experimental material and the specimen design.

First, the experimental material is a tough elastomer designed specifically for use in Army tank track pads and contains a large percentage of carbon black. The J-integral was determined for the S- material type, which was more difficult to machine and tougher than the other types, and consequently, it can be expected that its fracture resistance would be high. Second, the specimen geometry is elastically stable and catastrophic failure occurs when an instability is present in a structure. The basic geometry in this specimen is a short thick cylinder, more stable than a long cylinder of the same diameter, i.e., a larger applied load is required to cause an elastic stability. In addition, the specimen geometry, extended under displacement control, may have allowed a larger amount of stable crack growth when compared to conventional specimens, thus increasing the value of T_c.

3.8.8 Diametral Changes

Small changes in the inner diameter, d_e, were observed during deformation, independent of both crack length and material type. Figure 3.23 shows diametral changes, normalized by the undeformed inner diameter, D_{inner}, with increasing Δ. The bulging of the inner cylinder is demonstrated by the small fluctuations, or ripples, as the specimen deforms and d_e decreases, although the magnitude of these ripples is slightly larger in specimen S-3 compared to specimen M-2.

The amount of permanent set along the diameter was determined by measuring the diameter along the original crack surface in the fractured female specimen twenty-four hours after testing. As shown in Table 3.10, the inner diameter did not significantly change before and after experimentation in any of the specimens, including specimen S-2 which had undergone a load deformation cycle. The permanent set for the single notched virgin specimens was approximately 0.01 cm and was smallest in the softened specimen, S-2. The increase in diameter in specimens S-1 and M-1 is unexplained and is attributed to experimental error.
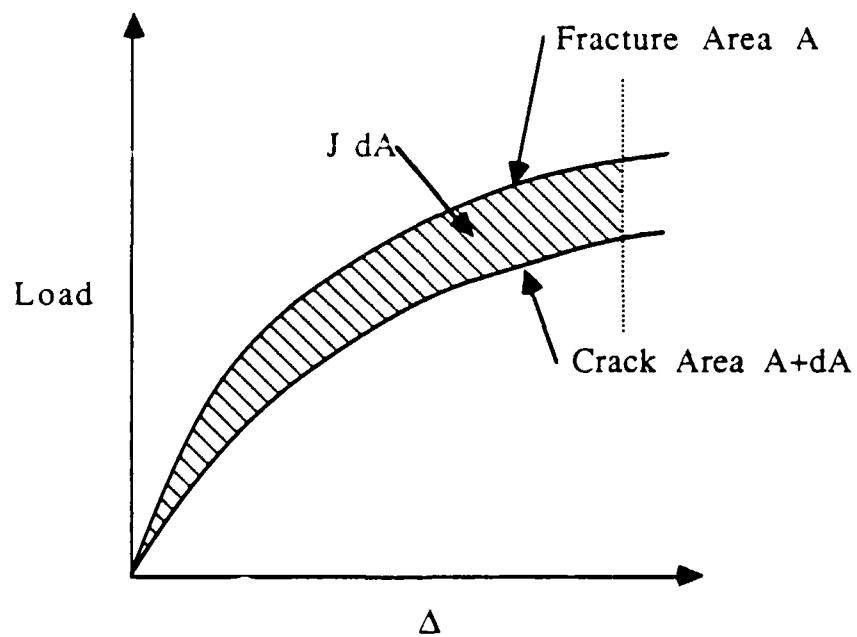
Figure 3.21: Graphical representation of the J-integral.
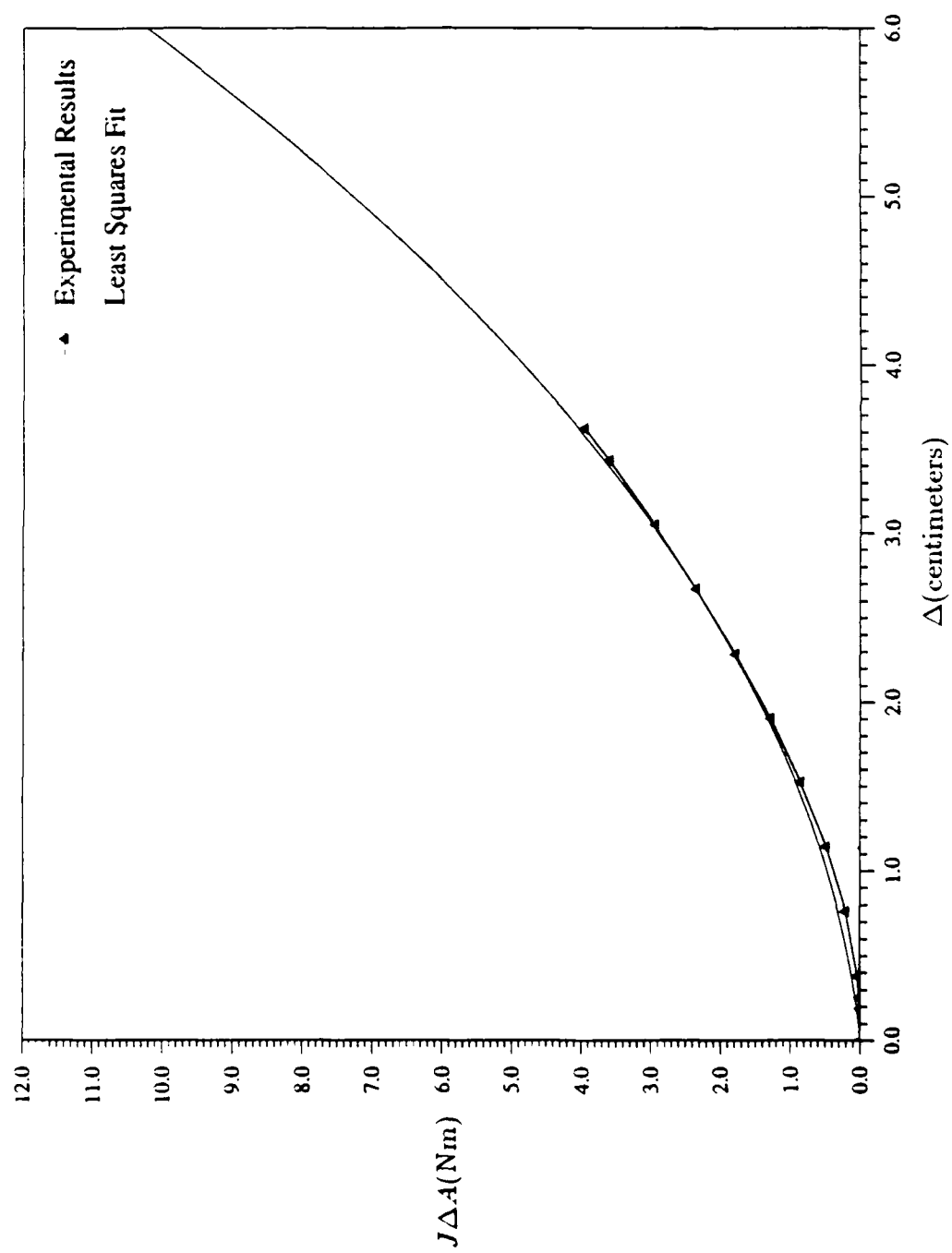
Figure 3.22: $J\Delta A$ versus Δ.

Δ(centimeters)
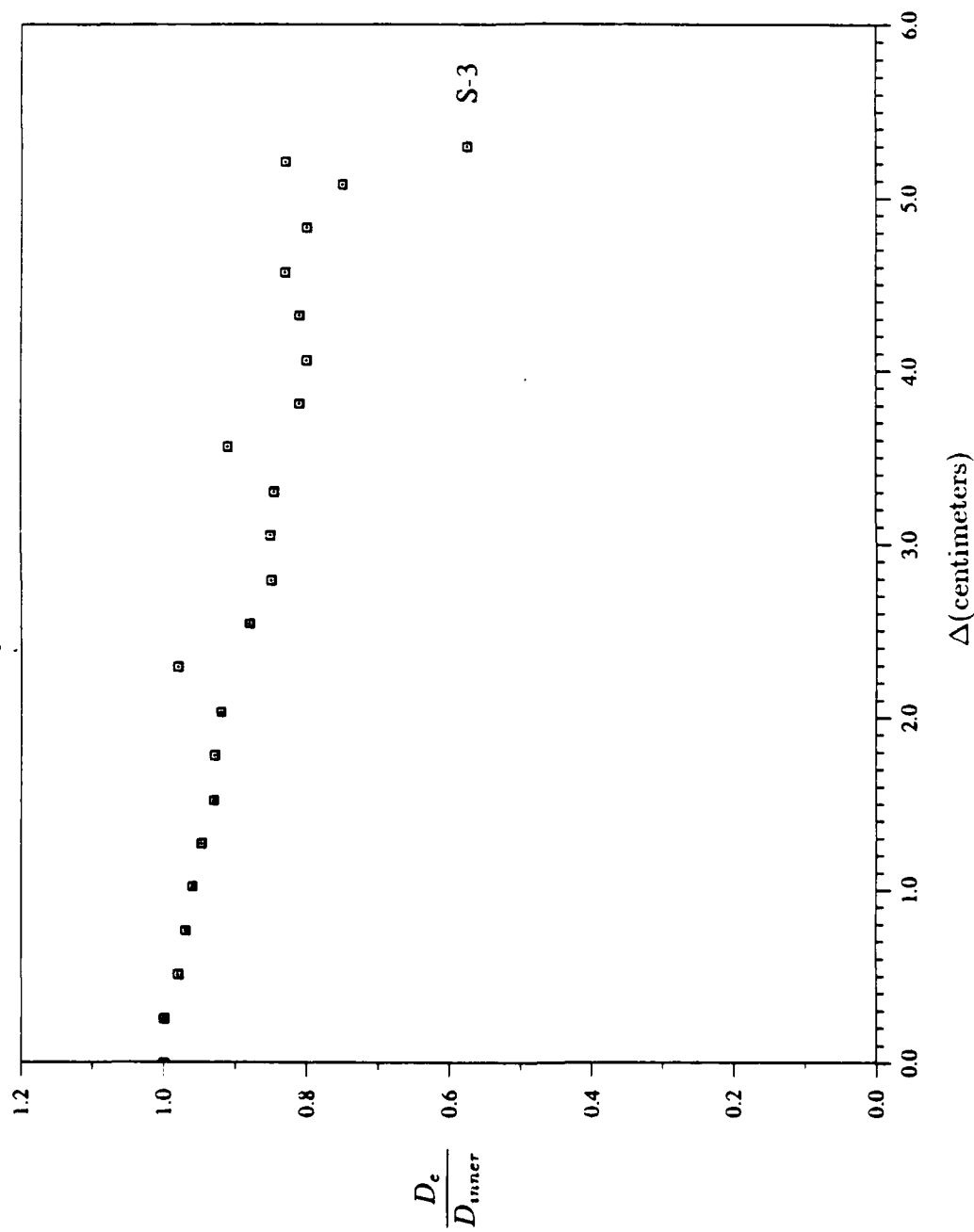
(a) Specimen S-3.

Figure 3.23: Diametral changes for specimens.
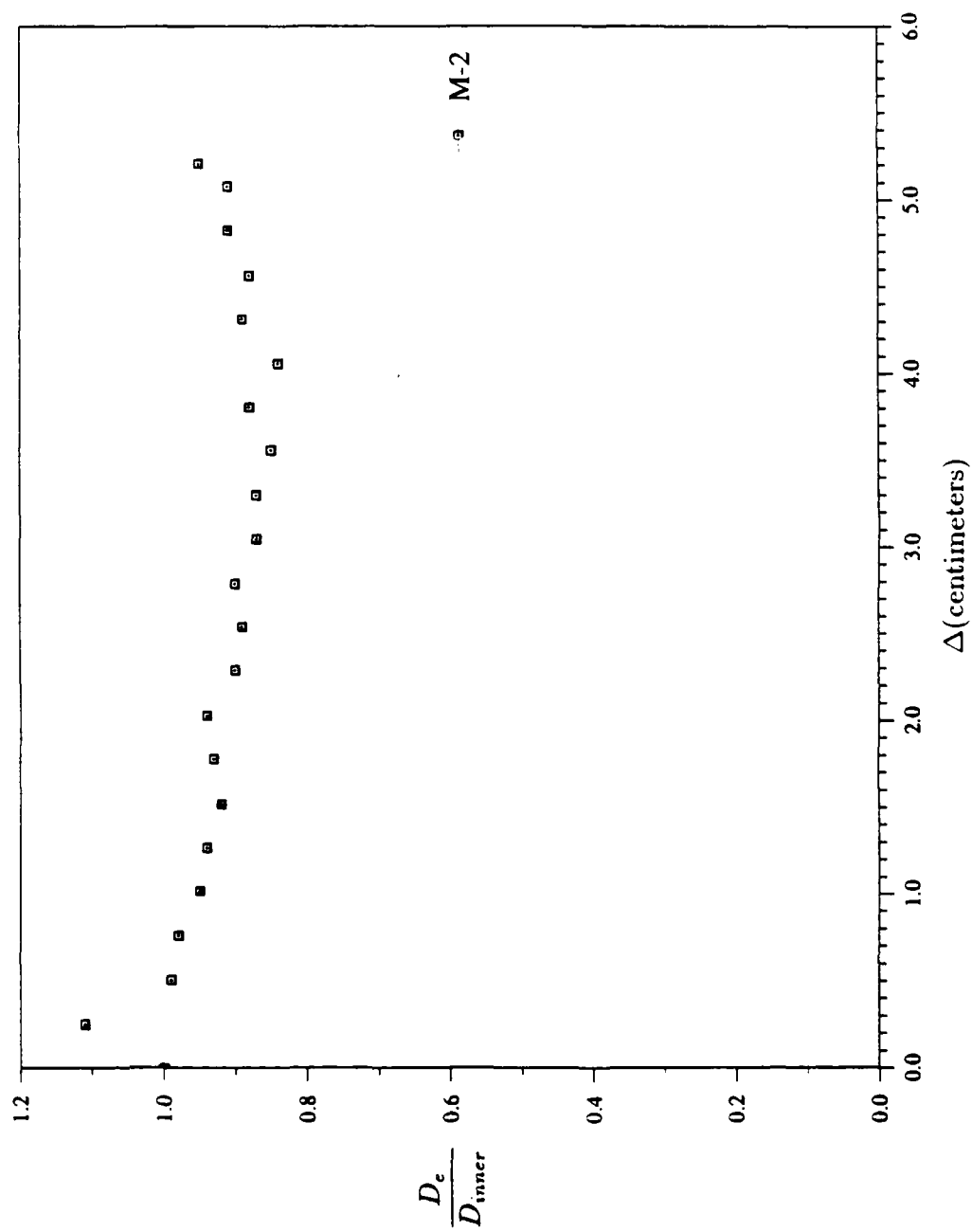
(b) Specimen *M-2*.

Figure 3.23: Diametral changes for specimens.

Specimen	D_{inner} (cm)	d_e (cm)	Permanent Set(cm)
M-1	2.341	2.296	-
M-2	2.360	2.346	0.014
S-1	2.324	2.335	-
S-2	2.327	2.324	0.003
S-3	2.197	2.184	0.013
U-1	2.474	2.466	0.008

Table 3.10: Specimen diametral changes.

3.9 Discussion

Experiments were performed to investigate the Mode I fracture in thick elastomers using a new specimen with a cylindrical dumbbell geometry. This investigation served two purposes: (1) to design a test specimen for examining failure in elastomers under near plane strain conditions and (2) to observe and quantify the failure process. The discussion will be divided into two sections, an evaluation of the specimen performance and design and an interpretation of the experimental results.

3.9.1 Specimen Evaluation

The design of the test specimen was successful in that the tear behavior, delamination and crack extension of thick elastomers could be observed directly, while the specimen was deforming. These observations are invaluable to understanding the process of tearing found in these specimens as it is much more difficult to characterize the fracture process solely on the physical evidence found in the ruptured specimens pieces. Experimental results from the use of this test geometry were consistent in that failure occurred under large deformations and the mode of failure, rupture, was common to all specimens. Quantitative results, discussed elsewhere, were meaningful and consistent with predictions from fracture mechanics.

However, manufacturing test specimens with uniform geometries and low dimensional tolerances proved a formidable task, as difficulties in manufacturing were associated with fabricating the specimens from molded circular cylinders, resulting

in a lack of concentricity between the inner and outer cylinders in the short dumb-bell specimen and a nonuniform inner diameter, D_{inner}. Elastomers are known to require special machining techniques and equipment due to their toughness and thus, it is recommended that, should this specimen geometry be employed again, the specimens should be made by experienced machinists or by molding the specimens directly to improve size tolerances.

Although large tolerances in D_{inner} and L_e were found in these specimens, the tearing process itself was not significantly affected because asymmetric tearing behavior was found in specimen U-1, which had the most uniform D_{inner} across H_{inner} and the difference in L_e along a given diameter was 0.01 cm, the width of the crack.

The only experimental objective that was not met was verifying the reproducibility of the quantitative experimental results through the use of two specimens with equal crack lengths, a consequence of the difficulties encountered in crack manufacture. Fabricating the circumferential crack also required special techniques and skill and could only be successfully made by introducing a small circumferential notch and then gradually increasing the crack length to the desired value. The point at which the blade is introduced into the specimen must be carefully chosen so that the blade is normal to the outer surface along D_{inner} at exactly the mid-height of the specimen. Bending of the dumbbell test specimen, due to the lateral force of the knife, is another source of error. As much as a three percent error was found between the actual and intended crack length and was attributed to fabrication difficulties. Due to this variation, the reproducibility of the experimental data for cracks of equal length could not be checked although load histories and nominal fracture strength were consistent with experimental predictions.

Both sets of grips, those required for specimen fabrication and those used for the experiment, functioned well and satisfied design criteria. The test specimens could be easily mounted in and removed from the grips while the grips did not interfere with machining or experimental testing.

3.9.2 Discussion of Experimental Results

A complex yet distinctive macroscopic tearing process of delamination and crack extension in the load direction was observed in all six specimens, independent of material type and crack length. Failure at large nominal deformations, $\lambda_f \sim 3$, occurred by rupture of the specimens.

Failure of material layers was observed in two localized regions, along an extended inner core of material connecting the top and bottom portions of the test specimen.

and above and beneath the fabricated crack surface, as shown in Figure 3.24. The inner core represented newly created surface area and was accompanied by extensive asymmetric blunting of the crack tip region and crack growth normal to the undeformed crack surface. This process was found even at low deformations as new surface area was visibly exposed at $\Delta = 0.4$ cm, or $\lambda \sim 1.16$. Just prior to failure, the length of the extended inner core was approximately 2.5 cm, indicating the magnitude of the large deformations surrounding the crack tip region and confirming that the size of the nonlinear crack tip zone region extended far beyond the undeformed ligament length. However near plane strain conditions are approximated in the blunted crack tip region.

Consider an undeformed volume element of elastomer material at the crack tip of width, w_o, height, h_o, and length, l_o, as in Figure 3.25(a). Under applied tensile loading, finite blunting of the crack tip occurs, Figure 3.25(b). The volume element has been highly deformed to width, w, height, h, and length, l, while a traction free boundary condition now exists along the blunted crack surface. The principal stretch ratios can be represented as

$$\begin{aligned}
\lambda_1 &= \lambda \sim h/h_o \gg 1 \; , \\
\lambda_2 &\sim w/w_o \ll 1 \; , \\
\lambda_3 &\sim l/l_o \sim 1 \; .
\end{aligned} \qquad (3.3)$$

Noting that $\lambda \gg \lambda_2$, λ_3 and invoking the incompressibility condition, λ_2 can be approximated as

$$\lambda_2 \sim 1/\lambda \; . \qquad (3.4)$$

Thus, the crack tip field in the presence of finite blunting approximates a plane strain condition, denoted by λ_i as $[\lambda, 1/\lambda, 1]$.

This elastomer material is fracture resistant because it has strong crack arrest properties which constrain crack growth along the crack front. The tearing process observed in this material resists fracture by effectively reducing the triaxial stress state found at the crack tip region through delamination, viscoelasticity, and crack growth in the load direction.

Delamination reduces the magnitude of the mechanical crack tip stress field by the generation of new surface area which is free to deform and blunt the initially sharp crack tip, shown schematically in Figure 3.24. Stresses normal to this new surface area, the extended inner core, are zero so that the radial stresses found in the crack tip region have decreased. In addition, the blunting of the crack tip lowers the magnitude of the load amplitude constants associated with the mechanical crack tip stress field, decreasing the amplitude of the singularities found there.

The viscoelastic behavior found in elastomers also enhances fracture resistance by reducing the strength of the mechanical crack tip stress field after stable crack growth has occurred. When the crack extends, the newly created surface undergoes a load deformation cycle and the subsequent material response is softer in the next loading cycle.

Finally, stable crack growth in the load direction enhances further blunting of the crack tip, reinforcing the above mechanisms which decrease the triaxial stress state in the crack tip region. The crack tip is no longer sharp and crack extension normal to the load direction has been minimized.

Although a value of the J-integral was determined at failure, it would be more appropriate to consider a J-resistance curve, which measures the increasing resistance to fracture with stable crack extension and where stable crack growth occurs when $J > J_R$, as shown in Figure 3.26. Here, it is assumed that J_R increases with crack growth or that, with increasing amounts of crack growth, higher stresses and a larger crack driving force, J, are required. Preliminary experimental evidence for this type of behavior may be provided by Figure 3.22, where the product of J and an undeformed area quantity increases with Δ, noting that crack propagation begins at low Δ and then increases with Δ.

A series of material delamination layers were found in the ruptured specimen pieces along the perimeter of the fabricated crack tip. The thickness and the height of the tearing layers increased with distance from the fabricated crack tip. These size effects may be understood through the failure behavior discussed previously. The height of the tearing layers increases because the tear plane, initially found along the mid-height of the deformed specimen, separates into tear planes above and below the mid-height, which move towards the ends of the specimen with increasing elongation, as shown schematically in Figure 3.27(b) and 3.27(c) which are referenced to the undeformed configuration in Figure 3.27(a). A cross-sectional view of the ruptured female piece illustrating these effects is presented in Figure 3.27(d).

The thickness of the failed material layer can be related to the amount of crack growth in the load direction, and the increasing amount of crack growth, δL_1, is a direct consequence of the delamination process. Localized material failure along the inner core initiates around small holes followed by separation of the failed layer of elastomer material from the remaining inner core and retraction towards the fabricated crack surface. Material separation, or material failure in shear, commences at the small holes, the initial failure site, and extends in the load direction, beyond the fabricated crack surface, and stops in a region where stresses are lower due to a larger cross-sectional area and distance from the crack tip, refer to the schematic in Figure 3.28. The amount of crack growth is the thickness at

the base of the failed layer of material, determined by the distance between arrest locations between successive failed material layers. As the specimen elongates. stresses in the deformed inner core are intensified and the size of the nonlinear crack tip zone becomes larger. and therefore, material separation. or delamination. will stop at a location which is increasingly further away from the arrest point of the previous failed material layer, causing the thickness and δL_i to increase. Therefore, the amount of stable crack extension, δL_i, increases with specimen elongation where the total crack extension, δL_{Total}, is

$$\delta L_{Total} = \delta L_1 + \delta L_2 + \cdots + \delta L_i , \quad \delta L_{i+1} > \delta L_i \qquad (3.5)$$

When the total amount of crack extension in the load direction reached a critical value, the specimen ruptured.

Several macroscopic features described in the tearing process are similar to Gent's [42] microscopic observations of fracture surfaces in filled and unfilled rubbers. supporting the experimental results reported here. Gent [42] reported strands of rubber stretching across the fabricated tear tip, representing material surrounding tears which then extend in the load direction. After these strands break, they form matching crosshatched segments on either side of the torn surface. The plane at which tearing initiated did not remain constant, but separated into two planes which displaced by 2 to 10 microns in the load direction. The average distance between strands of rubber was approximately constant, 10 to 100 microns, the size of natural defects in rubber, but the thickness of the torn surface was not measured.

The strands of rubber observed by Gent [42] are similar to those surrounding the small holes at $\Delta < 3.6$ cm and those encompassing the entire outer surface of the deformed inner core at $\Delta > 3.6$ cm in this experiment and, after failure, the relaxed strands form the saw-toothed or crosshatched segments. Gent describes the strands as material surrounding tears which stretch in the load direction, the tear eventually growing to the length of the deformed inner core. After material failure, the torn surfaces of the strands comprise the saw-toothed or crosshatched segments. Crack extension was found in the load direction, above and below the fabricated crack surface, similar to the vertical displacement of the tear planes reported by Gent. Although the size of the saw-toothed segments was not constant. but increased in size with distance from the fabricated crack tip, this difference can be attributed to differences in specimen geometry (thin sheet of rubber [42] versus short cylindrical dumbbell specimen) and load conditions (bending load [42] to attain a specified rate of tearing versus a constant strain rate). Because sectioning of the ruptured test specimens, (required for further microscopic analysis), was not performed. additional comparisons could not be made.

Gent [42] proposed that tearing occurs by the linkage of secondary cracks, shown in

Figure 3.29, followed by extension in the load direction, causing vertical splitting at the fabricated tear tip . This type of tearing was visibly observed in this investigation at large deformations, $\Delta > 3.6$ cm.

Cavitation was not observed directly although it is presumed that the small holes, sites of localized material failure along the deformed inner core, all initiated from cavities or small defects. The experimental results are more consistent with Gent's model of the tearing process, the joining of secondary cracks across the fabricated crack front and do not confirm the failure model of Fukahori and Andrews [49], referring to Figure 3.30, where the fabricated crack overtakes and joins a secondary crack front located ahead of it because the elastomer strands connect material above and below the fabricated crack surface. Physical evidence confirms that material separation occurs between the deformed inner core and the material surrounding it.

The tearing model, Figure 3.31, proposed on the basis of this experiment is the initiation of material failure between the fabricated crack surfaces around small holes, followed by material separation of the failed material layer from the deformed inner core. Delamination occurs in the load direction and is arrested when regions of lower stress, above and beneath the fabricated crack surface, are encountered. The depth of the arrest point into this low stress region determines the thickness of the failed material layer and the amount of crack growth in the load direction. The benefits of this tear behavior is that blunting of the crack tip reduces the stress state at the crack tip, preventing crack extension along the plane of the undeformed crack front. Crack extension in the load direction enhances continued crack tip blunting while the stress softening of new surface area associated with crack extension further minimizes triaxial stresses. Specimen failure occurs when crack growth causes rupture. This model also explains the asymmetry of the failure process as the defects or microvoids which initiate tearing are not homogeneous throughout the specimen.

Key features of the failure process observed here have also been reported in the failure of thin elastomer sheets, i.e., asymmetric blunting of the crack tip, subcritical crack growth, and crack extension in the load direction [9,50,48]. At low deformation rates and room temperatures, associated with smooth tear behavior, crack extension has been reported to deviate slightly from the plane of the crack towards the load direction in deeply notched thin elastomer sheets. However, the extent of deviation observed in this investigation is more representative of deeply notched thin elastomer sheets tested at high temperatures, where knotty tear behavior can be found. In addition, the magnitude of the tearing energy and nominal fracture strength are high when compared to similar elastomer compounds [50,48]. In this investigation, tearing was found with a continuously increasingly load until just prior to failure, accompanied by crack extension in the load direction. Torn

layers of material, successively increasing in size with distance from the fabricated crack tip, were found but the ruptured fracture surface was smooth.

Based on the single set of experimental tests performed here, *thickness* appears to enhance fracture resistance in deeply notched specimens. The precise cause of this increased fracture resistance remains unknown, but the stability of the specimen geometry probably plays an important role in the fracture process. The specimen geometry, as well as the geometry of the testing system, could influence the viscoelastic and fracture properties of this material so that fracture resisting mechanisms are enhanced.

The tearing process of elastomers under large deformations is quite complex and includes stable crack growth in the load direction. A finite element analysis of the observed fracture behavior was not performed. The finite element model would have to be carefully designed to allow for crack extension in the load direction. In addition, a specific criterion for crack extension, (i.e., at what values of the J-integral does stable crack extension occur ?) would have to be adopted. However, the numerical analysis would provide much useful information such as the characterization of the crack tip field and its region of dominance. Sites of tear initiation may also be identified through the stress field. Finally, the analysis would quantify the reduction in the intensity of the crack tip field due to blunting, delamination, and crack extension.
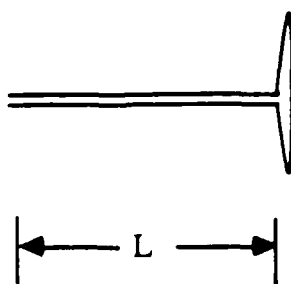
(a) Referenced to the undeformed configuration.
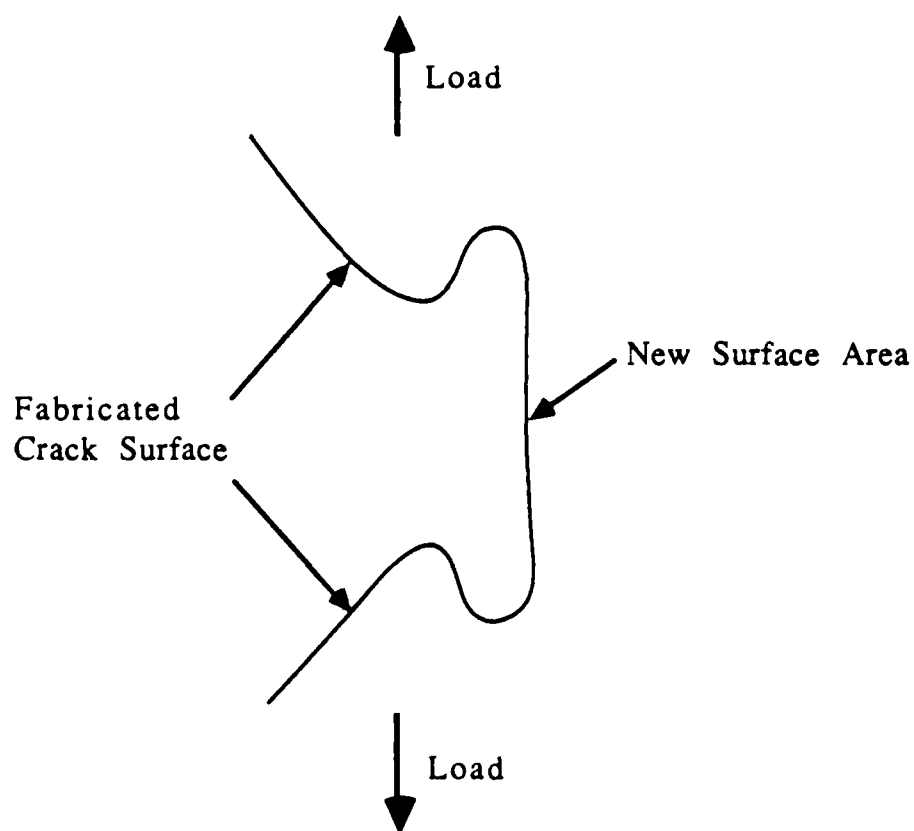
(b) Referenced to the deformed configuration.

Figure 3.24: Delamination of the fabricated crack tip.
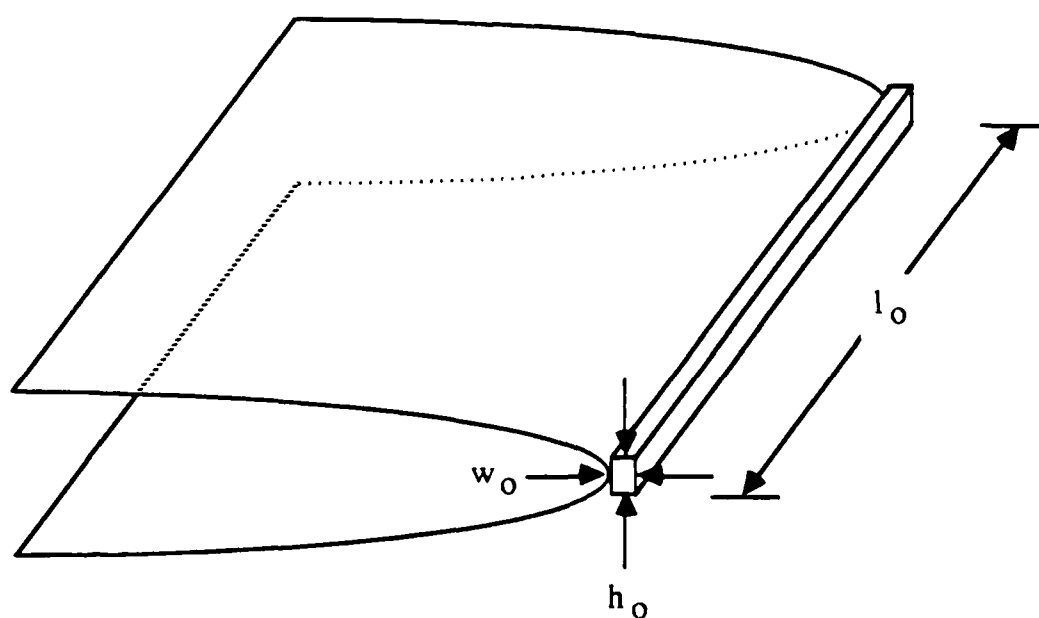
(a) In the undeformed configuration.

Figure 3.25: A volume element of elastomer material at the crack tip.
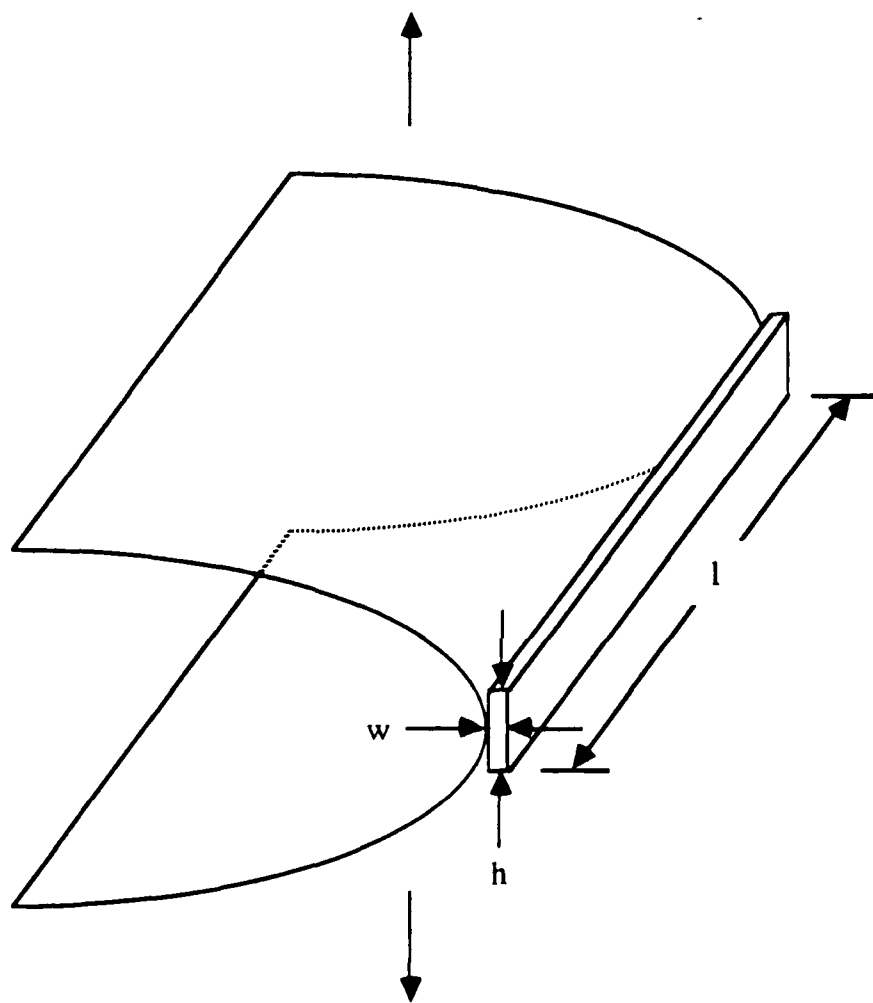
(b) After blunting of the crack tip.

Figure 3.25: A volume element of elastomer material at the crack tip.
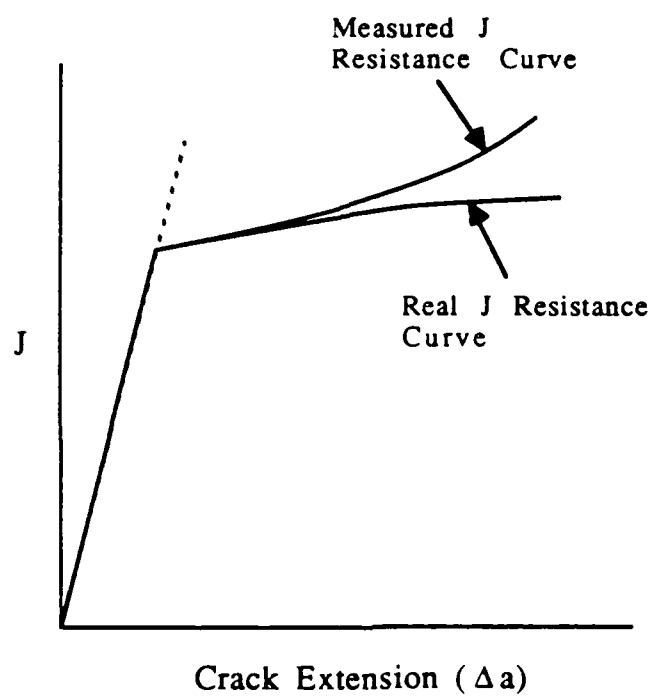
Figure 3.26: An example J_R curve.
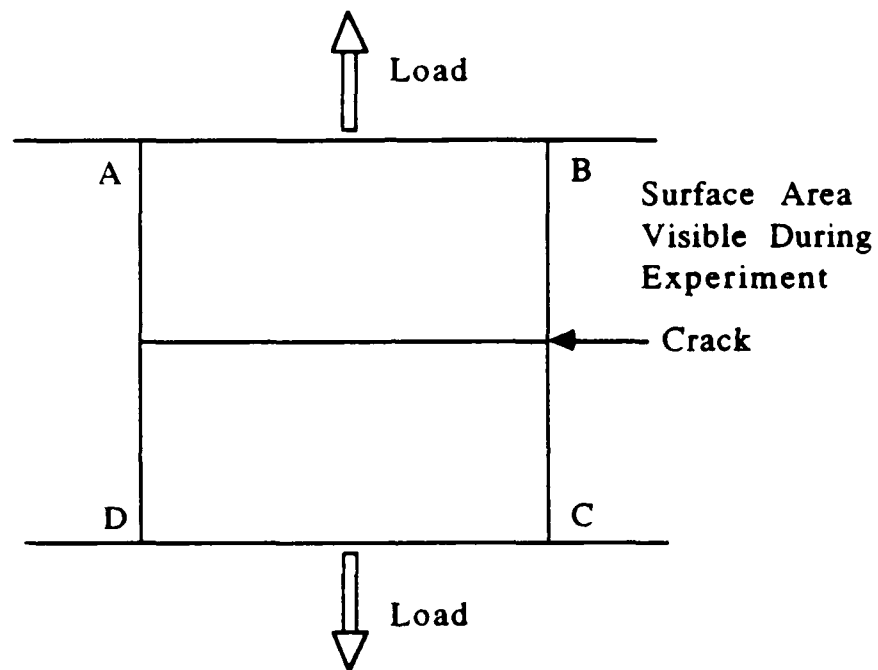
(a) Referenced to the undeformed configuration.

Figure 3.27: Increasing height of the torn material layers with specimen elongation.
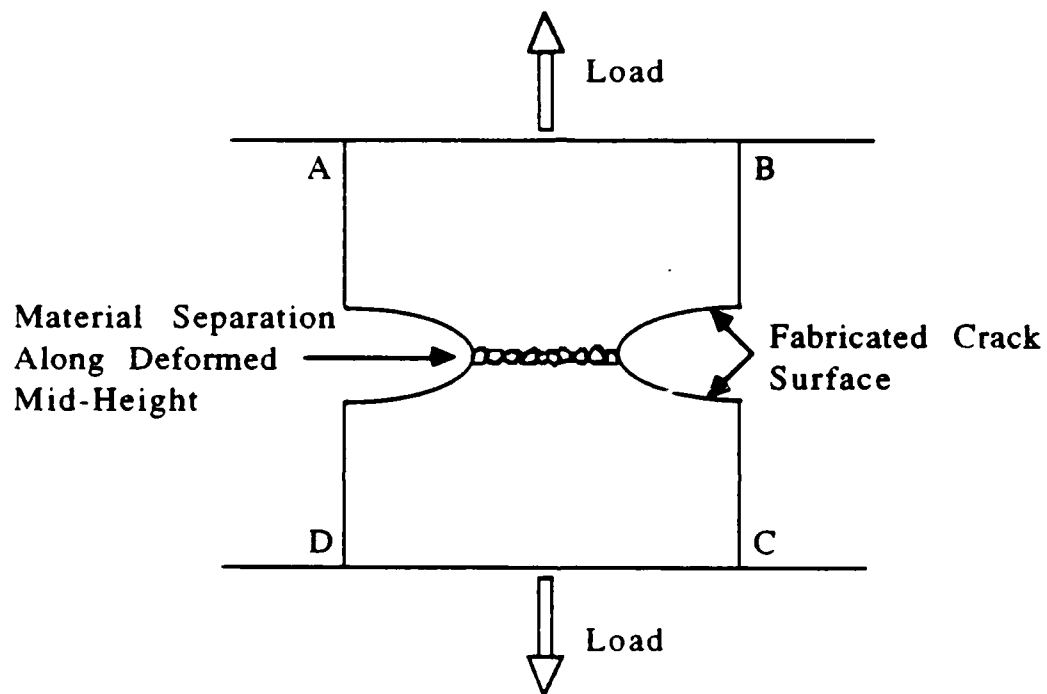
(b) At low Δ.

Figure 3.27: Increasing height of the torn material layers with specimen elongation.

(c) At high Δ.

Figure 3.27: Increasing height of the torn material layers with specimen elongation.

Delaminated Material
Layer at Low Δ

Delaminated Material
Layer at High Δ
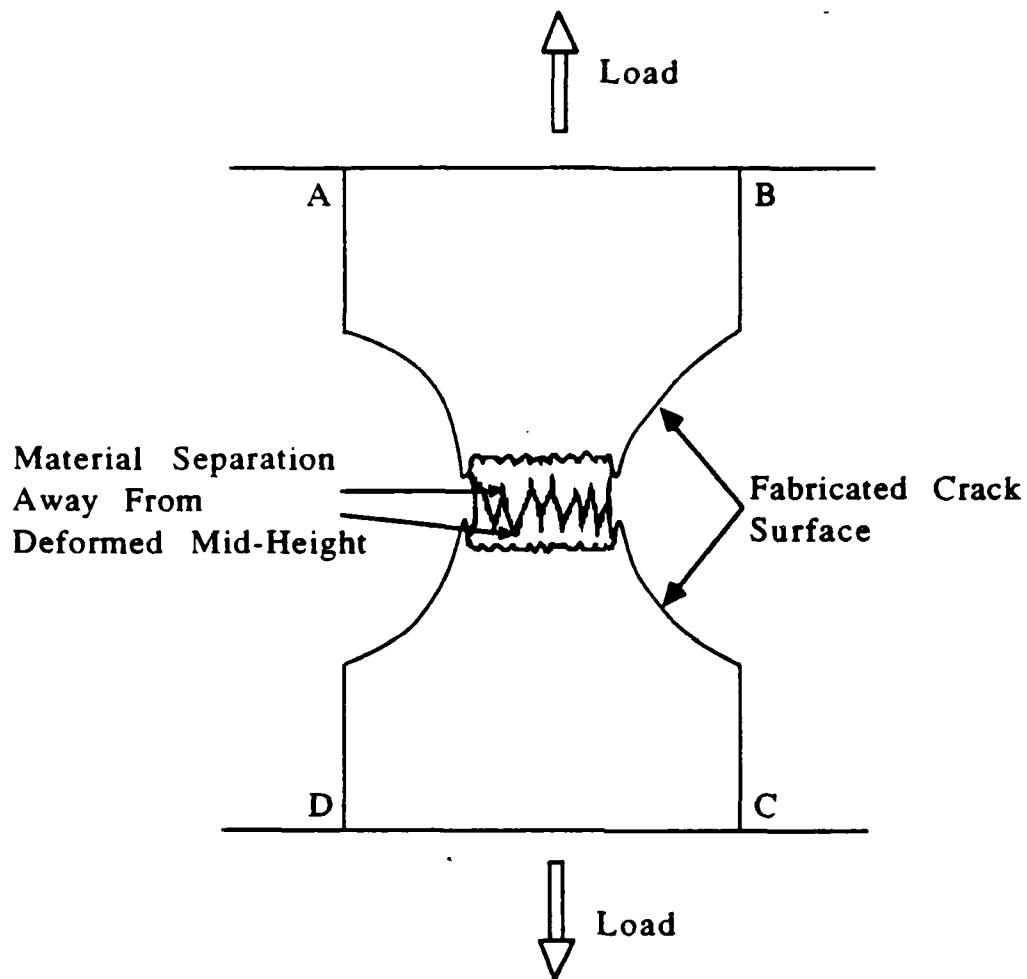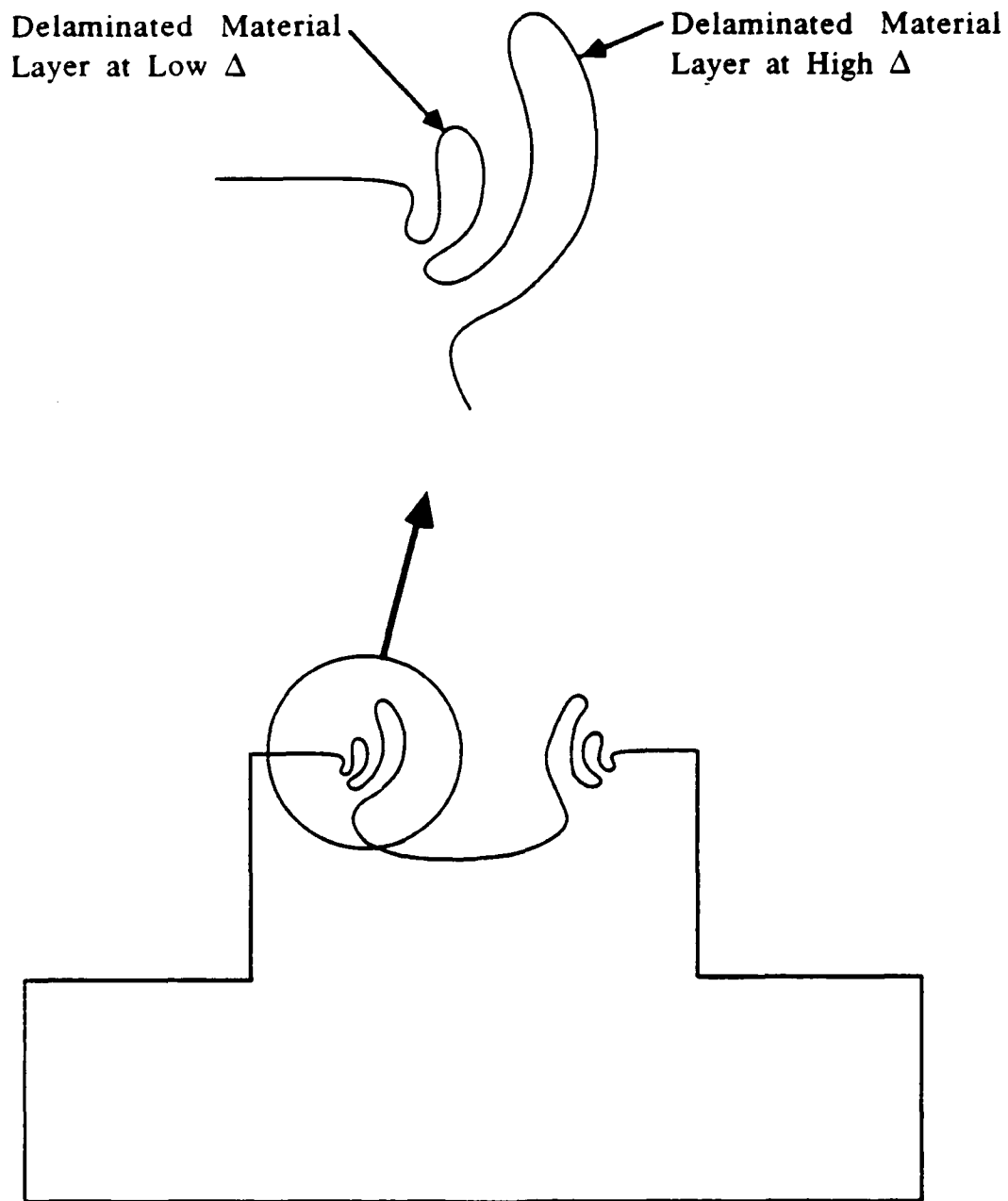
(d) A cross-sectional view of the ruptured female piece.

Figure 3.27: Increasing height of the torn material layers with specimen elongation.
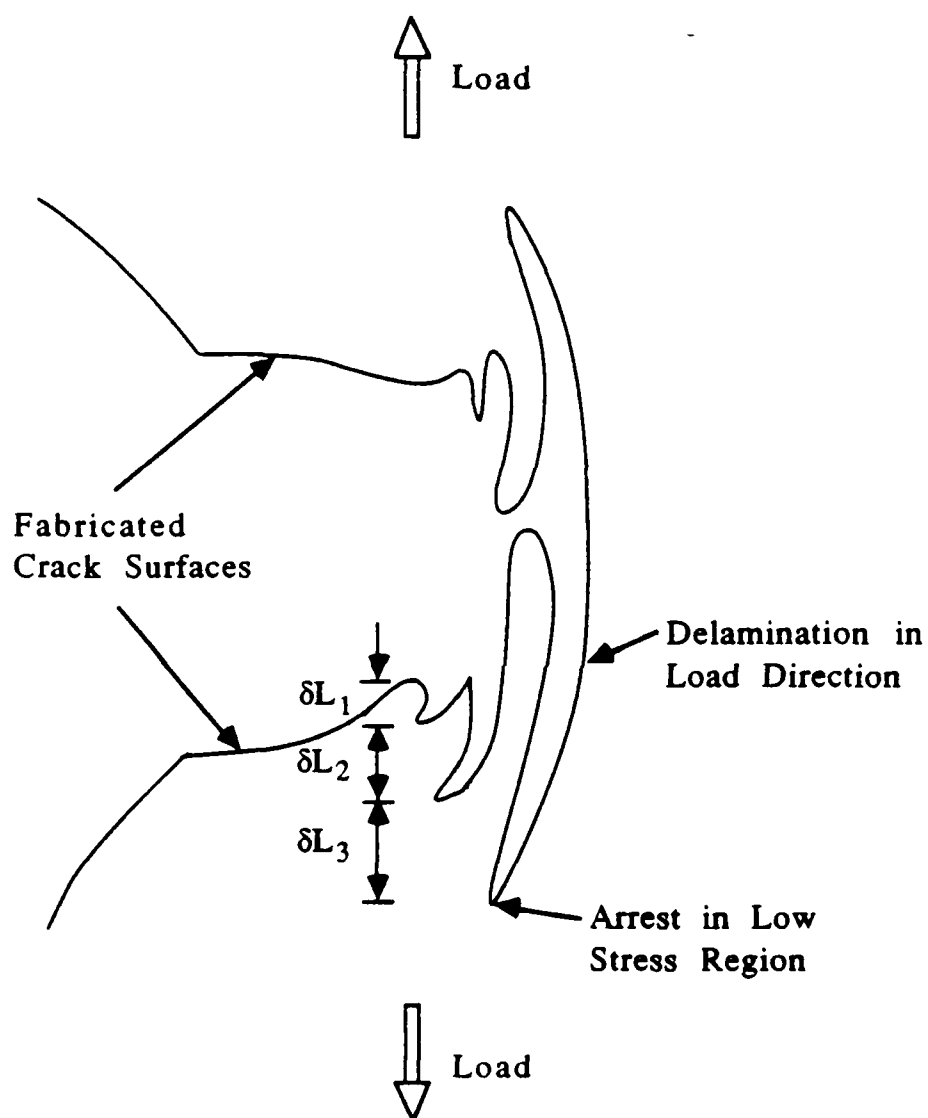
Figure 3.28: Increasing δL, with specimen elongation.
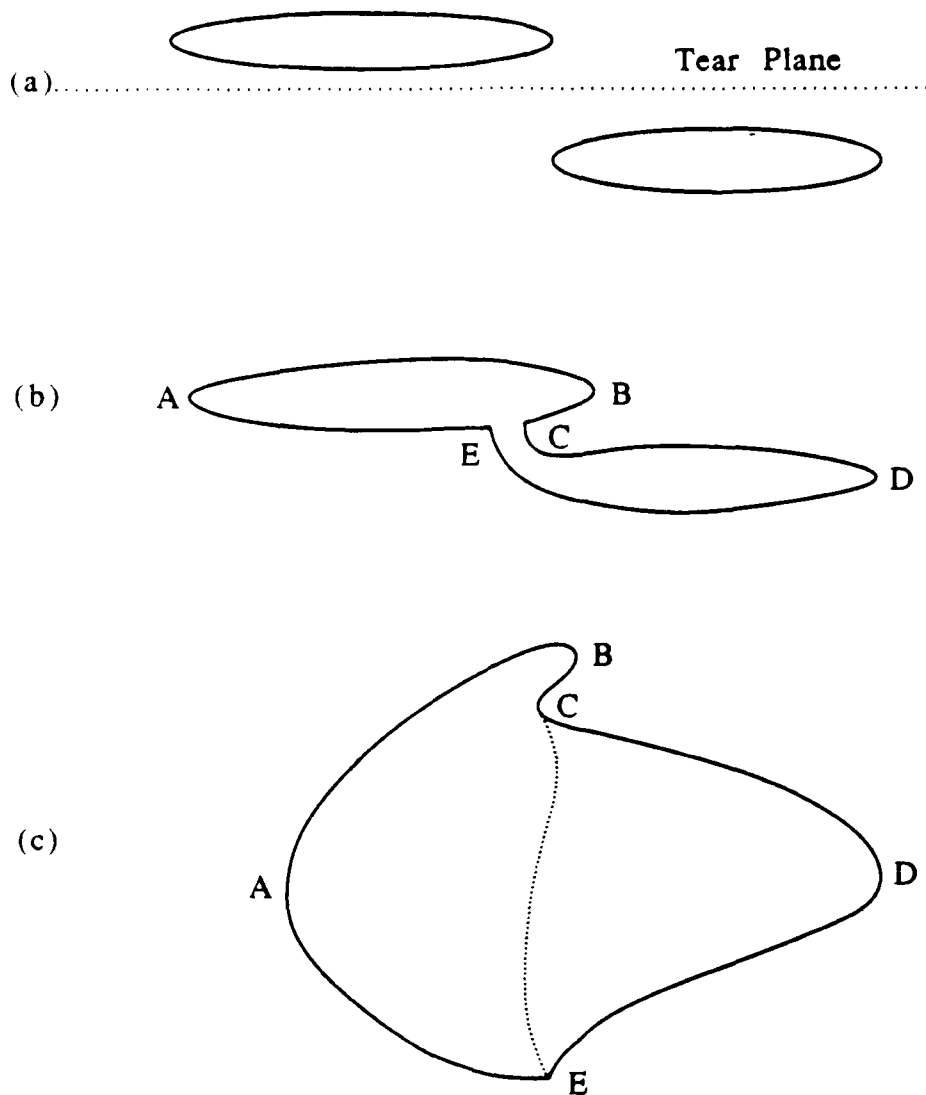
Proposed mechanism of step formation.
(a) Formation of secondary cracks at tear tip,
(b) joining of secondary cracks,
(c) sketch of joined cracks in the stretched state.

Figure 3.29: Micromechanical model of tearing by Gent. From Gent, A. N. and Pulford, C. T. R., Micromechanics of fracture in elastomers. *J. Mat. Sci.* **19** (1984) 3612.
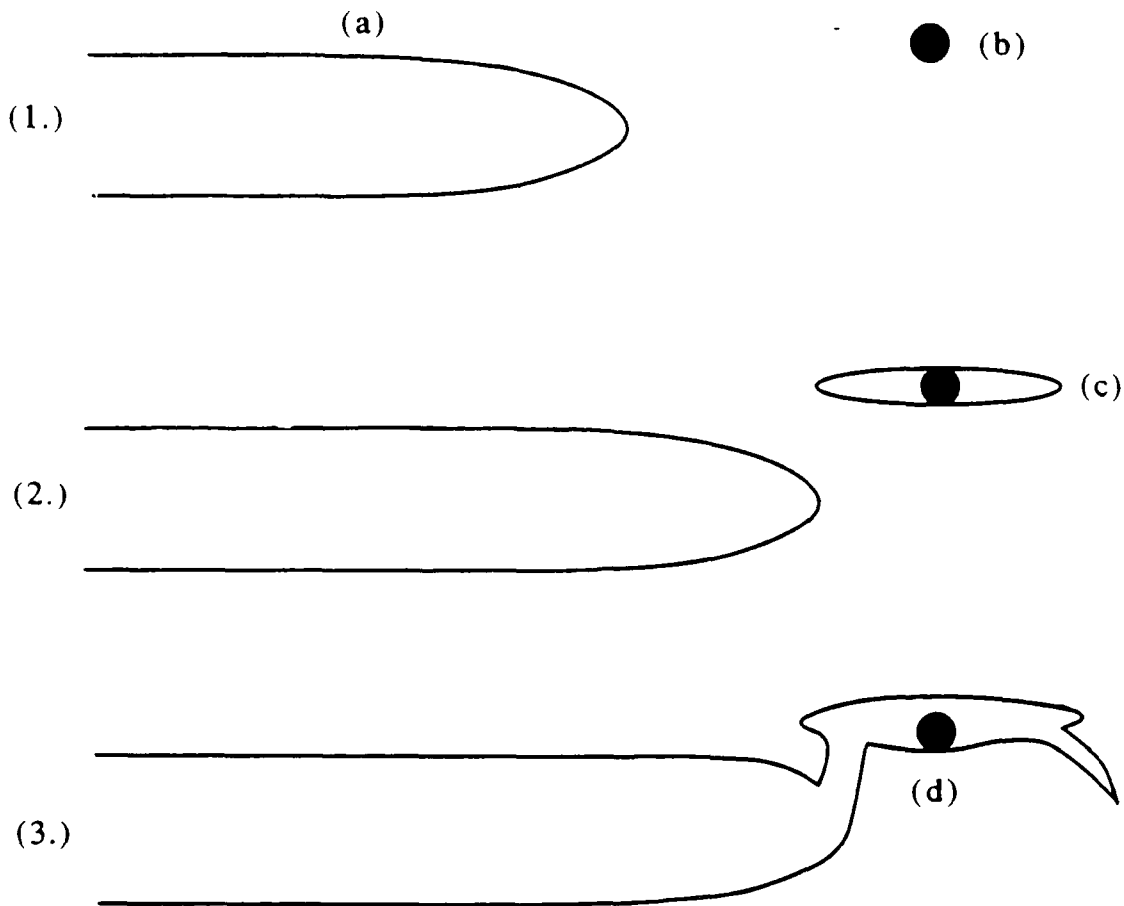
Formation of roughness by secondary fracture (schematic);
(a) crack, (b) stress-raiser, (c) secondary crack,
(d) roughness step caused by diversion of primary crack.

Figure 3.30: Micromechanical model of tearing by Fukahori and Andrews. From Fukahori. Y. and Andrews, E. H., Fracture surface roughness in highly deformable polymers. *J. Mat. Sci.* **13** (1978) 777.
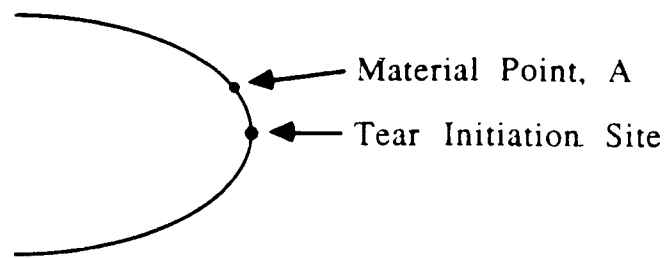
(a) Tear Initiation.
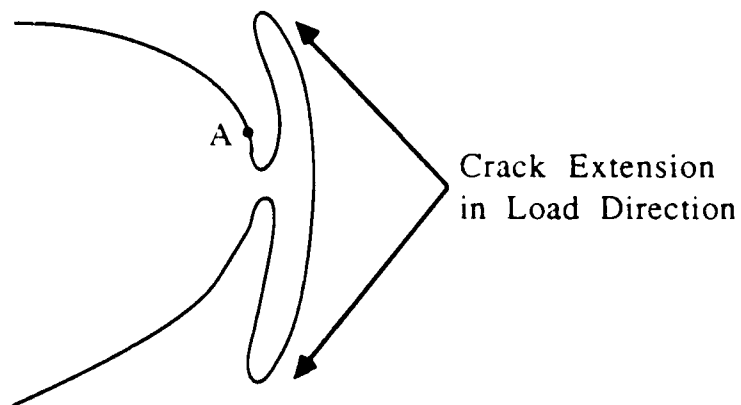
(b) Delamination and Crack Extension.
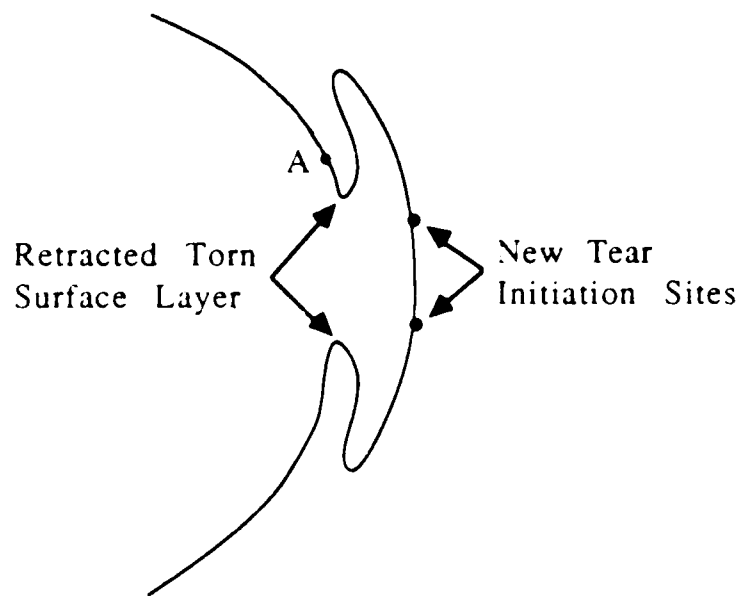
(c) Crack Tip Blunting and Continued Tearing.

Figure 3.31: Proposed tearing model.

Chapter 4

Conclusions

A thickness effect is present in the failure of elastomers in Mode I fracture and was found in both the computational and experimental studies. The computational analysis of a plane strain crack showed that the nonlinear crack tip field differs from that found under plane stress conditions. Experiments on carbon black filled elastomers demonstrated that the failure process is characterized by extensive blunting of the crack tip, successive delamination of material layers in the crack tip region and crack extension in the load direction.

4.1 Computational

A finite element analysis of a plane strain Mode I crack in an incompressible material was performed under the assumptions of small scale nonlinearity. The finite element mesh was coarse in the immediate vicinity of the crack tip, of radius $10^{-6}L$, but was then further refined to verify the nonlinear elastic asymptotic solution [5] at larger radii and to determine its region of dominance. The effect of the constitutive model on the asymptotic solution was examined by using two invariants of the Rivlin material model, the Mooney-Rivlin law ($n = 1$) and the third order invariant ($n = 3$). Finally, a local cavitation criteria [22] was used to predict failure and was applied to find a critical length scale defined by the microstructure of the material, i.e., the mean particle spacing between carbon black aggregates.

The highly localized nonlinear elastic crack tip field, of radius $10^{-4}L$ around the crack tip, is characterized by large deformations and rotations and is surrounded by a region of small deformations and large rotations. The conditions of small

scale nonlinearity were satisfied at all load levels while the J-integral was path independent throughout the refined mesh region, for all $r > 10^{-6}L$ for both constitutive models.

The nonlinear mechanical crack tip field confirmed the presence of the nonlinear elastic asymptotic solution. The τ_{22} stress component, containing the dominant singularity, $o(r^{-1})$, showed the closest agreement with the nonlinear asymptotic field and was much larger than τ_{12}, $o(r^{-1/2})$, and τ_{11}, $o(1)$. As r increased, the stress field gradually transitioned to the linear elastic asymptotic field. The deformation field exhibited similar behavior. The nonlinear elastic asymptotic deformation field was present at small r, but as r increased, the deformation field slowly changed to the linear asymptotic solution. The crack surface ($\theta = 180$) was parabolic with a tip radius of curvature equivalent to that of the linear elastic solution. Because the nonlinear region was small, the load amplitude constants, b and d, associated with nondominant terms in the nonlinear elastic solution could not be determined with accuracy, but were of $o(1)$. Further mesh refinement in the nonlinear zone could assist in finding the magnitude of these constants.

The effect of the order of the invariant of the constitutive model on the asymptotic solution was seen primarily in the size and shape of the zones defined by material and kinematic nonlinearities. When the mechanical crack tip field for ($n = 1$) is compared to that of ($n = 3$), the region containing material nonlinearities is approximately the same size but is more elliptic in shape, in contrast to the region of kinematic nonlinearities, which has the same shape but is larger in magnitude. For both analyses, ($n = 1$) and ($n = 3$), nonlinear material behavior completely surrounds the crack tip while large rotations are not found in front of the crack tip but are located above and behind it.

The additional finite element kinematic constraint, Figure 2.20, applied for ($n = 3$) influenced the nonlinear elastic stress field by replacing the square root singularity for λ as $r \to 0$, predicted by the nonlinear asymptotic solution, with a weaker singularity. Subsequently the magnitude of the stress field was reduced. Also, oscillatory behavior was found in the τ_{11} stress component and τ_{12} reverted back to the linear elastic solution at small r in the refined mesh region only for ($n = 3$) and these results may be related to the weaker singularity at the crack tip

The findings of this computational analysis show that, in the problem defined, the nonlinear region is highly localized compared to the crack length and that the local cavitation criterion is satisfied in the transition region between the nonlinear and linear elastic asymptotic fields. Because failure is known to initiate at small loads, the linear elastic fracture mechanics approach can be useful in examining failure under plane strain conditions in elastomers, assuming small scale nonlinearity or that the effects of finite strain are negligible. At the onset of crack propagation,

a critical cavitation event was predicted at 0.006 mm ahead of the crack tip, consistent with the amount of experimentally reported subcritical crack growth which has already occurred. However, the physical significance of this result requires further study due to the material delamination, molecular alignment, and shear failure which can be found in the nonlinear crack tip region. Finally, this computational investigation was performed under small scale nonlinearity, where only small geometry changes and linear material behavior are found far from the crack tip. The effect on the mechanical crack tip field due to finite strain loading was not determined.

4.2 Experimental

The experimental investigation demonstrates that a thickness effect exists in the failure of filled elastomers as the fracture resistance is enhanced by specimen thickness. Although only a single set of tests were performed, similarities to the fracture process in thin elastomer sheets were observed, while fracture strengths and the catastrophic tearing energy were greater than that reported for SEN specimens of similar elastomer compounds. The deeply notched test specimens, having a short cylindrical dumbbell geometry, were newly designed and functioned well as both quantitative data and a visual description of failure could be directly and easily obtained.

Ultimate failure of the test specimens under load occurred by rupture under finite strains, $\lambda_f \sim 3$, but was preceded by asymmetric blunting of the crack tip, delamination and small amounts of stable crack growth in the load direction. Localized sites of material failure were found at two different places in the test specimen, between the fabricated crack surfaces, and above and beneath the fabricated crack surfaces. Between the fabricated crack surfaces, tearing of elastomer material around ellipsoidal holes was observed, where the torn surfaces resembled saw-toothed or crosshatched segments. Associated with tearing was the delamination of a surface layer in front of the blunted crack tip region. Delamination of the failed material layer continued in the load direction, stopping at sites above or below the fabricated crack surface. Consequently, material failure was also found above and below the fabricated crack surface, leading to crack extension in the load direction. This failure process, tearing,delamination, and crack extension in the load direction, continued until the specimen ruptured. Rupture was initialized at a site above or below the fabricated crack surface, causing the specimen to break into two pieces, a male and a female.

The failure process was observed even at small deformations and continued with increased loading until rupture. However, as the specimen elongated, physical

characteristics associated with tearing, delamination, and crack extension inten-
sified, described below. At low deformations, the torn surfaces were blunted and
the delaminated material layer was thin, while the incremental amount of crack
extension in the load direction was small. In contrast, at large deformations, the
torn surfaces became more jagged while the thickness of the delaminated mate-
rial layer and the incremental amount of crack extension in the load direction
increased.

Each characteristic of the failure process prior to rupture, i.e., blunting of the
crack tip, delamination, and crack extension in the load direction, reduces the
intensity of the stress field in the region of localized material failure, lowering the
energy available for crack propagation. Viscoelastic effects, or stress softening of
newly created surface area which has undergone a load deformation cycle, also
contributes to lowering the triaxial stress field.

Two parameters, material type and fabricated notch length, were varied in this
experiment. Within batch variations observed during specimen manufacture led to
the separation of the specimens into two groups, those easy (M-) and those difficult
to machine (S-). A third material type (U-) was introduced by a prototype used
to test specimen fabrication techniques. Notch lengths varied from 0.518 cm to
0.658 cm. While the same failure process, described previously, was observed
in all specimens independent of crack length or material type, the experimental
data demonstrated the influence of the material type and the notch length. Load
and CMOD histories, essentially linear for all specimens, were more stiff for the
M- specimens and the single U- specimen. However, within a material type,
load histories were softer with increasing crack length, consistent with fracture
mechanics theory. The effect of the crack length on the CMOD history over the
range of crack lengths tested was less apparent. The load and CMOD histories were
smooth and could not be correlated with the ongoing tearing and delamination
behavior observed during the experiment. However, rupture of the specimens was
preceded by a sudden decrease in the slope of the $P - \Delta$ curve.

The value of the J-integral at rupture, determined for the S-specimens, was higher
than previously reported values for filled elastomers in conventional test specimens
and was attributed to the stability of the cylindrical dumbbell geometry and the
toughness of the material. Finally, the applicability of a J resistance curve was
considered, given the stable crack growth found experimentally.

4.3 Recommendations for Future Work

As this experimental investigation represents a preliminary study of failure in thick filled elastomers, involving a new specimen design, much additional work remains to be accomplished. To complete the research started here, the ruptured specimen pieces should be sectioned to measure the amount of crack growth in the load direction for each delaminated material layer. The tearing energy should be experimentally determined in a conventional test specimen for this material to confirm differences in the failure process, such as the amount of subcritical crack growth, which are thickness dependent.

Should this experiment be repeated, it is recommended that the test specimens be molded to obtain a more uniform geometry. However, variations in material properties may still be present as a result of curing inhomogenities in thick elastomers. Consequently, a sensitivity study should be performed to determine the tolerances on notch length and reproducibility of the experimental data, i.e., the maximum tolerance in notch length which does not produce significant differences in load and CMOD histories. Finally, improved techniques for introducing the notch and minimizing the difference between the intended notch length and the actual notch length, which can only be determined after failure, should be developed.

The effect of strain rate, temperature, carbon black concentration, fatigue loading, and the use of stress softened materials on the experimental results should also be investigated. It is possible that experimental load histories in softer, unfilled elastomers may show some load fluctuations during the failure process, similar to load fluctuations found at the onset of cavitation in cylinders [3]. Finally, an experimental procedure should be devised to determine a J-resistance curve, requiring measured amounts of crack growth with increasing load.

A finite element analysis should be conducted to model this failure process and determine the stress fields in the highly localized regions of failure and the radius of the nonlinear crack tip field. Although incompressibility may be initially assumed, viscoelastic effects should be noted to determine the importance of stress softening in decreasing the strength of the stress fields. A computational analysis would also quantify the reduction in the triaxial stress field due to delamination and crack extension and may also be used to predict the site below the fabricated crack surface where delamination of a torn surface layer is arrested.

Furthermore, this computational analysis would demonstrate the effect of finite strain loading on the nonlinear asymptotic field [5] in plane strain and determine the magnitude of the load amplitude parameters, including their relationship to the applied load. The J-integral should be evaluated as a measure of the tearing

energy, which can then be compared to experimental results, and to confirm its path independence. The application of Ball's local cavitation criteria would also show if cavitation would still occur in the transition region, as in small scale nonlinearity, or further away from the crack tip. Finally, the Rice-Johnson failure model [30] could be used to find the relationship between experimentally measured failure quantities and microstructural material properties.

Bibliography

[1] Broek, D., Elementary engineering fracture mechanics. *Martinus, Nijhoff Pub.*, Boston, (1986).

[2] Kinloch, A. J. and Young, R. J., Fracture behavior of polymers. *Elsevier Applied Science Pub.* New York (1983).

[3] Gent, A. N. and Lindley, P. B., Internal rupture of bonded rubber cylinders in tension. *Proc. Roy. Soc.* **A249** (1958) 195.

[4] Cho, K., Gent, A. N. and Lam, P. S., Internal fracture in an elastomer containing a rigid inclusion. *J. Mat. Sci.* **22** (1987) 2899.

[5] Knowles, J. K., Finite elastostatic fields with unbounded deformation gradients. In: *Finite Elasticity*, Applied Mechanics Division, ASME, **27** (1977) 23.

[6] Stephenson, R., The equilibrium field near the tip of a crack for finite plane strain of incompressible elastic materials. *J. Elasticity* **12** (1982) 65.

[7] Wang, N. M. and Oh, H., Finite element analysis of crack problems in highly elastic materials. *Fracture* 1977, Vol. **3**, ICF4, Waterloo, Canada, (1977) 467.

[8] Gent, A. N., Fracture of elastomers. in *Fracture: An Advanced Treatise* (Edited by H. Liebowitz), Vol 7, Academic Press New York (1972) 315.

[9] Eirich, F. R. and Smith, T. L., Molecular mechanical aspects of the isothermal rupture of elastomers. in *Fracture: An Advanced Treatise* (Edited by H. Liebowitz), Vol 7, Academic Press New York (1972) 351.

[10] Halpin, J. C., Molecular view of fracture in amorphous materials. *Rubber Chem. & Tech.* **38** (1965) 1007.

[11] Kausch, H., Polymer fracture. *Springer-Verlag*, New York, (1987).

[12] Grosch, K., Harwwod, J. and Payne, A., Breaking energy of rubbers. *Nature* **212** (1966) 497.

[13] Rivlin, R. S. and Thomas, A. G., I. Characteristic energy for tearing. *J. Polymer Sci.*. **10** (1953) 291.

[14] Greensmith, H. W. and Thomas, A. G., Rupture of rubber. III. Determination of tear properties. *J. Polymer Sci.* **18** (1955) 189.

[15] Greensmith, H. W., Rupture of rubber. VII. Comparison of tear and tensile rupture measurement. *J. App. Poly. Sci.* **3** (1960) 183.

[16] Ahagon, A. et. al., Fracture energy of elastomers in Mode I (cleavage) and Mode III(lateral shear). *Rub. Chem. Tech.* **48** (1976) 896.

[17] Rice, J. R., Mathematical analysis in the mechanics of fracture, in *Fracture: An Advanced Treatise* (Edited by H. Liebowitz), Vol 2, Academic Press New York (1968) 191.

[18] Chang, S., A path-independent integral for rupture of perfectly elastic materials. *ZAMP* **23** (1972) 149.

[19] Thomas, A. G., II. The strain concentration at an incision. *J. Polymer Sci.* **18** (1955) 177.

[20] Gent, A., Lindley, P. and Thomas, A., Cut growth and fatigue of rubbers. I. The relationship between cutgrowth and fatigue. *J. App. Poly. Sci.*. **8** (1964) 455.

[21] Andrews, E. H., Crack propagation in a strain-crystallizing elastomer, *J. App. Phys.* **32** (1963) 542.

[22] Ball, J. M., Discontinuous equilibrium solutions and cavitation in nonlinearity elasticity, *Phil. Trans. Roy. Soc.* **A306** (1982) 189.

[23] Oberth, A. E. and Bruenner, R. S., Tear phenomena around solid inclusions in castable elastomers. *Trans. Soc. Rheo.* **9** (1965) 165.

[24] Stringfellow, R. and Abeyaratne, R., Cavitation in an elastomer: comparison of theory with experiment. *Mat. Sci. Eng.* **A112** (1989) 127.

[25] Singh, S., Deformation behavior and thermomechanical failure of carbonblack-filled elastomers. Ph.D. Thesis, M.I.T. (1987).

[26] Gent, A. N., Detachment of an elastic matrix from a rigid spherical inclusion. *J. Mat. Sci.* **15** (1980) 2884.

[27] Gent, A. N. and Park, B., Failure processes in elastomers at or near a rigid spherical inclusion. *J. Mat. Sci.* (1984) 1947.

[28] Cho, K. and Gent, A. N., Cavitation in model elastomer composites. *J. Mat. Sci.* **23** (1988) 141.

[29] Gent, A. and Hwang, Y.-C., Elastic behavior of a rubber sphere bonded between two rigid spheres. *Rub. Chem. Tech.* **61** (1988) 630.

[30] Rice, J. R. and Johnson, M. A., The role of large crack tip geometry changes in plane strain fracture. In: *Inelastic Behavior of Solids.* (Edited by : Kanninen, M. et.al.) McGraw-Hill New York (1970) 641.

[31] Williams, M. L., On the stress distribution at the base of a stationary crack. *J. App. Mech.*, **24** (1957) 109.

[32] Hutchinson, J. W., Nonlinear Fracture Mechanics, The Technical University of Denmark, (1979).

[33] ABAQUS, Version 4.7, Hibbitt, Karlsson, and Sorensen, Inc., Providence, R.I.

[34] Moran, B. and Shih, C. F., Crack tip integrals and associated domain integrals from momentum and energy balance, *Eng. Frac. Mech.*, **27** (1987) 615.

[35] Parks, D. M., The virtual crack extension method for nonlinear material behavior, *Comp. Meth. Appl. Mech. Engng.*, **12** (1977) 353.

[36] Treloar, L. R., The physics of rubber elasticity. *Clarendon Press, Oxford,* (1958).

[37] Rivlin, R. S., Large elastic deformations of isotropic materials IV Further Developments of the General Theory. *Phil. Trans.*, **A.241** (1948) 47.

[38] Rivlin, R. S. and Saunders, D. W., Large deformations of isotropic materials vii. Experiments in the deformation of rubber. *Phil. Trans.*, **A.243** (1951) 251.

[39] James, A. G., Green, A., and Simpson, G. M., Strain energy functions of rubber. I. Characterization of gum rubber vulcanizates. *J. Appl. Poly. Sci.* **19** (1975) 2033.

[40] Fried, I. and Yang, S., Best finite elements distribution around a singularity. *A.I.A.A. J.* **10** (1972) 1244.

[41] Johnson, A. R., On the accuracy of polynominal finite elements for crack problems. *Int. J. Num. Meth. Eng.*, **17** (1981) 1835.

[42] Gent, A. N. and Pulford, C. T. R., Micromechanics of fracture in elastomers. *J. Mat. Sci.* **19** (1984) 3612.

[43] Ravichandran, G. and Knauss, W. G., A finite elastostatic analysis of bimaterial interface cracks. *Int. J. Fract.* **39** (1989) 235.

[44] Knowles, J., and Sternberg, E., Large deformations near a tip of an interface-crack between two Neo-Hookean sheets. *J. Elas.* **13** (1983) 257.

[45] Stacer, R. G. and Kelley, F. N., Criteria for unstable tearing in elastomers. *Rubber Chem. Tech.* **58** (1985) 924.

[46] Stacer, R. G. et. al., Observations on the tearing of elastomers. *Rubber Chem. Tech.* **58** (1985) 421.

[47] Johnson, A.R., private communication.

[48] Goldberg, A., et. al., Influence of notch depth on tearing morphology and tearing energy in carbon-black-loaded SBR. *Lawrence Livermore Nat. Lab.* **UCID-20979**, (1987).

[49] Fukahori, Y. and Andrews, E. H., Fracture surface roughness in highly deformable polymers. *J. Mat. Sci.* **13** (1978) 777.

[50] Goldberg, A., et. al., Tearing, cut growth, and fracture of styrene-butadiene rubber and natural rubber containing various amounts of carbon black. *Lawrence Livermore Nat. Lab.* **UCID-20287**, (1984).

[51] Abeyaratne, R. C., Discontinuous deformation gradients in plane finite elastostatic of incompressible materials. *J. of Elasticity* **10** (1980) 255.

[52] Knowles, J. K. and Sternberg, Eli., Finite-deformation analysis of the elastostatic field near the tip of a crack: reconsideration and higher order results. *J. of Elasticity* **4** (1974) 201.

Appendix A

Derivation of the Asymptotic Solution for a Plane Strain Crack in a Mooney-Rivlin Material.

The derivation of the asymptotic solution for a plane strain Mode I crack in a Mooney-Rivlin material will be presented in this appendix. This solution was first obtained by Knowles [5], in conjunction with Sternberg, under the assumptions of finite strain elasticity. Knowles [5] considered the dominant singularity plus higher order terms necessary for a one to one mapping between the deformed and undeformed coordinate systems. Stephenson [6] extended the asymptotic solution to include additional terms. Although Stephenson [6] used a constitutive model which allowed for hardening and softening in shear, attention will be restricted to the case of linear behavior in shear. This constitutive model is known as the Mooney-Rivlin material law.

A.1 Plane Strain and Finite Elasticity

Consider a deformed coordinate system, y_i, and an undeformed coordinate system, x_i. It is assumed that y_i is twice differentiable and that

$$y_i = x_i + u_i \ .$$

(A.1)

where u_i denotes the displacement. The deformation gradient is represented by F_{ij}, where

$$F_{ij} = \frac{\partial y_i}{\partial x_j} \ . \tag{A.2}$$

Under the assumptions of incompressibility, the determinant of F_{ij} equals one. The deformation gradient can be decomposed into an orthogonal rotation tensor, R_{ij}, and a symmetric right stretch tensor, U_{ij}, thus,

$$F_{ij} = R_{ik}U_{kj} \ . \tag{A.3}$$

The tensor U_{ij} is positive definite. The principal values of U_{ij} are defined as the principal stretch ratios, λ_i. The principal stretch ratios are real, positive, and invariant. They are used to define the principal strain invariants, I_i, given by,

$$
\begin{aligned}
I_1 &= \lambda_1^2 + \lambda_2^2 + \lambda_3^2 \ , \\[2mm]
I_2 &= \lambda_1^2\lambda_2^2 + \lambda_2^2\lambda_3^2 + \lambda_1^2\lambda_3^2 \ , \\[2mm]
I_3 &= \lambda_1^2\lambda_2^2\lambda_3^2 \ .
\end{aligned}
\tag{A.4}
$$

For incompressible materials, I_3 equals one and, under the assumptions of plane strain, λ_3 equals one. From equation (A.4)

$$I_3 = 1 = \lambda_1^2\lambda_2^2 \ , \tag{A.5}$$

and consequently, it is easily noted that

$$\lambda_1 = 1/\lambda_2 \ . \tag{A.6}$$

For incompressible materials in plane strain, it can now be determined that I_1 equals I_2. By substituting equation (A.6) into the definitions for I_1 and I_2 in equation (A.4), it is found that

$$
\begin{aligned}
I_1 &= \lambda_1^2 + 1/\lambda_2^2 + 1 \ , \\[2mm]
I_2 &= 1 + 1/\lambda_2^2 + \lambda_1^2 \ .
\end{aligned}
\tag{A.7}
$$

In this analysis, the strain invariant is denoted by I, where

$$I = I_1 = I_2 \ . \tag{A.8}$$

Expressed in terms of the deformation gradient, the strain invariant, I, becomes

$$I = tr F^T F \ . \tag{A.9}$$

The Cauchy stress is denoted as τ_{ij}. In the absence of body forces, equilibrium is given as

$$\tau_{ij,j} = 0 \ , \tag{A.10}$$

where $(\bullet)_{,j} = \partial(\bullet)/\partial y_j$. The nominal stress, σ_{ij} is defined by

$$\sigma_{ij} = \tau_{ik} F_{jk} \ . \tag{A.11}$$

Again, in the absence of body forces, the equilibrium condition is

$$\sigma_{ij,j} = 0 \ , \tag{A.12}$$

where $(\bullet)_{,j} = \partial(\bullet)/\partial x_j$. While the Cauchy stress is symmetric, the nominal stress is not. However, it is noted that

$$\sigma_{ik} F_{jk} = F_{ik} \sigma_{jk} \ . \tag{A.13}$$

The nominal and Cauchy traction vectors are represented by s_i and t_i, respectively, where

$$s_i = \sigma_{ij} n_j \ . \tag{A.14}$$

and

$$t_i = \tau_{ij} n_j^* \ . \tag{A.15}$$

The unit normal in the undeformed configuration is n_j and the unit normal in the deformed configuration in the deformed configuration is n_j^*. The relationship between n and n^* provides that

$$n^* = Fn \ . \tag{A.16}$$

where n^* has been rotated and stretched through the deformation gradient. The magnitude of n^* is scaled by the determinant of F, which equals one under incompressibility and, therefore, n^* is a unit normal. The significance of this definition of n^* is that s_i vanishes in the undeformed configuration if and only if t_i vanishes in the deformed configuration. Thus, the boundary condition at a traction free surface can be specified by σ_{ij} without knowing the deformed shape of the surface.

The strain energy per unit undeformed volume, W, is assumed to be a function of the strain invariant, I. For a Mooney-Rivlin material

$$W = \frac{\mu}{2}(I - 2) \ , \tag{A.17}$$

where μ is the shear modulus. This constitutive law assumes the material is homogenous and isotropic. For this constitutive law, the nominal and Cauchy stresses are expressed respectively as

$$\sigma = 2\frac{\partial W}{\partial I}F - pF^{-T} \ , \tag{A.18}$$

and

$$\tau = 2 \frac{\partial W}{\partial I} F F^T - p\delta \ . \tag{A.19}$$

The indeterminate pressure, p, is a consequence of incompressibility and is determined to specify the boundary conditions and equilibrium. ˉ

Displacement equations, derived from equilibrium, equations (A.12) and (A.18), and incompressiblity $(I_3 = 1)$, are elliptic at the solution vector, u_i, and at any material point x_i if and only if

$$\frac{\partial W}{\partial I} \neq 0 \quad \text{and} \quad 2 \frac{\partial^2 W/\partial I^2}{\partial W/\partial I}(I-2) + 1 > 0 \ . \tag{A.20}$$

This was proven by Abeyaratne [52]. For a Mooney-Rivlin material, the ellipticity condition in equation (A.20) is automatically satisfied.

A.2 Description of a Mode I Crack

Consider an infinite body containing a stationary crack of length $2L$, as shown in Figure (A.1). The crack faces are traction free and a uniform uniaxial tensile stress normal to the crack is applied at infinity. Along the crack faces, the traction free boundary condition is represented as

$$\left. \begin{array}{rcl} \sigma_{\alpha 2}(x_1, 0_+) &=& 0 \\[2mm] \sigma_{\alpha 2}(x_1, 0^-) &=& 0 \end{array} \right\} \quad -L < x_1 < L \ . \tag{A.21}$$

Given these boundary conditions, the deformation field, y_i, which satisfies the constraint of incompressibility, and the stress field, τ_{ij}, will be found. It is further required that

$$y = F^* x \quad \text{as} \quad x_1^2 + x_2^2 \to \infty \ . \tag{A.22}$$

Here, F^* is a constant tensor whose determinant equals one. The deformation field, y_i, is twice differentiable and continuous throughout the body. The deformation gradient at infinity, F^*, can be defined as

$$F^* = \begin{bmatrix} \lambda & 0 & 0 \\ 0 & \lambda^{-1} & 0 \\ 0 & 0 & 1 \end{bmatrix} \quad \text{for} \quad \lambda > 0 \ , \tag{A.23}$$

provided λ and λ^{-1} are the principal stretch ratios applied normal to the crack at infinity. The symmetry axes of F^* are y_i for a Mode I crack, where the crack is parallel to the y_1-axis.

A.3   Asymptotic Solution

This finite strain asymptotic solution was derived by Knowles [5] and Sternberg, and by Stephenson [6]. A description of their method of solution follows. First, a separable form of the deformation field is assumed. Next, a rigid body rotation about the origin is applied to the deformation field. Based on the constraints imposed by incompressiblity, equilibrium, and the boundary conditions, an eigenvalue problem is formulated and solved. Using the resulting deformating field, the determinant of the local deformation field and the pressure field are evaluated. If the determinant vanishes or if only a weak approximation of the pressure field is obtained, additional higher order terms are included in the deformation field and the entire anaylsis is repeated. Knowles [5] and Sternberg follow this procedure twice, while Stephenson [6] repeates it for a third time. Their solution is outlined below.

The undeformed coordinate system in Figure A.1 can be redefined in terms of polar coordinates as

$$\left. \begin{array}{rcl} x_1 - L &=& r\cos\theta \\[2mm] x_2 &=& r\sin\theta \end{array} \right\} \quad 0 \le r < \infty \; : \; -\pi \le \theta \le \pi \; . \qquad (A.24)$$

The deformation field is assumed to be of the form

$$\left. \begin{array}{rcl} y_1 &\sim& L + r^{m_1} v_1(\theta) \\[2mm] y_2 &\sim& r^{m_2} v_2(\theta) \end{array} \right\} \quad -\pi \le \theta \le \pi \; , \qquad (A.25)$$

where the function $v_\alpha, (\alpha = 1, 2)$, are twice differentiable and continuous. The constants m_α are positive because the displacement field must be finite at the crack tip. In addition, either m_1 and/or m_2 must be less than one to ensure that not all deformation gradients will be bounded at the crack tip, thus

$$m_\alpha > 0 \quad \text{either} \quad m_1 < 1 \quad \text{and/or} \quad m_2 < 1 \; . \qquad (A.26)$$

If $m_\alpha > 1$ then the strain invariant and the determinant of F would vanish as $r \to 0$ and the crack tip would undergo extreme contractions. If ($m_1 = 1$ and $m_2 \ge 1$) or ($m_1 \ge 1$ and $m_2 = 1$) then I and the determinant of F are still bounded as $r \to 0$. Therefore, at least one of the two exponents, either m_1 or m_2, must be less than unity. A separable form of the pressure field is represented as

$$p(x_1, x_2) \sim r^k p(\theta) \quad \text{as} \quad r \to 0 \; . \qquad (A.27)$$

This pressure field is once continuously differentiable. Under the assumption that the deformation and pressure fields can be characterized as separable functions

of r and θ, the governing field equations and the boundary conditions can now be redefined in terms of the partial derivatives of the deformation field. The incompressibility condition is satisfied when the determinant of the deformation gradient equals one. For a polar coordinate system, this condition is given as

$$J = \frac{1}{r}\left(\frac{\partial y_1}{\partial r}\frac{\partial y_2}{\partial \theta} - \frac{\partial y_2}{\partial r}\frac{\partial y_1}{\partial \theta}\right) = 1 \ . \tag{A.28}$$

The definitions of incompressiblity (A.28) and the nominal stress tensor (A.18) can be applied to the equilibrium condition in equation (A.12) to obtain

$$\frac{\partial p}{\partial r} = \mu \frac{\partial y_\alpha}{\partial r}\nabla^2 y_\alpha \ , \tag{A.29}$$

and

$$\frac{\partial p}{\partial \theta} = \mu \frac{\partial y_\alpha}{\partial \theta}\nabla^2 y_\alpha \ . \tag{A.30}$$

The strain invariant, I, in equation (A.9), can be expressed in terms of the partial derivatives of the deformation field as

$$I = g_{rr} + \frac{1}{r^2} g_{\theta\theta} \ . \tag{A.31}$$

where

$$g_{rr} = \frac{\partial y_\alpha}{\partial r}\frac{\partial y_\alpha}{\partial r} \ .$$

$$g_{\theta\theta} = \frac{\partial y_\alpha}{\partial \theta}\frac{\partial y_\alpha}{\partial \theta} \ . \tag{A.32}$$

$$g_{r\theta} = \frac{\partial y_\alpha}{\partial r}\frac{\partial y_\alpha}{\partial \theta} \ .$$

The boundary conditions in equation (A.21) require that the crack faces are traction free. Given the deformation field and the nominal stress tensor (A.18), these boundary conditions are characterized at $\theta = \pm\pi$ as

$$2\mu\frac{\partial y_1}{\partial \theta} + rp\frac{\partial y_2}{\partial r} = 0$$

$$2\mu\frac{\partial y_2}{\partial \theta} - rp\frac{\partial y_1}{\partial r} = 0 \tag{A.33}$$

Applying the incompressibility constraint (A.28) and the definitions in equations (A.32), the above boundary conditions, at $\theta = \pm\pi$, now become

$$p = \frac{2\mu}{g_{rr}} = \frac{2\mu}{r^2}g_{\theta\theta} \tag{A.34}$$

$$g_{r\theta} = 0 \ .$$

The first boundary condition is obtained by multiplying the first equation in equation (A.33) by y_2/r and the second by y_1/r. The equations are then added and simplified using equations (A.28) and (A.32). The second can be determined in a similar manner. For a separable form of the deformation field as in equation (A.25), incompressibility (A.28), equilibrium (A.29), and the boundary conditions (A.33) and (A.34) can now be applied. Solutions to m_α and v_α which satisfy these equations will be examined. First, however, a new form of the deformation field in equation (A.25) is found by applying a rigid body rotation of the deformed body about the origin. The pressure field remains invariant under such a rotation. It can be shown that a deformation field U_α exists, such that

$$y_\alpha \sim r^m U_\alpha(\theta) \quad \text{as} \quad r \to 0 . \tag{A.35}$$

The smallest exponent m in the range between $(0, 1)$ and the functions U_α which satisfy the governing field equations and the boundary conditions will now be found. Based on the deformation field in equation (A.35), the strain invariant, I, will be determined. The incompressibility constraint, the boundary conditions and equilibrium are used to formulate an eigenvalue problem in terms of m and U_α, which is then solved to determine m and U_α. Once the deformation field in equation (A.35) is updated, the pressure field, p, and the determinant of the deformation field are evaluated to determine if higher order terms are necessary. Higher order terms are required in the deformation field if the determinant vanishes or if a weak approximation of the pressure field results.

Given the deformation field in equation (A.35), the invariant, I, in equation (A.31) is expressed as

$$I \sim r^{2(m-1)} \left\{ \dot{U}_1^2(\theta) + \dot{U}_2^2(\theta) + m^2 \left[U_1^2(\theta) + U_2^2(\theta) \right] \right\} , \tag{A.36}$$

where $(\bullet)$ differentiation with respect to θ. The coefficient of $r^{2(m-1)}$ must not vanish on the domain $[-\pi, \pi]$. Consequently, it is assumed that $U_1(\theta)$ and $U_2(\theta)$ do not have common multiple zeros over the domain. The incompressibility condition (A.28) becomes

$$J = m \, r^{2(m-1)} \left[U_1(\theta)\dot{U}_2(\theta) - U_2(\theta)\dot{U}_1(\theta) \right] + o\left(r^{2(m-1)} \right) = 1 . \tag{A.37}$$

This equation is divided by $r^{2(m-1)}$. Since the constant m is less than one, in the limit as $r \to 0$,

$$U_1 \dot{U}_2 - U_2 \dot{U}_1 = 0 \quad \text{n} \quad [-\pi, \pi] \tag{A.38}$$

Thus, U_α must be of the form

$$U_\alpha = a_\alpha U \quad \text{on} \quad [-\pi, \pi] \quad \text{with} \quad a_\alpha \neq 0 , \tag{A.39}$$

for a function $U(\theta)$ and constants a_α.

The above definition of U_α is now applied to the deformation field in equation (A.35) to obtain

$$y_\alpha \sim r^m \, a_\alpha U(\theta) \quad \text{as} \quad r \to 0 \ . \tag{A.40}$$

Based on the current form of the deformation field, the equilibrium condition is expressed as

$$\frac{\partial p}{\partial r} \ \sim \ \mu \, a^2 \, m \, U(\theta) \, Z(\theta) \ , $$

$$\tag{A.41}$$

$$\frac{\partial p}{\partial \theta} \ \sim \ \mu \, a^2 \, r^{2(m-1)} \, \dot{U}(\theta) \, Z(\theta) \ . $$

where

$$\left. \begin{array}{rcl} a & = & \sqrt{a_1^2 + a_2^2} \\[2mm] Z & = & \ddot{U} + m^2 \, U \end{array} \right\} \quad \text{on} \ \ [-\pi, \pi] \ . \tag{A.42}$$

The boundary conditions in equation (A.34) become

$$\left. \begin{array}{rcl} U \dot{U} & = & 0 \\[3mm] p & \sim & \mu \, a^2 \, r^{(2(m-1))} \, \dot{U}^2 \end{array} \right\} \quad \text{at} \ \ \theta = \pm\pi \ . \tag{A.43}$$

Now it is proven that equations (A.41) and (A.43) can be satisfied simultaneously if

$$Z \ = \ 0 \ \ \text{on} \ \ [-\pi, \pi] \ , $$

$$\tag{A.44}$$

$$\dot{U}(-\pi) = \dot{U}(+\pi) \ = \ 0 \ . $$

First, the partial derivative of the pressure field in equation (A.41) with respect to r is integrated, providing

$$p \sim \mu \, a^2 \, r^{2(m-1)} \, \frac{m \, U(\theta) \, Z(\theta)}{2(m-1)} \ . \tag{A.45}$$

The first boundary condition in equation (A.43) and the assumption that $U(\theta)$ has no multiple zeros on the domain $[-\pi, \pi]$ implies that either $U(\pi)$ or $\dot{U}(\pi)$ must vanish. If it is assumed that

$$U(\pi) = 0 \ \text{and} \ \dot{U}(\pi) \neq 0 \ , \tag{A.46}$$

then from equation (A.43), the pressure field at $\theta = \pi$ is

$$p(r, \pi) = o\left(r^{2(m-1)}\right) \quad \text{as} \quad r \to 0 \ . \tag{A.47}$$

This contradicts the value of the pressure field in equation (A.45), which vanishes at θ equal to π. For both equations to be satisfied at $\theta = \pi$, it is necessary for $\dot{U}(\pi) = 0$ and

$$Z(\pi) = Z(-\pi) = 0 . \tag{A.48}$$

If equation (A.45) is differentiated with respect to θ and subtracted from the second equation in (A.41), it is found that

$$U\dot{Z} + \left[1 + \frac{2(1 - m)}{m}\right] Z\dot{U} = 0 \quad \text{on} \quad [-\pi, \pi] . \tag{A.49}$$

At $\theta = \pi$, $\dot{U}$ and, consequently, $\dot{Z}$ equals zero. Similar arguments can be made for $\theta = -\pi$. Because both Z and $\dot{Z}$ vanish at $\theta = \pm\pi$, Z must vanish over the domain $[-\pi, \pi]$, or

$$Z(\theta) = 0 \quad \text{on} \quad [-\pi, \pi] . \tag{A.50}$$

Based on equations (A.42) and (A.44), an eigenvalue problem can be formulated as

$$\ddot{U} + m^2 U = 0 \quad , \quad \dot{U}(\pm\pi) = 0 . \tag{A.51}$$

The solution to equation (A.51) provides an eigenvalue and an associated eigenvalue given respectively as

$$m = 1/2 ,$$
$$\tag{A.52}$$
$$U(\theta) = \sin(\theta/2) .$$

The deformation field in equation (A.40) is now given as

$$y_\alpha = r^{1/2} a_\alpha \sin(\theta/2) . \tag{A.53}$$

However, when this deformation field is substituted into the pressure field, equation (A.45), and the determinant, equation (A.37), the results provide

$$\left.\begin{array}{rcl} J & = & o\left(r^{2(m-1)}\right) \\[2ex] p & = & o\left(r^{-1}\right) \end{array}\right\} \quad \text{as} \quad r \to 0 . \tag{A.54}$$

This deformation field is inadequate because it provides only weak estimates of the pressure field and the determinant of the deformation field equals zero. Consequently, the lowest order appproximation to the deformation field does not provide a one to one mapping between the undeformed and the deformed coordinate systems. Higher order terms are required in the deformation field. A new deformation field is given as

$$y_\alpha(r, \theta) = a_\alpha r^m U(\theta) + r^{m'} V_\alpha(\theta) + o(r^m) . \tag{A.55}$$

The constant m' and the functions $V_\alpha(\theta)$ will be found assuming

$$m' > m \ . \qquad (A.56)$$

The deformation field is smooth and twice differentiable. The process used to determine $U(\theta)$ and m will be reapplied to evaluate m' and $V_\alpha(\theta)$. However, the result will be the formulation of two eigenvalue problems. From the application of the incompressibility constraint, the first eigenvalue problem will be found. When the boundary conditions and equilibrium are considered, a second eigenvalue problem will result. The constant m' is the eigenvalue common to both problems, which will then be solved to provide a solution for m' and $V_\alpha(\theta)$.

First, the determinant, equation (A.28), is found for the deformation field in equation (A.55),

$$J = a_\alpha r^{m+m'-2} \left(mU\dot\Psi - m'\dot U\Psi \right) + o\left(r^{m+m'-2} \right) = 1 \ . \qquad (A.57)$$

Here, Ψ represents the function

$$\Psi = a_1 V_2 - a_2 V_1 \quad , \text{on } [-\pi, \pi] \ . \qquad (A.58)$$

The determinant in equation (A.57) is divided by $r^{m+m'-2}$ and, in the limit as $r \to 0$, it is required that

$$m + m' - 2 \leq 0 \ , \qquad (A.59)$$

in addition to

$$mU\dot\Psi - m'\dot U\Psi = 0 \quad \text{on } [-\pi, \pi] \text{ if } m < m' < 2 - m \ , \qquad (A.60)$$

and

$$mU\dot\Psi - m'\dot U\Psi = 1 \quad \text{on } [-\pi, \pi] \text{ if } m' = 2 - m \ . \qquad (A.61)$$

The strain invariant, I, equation (A.31) is determined to be

$$I \sim r^{2(m-1)} am^2 G + r^{m+m'-2} 2K + r^{2(m'-1)} \left[m'^2 \left(V_1^2 + V_2^2 \right) + \dot V_1^2 + \dot V_2^2 \right] \ , \qquad (A.62)$$

where

$$\left. \begin{array}{rcl} K & = & \dot\chi\dot U + mm'\chi U \\[2ex] G & = & \dot U^2 + m^2 U^2 \end{array} \right\} \quad , \text{on } [-\pi, \pi] \ . \qquad (A.63)$$

with the function χ defined as

$$\chi = a_1 V_1 + a_2 V_2 \ . \qquad (A.64)$$

Over the domain $[-\pi, \pi]$, the functions V_1 and V_2 must not have common multiple zeros to prevent the coefficient to $r^{2(m'-1)}$ from vanishing. When equilibrium is applied through equation (A.29),

$$
\begin{aligned}
\frac{1}{\mu}\frac{\partial p}{\partial r} = \ & r^{2m-3}a^2 mU\left[m^2U + \ddot{U}\right] \\
& + r^{m+m'-3}\left[mU\left(m'^2\chi + \ddot{\chi}\right) + 2m\chi\left(m^2U + \ddot{U}\right)\right] \\
& + r^{2m'-3}m'\left[V_1\left(m'^2V_1 + \ddot{V}_1\right) + V_2\left(m'^2V_2 + \ddot{V}_2\right)\right] \ ,
\end{aligned}
$$

$$(A.65)$$

$$
\begin{aligned}
\frac{1}{\mu}\frac{\partial p}{\partial \theta} = \ & r^{2(m-1)}a^2\dot{U}\left[m^2U + \ddot{U}\right] \\
& + r^{m+m'-2}\left[\dot{\chi}\left(m^2U + \ddot{U}\right) + \dot{U}\left(m'^2\chi + \ddot{\chi}\right)\right] \\
& + r^{2(m'-1)}\left[\dot{V}_1\left(m'^2V_1 + \ddot{V}_1\right) + \dot{V}_2\left(m'^2V_2 + \ddot{V}_2\right)\right] \ .
\end{aligned}
$$

The value of p at $\theta = \pm\pi$ is determined from equation (A.34),

$$
p(\pi) \sim r^{2(m-1)}a^2\dot{U}^2 + r^{m+m'-2}2\chi\dot{U} + r^{2(m'-1)}\left(\dot{V}_1^2 + \dot{V}_2^2\right) \ . \tag{A.66}
$$

Now, Stephenson [6] defines a function $Y(\theta)$ such that

$$
Y = G\left(\ddot{\chi} + m'^2\chi\right) + 2K\left(\ddot{U} + m^2U\right) \ . \tag{A.67}
$$

Following the same arguments which proved that $Z = 0$ in equation (A.50), it can be shown

$$
Y = 0 \quad \text{on} \quad [-\pi, \pi] \quad \text{if} \quad m < m' < 2 - m \ , \tag{A.68}
$$

and

$$
Y = 2\left(\ddot{U} + m^2U\right) \quad \text{on} \quad [-\pi, \pi] \quad \text{if} \quad m' = 2 - m \ . \tag{A.69}
$$

The boundary conditions, equation (A.66), are restated as

$$
\dot{\chi}(\pm\pi) = 0 \quad \text{if} \quad m < m' \leq 2 - m \ , \tag{A.70}
$$

$$
\dot{\Psi}(\pm\pi) = 0 \quad \text{if} \quad m < m' < 2 - m \ , \tag{A.71}
$$

and

$$
\left.\begin{aligned}
\dot{\Psi}(\pi) &= 1/mU(\pi) \\
\dot{\Psi}(-\pi) &= 1/mU(-\pi)
\end{aligned}\right\} \quad \text{if} \quad m' = 2 - m \ . \tag{A.72}
$$

The two eigenvalue problems can now be reformulated. The first eigenvalue problem results from equations (A.67), (A.68) and (A.70), or

$$
\left.\begin{aligned}
G\left(\ddot{\chi} + m'^2\chi\right) + 2K\left(\ddot{U} + m^2U\right) &= 0 \\
\dot{\chi} &= 0
\end{aligned}\right\} \quad \text{if} \quad m < m' \leq 2 - m \ . \tag{A.73}
$$

The boundary conditions in equations (A.71) and (A.72) are implicitly stated in equations (A.60) and (A.61). To obtain a solution for Ψ, it is further assumed that Ψ has continuous derivatives of all orders over the domain $[-\pi, \pi]$. The second eigenvalue problem is to find all values of m' on $(m, 2-m)$ such that Ψ in equations (A.60) and (A.61) will be continuously differentiable. The solutions to these eigenvalue problems will now be presented. A value for m' is found which satisfies both eigenvalue problems with eigenfunctions represented by χ and Ψ.

Consider the eigenvalue problem posed by equations (A.60) and (A.61). Given that U represents the eigenfunction to equation (A.56), it can be concluded

$$
\left.
\begin{aligned}
\Psi &= a_3 U^{\cdot m'/m} \quad \text{on} \quad (0, \pi] \\[6pt]
\Psi &= a_4 U^{-m'/m} \quad \text{on} \quad [-\pi, 0)
\end{aligned}
\right\} \quad \text{as} \quad r \to 0 \ , \tag{A.74}
$$

where a_3 and a_4 denote constants. The value of m'/m is a positive integer as Ψ is infinitely smooth and differentiable over the domain $[-\pi, \pi]$. The smallest value of m', for m' greater than m, which satisfies equation (A.74) is

$$
m' = 2m = 1 \ . \tag{A.75}
$$

The eigenfunction Ψ becomes

$$
\Psi = b_2 U^2 \ . \tag{A.76}
$$

The constant b_2 is nonzero.

The first eigenvalue problem, equation (A.73), is now considered. The function χ is redefined as

$$
\chi = \chi' + \chi'' \quad \text{on} [-\pi, \pi] \ , \tag{A.77}
$$

provided

$$
\left.
\begin{aligned}
\chi'(\theta) &= \tfrac{1}{2}[\chi(\theta) - \chi(-\theta)] \\[6pt]
\chi''(\theta) &= \tfrac{1}{2}[\chi(\theta) + \chi(-\theta)]
\end{aligned}
\right\} \quad -\pi \le \theta \le \pi \ . \tag{A.78}
$$

The original eigenvalue problem will be reformulated into two new ones. The new eigenfunctions will be χ' and χ''. Once χ' and χ'' are determined, a solution can be found for χ. The eigenvalue problem posed in equation (A.73) becomes

$$
G\left(\ddot{\chi}' + m'^2 \chi'\right) + 2K'\left(\ddot{U} + m^2 U\right) = 0 \quad \text{on} \ [0, \pi] \ , \tag{A.79}
$$

$$
G\left(\ddot{\chi}'' + m'^2 \chi''\right) + 2K''\left(\ddot{U} + m^2 U\right) = 0 \quad \text{on} \ [0, \pi] \ , \tag{A.80}
$$

with

$$
K' = \dot{\chi}' U + mm' \chi' U \quad \text{and} \quad K'' = \dot{\chi}'' U + mm' \chi'' U \ . \tag{A.81}
$$

The boundary conditions, equation (A.70), are obtained in terms of χ' and χ'', equation (A.78), or

$$\dot{\chi}'(\pi) = 0 \; ; \quad \chi'(0) = 0 \; ; \; , \qquad (A.82)$$

$$\dot{\chi}''(\pi) = 0 \; , \quad \dot{\chi}''(0) = 0 \; . \qquad (A.83)$$

The eigenvalue problems for χ', equations (A.79) and (A.82), and for χ'', equations (A.80) and (A.83), can now be solved.

The eigenvalue problem for χ' was solved by Knowles and Sternberg [52] by transforming equations (A.79) and (A.82) to

$$\ddot{W}_1(\xi) + \lambda^2 W_1(\xi) \;=\; 0 \;\; \text{on} \;\; 0 \le \xi \le \pi/2 \; ,$$

$$\dot{W}_1(0) = W_1(\pi/2) \;=\; 0 \; . \qquad (A.84)$$

using

$$\cos(\xi) \;=\; \cos\theta/2 \; ,$$

$$W_1(\xi) \;=\; 1^{-m'}\chi'(\theta) \; , \qquad (A.85)$$

$$\lambda^2 \;=\; 4m'^2 \; .$$

Here, a one-to-one mapping was introduced over the interval $0 \le \theta \le \pi$ onto $0 \le \xi \le \pi/2$, in which $\theta = 0$ and $\theta = \pi$ is mapped to $\xi = \pi/2$ and $\xi = 0$, respectively. The solution to this problem is

$$W_1(\xi) = b_0 \cos\lambda\xi \; , \quad \lambda = j \;\; (j = 1, 3, 5, \ldots) \; , \qquad (A.86)$$

where b_0 is a constant.

A similar transformation is made to solve equations (A.80) and (A.83). Let

$$W_2(\xi) \;=\; 1^{-m'}\chi''(\theta) \; , \qquad (A.87)$$

and the eigenvalue problem is now

$$\ddot{W}_2(\xi) + \lambda^2 W_2(\xi) \;=\; 0 \;\; 0 \le \xi \le \pi/2 \; ,$$

$$\dot{W}_2(0) = \dot{W}_2(\pi/2) \;=\; 0 \; . \qquad (A.88)$$

Its solution is

$$W_2(\xi) = b_1 \cos\lambda\xi \; , \quad \lambda = j \;\; (j = 2, 4, 6, \ldots) \; . \qquad (A.89)$$

where b_1 denotes a constant.

Values of m' representing eigenvalues of the problem posed in equation (A.73) are

$$4m'^2 = j^2 \ , \quad (j = 1, 2, 3, \ldots) \ . \tag{A.90}$$

Because m' is greater than m, the minimum value of m' is found when $j = 2$. Consequently,

$$m' = 1 \ . \tag{A.91}$$

The eigenfunction, χ, can now be found. For $j = 2$, $\chi'(\theta)$ vanishes over the range $[-\pi, \pi]$ and the function χ'' in equation (A.87) provides a solution to χ. From the definitions for χ'' (equation (A.78)) and $\cos(\xi)$ (equation (A.85)) χ can be expressed as

$$\chi(\theta) = b_1 \cos\theta \ . \tag{A.92}$$

Consequently, the solution to the deformation field in equation (A.55) has been determined in terms of auxiliary functions, Ψ (equation (A.58)) and χ (equation (A.92)) for m' equal to one. These functions are

$$\chi = b_1 \cos\theta \quad \text{and} \quad \Psi = b_2 \sin^2 \frac{\theta}{2} \ . \tag{A.93}$$

A rigid body rotation, defined by

$$[Q] = \begin{bmatrix} a_2/a & -a_1/a \\ a_1/a & a_2/a \end{bmatrix} \quad \text{with} \quad a = \sqrt{a_1^2 + a_2^2} \ , \tag{A.94}$$

will now be applied to the deformation field in equation (A.55). The deformation field is now expressed in terms of U, Ψ, equation (A.58), and χ, equation (A.64), as

$$y_1(r, \theta) = -\frac{1}{a} r^{m'} \Psi(\theta) + o(r^{m'}) \ , \tag{A.95}$$

$$y_2(r, \theta) = a r^m U(\theta) + \frac{1}{a} r^{m'} \chi(\theta) + o(r^{m'}) \ ,$$

or, using equation (A.93),

$$y_1(r, \theta) = -\frac{1}{a} r^{m'} b_2 \sin^2 \frac{\theta}{2} + o\left(r^{m'}\right) \ , \tag{A.96}$$

$$y_2(r, \theta) = a r^m \sin \frac{\theta}{2} + \frac{1}{a} r^{m'} b_1 \cos(\theta) + o\left(r^{m'}\right) \ .$$

Noting that the deformation field must be symmetric about the x_1-axis for a Mode I crack, it is determined that

$$a_1 = 0 \, , \, a_2 = a \, , \text{ and } b_1 = 0 \ . \tag{A.97}$$

The pressure field. as given by equation (A.27), will now be considered. The equations for the determinant equation (A.28) and equilibrium, equations (A.29) and (A.31) can be manipu'. ed to obtain

$$\frac{\mu}{2} \nabla^2 y_1 = \frac{1}{r} \left(\frac{\partial p}{\partial r} \frac{\partial y_2}{\partial \theta} - \frac{\partial p}{\partial \theta} \frac{\partial y_2}{\partial r} \right) \tag{A.98}$$

Given the 'eformation field in equation (A.96), this equation becomes

$$2\mu b_2 G r^{-1} + o\left(r^{-1}\right) = a r^{m+k-2} \left(kp\dot{U} - mp\dot{U}\right) + o\left(r^{m+k-2}\right) \tag{A.99}$$

The boundary conditions in equation (A.34) provide

$$r^k p(\pm\pi) = 2\mu \left[maU\left(\pm\pi\right) \right]^{-2} r \tag{A.100}$$

For both equations (A.99) and (A.100) to be satisfied. either k equals zero or $p(\theta)$ vanishes at $\theta = \pm\pi$. It can be seen that

$$k \leq 1 - m \tag{A.101}$$

Therefore. it is concluded that

$$p(\pm\pi) = 0 \tag{A.102}$$

The value of k will now be found. If k is less than $1/2$, then the coefficient to r^{m+k-2} in equation (A.99) is given as

$$kp\dot{U} - mp\dot{U} = 0 \quad \text{on} \quad [-\pi, \pi] \tag{A.103}$$

This result. taken with the conclusion that $p(\pm\pi)$ equals zero, implies that $p(\theta)$ would vanish over the domain $[-\pi, \pi]$. Therefore,

$$k = 1/2 \quad.$$

$$kp\dot{U} - mp\dot{U} = 2\mu \frac{b_2}{a} G \quad \text{on} \quad [-\pi, \pi] \tag{A.104}$$

$$p(\pm\pi) = 0 \quad.$$

From the above equation, $p(\theta)$ becomes

$$p(\theta) = -\frac{2\mu b_2}{a} \cos\frac{\theta}{2} \tag{A.105}$$

The deformation and pressure fields can now be expressed in terms of polar coordinates from equations (A.96), (A.97), and (A.105),

$$y_1(r,\theta) \;=\; -\frac{b_2 r}{a}\sin^2\frac{\theta}{2} + o(r)\;,$$

$$y_2(r,\theta) \;=\; a r^{1/2}\sin\frac{\theta}{2} + o(r)\;, \tag{A.106}$$

$$p(r,\theta) \;=\; -\frac{2\mu b_2}{a}\, r^{1/2}\cos\frac{\theta}{2} + o\left(r^{1/2}\right)\;.$$

The amplitude constants are a, and b_2. Stephenson included additional higher order terms in the deformation field and repeated this analysis for a third time. The details of this higher order analysis will not be given; the interested reader is referred to reference [6]. The final form of the deformation field is presented as

$$
\begin{aligned}
y_1(r,\theta) \;=\;& -\frac{1}{a}r b_2 \sin^2\frac{\theta}{2} + \frac{1}{a}r^{3/2}\left[4\sin^2\frac{\theta}{2}\cos\frac{\theta}{2} + \frac{4}{3}\cos^3\frac{\theta}{2}\right] \\
& -\frac{1}{a}r^2\left[d_1\sin^4\frac{\theta}{2} + \frac{2b_2}{a^2}\left(3c_1 - \frac{b_2^2}{2a^2}\right)\sin^2\frac{\theta}{2}\right] + o\left(r^2\right)\;,
\end{aligned}
$$

$$
\begin{aligned}
y_2(r,\theta) \;=\;& a r^{1/2}\sin\frac{\theta}{2} + \frac{1}{a}r^{3/2}\left[c_1\sin\frac{3\theta}{2} - \frac{b_2^2}{2a^2}\sin\frac{\theta}{2}\right] \\
& + \frac{b_2}{a^3}r^2\left[2\sin\theta - \sin 2\theta\right] + o\left(r^2\right)\;,
\end{aligned} \tag{A.107}
$$

$$
p(r,\theta) \;=\; -2\mu\frac{b_2}{a}r^{1/2}\cos\frac{\theta}{2} + \frac{2\mu}{a^2}r(3 - \cos\theta) + o(r)\;.
$$

Load amplitude constants are denoted by a, b_2, c_1, and d_1. To obtain an equivalent form of the deformation field, as derived by Knowles [5], the following substitutions must be made,

$$b \;=\; b_2/a\;.$$

$$\tag{A.108}$$

$$d \;=\; c_1/a\;.$$

The Cauchy stress field can be determined from (A.18). When the deformation field in equation (A.107) is used to calculate the deformation gradient, equation (A.2), the leading terms of the stress field are

$$\tau_{11} \sim \frac{\mu}{2}\frac{b_2}{a}(1 - \cos\theta) \ ,$$

$$\tau_{22} \sim \frac{\mu}{2}\frac{a^2}{r} \ , \qquad\qquad (A.109)$$

$$\tau_{12} \sim \frac{\mu}{2}\frac{b_2}{\sqrt{r}}\sin\frac{\theta}{2} \ .$$
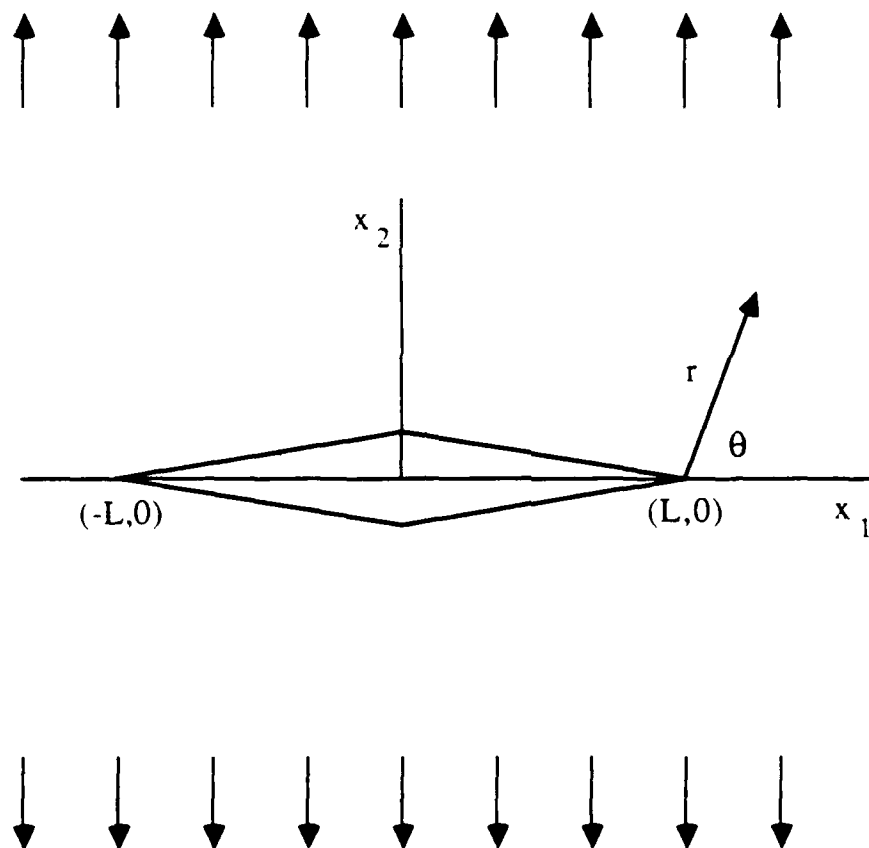
Figure A.1: A Mode I crack in an infinite plate.

Appendix B

Determination of Load Amplitude Constant, a, Under the Assumptions of Small Scale Nonlinearity

The nonlinear elastic deformation field for a Mode I crack in a Mooney-Rivlin material as derived by Knowles [5] is

$$y_1(r, \theta) = br \sin^2 \frac{\theta}{2} + \frac{1}{a} r^{3/2} \left(2 \cos \frac{\theta}{2} - \frac{2}{3} \cos \frac{3\theta}{2} \right) ,$$

$$(B.1)$$

$$y_2(r, \theta) = ar^{1/2} \sin \frac{\theta}{2} + r^{3/2} \left(d \sin \frac{3\theta}{2} - \frac{b^2}{2a} \sin \frac{\theta}{2} \right) .$$

The unknown load amplitude constants are a, b, and d. In small scale nonlinearity. the amplitude constant, a, can be determined as a function of the applied load using the energy conservation line integral. J. A small tensile load is applied at infinity as in Figure A.1. At the crack tip, as $r \rightarrow 0$, the deformation field in equation (B.1) is found. This deformation field will be used to evaluate the J-integral, where

$$J = \int_\Gamma (W \, dx_2 - s_i u_{i,1} \, ds)$$

$$(B.2)$$

with the assumption that the J-integral is path independent for a suitable contour. Γ. surrounding the crack tip. The circular contour. Γ. with radius, r, was selected in the undeformed configuration. as shown in Figure B.1. The J-integral. equation (B.2) will be evaluated from the bottom of the crack surface at $\theta = -\pi$,

parallel to the x_1 axis, to the top crack surface at $\theta = \pi$. For this contour it is noted that

$$
\begin{aligned}
dx_2 &= r\cos\theta d\theta \ , \\
ds &= rd\theta \ ,
\end{aligned}
\tag{B.3}
$$

and

$$
\left(\frac{\partial}{\partial x_1}\right) = \cos\theta \left(\frac{\partial}{\partial r}\right) - \frac{\sin\theta}{r}\left(\frac{\partial}{\partial \theta}\right) \ .
\tag{B.4}
$$

The strain energy per unit undeformed volume, W, for a Mooney-Rivlin material is

$$
W = C_{10}(I_1 - 3) + C_{01}(I_2 - 3) \ .
\tag{B.5}
$$

where μ equals $2(C_{10} + C_{01})$. Referenced to the undeformed configuration, the nominal traction vector, s_i, is defined as

$$
s_i = \sigma_{ji} n_j \ .
\tag{B.6}
$$

Here, n_j is the outward unit normal in the nominal stress tensor, σ_{ij}, for an incompressible material is given by

$$
\sigma_{ji} = 2(W_{,1} + I_1 W_{,2}) F_{ji} - 2 W_{,2} B_{jk} F_{ki} - p F_{ij}^{-1} \ .
\tag{B.7}
$$

The left Cauchy Green strain tensor, B_{ij} , is

$$
B_{ik} = F_{ij} F_{kj} \ .
\tag{B.8}
$$

Finally, it is noted that

$$
F_{ij} = \delta_{ij} + u_{i,j} = \frac{\partial y_i}{\partial x_j} \ ,
\tag{B.9}
$$

where u_i represents the displacement field. The term F_{ij}^{-1} refers to that Cartesian component of the inverse of the deformation gradient, F_{ij}. The arbitrary pressure, p, is associated with the isochoric constraint.

In plane strain, I_1 equals I_2 and can expressed in terms of the deformation gradient,

$$
I_1 = I_2 = B_{ii} = F_{ij} F_{ij} = tr(FF^T) \ .
\tag{B.10}
$$

This relationship can be used to redefine W, (B.5), and σ_{ij}, (B.7), as

$$
W = \frac{\mu}{2}\left(tr(FF^T) - 3\right)
\tag{B.11}
$$

and

$$
\sigma_{ji} = 2 W_{,1} F_{ji} - p F_{ij}^{-1} \ .
\tag{B.12}
$$

The J-integral can now be evaluated. First the deformation gradient is found from the deformation field in equation (B.1),

$$F_{11} = \frac{\sqrt{r}}{a} \left[\cos\frac{3\theta}{2} + \cos\frac{\theta}{2} \right] + \frac{b}{2}[\cos\theta - 1] ,$$

$$F_{12} = \frac{\sqrt{r}}{a} \left[\sin\frac{3\theta}{2} + 3\sin\frac{\theta}{2} \right] + \frac{b}{2}\sin\theta ,$$

$$F_{21} = \sqrt{r} \left[\frac{-b^2}{4a}\sin\frac{3\theta}{2} + \left(\frac{3d}{2} + \frac{b^2}{2a}\right)\sin\frac{\theta}{2} \right] - \frac{a}{2\sqrt{(r)}}\sin\frac{\theta}{2} ,$$

$$F_{22} = \sqrt{r} \left[\frac{b^2}{4a}\cos\frac{3\theta}{2} + \left(\frac{3d}{2} - \frac{b^2}{2a}\right)\cos\frac{\theta}{2} \right] + \frac{a}{2\sqrt{(r)}}\cos\frac{\theta}{2} .$$

(B.13)

The strain energy, W, and the nominal stress tensor, σ_{ij}, in equations (B.11) and (B.12) are determined from F_{ij} in equation (B.13). Taking the limit as $r \to 0$, the J-integral, equation (B.2), becomes

$$J = a^2\mu \int_{-\pi}^{\pi} \left[\frac{1}{4}\cos\theta - \frac{1}{8}(\cos 2\theta - 1) \right] d\theta .$$

(B.14)

Evaluation of the J-integral provides that

$$J = \frac{\pi a^2 \mu}{4} .$$

(B.15)

In small scale nonlinearity, the stress intensity factor, K_I, is related to the J-integral by

$$J = \frac{K_I^2(1 - \nu^2)}{E} .$$

(B.16)

Noting that ν equals $1/2$ for an incompressible material,

$$\frac{\pi a^2 \mu}{4} = \frac{K_I^2}{E}\frac{3}{4} .$$

(B.17)

Here, K_I is defined as

$$K_I = \sigma\sqrt{\pi l} ,$$

(B.18)

and consequently,

$$a = \frac{\sigma}{\mu}\sqrt{l} .$$

(B.19)

This result agrees with that obtained by Knowles [5] and Stephensen [6]. The value of the load amplitude constant, a, is directly proportional to the applied load. It is also a function of the crack length and the shear modulus at infinitesimal deformations. This expression for a is valid only under the assumptions of small scale nonlinearity.
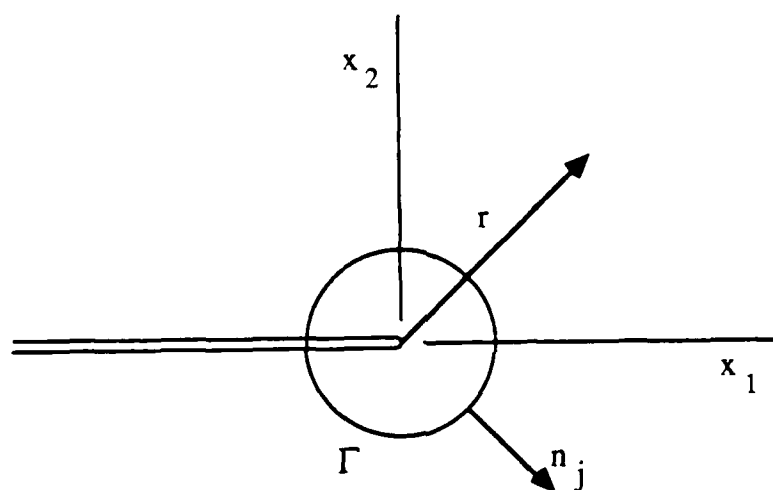
Figure B.1: Contour used to evaluate the J-integral.

Appendix C

Experimental Data

Table C.1: Specimen $M - 1$.

Δ (cm)	Load(N)	Δ (cm)	Load(N)
0.000	0.0	0.610	264.6
0.010	20.9	0.660	280.2
0.020	23.3	0.711	302.4
0.030	24.4	0.762	313.5
0.041	38.7	0.787	320.2
0.061	57.8	1.041	373.6
0.081	72.9	1.295	429.2
0.107	84.5	1.372	444.8
0.127	96.0	1.626	489.2
0.147	106.7	1.895	551.5
0.170	116.5	2.149	604.9
0.191	125.8	2.449	662.7
0.211	134.7	2.703	713.9
0.234	143.6	2.972	773.9
0.254	151.6	3.226	827.3
0.274	159.2	3.495	876.2
0.297	164.5	3.749	925.1
0.317	174.3	4.003	987.4
0.338	181.4	4.257	1023.0
0.361	189.0	4.511	1076.4
0.381	195.7	4.587	1107.5
0.401	202.3	4.714	1129.7
0.424	209.0	4.968	1178.7
0.444	217.9	5.207	1223.2
0.465	221.9	5.222	1223.2
0.488	226.8	5.232	1227.6
0.508	232.6	5.283	1240.9
0.528	237.9	5.309	1245.4
0.559	249.0	5.334	1232.1

Table C.2: Specimen $M - 2$.

Δ(cm)	Load(N)	CMOD(cm)	Δ(cm)	Load(N)	CMOD(cm)
0.000	0.0	-	1.463	436.7	0.819
0.076	56.2	0.024	1.516	448.3	0.847
0.130	83.4	0.050	1.570	460.3	0.877
0.160	104.7	0.077	1.628	471.9	0.910
0.218	129.1	0.107	1.676	482.6	0.937
0.241	148.9	0.120	1.725	492.8	0.966
0.274	·	0.161	1.775	503.9	1.002
0.381	175.6	0.179	1.824	514.6	1.026
0.437	197.9	0.224	1.882	525.3	1.047
0.480	211.7	0.249	1.943	537.7	1.093
0.516	221.9	0.269	1.994	548.8	1.127
0.559	-	0.283	2.197	583.5	1.221
0.597	241.5	0.302	2.256	591.5	1.274
0.640	251.7	0.335	2.314	600.4	1.308
0.673	260.6	0.354	2.367	606.7	1.350
0.706	269.5	0.373	2.446	620.9	1.392
0.742	277.5	0.389	2.487	628.9	1.411
0.782	291.3	0.431	2.543	639.1	1.453
0.846	302.4	0.455	2.588	647.6	1.490
0.897	314.9	0.479	2.642	656.5	1.513
0.940	322.0	0.509	2.705	670.7	1.546
0.996	336.2	0.545	2.751	680.1	1.575
1.031	345.1	0.565	2.819	-	1.606
1.085	354.9	0.599	2.873	707.6	1.636
1.125	363.8	0.621	2.926	719.2	1.662
1.166	373.1	0.646	3.030	741.9	1.711
1.222	384.3	0.671	3.086	755.2	1.740
1.262	394.5	0.706	3.147	768.1	1.770
1.354	412.3	0.755	3.238	784.6	1.830
1.402	424.3	0.798	3.282	797.0	1.829

Table C.2: Specimen $M - 2$ (continued).

Δ(cm)	Load(N)	CMOD(cm)
3.373	814.8	1.831
3.442	829.1	1.892
3.500	843.3	1.925
3.556	857.5	1.887
3.627	871.8	1.988
3.696	886.0	1.996
3.769	903.8	2.040
3.843	918.0	2.069
3.922	926.9	2.096
3.978	930.5	2.153
4.064	932.3	2.206
4.145	928.7	2.285
4.216	946.5	2.371
4.270	918.0	2.412
4.341	950.0	2.438
4.425	969.6	2.584
4.491	978.5	2.591
4.572	996.3	2.626
4.630	1010.5	2.668
4.704	1021.2	2.722
4.762	1037.2	2.791
4.831	1049.7	2.844
4.910	1062.1	2.888
5.062	1090.6	2.965
5.138	1078.2	3.022

Table C.3: Specimen $S - 1$.

Δ(cm)	Load(N)	CMOD(cm)	Δ(cm)	Load(N)	CMOD(cm)
0.000	0.0	-	2.235	-	1.309
0.064	33.8	-	2.286	622.7	-
0.095	48.9	-	2.413	-	1.321
0.127	66.7	-	2.527	-	1.360
0.147	-	0.066	2.540	-	1.333
0.191	102.3	-	2.629	-	1.308
0.254	124.5	0.105	2.667	693.8	-
0.381	171.2	-	2.705	-	1.298
0.394	-	0.140	2.807	-	1.316
0.533	-	0.162	2.908	-	1.365
0.572	-	0.100	2.943	-	1.408
0.648	-	0.123	3.048	765.0	-
0.762	284.6	-	3.112	-	1.426
0.775	-	0.209	3.213	-	1.507
0.902	-	0.291	3.302	-	1.558
0.965	-	0.351	3.391	-	1.595
1.041	-	0.410	3.429	840.6	-
1.143	378.0	-	3.518	-	1.609
1.156	-	0.469	3.594	-	1.643
1.232	-	0.525	3.619	885.1	-
1.308	-	0.597	3.715	778.4	-
1.410	-	0.631	3.810	813.9	-
1.473	-	0.671	4.013	-	2.056
1.524	462.5	-	4.128	-	2.589
1.537	-	0.692	4.191	920.7	-
1.613	-	0.750	4.216	-	2.636
1.689	-	0.773	4.381	-	2.159
1.753	-	0.822	4.483	-	2.286
1.854	-	0.880	4.572	996.3	2.413
1.905	542.6	-	4.674	-	2.413
1.956	-	0.916	4.813	-	2.540
2.019	-	0.940	4.915	-	2.540
2.108	-	1.234	4.953	1085.3	-
2.172	-	1.273			

Table C.4: Specimen $S - 2$ Loading.

Δ(cm)	Load(N)	CMOD(cm)
0.000	0.0	0.010
0.089	71.1	0.076
0.147	102.3	0.074
0.203	120.5	0.138
0.267	142.3	0.164
0.317	155.6	0.152
0.356	167.2	0.175
0.406	177.9	0.183
0.470	195.7	0.229
0.521	209.0	0.259
0.597	229.0	0.315
0.660	241.0	0.335
0.732	255.7	0.359
0.813	273.5	0.406
0.864	284.6	0.431
0.914	295.3	0.461
0.973	306.9	0.500
1.029	317.5	0.525
1.079	326.9	0.570
1.156	342.0	0.598
1.232	354.9	0.632
1.300	366.9	0.669
1.364	379.8	0.698
1.422	388.7	0.742
1.504	400.3	0.777
1.562	414.1	0.844
1.664	430.1	0.848
1.714	442.5	0.895
1.819	460.8	0.931
1.892	472.8	0.970
1.956	484.3	1.005
2.019	495.5	1.032
2.101	510.1	1.078
2.172	522.2	1.091
2.248	535.5	1.144
2.311	547.9	1.176
2.400	563.1	1.224
2.515	580.0	1.226
2.642	609.3	1.331

Table C.5: Specimen $S - 2$ Unloading.

Δ(cm)	Load(N)	CMOD(cm)
2.591	475.0	1.331
2.502	453.3	1.293
2.438	435.5	1.276
2.349	-	1.214
2.248	383.4	1.181
2.172	360.3	1.292
2.090	343.4	1.257
1.664	258.0	0.889
1.600	249.5	0.869
1.537	237.5	0.824
1.486	229.1	0.792
1.448	221.5	0.776
1.397	213.9	0.747
1.346	206.8	0.730
1.308	199.7	0.684
1.245	189.5	0.659
1.168	179.7	0.599
1.156	173.0	0.620
1.079	164.6	0.567
1.034	157.5	0.546
1.003	151.2	0.508
0.940	142.3	0.468
0.902	136.6	0.469
0.851	126.8	0.415
0.787	115.7	0.381
0.737	107.6	-
0.698	101.0	0.321
0.610	82.7	0.277
0.589	73.4	0.234
0.503	63.2	0.226
0.462	55.2	0.200
0.406	41.4	0.194
0.368	34.7	0.141
0.165	12.4	-

Table C.6: Specimen $S - 2$ Reloading.

Δ(cm)	Load(N)	CMOD(cm)	Δ(cm)	Load(N)	CMOD(cm)
0.000	0.0	-	1.478	342.9	0.887
0.076	38.3	-	1.537	353.6	0.916
0.122	63.1	0.069	1.603	364.2	0.947
0.157	76.1	0.092	1.664	375.4	0.983
0.185	77.8	0.109	1.737	389.2	1.026
0.244	103.6	0.140	1.791	398.9	1.046
0.269	115.6	0.170	1.836	408.7	1.077
0.351	129.5	0.185	1.900	419.0	1.115
0.386	137.8	0.208	1.920	431.4	1.133
0.437	149.6	0.243	2.014	443.9	1.166
0.470	157.4	0.262	2.075	455.4	1.189
0.508	166.3	0.292	2.144	470.1	1.215
0.572	176.1	0.283	2.215	484.8	1.253
0.648	191.7	0.362	2.276	495.0	1.281
0.653	198.8	0.394	2.332	510.1	1.312
0.724	206.8	0.411	2.395	524.8	1.346
0.762	215.7	0.450	2.469	542.6	1.358
0.813	223.7	0.485	2.532	561.7	1.390
0.864	231.7	0.509	2.611	577.3	1.420
0.902	241.5	0.552	2.680	595.1	1.449
0.958	250.8	0.574	2.781	623.6	1.495
1.016	258.4	0.595	2.908	654.7	1.539
1.069	269.1	0.640	2.941	672.0	1.586
1.123	276.2	0.673	3.061	686.7	1.605
1.161	285.1	0.693	3.178	707.6	1.648
1.212	294.4	0.728	3.251	720.1	1.679
1.260	303.8	0.764	3.330	734.3	1.703
1.333	315.3	0.791	3.393	743.2	1.727
1.384	324.2	0.832	3.459	753.0	1.767
1.430	331.3	0.864	3.548	764.1	1.814

Table C.6: Specimen $S-2$ Reloading (continued).

Δ(cm)	Load(N)	CMOD(cm)
3.711	766.8	1.946
3.780	777.9	1.995
3.879	799.7	2.030
3.950	811.3	2.070
4.021	827.3	2.092
4.097	841.5	2.132
4.199	855.8	2.139
4.280	878.0	2.214
4.351	893.1	2.230
4.458	910.9	2.280
4.509	923.4	2.305
4.575	935.8	2.309
4.646	949.6	2.313
4.712	962.5	2.412
4.806	982.1	2.458
4.884	998.1	2.484
4.976	1010.5	2.527
5.062	1037.2	2.560
5.138	1053.2	2.593
5.222	1071.0	2.628
5.380	1099.5	2.689
5.464	1099.5	2.737

Table C.7: Specimen $S-3$.

Δ(cm)	Load(N)	CMOD(cm)	Δ(cm)	Load(N)	CMOD(cm)
0.000	0.0	-	1.316	321.5	0.678
0.051	42.1	0.020	1.356	327.8	0.715
0.089	60.9	0.039	1.410	334.0	0.737
0.140	76.5	0.055	1.455	344.2	0.766
0.206	96.9	0.100	1.491	352.2	0.796
0.239	108.9	0.119	1.544	359.8	0.820
0.279	120.1	0.140	1.585	367.4	0.846
0.328	130.7	0.156	1.659	379.8	0.864
0.386	145.4	0.191	1.699	386.9	0.896
0.439	156.5	0.244	1.786	401.2	0.935
0.498	168.5	-	1.844	411.8	0.959
0.538	177.9	0.265	1.890	419.0	0.988
0.592	189.0	0.290	1.930	426.1	1.012
0.625	196.1	0.308	1.956	433.6	1.026
0.660	202.8	0.319	2.022	440.8	1.103
0.698	210.8	0.347	2.065	447.9	1.085
0.747	-	0.373	2.126	456.3	1.109
0.762	225.0	0.391	2.169	470.1	1.118
0.825	234.4	0.411	2.220	470.1	1.146
0.859	241.0	0.445	2.266	476.8	1.171
0.902	-	0.461	2.304	483.0	1.190
0.930	253.5	0.481	2.375	498.1	1.222
0.978	-	0.505	2.421	-	1.260
1.021	269.5	0.550	2.469	505.7	1.283
1.059	276.6	0.549	2.537	519.0	1.330
1.097	283.7	0.588	2.591	525.3	1.356
1.143	289.5	0.583	2.637	534.2	1.379
1.199	300.6	0.626	2.700	545.3	1.394
1.229	306.4	0.649	2.766	556.0	1.431
1.270	313.1	0.665	2.822	564.9	1.447

Table C.7: Specimen $S-3$ (continued).

Δ(cm)	Load(N)	CMOD(cm)
2.873	573.7	1.476
2.926	582.2	1.496
2.969	589.8	1.515
3.142	619.6	1.586
3.200	628.9	1.600
3.254	638.2	1.632
3.315	647.6	1.652
3.365	654.7	1.673
3.426	661.8	1.700
3.475	-	1.727
3.518	675.6	1.761
3.589	685.4	1.799
3.635	691.6	1.819
3.696	700.5	1.829
3.767	709.9	1.882
3.807	717.9	1.903
3.861	726.8	1.925
3.924	734.8	1.960
3.973	744.1	1.989
4.039	756.1	2.000
4.107	767.7	2.032
4.216	779.2	2.088
4.290	788.1	2.132
4.348	800.6	2.171
4.425	802.4	2.203
4.514	816.6	2.278
4.597	834.4	2.324
4.679	850.4	2.353
4.742	859.3	2.371
4.821	869.5	2.410
4.961	889.6	2.441
5.210	907.3	2.654

Table C.8: Specimen $U - 1$.

Δ(cm)	Load(N)	CMOD(cm)
0.000	0.0	0.013
0.102	109.8	0.032
0.152	150.3	0.066
0.203	183.2	0.081
0.244	203.2	0.128
0.279	222.4	0.155
0.330	249.0	0.166
0.394	-	0.203
0.432	288.6	0.231
0.483	313.1	0.258
0.533	335.8	0.295
0.572	353.6	0.327
0.648	374.5	0.359
0.686	389.6	0.380
0.732	400.3	0.406
0.795	426.1	0.436
0.851	445.6	0.475
0.902	460.3	0.505
0.940	477.2	0.535
0.978	491.5	0.541
1.036	510.6	0.574
1.079	528.4	0.610
1.118	538.2	0.630
1.163	554.6	0.663
1.224	573.7	0.685
1.265	588.9	0.706
1.321	607.6	0.737
1.384	618.7	0.782
1.425	630.7	0.810
1.466	641.8	0.840
1.514	655.1	0.865
1.570	674.7	0.897
1.631	692.1	0.935
1.676	712.5	0.989
1.735	725.4	1.007
1.791	743.7	1.064
1.849	765.9	1.092

DISTRIBUTION LIST

No. of Copies	To

1   Office of the Under Secretary of Defense for Research and Engineering, The Pentagon, Washington, DC 20301

     Commander, U.S. Army Materiel Command, 5001 Eisenhower Avenue, Alexandria, VA 22333-0001
1   ATTN: AMCLD

     Commander, U.S. Army Laboratory Command, 2800 Powder Mill Road, Adelphi, MD 20783-1145
1   ATTN: AMSLC-IM-TL
1   AMSLC-CT

     Commander, Defense Technical Information Center, Cameron Station, Building 5, 5010 Duke Street, Alexandria, VA 22304-6145
2   ATTN: DTIC-FDAC

1   Metals and Ceramics Information Center, Battelle Columbus Laboratories, 505 King Avenue, Columbus, OH 43201

     Commander, Army Research Office, P.O. Box 12211, Research Triangle Park, NC 27709-2211
1   ATTN: Information Processing Office

     Commander, U.S. Army Electronics Technology and Devices Laboratory, Fort Monmouth, NJ 07703-5000
1   ATTN: SLCET-DT

     Commander, U.S. Army Missile Command, Redstone Arsenal, AL 35898-5247
1   ATTN: AMSMI-RD-CS-R/Doc
1   Technical Library

     Commander, U.S. Army Armament, Munitions and Chemical Command, Dover, NJ 07801
2   ATTN: SMCAR-TDC

     Commander, U.S. Army Natick Research, Development and Engineering Center, Natick, MA 01760-5010
1   ATTN: Technical Library

     Commander, U.S. Army Tank-Automotive Command, Warren, MI 48397-5000
1   ATTN: AMSTA-R

     Commander, U.S. Army Engineer Waterways Experiment Station, P.O. Box 631, Vicksburg, MS 39180
1   ATTN: Research Center Library

     Director, U.S. Army Ballistic Research Laboratory, Aberdeen Proving Ground, MD 21005
1   ATTN: SLCBR-DD-T (STINFO)
1   SLCBR-IV-M, Dr. W. H. Drysdale
1   SLCBR-TB-W, Dr. J. Walter

     Director, Benet Weapons Laboratory, LCWSL, USA AMCCOM, Watervliet, NY 12189
1   ATTN: AMSMC-LCB-TL

     Commander, U.S. Army Foreign Science and Technology Center, 220 7th Street, N.E., Charlottesville, VA 22901-5396
3   ATTN: AIFRTC, Applied Technologies Branch, Gerald Schlesinger

     Commander, U.S. Army Aviation Systems Command, Aviation Research and Technology Activity, Aviation Applied Technology Directorate, Fort Eustis, VA 23604-5577
1   ATTN: SAVDL-E-MOS

     NASA - Langley Research Center, Hampton, VA 23665
1   ATTN: Aerostructures Directorate

     Naval Research Laboratory, Washington, DC 20375
1   ATTN: Code 5830

     Office of Naval Research, 800 North Quincy Street, Arlington, VA 22217-5000
1   ATTN: Mechanics Division, Code 1132-SM

No. of Copies	To

Naval Air Development Center, Warminster, PA 18974-5000
1 ATTN: Code 6064
1   AVCSTD/6043

Commander, David Taylor Naval Ship Research & Development Center, Bethesda, MD 20084
1 ATTN: Code 172

U.S. Air Force Office of Scientific Research, Bolling Air Force Base, Washington, DC 20332
1 ATTN: Mechanics Division

Commander, U.S. Air Force Wright Research & Development Center, Wright-Patterson
Air Force Base, OH 45433-6523
1 ATTN: WRDC/MLLN

NASA - Marshall Space Flight Center, Huntsville, AL 35812
1 ATTN: EH01, Dir, M&P lab

1 Committee on Marine Structures, Marine Board, National Research Council, 2101 Constitution
Avenue, N.W., Washington, DC 20418

Director, U.S. Army Materials Technology Laboratory, Watertown, MA 02172-0001
2 ATTN: SLCMT-TML
1   Author

U.S. Army Materials Technology Laboratory,
Watertown, Massachusetts 02172-0001
A COMPUTATIONAL AND EXPERIMENTAL INVESTIGATION
OF MODE I FRACTURE IN AN ELASTOMER -
Claudia J. Quigley

Technical Report MTL TR 90-46, September 1990, 223 pp -
illus-tables

A thickness effect was identified in the Mode I fracture of incompressible hyper-elastic mate-
rials. The plane strain mechanical crack tip field was examined under the assumptions of small
scale nonlinearity using the finite element method. The effect of the constitutive law on the
numerical results was determined by using two different invariants of the Rivlin constitutive
model: the Mooney-Rivlin law and the third order invariant. Crack tip field quantities from
both constitutive laws agreed with the nonlinear asymptotic solution for this problem, although
the region of dominance was small. The nature of the nonlinear crack tip zone was character-
ized both geometrically and kinematically. Application of a local cavitation criterion to the
mechanical crack tip field showed a relationship between the physical properties of a carbon
black filled natural rubber and a critical cavitation event ahead of the crack tip to the amount
of subcritical crack growth prior to crack propagation. Experiments were also performed to
study the thickness effect under near plane strain conditions. Deeply notched cylindrical dumb-
bell test specimens made from a carbon black filled elastomer were loaded in tension until frac-
ture at finite strains. A failure process consisting of extensive blunting of the crack tip,
delamination, and stable crack extension normal to the load direction (i.e., orthogonal to the
pre-existing crack plane) was observed. This process was initialized under small loads and con-
tinued until ultimate rupture of the test specimen into two pieces. As the specimen elongated,
the thickness of successive layers of delaminated material and the incremental amount of stable
crack extension increased. Load and CMOD histories were smooth and could not be related to the
localized material failure occurring under deformation. The value of the J-integral at catastro-
phic rupture was 400kJ/m². A model was presented to explain this failure process.